Spring 2022

Investigation of the thermodynamics of iron phosphate melts and stability of iron phosphate glasses: effects of composition and iron redox ratio

Melodie Linda Schmitt

Department: Materials Science and Engineering

INVESTIGATION OF THE THERMODYNAMICS OF IRON PHOSPHATE MELTS AND STABILITY OF IRON PHOSPHATE GLASSES: EFFECTS OF COMPOSITION AND IRON REDOX RATIO

by

MELODIE LINDA SCHMITT

A DISSERTATION

Presented to the Graduate Faculty of the

MISSOURI UNIVERSITY OF SCIENCE AND TECHNOLOGY

In Partial Fulfillment of the Requirements for the Degree

DOCTOR OF PHILOSOPHY

in

MATERIALS SCIENCE AND ENGINEERING

2022

Approved by:

Richard Brow, Advisor
William Fahrenholtz
Jay Switzer
Jeff Smith
Cheol-Woon Kim

ABSTRACT

Iron phosphate glasses with Fe/P = 0.33 – 0.67, O/P = 3.0 – 3.5 and $Fe^{2+}/\Sigma Fe$ = 0.16 – 0.52 were prepared by altering batch compositions and melt conditions. Thermal analyses indicate polyphosphate glasses with intermediate chain lengths are most stable against devitrification. Heterogeneous crystallization occurs on the glass surface and is dependent on iron valence state, particle size, heating rate, temperature and oxygen availability in the atmosphere. Oxidation of ferrous iron on the glass surface occurs at temperatures as low as T_g, and thus crystallization behavior and stability can be altered via post-melt heat treatments. A novel preparation of thin glass "bubbles" was developed to allow examination of iron phosphate glasses using optical spectroscopy. Absorption near ~476 nm was determined to be predictive of iron valence state, and a deconvolution method is proposed to analyze iron coordination environments. Two models were developed using optical basicity and a statistical, bonding-level representation of the glass structure to investigate the effects of composition on iron redox equilibria and aqueous dissolution behavior. A new approach of calculating heats of formation from group basicities yields a linear correlation with thermochemical data for equivalent crystalline compounds, and the thermodynamic model of iron redox equilibria predicts trends in melt viscosity with bulk basicity, chain length and alkali mixing. An empirical fit of the model predicts iron redox ratios of glasses prepared here within experimental uncertainty. The bond hydration model yields similar spread in predicted versus experimental dissolution rates as previously established models based on free energies of hydration, yet is based solely on composition with no requisite for thermochemical data.

ACKNOWLEDGMENTS

First and foremost, my most heartfelt gratitude is extended to Dr. Richard Brow. I can think of no other person who would have stayed supportive and patient throughout this process, especially given my most unusual timeline. Words will never fully express my appreciation, but please know the examples that you continually set of kindness, patience, leadership, and compassion have inspired and shaped who I am more than any degree program ever could. Thank you.

My coworkers and teachers are too many to name, but thank you for being part of my journey. Thank you especially to my merciful committee members, who generously gave their time despite little notice, and to my friend, Jeremy, for his presence in my life.

To my beautiful Lillietta and my sweet Porter, thank you for motivating me to be the best version of myself and illuminating my priorities. My path in life will forever be guided by you. And Harlan- thank you for your steadfast support and encouragement. I love our family and the life we have created with all of who I am.

While my dad didn't get to see me unexpectedly finish this degree, he was proud of me even when I hadn't. I am grateful that his love of science found its way to me. Mom- You are the most consistent thing in my life, cheering me on from first breath until present day. Thank you for always believing in me and wanting what is best for me.

To anyone reading this who is currently writing your own story- Not much of my first 40 years of life have gone as planned. Yours might not either. Embrace as much of the unexpected as you can. You are stronger than you think you are, and you are capable of wonderful things. Your journey will create waves in places you never expected.

TABLE OF CONTENTS

Page

LIST OF ILLUSTRATIONS

Page

LIST OF TABLES

Page

1. INTRODUCTION

Phosphate glasses can be utilized in many specialty applications due to their diverse and useful properties. In general, phosphate glass melts are better solvents than many other melts and often tend to form larger glass forming regions with alkali and alkaline earth oxides, as well as transition metal oxides and rare earth oxides [1], [2]. One of the most well-known applications for phosphate glasses is an amplifier for high power lasers. Compared to other glass systems, rare earth-doped phosphates have large, simulated emission cross-sections and low thermal-optical coefficients [3], [4]. New interest has also manifested itself in glass fiber lasers and amplifiers for telecommunications for which phosphate glasses would make an obvious choice as host glass [4].

While many phosphate glasses exhibit poor chemical durability and low strength, which often influence feasible applications for these materials, iron phosphate glasses are among the exceptions as they display remarkably durable glass properties, in addition to semiconducting behavior and useful magnetic properties [3], [5]–[8]. The high chemical durability and high solubility of oxides in iron phosphate glasses have led to their development as candidates for vitrifying both high level nuclear wastes (HLW) and low activity wastes (LAW) [9]–[15]. Borosilicate glasses are presently the only glasses approved in the United States for such applications [16] but have proven to be inefficient in the immobilization of certain wastes, such as phosphates, iron oxides, fluorines and heavy metal oxides, such as Bi_2O_3, La_2O_3, Cr_2O_3 and U_3O_8 [9]. The solubilities of many

of these wastes are much higher in iron phosphate glass than borosilicate glass, thus increasing the waste loading potential and decreasing the effective waste volume and cost. Iron phosphates also offer several other advantages over borosilicate compositions, including lower melting temperatures, which could reduce production costs. In addition, these glasses do not undergo liquid-liquid phase separation, commonly present in borosilicate glasses [17], [18].

High level waste glasses must withstand temperature variations and corrosive environments to maintain functionality. Certain properties of iron phosphate glasses, such as crystallization behavior and chemical durability, must therefore be better understood in order to determine the compositions and processing conditions which are most suitable to produce glasses for waste remediation. In addition, the alteration of glass properties and structure with changes in composition and iron redox ratio within the glass need to be investigated. Iron phosphate glasses rarely have the same nominal composition as batched composition due to oxidation or reduction of iron in the melt. Changes in the iron redox ratio are accompanied by changes in the O-to-P ratio of the glass, which in turn alters the glass structure and properties. Understanding how melt and post-melt processing conditions affect the iron redox ratio is essential to controlling glass stability. One goal of this dissertation is to provide such information.

To investigate the effect of chemistry on glass properties, iron phosphate glasses were prepared with a range of Fe/P and $Fe^{2+}/\Sigma Fe$ ratios by altering batch compositions and melt conditions. Batch compositions include glasses with various nominal O/P ratios such that samples would be obtained with a wide range in chain lengths, from the "infinite" chains of the metaphosphates (O/P ~ 3.0) to the two-member dimers of the

pyrophosphates (O/P ~ 3.5). However, the polyphosphate series (O/P ~ 3.25) with intermediate chain lengths was chosen to be most thoroughly studied.

An analytical thermodynamic model has been developed using a statistical distribution of melt constituents and bond energies based on optical basicity to predict the iron redox ratio in iron phosphate glasses using only batch composition and melt conditions. In addition, the effect of post-melt heat treatments on the iron redox ratio and crystallization behavior has been studied for iron phosphate glasses with variations in initial composition, as well as at different heat treatment temperatures. A novel method of using optical absorption spectra of these typically opaque glasses to assess iron valence information is also introduced here.

The glass stability against crystallization and factors associated with crystallization kinetics, such as activation energy, have been evaluated with changes in glass composition (signified by changes in Fe/P and iron redox ratios). Effects of atmosphere and particle size are considered, and changes in the iron redox ratio upon heating are investigated. In addition, an aqueous dissolution model has been developed to predict the corrosion behavior of phosphate glasses based on composition and structure, as well as microscopic basicity of specific oxygen environments.

Several outcomes of this project contribute to the current understanding within the field of glass science. Both analytical models presented here are unlike previously published models and provide new insight into the role of composition and experimental conditions on glass properties and stability. The thermodynamic model is the first of its kind to use a statistical representation of the glass structure and group basicity calculations to calculate thermodynamic parameters, and provides a deeper understanding

into the factors which influence redox conditions of glasses beyond the binary iron phosphate system. It also may help determine how processing conditions can be managed to achieve optimized glass properties.

The corrosion model is the first to model phosphate dissolution based on hydration rates of specific $Q^n - O - M$ bonds rather than bulk glass composition, where Q^n represents phosphate tetrahedra with n bridging oxygen. Approaching dissolution on a per bond basis will allow for changes in predicted dissolution rate due to factors such as coordination changes, distribution of chain lengths, and preferential bonding, all of which could not previously be accounted for. This model may provide new insight into compositional and structural factors which affect the chemical durability of glass and will apply to glass compositions outside of the iron phosphate system.

More specific to the study of iron phosphate glasses, this is one of the first research investigations to focus on the effects of composition on properties and crystallization behavior. Most past work focused on iron pyrophosphate compositions, yet this present research has shown that the polyphosphate compositions are most stable against crystallization. At the time of research completion, crystallization kinetics of iron phosphate glasses had not been extensively studied in previous research. Evaluating the relative stabilities of the different iron phosphate compositions and how those stabilities change with variations in the iron redox ratio will facilitate the optimization of glass composition for the desired applications.

2. BACKGROUND

2.1. THE WONDER OF GLASS

People have long marveled at the beauty and wonder of glass, even before they understood what the material was made of or how to create it. As knowledge was gained and technology improved, scientists were able to fabricate glass in ways that made use of its beneficial properties, not just its beauty. The ability to shape glass made it possible to create vessels and its transparency led the way to the first enclosed windows. Scientists and artisans learned how to tailor compositions to create glasses with different colors, as well as glasses with improved chemical durability and strength. Even today, scientists are still learning how to tailor glass compositions and processing methods in ways to meet the demands for new and innovative products and applications.

One of the remarkable virtues of glass is that it can be composed of any materials, from the most common inorganic constituents to metals, polymers and organic matter, and can be formed through many means, from traditional melting to sol gel synthesis and vapor deposition [2], [19]. It can occur naturally, as obsidian, tektites or fulgurites [20], or can be manmade. The only “requirements” for a material to be classified as a glass is the lack of long-range order and the presence of a glass transformation region [2].

Theories of glass formation were traditionally based on structural theories, including ideas put forth by Zachariasen [21], Smekal [22], Stanworth [23], Sun [24] and Dietzel [25], which focus on compositional criterion to glass formation. Theories considered coordination environments, bond strengths and ionic character of bonds, often quantified using electronegativity. More recent theories of glass formation are based on

kinetic theories, which focus on processing conditions necessary to avoid crystallization of a melt upon cooling. Kinetic theories have provided a basis for investigation of glass viscosity, nucleation and growth, and ways to quantify both glass forming ability and glass stability. While glass forming ability refers to the ability of a glass to resist crystallization upon cooling and is an important concept in the production of glass, glass stability refers to the resistance to crystallization upon reheating and is important for glass reforming or when applications involve elevated temperatures [2].

2.2. PHOSPHATE GLASSES

Along with silica and boric oxide, phosphoric oxide (P_2O_5) is considered a primary glassformer that can readily form a single component glass [2], [21]. However, vitreous P_2O_5 is both extremely hygroscopic and volatile, and does not have many practical applications [19], [26], [27]. The structure of vitreous P_2O_5 consists of PO_4^{3-} tetrahedra which create an interconnected network via P-O-P, or bridging oxygen (BO), bonds with adjacent tetrahedra [26], [28]. Tetrahedra are connected via three BO corners, while the fourth corner contains a double-bonded, terminal oxygen (DBO or TO). The addition of oxides to P_2O_5 will increase the O-to-P ratio, which will depolymerize the structure as non-bridging oxygens (NBO) replace BO, as shown in Figure 2.1 [27], [29], [30]. The phosphate tetrahedral units are classified according to the nature of their oxygen bonds and are described as Q^n units, where n represents the number of bridging oxygens per tetrahedron. Increasing the O-to-P ratio corresponds to shorter chain lengths and a more disconnected structure, changing both the glass structure and glass properties.

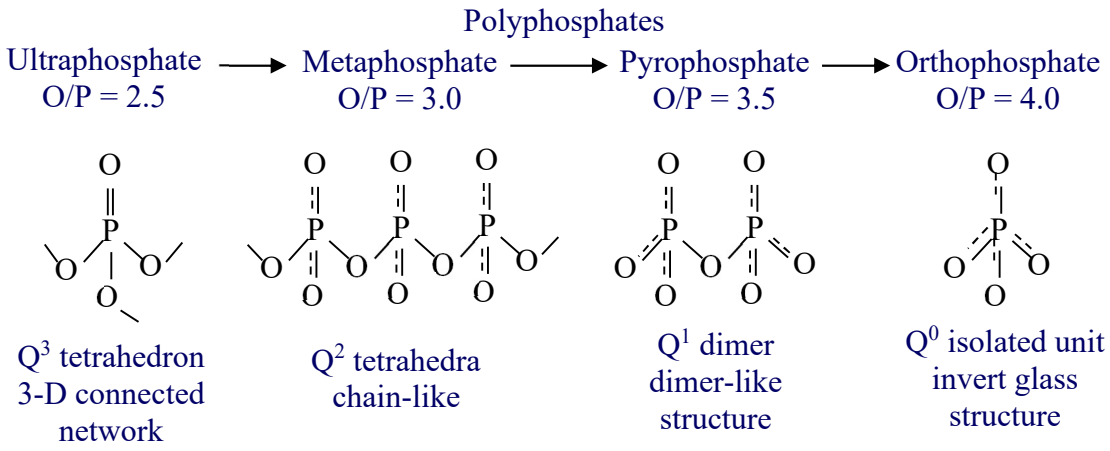

Figure 2.1. Diagram describing the change in phosphate glass structure as the O/P ratio increases.

Phosphate glasses are in general regarded as having low processing temperatures, high thermal expansion coefficients, poor chemical durability, and low glass transition temperatures [2], [26], [28], [31], [32]. However, these properties can be altered via compositional changes, the extent of which is dependent on cation identity and concentration, as well as Q^n species present in the glass. Longer chain lengths can increase the viscosity of the melt, thereby increasing glass transition temperature and crystallization temperature, as longer chains obstruct the rearrangement of atoms necessary for crystallization [28]. Divalent and trivalent cations will provide links between chains and tetrahedra via ionic bonding with non-bridging oxygen, increasing the connectivity of the structure and affecting both thermal expansion and chemical durability. Manipulation of these properties through compositional control has allowed for many suitable applications, several unique to phosphate glasses.

High thermal expansion coefficients and low transition temperatures have led to the development of phosphate glasses as sealing glasses, including applications for alkali

aluminophosphates as aluminum-copper seals and zinc borophosphate glasses as hermetic seals for flat panel displays [33]–[35]. Fast ion conductivity has allowed phosphorus oxynitride glasses [36], [37] and lithium containing phosphate glasses [38], [39] to be used as solid-state electrolytes. The fully resorbable characteristics of phosphate glasses, biocompatibility and ease of fiber preparation has resulted in many biomedical applications in tissue engineering and fiber reinforcement [28], [40]–[43]. High solubility of rare earth oxides and UV transparency make phosphate-based glasses great choices as laser host materials [44]–[46]. Titanophosphate glasses are sustainable and high-index optical glasses [47] as well as electronic conducting glasses [48]–[50]. Zinc phosphates have been used as optical wave guides, glass-polymer composites and solders [51], [52], and the ability to tailor ternary zinc phosphate compositions to achieve controlled zinc leach rates has led to their development as agricultural nutrient sources [53].

2.3. IRON PHOSPHATE GLASSES

Iron phosphate glasses have many beneficial properties and unique applications, some of which are contingent on the iron redox ratio.

2.3.1. Properties and Applications. The addition of iron to phosphate glasses improves chemical durability and results in higher glass strengths [54], [55] in addition to semiconducting properties in glasses with lower thermal expansion coefficients than alkali phosphates [56]. Iron phosphate glasses have many applications. Calcium iron phosphate glass fibers exhibit superior corrosion resistance compared to borosilicate fibers and have been used to strengthen concrete [57], [58]. Iron oxides have also been

added to calcium and sodium phosphate glass fibers for applications as orthopedic implants [59]. Compositions are strengthened and made more durable by addition of iron oxide, and bioabsorptivity can be tailored to degrade at the rate of natural bone healing [60]. Iron phosphates also exhibit semiconducting behavior due to electron hopping between iron valence states [61]–[64].

Recent studies have also suggested iron phosphate glasses as candidates for high level nuclear waste (HLW) remediation [55], [65]–[79]. Borosilicate glasses are currently approved for use in the United States for HLW encapsulation, although sodium aluminophosphates have been used in other countries [72], [80], [81]. Iron phosphate glasses exhibit chemical durability that is equal to or better than borosilicate alternatives, and melting temperatures that are lower by hundreds of degrees, which saves energy and time associated with melting [55], [72], [75], [76], [78]. The improved chemical durability is attributed to the better durability of $Fe-O-P$ bonds as compared to $P-O-P$ bonds. Additionally, neither structure nor chemical durability of the glass changes appreciably with waste loading [55], [76]. In addition to P_2O_5 and Fe_2O_3, many other oxides found in HLW (such as Bi_2O_3, La_2O_3 and U_3O_8) have higher solubility in iron phosphate compositions, which increases waste loading and decreases volume and costs [61], [69], [72], [73], [78]. For example, Huang et al. [73] found that the increased waste loading of chrome oxide in iron phosphate glasses reduced the volume of glass necessary for encapsulation by a factor of nine as compared to alkali aluminum borosilicate glass.

Despite these many beneficial properties, the iron pyrophosphate composition most commonly studied for this application, $40Fe_2O_3 \cdot 60P_2O_5$ $(mol\%)$, exhibits low crystallization temperatures and lacks thermal glass stability [82]–[84], which is a

concern for the application of interest. In order to be effective for HLW encapsulation, certain properties of iron phosphate glasses must be better understood, including crystallization behavior and compositional effects on chemical durability. Changes in composition and processing conditions will vary glass structure and properties, affecting their suitability for remediation.

Although outside the scope of this dissertation, radiation effects have also been studied for iron phosphate glasses [85]–[89]. Sun et al. [88] reported preferential mass loss of P and O compared to Fe, and no detectable change in iron valence state under electron irradiation. Dube et al. [85], however, reported reduction of ferric to ferrous iron, and the crystallization of both ferric and ferric-ferrous phosphate phases upon ion beam irradiation. Jolley and Smith [86] simulated radiation damage cascades for amorphous meta-, pyro- and orthophosphate compositions and determined the quickest phosphate polyhedral recovery times for glasses with low Fe^{2+} content.

2.3.2. Iron Valence State and Structure. A thermodynamic equilibrium will exist between Fe^{3+} and Fe^{2+} ions in a melt, resulting in a ternary oxide glass system, eg. $FeO\text{-}Fe_2O_3\text{-}P_2O_5$. Assuming negligible or minor phosphate volatilization, oxidation or reduction of iron in a melt will alter the O-to-P ratio and thus affect the glass structure and properties.

Figure 2.2 shows a ternary phase diagram for the $FeO\text{-}Fe_2O_3\text{-}P_2O_5$ system, with constant Fe/P ratio lines in blue and constant O/P ratio lines in red. Note that upon reduction of Fe^{3+} to Fe^{2+}, for example, a ferric pyrophosphate composition ($40Fe_2O_3\text{-}60P_2O_5$, O/P = 3.5, Fe/P = 2/3) will convert to a ferric-ferrous polyphosphate as the O/P ratio is decreased, signifying an increase in the average chain length within the glass. The

iron redox ratio and concentration is consequently expected to have an effect on both structure and properties, including possibly crystallization and dissolution.

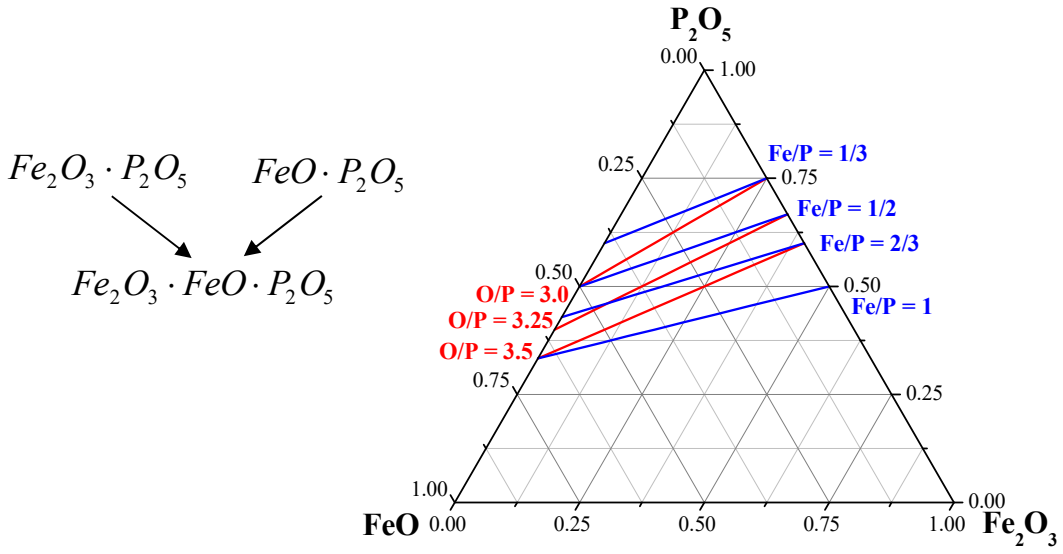

Figure 2.2. Ternary Fe_2O_3-FeO-P_2O_5 diagram showing the change in O/P ratio as iron is oxidized or reduced within a glass.

Glass composition is likely to dictate crystallization products, and thus changing the iron redox ratio changes the likelihood of crystallization. Many iron phosphate crystals and compounds have been reported [90], although most lie far outside of the practical glassforming compositional region. Much of the limited work which has been done on liquidus surfaces within the iron phosphate system [91], [92] has shown inconsistencies with experimental results. Recent improvements to the phase diagram and liquidus surface between $Fe(PO_3)_3$ and Fe_3PO_7 have been reported by Zhang et al. [93] with a reported eutectic at 37.2 mol% Fe_2O_3, which has a slightly lower Fe/P ratio than the often studied pyrophosphate ($40Fe_2O_3 \cdot 60P_2O_5$) composition.

The coordination environments of both ferrous and ferric iron in phosphate glasses have been extensively studied [55], [75], [82], [94]–[102]. Most studies reached similar conclusions that Fe^{3+} can exist in both octahedral and tetrahedral coordination environments and can act as a modifier or network former, while Fe^{2+} is mainly octahedral, with the possibility of also existing in 5-fold coordination. Distortion of the octahedral environment is present for both valencies, and increasing the total iron content increases distortion as well as increases the amount of Fe^{3+} in tetrahedral environments. Karabulut et al. [97] and Concas et al. [102] reported two distinct octahedral sites occupied by Fe^{3+}, but only one by Fe^{2+}.

2.4. IRON REDOX RATIO IN GLASSES

Iron redox ratio plays a crucial role in many glass compositions and properties. The presence of two valence states is responsible for the semiconducting properties of iron phosphate glasses [61]–[64]. Even at trace impurity levels, the iron redox ratio has been shown to influence the UV transmission of high purity optical glasses due to extrinsic charge transfer and s → p absorption bands [103]–[105]. Iron redox state is a very important variable in metallurgical slags [106]–[111], and can effect viscosity, surface tension, oxygen transport and foaming behavior. Manipulating the iron redox ratio is also important in controlling color of soda-lime silicate glasses [112]–[115].

As discussed above, the iron redox ratio in iron phosphate glasses will directly affect glass structure and properties. Kumar and Lin [116] reported a 25% reduction in dissolution rate of $CaO\text{-}P_2O_5\text{-}Fe_2O_3$ glasses with decreasing ferrous iron concentrations, achieved by melting under flowing oxygen atmosphere. Iron redox ratio also impacts

melt viscosities [117] as well as glass transition temperatures and crystallization behavior [83], [118].

Many studies have shown a significant dependence of iron redox ratio on glass melting temperature [83], [84], [118]–[122]. For example, Ray et al. [83] reported an increase in ferrous iron concentrations in $40Fe_2O_3 \cdot 60P_2O_5$ $(mol\%)$ glass from 17% to 57% when melt temperature is increased from 1150°C to 1450°C. Some studies also suggest the ability to alter redox ratio via control of melting atmosphere [82], [97], [119]. Iron redox ratios can also be controlled via reduction reactions with other polyvalent ions in the melt [123]. Many studies have observed a change in iron redox ratio with base glass composition, both changing with cation identity and concentration in binary alkali-silicate melts [119], [124]–[127] and with increasing total iron content [95], [101], [128]. This change with glass composition has often been attributed to the effects of melt optical basicity on redox equilibria.

Optical basicity is a concept established by Duffy and Ingram [129], [130] to provide a measure of the electron donor power of the oxides in a glass or melt and has been extensively studied and reported on [124], [126], [129]–[167]. Optical basicity provides a means to consider acid-base properties within a melt, which is vital to controlling redox equilibria. The optical basicity of an oxide is determined by measuring the spectroscopic frequency shifts in the $^1S_0 \rightarrow {}^3P_1$ bands of a cationic $d^{10}s^2$ probe ion, most commonly Pb^{2+}, Tl^+, and Bi^{3+}. Increased basicity, or electron donation of the oxygens, decreases absorption frequency of the probe ion due to orbital expansion effects within the probe ion, known as the nephelauxetic effect. Theory and measurement procedure of optical basicity are explained in detail in Duffy and Ingram [130], [132].

Basicity of an oxide is calculated using Equation 2.1 [132],

$$\Lambda_{oxide} = \frac{\nu_{free\ ion} - \nu_{oxide}}{\nu_{free\ ion} - \nu_{CaO}} \quad \text{(Equation 2.1)}$$

where Λ is the optical basicity, and ν is the frequency of the $^1S_0 \rightarrow {}^3P_1$ transition for the probe ion in the oxide of interest, in CaO, or as a free probe ion ($\nu_{free\ ion}$ = 60700 cm^{-1} for Pb^{2+}). Calcium oxide is used as the reference for frequency shifts and is therefore designated as having a basicity equal to 1.0. Duffy also defines the basicity modifying parameter, γ, as the inverse of the optical basicity:

$$\gamma = \frac{1}{\Lambda} \quad \text{(Equation 2.2)}$$

The bulk basicity of a glass can be calculated from the optical basicities of the oxide components in the compositions,

$$\Lambda_{bulk} = \sum_i X_i \Lambda_i \quad \text{(Equation 2.3)}$$

where X_i is the fraction of total oxygens contributed by oxide i and Λ_i is the basicity of oxide i. Duffy's concept of basicity can also be applied to individual oxygen atoms or cation groups, and calculations of the average negative charge borne on the oxygen or group can be expressed as microscopic and group basicities, respectively. These concepts and calculations are further detailed in Duffy and Ingram [130] and also in Section 4.3 of this dissertation.

Optical basicity has been shown to be correlated to many properties of ions, oxides and melts, including electronegativity [134], [168]–[170], polarizability [142], [153]–[156], [170], refractive index [169], [171], [172], single bond strength [140], [157]–[163], heat of formation [134], [168], and viscosity [135], [144], [164]–[167], as well as being directly linked to redox ratios of polyvalent ions in glasses [124]–[127], [149], [150], [169], [173]. In fact, when iron redox ratios are plotted versus composition

of alkali silicate glasses expressed as basicity instead of mol% alkali additions (at constant melting temperature), the curves for Li_2O, Na_2O and K_2O all converge to the same line [126], [136], [170], [174]. The concept and calculations of optical basicity and how it pertains to glass properties and behavior will be explored throughout this dissertation.

3. GLASS PREPARATION AND COMPOSITIONAL ANALYSIS

3.1. GLASS PREPARATION

Glasses were prepared as follows for use throughout this dissertation study.

3.1.1. Bulk Glass Batching and Melting. Glasses of composition $x Fe_2O_3$-$(100-x) P_2O_5$ (mol%) with x = 25, 33.33, and 40 were batched from Fe_2O_3 (Alfa Aesar, purity >99.5%) and $NH_4H_2PO_4$ raw materials (Alfa Aesar, purity > 98.0%), and glasses of composition $x Fe_3O_4$-$(100-x) P_2O_5$ (mol%) with x = 23.7, 29.3 and 31.8 were batched from Fe_3O_4 (LaPine Scientific Company) and $NH_4H_2PO_4$ raw materials. Glass of composition $33.33 Fe_2O_3$-$66.67 P_2O_5$ (mol%) was also batched from $Fe_4(P_2O_7)_3$ (Johnson Matthey Electronics) and $NH_4H_2PO_4$ raw materials.

All glasses were melted in alumina crucibles and in ambient atmosphere. Batches containing Fe_2O_3 and $Fe_4(P_2O_7)_3$ raw material were preheated to 800ºC for at least 1 hour to burn off NH_3 and H_2O. Batches containing Fe_3O_4 raw material were more prone to foaming and bubbling over the crucible, so batches were burned off slowly at temperatures between 400 – 800ºC over the course of at least 2 hours.

Crucibles were then transferred to a furnace at 900ºC and ramped up to melting temperatures of 1200 to 1400ºC to obtain different iron redox ratios. The melts were removed after 2 hours, poured onto a steel plate and plate quenched with another steel plate to thicknesses of ~ 4 mm.

Figure 3.1 shows a typical bulk, black iron phosphate glass sample made from melting and pouring.

Figure 3.1. A typical black, opaque iron phosphate glass which results from melting, pouring and quenching.

3.1.2. Glass Bubble Preparation. In addition to bulk glasses, thin, transparent glass segments were obtained by producing glass "bubbles". Glasses of composition $33.33Fe_2O_3$-$66.67P_2O_5$ (mol%) were batched using two different sets of raw materials (Fe_2O_3 + $NH_4H_2PO_4$ and $Fe_4(P_2O_7)_3$ + $NH_4H_2PO_4$,) and were melted in alumina crucibles at 1200ºC in air following the same procedure described for the bulk glasses.

After melting for 2 hours, a silica tube that was attached to an argon tank was inserted into the melt and a gob of molten glass was collected at the end of the tube (see Figure 3.2). The tube and gob of glass were raised above the crucible and the argon was immediately turned on in order to blow a glass "bubble". Bubble wall thicknesses typically ranged from 20 – 60 μm.

3.1.3. Glasses Melted in Argon Atmosphere. Glasses of composition $33.33Fe_2O_3$-$66.67P_2O_5$ (mol%) were also melted under flowing argon atmosphere. Glasses were batched using Fe_2O_3 and $NH_4H_2PO_4$ raw materials and were burned off as described in Section 3.1.1. The crucibles were then placed in a furnace and covered with a hollow silica tube. The tube was fitted with a rubber stopper with two openings. A small silica tube which was attached to an argon tank was inserted into one of the

openings and the second opening was left empty. A diagram depicting this set up is shown in Figure 3.3.

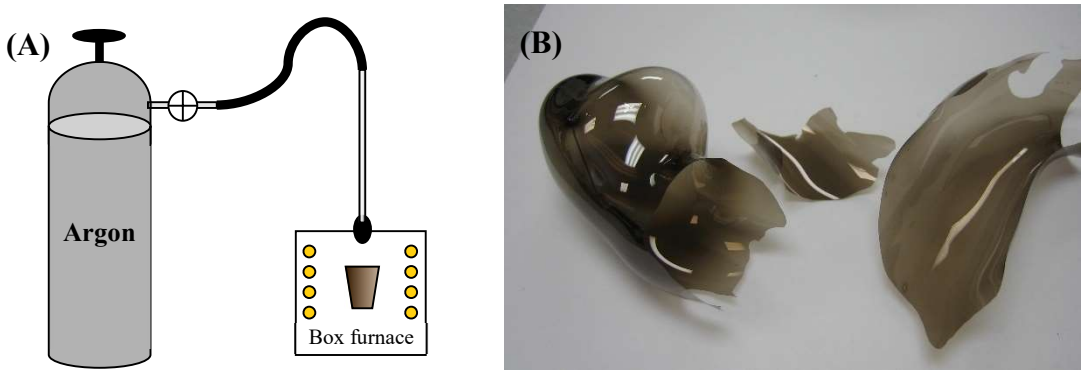

Figure 3.2. (A) Diagram depicting the set-up used for creating thin, glass bubbles; (B) Pieces of iron phosphate glass bubbles produced using such a set-up.

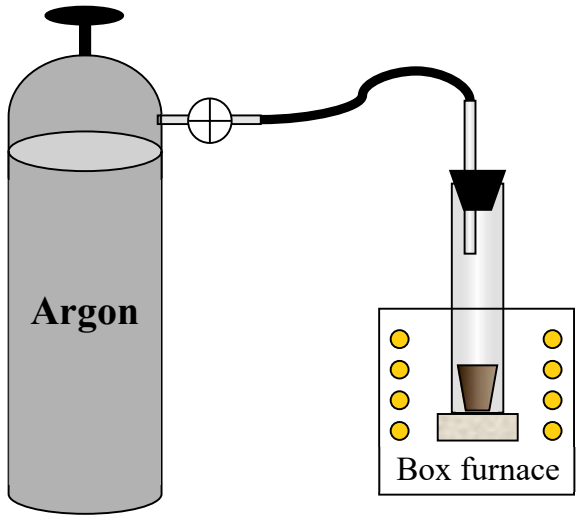

Figure 3.3. Diagram depicting set up for melting under a flowing argon environment.

After the crucibles were placed in the furnace and encased by the silica tube, the argon was turned on and the tube was allowed to fill and equilibrate with the gas for at

least 30 min. The furnace temperature was then increased to melting temperatures of 1200 and 1350°C. Glasses were melted for two hours and were poured and quenched as described in Section 3.1.1.

3.2. GLASS NOMENCLATURE

Glass nomenclature is as follows: The first number indicates the initial O/P ratio of the batch, the middle letters designate the raw materials used, and the last number specifies the melting temperature. For the example 325Fe(III)1200, "325" indicates a polyphosphate batched glass with initial O/P ratio of 3.25, "Fe(III)" indicates ferric iron oxide (Fe_2O_3) was used as the iron source, and "1200" indicates a melting temperature of 1200ºC. "Fe(II/III)" in the glass ID indicates that mixed valence iron oxide (Fe_3O_4) was used as a raw material and "FPP" denotes iron (**F**e) **P**yro**P**hosphate ($Fe_4(P_2O_7)_3$) was used in the batch. Also, glass samples that were prepared as bubbles instead of poured, bulk glasses have "bub" at the end of the sample name, and glasses melted under flowing argon have "Ar" at the end of the sample name.

3.3. COMPOSITIONAL ANALYSIS PROCEDURES

X-ray fluorescence (XRF) and inductively coupled plasma-optical emission (ICP-OE) analysis were used to determine the glass constituents, while Mössbauer spectroscopy and wet chemistry techniques were used to determine iron redox ratios.

3.3.1. XRF Experimental Procedure. XRF was completed at MoSci Corp. in Rolla, Missouri using a SPECTRO X-Lab 2000 spectrometer to determine glass

constituents for the 325Fe(III) and 325FPP series of glasses. Glasses were first crushed using a steel mortar and pestle and sieved to a particle size of 75 – 106 μm.

3.3.2. ICP-OE Experimental Procedure. ICP-OE was performed by the Center for Characterization and Development of Materials (CCDM) at UFSCar/UNESP in São Carlos, Brazil using a Varian VISTA spectrometer on the 300Fe(III) and 350Fe(III) glass series, in addition to the 325Fe(III)1300 sample. Glasses were first crushed using a steel mortar and pestle and sieved to a particle size of 75 – 106 μm.

3.3.3. Mössbauer Experimental Procedure. Mössbauer was performed at Missouri University of Science and Technology in Rolla, Missouri on the 325Fe(III) and 325FPP glass series, in addition to the 300Fe(III)1250, 300Fe(III)1350 and 350Fe(III)1350 glass samples. The Mössbauer spectra were obtained at room temperature, on a spectrometer which utilized a 50mCi cobalt-57 source embedded in a rhodium matrix. The spectrometer was calibrated at room temperature with α-iron foil and the line width of the α-iron spectrum was 0.27 mm/s. Mössbauer absorbers of approximate thickness 100 mg/cm^2 where prepared using 75 – 106 μm powders. The Mössbauer spectra were fit with broadened paramagnetic Lorentzian doublets. Details of this fitting procedure have been discussed previously [6].

Mössbauer on all Fe(III) and Fe(II/III) glasses was performed at the University of Tennessee Space Institute. ^{57}Fe spectra were obtained at room temperature using a SEE Co (Minneapolis, MN) Mössbauer Spectrometer, and Mössbauer spectra were acquired by W302 software and analyzed by Mössbauer spectral analysis software which uses simple Lorentzian functions. Chemical shifts of 1.4 mm/s for Fe^{2+} and 0.3 mm/s for Fe^{3+} were used in fitting the spectra.

3.3.4. Wet Chemistry Experimental Procedure. Titration was performed on all glass compositions. Glass powder was digested in 9M H_2SO_4 at ~70ºC until the glass was fully dissolved. The acid-glass solution was then titrated with a ~2 mM $KMnO_4$ solution until completion was indicated by a pink color [7]. The $KMnO_4$ solution was first standardized against solutions of ferrous ammonium sulfate dissolved in dilute H_2SO_4 (~1 M). The pink indicator color results from excess MnO_4^- in solution once the Fe^{2+} is completely oxidized according to the reaction:

$$MnO_4^- + 8H^+ + 5Fe^{2+} \rightarrow Mn^{2+}{}_{(aq)} + 4H_2O + 5Fe^{3+} \qquad \text{(Equation 3.1)}$$

At least 3 titrations were performed on each glass composition. The results were averaged and the error is taken as one standard deviation in the measurements.

3.4. COMPOSITIONAL ANALYSIS RESULTS

Table 3.1 gives the results of the XRF and ICP chemical analyses. Chemical analysis results shown in italics were determined via ICP-OES, while those shown in bold were determined via XRF. The ICP-OES analysis performed here only sought to detect iron and aluminum. The remaining constituents are assumed to be phosphorus and oxygen and can be calculated using the available data and the measured iron redox ratio.

Mössbauer and wet chemistry measurements of iron redox ratio are given in Table 3.2, and Table 3.3 gives the final glass compositions as calculated from the constituent analysis results in Table 3.1 and the iron redox ratios measured by titration shown in Table 3.2. Reasons for using titration results instead of Mössbauer results for the iron redox ratios are discussed in Section 3.5.1. For compositions where constituent analyses were not available, final glass compositions were calculated using batched Fe/P ratios.

Table 3.1. Chemical analysis results from XRF (shown in bold) and ICP-OES (shown in italics) spectroscopies.

Batched Composition	Melting Temp. (°C)	Sample ID	Chemical Analysis (wt%)			
			Fe	P	Al	Si
$25Fe_2O_3$-$75P_2O_5$ (Initial Fe/P = 0.33, Initial O/P = 3.0, Metaphosphates)	1200	300Fe(III)1200	*Melt crystallized to $Fe(PO_3)_3$*			
	1250	300Fe(III)1250	*21.07*		*0.48*	-
	1300	300Fe(III)1300	*21.99*		*0.79*	-
	1350	300Fe(III)1350	*22.46*		*1.35*	-
$33.33Fe_2O_3$-$66.67P_2O_5$ (Initial Fe/P = 0.50, Initial O/P = 3.25, Polyphosphates)	1200	325Fe(III)1200bub	*Chemical analysis not performed for this sample*			
	1200	325Fe(III)1200	**35.9**	**63.0**	**0.89**	**0.25**
	1250	325Fe(III)1250	**37.1**	**61.8**	**0.87**	**0.26**
	1300	325Fe(III)1300	**36.3** *25.08*	**62.0**	**1.48** *0.65*	**0.25**
	1350	325Fe(III)1350	**37.0**	**60.0**	**2.43**	**0.56**
$33.33Fe_2O_3$-$66.67P_2O_5$ (argon atmosphere)	1200	325Fe(III)1200Ar	*Chemical analysis not performed for this series*			
	1350	325Fe(III)1350Ar				
$33.33Fe_2O_3$-$66.67P_2O_5$ (Initial Fe/P = 0.50, Initial O/P = 3.25, Polyphosphates)	1200	325FPP1200bub	*Chemical analysis not performed for this sample*			
	1200	325FPP1200	**33.5**	**64.5**	**0.73**	
	1250	325FPP1250	**33.5**	**64.4**	**0.96**	
	1300	325FPP1300	**33.2**	**64.1**	**1.64**	
	1350	325FPP1350	**32.9**	**63.7**	**2.22**	
$40Fe_2O_3$-$60P_2O_5$ (Initial Fe/P = 0.67, Initial O/P = 3.5, Pyrophosphates)	1200	350Fe(III)1200	*30.05*		*0.06*	-
	1250	350Fe(III)1250	*31.14*		*0.2*	-
	1300	350Fe(III)1300	*Chemical analysis not performed for this sample*			
	1350	350Fe(III)1350	*29.49*		*0.75*	-
	1400	350Fe(III)1400	*30.62*		*1.21*	-
$23.7Fe_3O_4$-$76.3P_2O_5$ (Initial Fe/P = 0.47, Initial O/P = 3.12)	1200	312Fe(II/III)1200	*Chemical analysis not performed for this series*			
	1250	312Fe(II/III)1250				
	1300	312Fe(II/III)1300				
	1350	312Fe(II/III)1350				
$29.3Fe_3O_4$-$70.7P_2O_5$ (Initial Fe/P = 0.62, Initial O/P = 3.33)	1200	333Fe(II/III)1200	*Chemical analysis not performed for this series*			
	1350	333Fe(II/III)1350				
$31.8Fe_3O_4$-$68.2P_2O_5$ (Initial Fe/P = 0.70, Initial O/P = 3.43)	1200	343Fe(II/III)1200	*Chemical analysis not performed for this series*			
	1350	343Fe(II/III)1350				

3.5. DISCUSSION

The accuracy of analysis methods and redox ratio trends with melting conditions and batch composition are considered below.

3.5.1. Accuracy and Reproducibility of Analysis Methods. While using a consistent technique for all compositional analyses would have been ideal, methods were

chosen throughout the course of this study based on opportunity and availability. One sample (325Fe(III)1300) was analyzed using both XRF and ICP spectroscopies so as to provide a comparison between the techniques. It can be seen from the final glass compositions given in Table 3.3 that both techniques provided remarkably similar results for the proportion of constitutional phases.

Table 3.2. Mössbauer and wet chemistry iron redox ratio results.

Batched Composition	Melting Temp. (°C)	Sample ID	Redox ratio: $100*Fe^{2+}/\Sigma Fe$		
			Wet chemistry	Mössbauer (Missouri)	Mössbauer (Tennessee)
$25Fe_2O_3$-$75P_2O_5$ (Initial Fe/P = 0.33, Initial O/P = 3.0, Metaphosphates)	1200	300Fe(III)1200	Melt crystallized to $Fe(PO_3)_3$		
	1250	300Fe(III)1250	32.0 (1.3)	36.5	35
	1300	300Fe(III)1300	35.6 (1.0)		39
	1350	300Fe(III)1350	35.8 (0.5)	42.7	41
$33.33Fe_2O_3$-$66.67P_2O_5$ (Initial Fe/P = 0.50, Initial O/P = 3.25, Polyphosphates)	1200	325Fe(III)1200bub	16.7 (0.3)		
	1200	325Fe(III)1200	16.8 (0.6)	11.0	18
	1250	325Fe(III)1250	18.9 (0.4)	17.1	20
	1300	325Fe(III)1300	24.2 (0.2)	26.5	26
	1350	325Fe(III)1350	35.1 (1.4)	32.4	34
$33.33Fe_2O_3$-$66.67P_2O_5$ (argon atmosphere)	1200	325Fe(III)1200Ar	18.8 (3.1)		14
	1350	325Fe(III)1350Ar	38.1 (4.0)		32
$33.33Fe_2O_3$-$66.67P_2O_5$ (Initial Fe/P = 0.50, Initial O/P = 3.25, Polyphosphates)	1200	325FPP1200bub	18.9 (0.2)		
	1200	325FPP1200	17.8 (0.9)	12.3	
	1250	325FPP1250	23.6 (0.6)	21.8	
	1300	325FPP1300	29.2 (0.4)	22.5	
	1350	325FPP1350	32.8 (1.8)	31.6	
$40Fe_2O_3$-$60P_2O_5$ (Initial Fe/P = 0.67, Initial O/P = 3.5, Pyrophosphates)	1200	350Fe(III)1200	24.7 (1.4)		25
	1250	350Fe(III)1250	31.3 (0.3)		33
	1300	350Fe(III)1300	31.5 (0.3)		33
	1350	350Fe(III)1350	38.2 (0.7)	38.1	38
	1400	350Fe(III)1400	44.0 (0.5)		46
$23.7Fe_3O_4$-$76.3P_2O_5$ (Initial Fe/P = 0.47, Initial O/P = 3.12)	1200	312Fe(II/III)1200	30.2 (1.2)		21
	1250	312Fe(II/III)1250	37.5 (1.7)		32
	1300	312Fe(II/III)1300	42.0 (1.3)		37
	1350	312Fe(II/III)1350	45.0 (1.3)		39
$29.3Fe_3O_4$-$70.7P_2O_5$ (Initial Fe/P = 0.62, Initial O/P = 3.33)	1200	333Fe(II/III)1200	37.0 (1.3)		29
	1350	333Fe(II/III)1350	52.3 (2.0)		49
$31.8Fe_3O_4$-$68.2P_2O_5$ (Initial Fe/P = 0.70, Initial O/P = 3.43)	1200	343Fe(II/III)1200	20.1 (0.2)		14
	1350	343Fe(II/III)1350	39.6 (0.3)		32

Table 3.3. Calculated glass compositions and important ratios for all glasses. (Italicized compositions were calculated using ICP-OES results, bolded compositions were calculated using XRF results, and unchanged text was calculated using batched Fe/P ratios. Iron redox ratios used in these calculations were all measured via wet chemistry.)

Batched Composition	Melting Temp. (°C)	Sample ID	Glass composition (mol%)				Important ratios		
			Fe_2O_3	FeO	P_2O_5	Al_2O_3	O/P	Fe/P	$Fe^{2+}/\Sigma Fe$
$25Fe_2O_3$-$75P_2O_5$	1200	300Fe(III)1200	Melt crystallized to $Fe(PO_3)_3$						
(Initial Fe/P = 0.33,	1250	300Fe(III)1250	*17.1*	*16.1*	*65.6*	*1.2*	*3.04*	*0.38*	0.32
Initial O/P = 3.0,	1300	300Fe(III)1300	*16.6*	*18.4*	*63.0*	*1.9*	*3.09*	*0.41*	0.35
Metaphosphates)	1350	300Fe(III)1350	*16.8*	*18.8*	*61.1*	*3.3*	*3.15*	*0.43*	0.36
	1200	325Fe(III)1200bub	26.3	10.5	63.2		3.21	0.50	0.17
$33.33Fe_2O_3$-$66.67P_2O_5$	1200	325Fe(III)1200	**26.2**	**10.6**	**62.0**	**1.2**	**3.25**	**0.51**	0.17
(Initial Fe/P = 0.50,	1250	325Fe(III)1250	**26.2**	**12.2**	**60.5**	**1.2**	**3.28**	**0.53**	0.19
Initial O/P = 3.25,	1300	325Fe(III)1300	**23.5**	**15.0**	**59.5**	**2.0**	**3.27**	**0.52**	0.24
Polyphosphates)			*23.0*	*14.7*	*60.7*	*1.6*	3.23	0.50	0.24
	1350	325Fe(III)1350	**19.8**	**21.4**	**55.7**	**3.1**	**3.31**	**0.55**	0.35
$33.33Fe_2O_3$-$66.67P_2O_5$	1200	325Fe(III)1200Ar	25.5	11.8	62.7		3.20	0.50	0.19
(argon atmosphere)	1350	325Fe(III)1350Ar	18.3	22.5	59.2		3.15	0.50	0.38
	1200	325FPP1200bub	25.5	11.8	62.7		3.20	0.50	0.19
$33.33Fe_2O_3$-$66.67P_2O_5$	1200	325FPP1200	**24.3**	**10.5**	**64.2**	**1.0**	**3.17**	**0.46**	0.19
(Initial Fe/P = 0.50,	1250	325FPP1250	**22.2**	**13.7**	**62.8**	**1.3**	**3.17**	**0.46**	0.24
Initial O/P = 3.25,	1300	325FPP1300	**20.0**	**16.5**	**61.3**	**2.2**	**3.18**	**0.46**	0.29
Polyphosphates)	1350	325FPP1350	**18.6**	**18.2**	**60.3**	**2.9**	**3.19**	**0.46**	0.33
	1200	350Fe(III)1200	*27.2*	*17.8*	*54.8*	*0.2*	*3.41*	*0.66*	0.25
$40Fe_2O_3$-$60P_2O_5$	1250	350Fe(III)1250	*24.9*	*22.7*	*51.8*	*0.5*	*3.45*	*0.70*	0.31
(Initial Fe/P = 0.67,	1300	350Fe(III)1300	22.4	24.3	53.3		3.36	0.65	0.32
Initial O/P = 3.5,	1350	350Fe(III)1350	*20.7*	*25.6*	*51.9*	*1.8*	*3.40*	*0.65*	0.38
Pyrophosphates)	1400	350Fe(III)1400	*18.9*	*29.8*	*48.5*	*2.8*	*3.48*	*0.70*	0.44
	1200	312Fe(II/III)1200	20.2	17.5	62.3		3.13	0.46	0.30
$23.7Fe_3O_4$-$76.3P_2O_5$	1250	312Fe(II/III)1250	17.7	21.3	61.0		3.11	0.46	0.38
(Initial Fe/P = 0.47,	1300	312Fe(II/III)1300	16.3	23.5	60.2		3.10	0.47	0.42
Initial O/P = 3.12)	1350	312Fe(II/III)1350	15.3	25.0	59.7		3.09	0.47	0.45
$29.3Fe_3O_4$-$70.7P_2O_5$	1200	333Fe(II/III)1200	21.2	24.8	54		3.32	0.62	0.37
(Initial Fe/P = 0.62,									
Initial O/P = 3.33)	1350	333Fe(II/III)1350	15.2	33.4	51.4		3.27	0.62	0.52
$31.8Fe_3O_4$-$68.2P_2O_5$	1200	343Fe(II/III)1200	30.4	15.3	54.3		3.48	0.70	0.20
(Initial Fe/P = 0.70,									
Initial O/P = 3.43)	1350	343Fe(II/III)1350	21.4	28	50.6		3.41	0.70	0.40

Iron redox ratio results were not nearly as consistent between analysis techniques. For some glass series (ie. 325Fe(III) and 350Fe(III)), iron redox ratios measured by wet chemistry (titration) and Mössbauer are in qualitative agreement, while for other series (ie. 312Fe(II/III) and 343Fe(II/III)), the results are far outside of the expected

measurement uncertainties. It has been shown that Mössbauer results often underestimate the amount of Fe^{2+} and overestimate the amount of Fe^{3+} in glass samples by anywhere from 3 – 5% up to 20% [175]–[177] unless corrections are made for the various coordination states and absorption efficiencies of the iron cations. Some researchers suggest wet chemistry may be the more accurate method [176], [178], [179].

Figure 3.4 shows an example of a Mössbauer spectra obtained for an iron phosphate glass in this study, as well as the curves associated with Fe^{2+} and Fe^{3+} resulting from the fitting parameters used. Assumptions are often made in Mössbauer analyses that absorption efficiencies of ferric and ferrous iron are equivalent. However, it has been shown that this assumption is invalid in glasses with ferric oxide contents greatly than approximately 14 wt% [176]. Accurately fitting Mössbauer patterns also depends on the assigned coordination states of the cations. It is usually assumed that the ferrous oxide exists in a single, octahedrally coordinated environment, although this assumption has been shown to be often invalid [180], [181] and the coordination environment of Fe^{2+} can even be affected by quenching rate [182].

Figure 3.5 shows a comparison of Fe^{2+} content resulting from Mössbauer and titration analyses for the glasses studied here. While results between the two methods are similar for glasses in the Fe(III) series, Mössbauer results indicate a lower amount of ferrous iron in the Fe(II/III) glass series than suggested by titration. Although the reasons behind this result are not immediately clear, it may suggest that the raw material used to batch the glass could affect the coordination environment of the iron cations within the melt, which would alter the results of Mössbauer fitting but not that of titration.

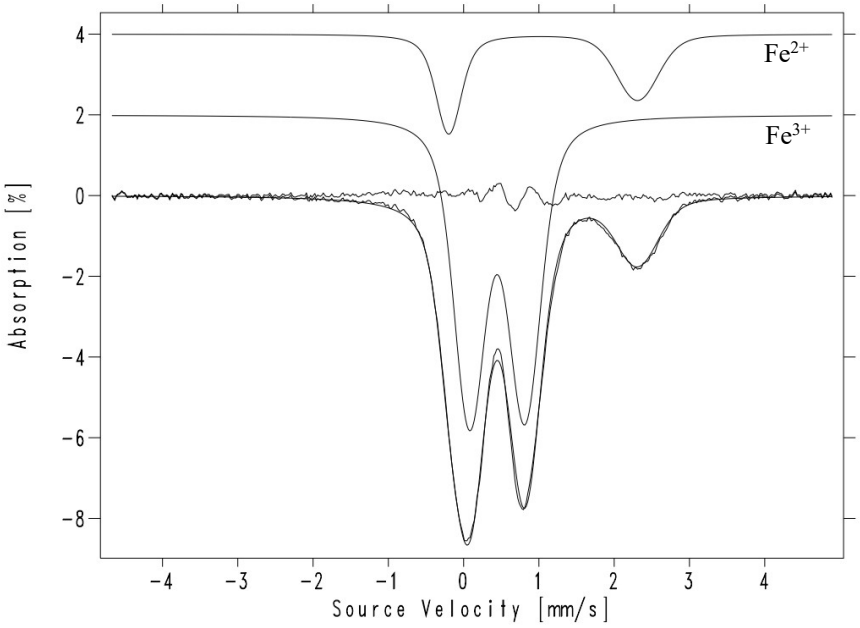

Figure 3.4. Example Mössbauer spectra and fitting patterns for an iron phosphate glass in this study.

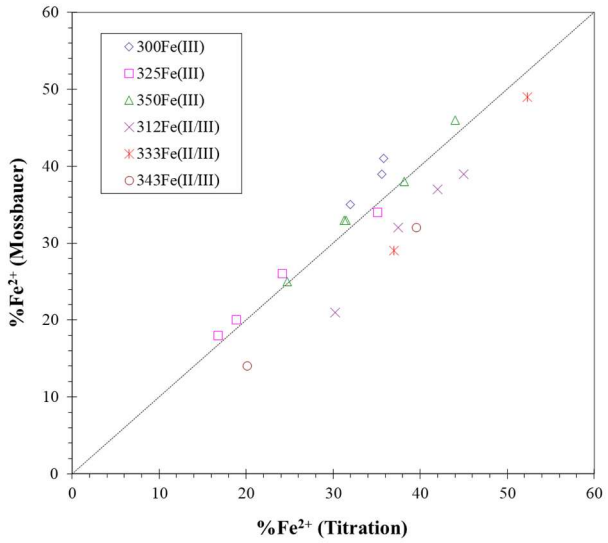

Figure 3.5. Comparison of Mossbauer and titration results for ferrous iron.

While the titration process yields reproducible results, no previously published evidence was found to suggest whether or not the digestion of glass in acid may alter the oxidation state of the iron. To assess the effect of the digestion conditions on the oxidation state of the iron ions, standard solutions with mixed iron valences were prepared using $FeSO_4(NH_4)\cdot 2SO_4\text{-}6H_2O$ and $Fe_2(SO_4)_3\text{-}8H_2O$. The iron compounds were dissolved in 9M H_2SO_4 and were held at ~70ºC for time periods equivalent to those required to fully dissolve the glass samples. The standard solutions were then titrated using the procedure described above, the results of which are shown in Figure 3.6. Error in measurement was taken as one standard deviation from the average. Error bars did not extend past the data markers and therefore are not shown on the figure.

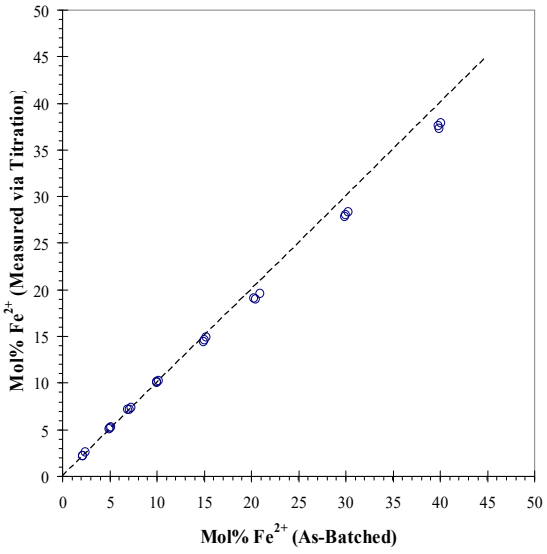

Figure 3.6. Measured versus expected Fe^{2+} content for standard iron solutions prepared using the same conditions used to digest the iron phosphate glasses.

While the ferrous iron content measured via titration slightly underestimates the actual amount in solution for $Fe^{2+} \geq 20$mol%, all values measured were within ±3% of the actual value which is at least as accurate as the results provided by Mössbauer. For consistency's sake and considering the numerous variables and possible errors that are involved in fitting Mössbauer spectra, only the redox ratios determined via titration were used in calculating final glass compositions in this study.

3.5.2. Compositional Trends. Compositional analysis shown in Table 3.3 indicates decreases in the amount of phosphorus with increasing melt temperature and small amounts of alumina and silica contamination from the melt crucible. The decrease in the amount of phosphorus with increased melt temperature is attributed to volatilization during melting [183], resulting in higher Fe/P ratios than expected from the batched glasses. Silica contamination was minor for the glasses for which it was measured and was not considered in determining the final glass compositions. Alumina contamination levels were more significant and increase with increasing melt temperature, reaching levels as high as 3.3 mol% for the metaphosphate composition melted at 1350ºC. The amount of alumina contamination was relatively consistent at a given melt temperature across the glass series studied, with only small increases in contamination as the metaphosphate composition was approached. This dissolution of alumina and large amounts of phosphate loss cause the metaphosphate series to exhibit the largest change in O/P ratio with changes in melt temperature, despite titration results showing not much change in iron redox ratio.

Compositional changes such as volatilization of melt components and contamination from melt crucibles will have an effect on glass properties and structure,

and consequently will be considered when analyzing experimental results. However, these compositional changes will not be considered in the theoretical aspects of the models presented here, as there are too many variables which would need to be accounted for in order to accurately predict the levels of phosphate loss or contamination. For that reason, the iron phosphate glasses will be considered part of the ternary $FeO - Fe_2O_3 - P_2O_5$ system for modeling considerations.

In general, the iron redox ratio increases with increased melt temperature, as seen in Figure 3.7. The glass series which exhibits the least marked dependence of iron redox ratio with temperature is the 300Fe(III) "metaphosphate" series. While this observation could be partially due to the fewer number of data points over which to observe the trend, it may be a result of the more extensive compositional changes due to phosphate volatilization which occur with increased temperature, as discussed above. Section 4 of this dissertation will also consider whether this observation may be explained by the longer average chain lengths or lower group basicity within the metaphosphate melt.

The two ferric polyphosphate series (325Fe(III) and 325FPP) are very similar in final compositions. In general, the 325FPP series lost less phosphate during melting, and thus have lower O/P and Fe/P ratios. In addition, titration results show slightly higher conversion of Fe^{3+} to Fe^{2+} in the 325FPP series, although all results are within experimental uncertainty. These results suggest that the raw materials used in the glass batch do not significantly change the iron redox ratio if starting from the same batched glass composition, although it should be noted that none of the iron sources used here contained oxidizing or reducing agents.

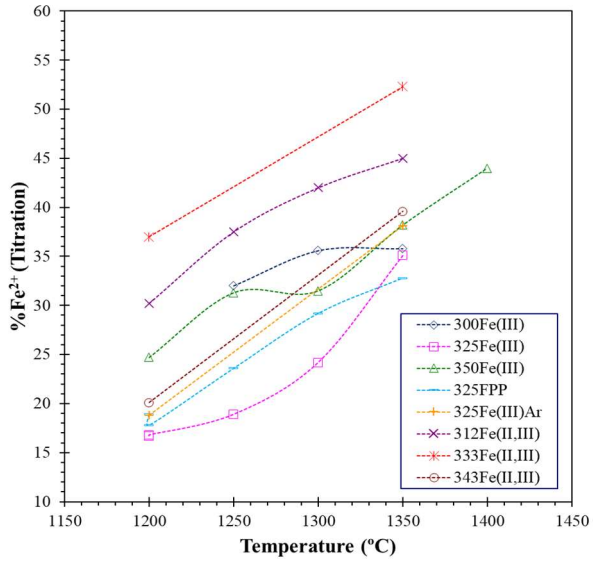

Figure 3.7. Dependence of ferrous iron on melting temperature for all glass series.

Although chemical analysis was not performed on the melts used for the glass bubbles, compositions are assumed to be similar to those for 325Fe(III)1200 and 325FPP1200 since the same raw materials and melting procedures were used. However, it is assumed that the bubbles underwent a faster quenching process than the bulk samples, and thus titration was completed to determine whether the iron redox state was similar to that resulting from the poured and plate quenched 325Fe(III)1200 and 325FPP1200 melts. Titration results given in Table 3.2 show that the two preparation methods yield similar iron redox states.

One unexpected result is the similarity in the iron redox ratios of the 325Fe(III) glasses melted in air and those melted in argon. General thermodynamic principles would suggest that differences in the partial pressure of oxygen will affect the oxidation-reduction reaction between the iron valence states. One possible explanation for this observation is that the oxygen partial pressure above the melt did not appreciably alter the

effective partial pressure, or oxygen fugacity, within the melt. Further studies involving additional melt environments, in addition to oxygen gas solubility measurements within the melt, may provide a deeper understanding and explanation of these results. Such studies were deemed outside the scope of this dissertation. However, other research has suggested that the iron redox equilibria is independent of the oxygen content in the melting atmosphere [6], [89]. This observation will be discussed further in Section 4.

Another interesting result was the notably higher ferrous iron content in the mixed valence polyphosphate glasses (312Fe(II/III) and 333Fe(II/III)) compare to the ferric polyphosphate series (325Fe(III)). Results suggest that the valency of the iron in the batch may affect the final glass iron redox ratio. This may be due to the initial O/P ratio of the melt, which will affect viscosity and kinetics, or could possibly be due to the effect of melt basicity on the redox reaction. It may also suggest that equilibrium was not reached within the melts. These ideas will be further explored in the next section.

Surprisingly, Figure 3.8 shows that there does not appear to be a consistent trend in iron redox ratio with Fe/P ratio within a given glass series at a specific melt temperature. This can be seen in the ferric oxide glasses (Fe(III) series), were Fe^{2+} content for a given melt temperature decreases from the metaphosphate to the polyphosphate compositions, but then increases from the polyphosphate to the pyrophosphate compositions. The opposite is seen in the mixed valency glasses (Fe(II/III) series), where the Fe^{2+} content increases from the 312Fe(II/III) to the 333Fe(II/III) polyphosphate compositions, but then decreases as the glass compositions approach that of pyrophosphate (343Fe(II/III)). The thermodynamic model presented in the next section will also aim to explain these observations in terms of glass basicity and structure.

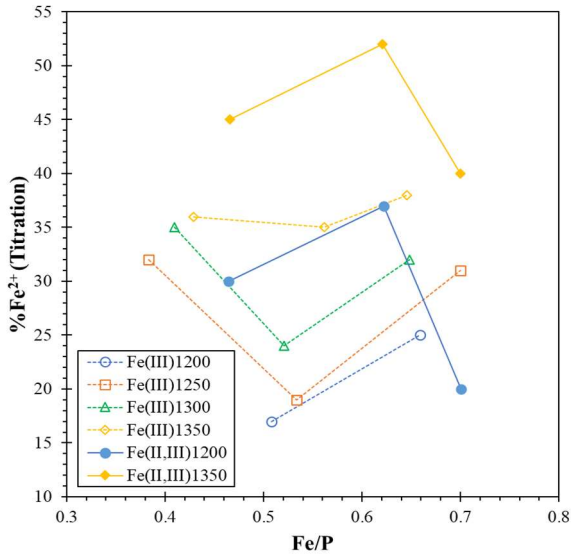

Figure 3.8. Change in ferrous iron content with Fe/P ratio.

3.6. SUMMARY

Bulk iron phosphate glasses have been prepared using the standard melt, pour, and plate quench procedure with compositions ranging from metaphosphate (O/P ~ 3.0) to pyrophosphate (O/P ~ 3.5) and iron to phosphorous ratios (Fe/P) ranging from roughly 0.4 – 0.7. Select compositions have also been prepared as thin glass "bubbles" for optical analysis. Compositional analyses were completed using a combination of XRF, ICP-OES, Mössbauer spectroscopy and wet chemistry. There was good agreement between XRF and ICP-OES results, and it was determined that wet chemistry provided the most reliable and reproducible results for iron redox ratios, with only small underestimations of Fe^{2+} content at total iron content greater than roughly 20%.

Phosphate volatilization is greatest in the glasses near the metaphosphate composition and increases with increasing melt temperature. Small amounts of alumina contamination from the crucible were seen in all glasses where compositional analysis

checked for its presence, reaching values as high as ~3 mol% in glasses melted at 1350ºC.

Different batch raw materials do not seem to affect the final iron redox ratio providing that the raw materials do not contain oxidizing or reducing agents and the batched compositions start with the same proportions of iron valence states. However, the iron valency in the batch did appear to affect the final iron redox ratio. The reasoning for this will be explored in the thermodynamic model proposed in the next section.

In general, increasing the melt temperature results in larger proportions of ferrous iron. However, changing the partial pressure of oxygen in the melt environment did not appear to appreciably change the iron redox ratio. The trend of the ferrous iron content with Fe/P ratio is a bit more complicated. Upon increasing the total iron content in the glass (expressed as Fe/P), glasses batched from raw materials containing all ferric iron first decrease in final ferrous iron content and then increase, while glasses batched from ferric-ferrous raw materials first show an increase in proportion of ferrous iron, followed by a decrease. This conflicting behavior will be explored again in later sections.

3.7. COLLABORATOR CONTRIBUTIONS

The authors gratefully acknowledge Cindy Schwartz for assistance with XRF measurements, Luciana Ghussn for assistance with ICP-OES measurements, and Charles Johnson and Manh Vu for Mössbauer results and fittings.

4. PREDICTING THE IRON REDOX RATIO IN IRON PHOSPHATE GLASSES: A THERMODYNAMIC MODEL

The iron redox equilibrium in iron phosphate glasses is associated with a polymerization reaction within the melt and will directly affect glass structure and properties. It is of interest to be able to predict how batch composition and melt conditions will affect the redox ratio in order to control properties of the final glass. A new method of modeling the thermodynamics of the melt via a bonding-level approach is proposed here. Glass structure is represented as a distribution of Q-units and cation bonds, and enthalpies of reaction are determined using group basicity calculations. Heats of formation calculated using group basicities are compared to reference values for crystalline compounds of equivalent composition and yield a direct correlation. The model is taken as far as could be accomplished without the aid of computational methods to determine configurational entropies. However, entropy values predicted by the model using experimental redox results follow expected trends based on O-to-P ratios, temperature and bulk basicities. This model and review of literature data suggest that melt viscosity plays a role in redox equilibria. It is not yet clear whether the effect of viscosity on redox ratio is due to changes in the entropy of the structural reaction or due to changes in oxygen diffusivity and fugacity within the melt. Future work is recommended to sort out many of the unknowns and to further develop the model to be utilized as intended.

4.1. GENERAL PRINCIPLES

Binary iron phosphate glasses of nominal molar compositions $y Fe_2O_3 \cdot (100-y) P_2O_5$ or $x FeO \cdot (100-x) P_2O_5$ exhibit an iron redox ratio ($Fe^{2+}/\Sigma Fe$) due to the reduction or oxidation of iron upon melting, respectively. This redox ratio and the Fe-to-P ratio directly affect the structure, crystallization and general properties of the glass and may be manipulated through compositional, melt and heat treatment variations [10], [184]–[187]. A model is proposed here to predict the iron redox ratio within the glass based on thermodynamic equilibria, as well as glass basicity and structure.

The reduction of iron within the melt is contingent on the availability of free oxygen anions, which are a result of polymerization of the phosphate network. The structural and energy changes resulting from the polymerization will be dependent on the Q-units and cations present in the melt. A novel statistical approach is taken assuming ideal distributions of melt components, and equilibrium constants and iron redox ratios are calculated with glass basicity considerations. Validity of the model is supported by the comparison of predicted redox ratios with experimental Mössbauer and wet chemistry results from current research and other published data, and the model is expanded beyond the binary iron phosphates to ternary and quaternary iron phosphate compositions. This model will help future researchers better understand the processing methods needed to optimize glass composition and properties for nuclear waste storage, as well as provide insight to redox equilibria within other glass systems.

4.2. DEVELOPING THE MODEL

Experimental procedures for glass preparation and compositional analysis used to fit the model are given in Section 3 of this dissertation.

4.2.1. Model Factors and Initial Assumptions. The goal of this analytical model is to develop an expression which will predict the iron redox ratio in iron phosphate glasses based on known variables, such as glass batch composition and melting conditions. In the most general case, the redox ratio is considered to be a function of batch composition (comp.), raw materials (mater.), melt temperature (T), melt time (t), and melt atmosphere (atmos.) [188]–[190], as in Equation 4.1:

$$\frac{Fe^{2+}}{Fe^{3+}} = f(comp., mater., T, t, atmos.) \qquad \text{(Equation 4.1)}$$

This model can be simplified by only considering cases where the raw materials contain no oxidizing or reducing agents and assuming that the melt is held for a sufficient amount of time such that equilibrium is reached. Under these conditions, the dependence of the iron redox ratio is simplified to a function of three variables:

$$\frac{Fe^{2+}}{Fe^{3+}} = f(comp., T, atmos.). \qquad \text{(Equation 4.2)}$$

The qualitative dependence of the iron redox ratio on each of these variables has been widely studied. It has been shown that, in general, increasing the basicity of a melt composition favors the oxidized state in basic melts yet favors the reduced state in acidic melts [124], [188], [191], [192] and that increasing the melt temperature favors the reduced state [83], [84], [121], [122], [192]. Also, increasing the oxygen fugacity in the melt atmosphere will result in greater iron oxidation [188], [191], [192].

4.2.2. Thermodynamic Equilibrium Expression. The thermodynamic equilibrium of iron ions in the melt is often expressed by Equation 4.3:

$$2Fe^{3+}{}_{(melt)} + O^{2-}{}_{(melt)} \rightarrow 2Fe^{2+}{}_{(melt)} + \frac{1}{2}O_{2(g)} \qquad \text{(Equation 4.3)}$$

where ferrous and ferric iron ions are in equilibrium with free oxygen anions and molecular oxygen [190], [193], [194]. It should be noted that Equation 4.3 describes the iron redox equilibrium in acidic melts (such as phosphates), and different equilibria have been shown to exist in basic glass melts [194]. Although some evidence exists suggesting that the redox ratio decreases slightly when a melt is quenched to form a glass [193], [195], this change is usually ignored and the redox ratio of the melt at the melt temperature is assumed to be the same as that in the resulting glass [193]. As noted by Alberto et al. [196], several studies have concluded using spectroscopic [197], [198], relaxation [199] and calorimetric [200] data that only small changes in local glass structure were observed between quenched glasses, glasses at temperatures near their glass transition, and supercooled melts, and that these small structural changes did not indicate changes in iron redox equilibria outside of the analytical error. Additional studies on other transition metal-phosphate glasses have shown no effect of cooling rate on oxidation-reduction equilibria [201].

For simplicity of this model, we will assume a sufficiently fast quenching rate such that the redox ratio is locked in at the melt temperature. Therefore, we can approximate the iron redox ratio in a glass by finding the thermodynamic equilibrium which exists for Equation 4.3 in a given iron phosphate melt at melt temperature.

The Gibbs free energy change for Equation 4.3, which will be designated with the subscript “rdx” to denote it as the “redox” reaction, is given by:

$$\Delta G_{rdx} = \Delta G^o_{rdx} + RT\, ln\, K_{rdx} \quad \text{(Equation 4.4)}$$

where ΔG^o_{rdx} is the Gibbs free energy change for Equation 4.3 in the standard state, R is the universal gas constant, T is temperature, and K_{rdx} is the thermodynamic equilibrium constant. When Equation 4.3 is in equilibrium, Equation 4.4 will be equal to zero and an expression for the equilibrium constant can be written:

$$K_{rdx} = exp\left(-\frac{\Delta G^o_{rdx}}{RT}\right) = \frac{\left(a_{Fe^{2+}}\right)^2 (fO_2)^{1/2}}{\left(a_{Fe^{3+}}\right)^2 \left(a_{O^{2-}}\right)} \quad \text{(Equation 4.5)}$$

where $a_{Fe^{3+}}$, $a_{Fe^{2+}}$ and $a_{O^{2-}}$ are the thermodynamic activities of the Fe^{3+}, Fe^{2+} and O^{2-} ions in the melt, respectively, and fO_2 is the fugacity of oxygen in the melt.

The standard Gibbs free energy change of Equation 4.3 can be calculated from the changes in standard enthalpy and entropy of the reaction (Equation 4.6), which are calculated from the difference in enthalpy and entropy of the products and reactants in Equation 4.3 (Equations 4.7 and 4.8, respectively).

$$\Delta G^o_{rdx} = \Delta H^o_{rdx} - T\Delta S^o_{rdx} \quad \text{(Equation 4.6)}$$

$$\Delta H^o_{rdx} = 2H^o_{Fe^{2+}{}_{(melt)}} + \frac{1}{2}H^o_{O_{2(gas)}} - 2H^o_{Fe^{3+}{}_{(melt)}} - H^o_{O^{2-}{}_{(melt)}} \quad \text{(Equation 4.7)}$$

$$\Delta S^o_{rdx} = 2S^o_{Fe^{2+}{}_{(melt)}} + \frac{1}{2}S^o_{O_{2(gas)}} - 2S^o_{Fe^{3+}{}_{(melt)}} - S^o_{O^{2-}{}_{(melt)}} \quad \text{(Equation 4.8)}$$

While enthalpy and entropy data are readily available for gaseous ions, they are not easily found for ions in the melt state. However, Ottonello et al. [178] studied the oxidation state of iron in silicate melts and estimated values for standard state molar enthalpies and entropies (H^o and S^o, respectively) of Fe^{3+}, Fe^{2+} and O^{2-} ions in the melt state at a reference temperature (T_r) of 1000 K. The authors also provide heat capacities (C_p) for the ions in the temperature range of 1000 – 2000 K, in addition to enthalpy and entropy data for gaseous oxygen. From these values, the standard state enthalpy and

entropy of all species can be calculated as a function of temperature using Equations 4.9 and 4.10.

$$H_i^o(T) = H_{i,T_r}^o + \int_{T_r}^{T} C_{p,i} dT \qquad \text{(Equation 4.9)}$$

$$S_i^o(T) = S_{i,T_r}^o + \int_{T_r}^{T} \frac{C_{p,i}}{T} dT \qquad \text{(Equation 4.10)}$$

The calculations involved in determining both ΔH_{rdx}^o and ΔS_{rdx}^o, as well as $\Delta H_{rdx(net)}^o$ and $\Delta S_{rdx(net)}^o$ to be introduced later, are shown in Appendix A.

It should be noted that although Ottonello et al. [178] estimated the thermodynamic data for ions in a silicate melt, all data was derived from pure components and crystals except for heat capacities. The authors note that the heat capacity for the FeO melt is not appreciably affected by compositional changes, and that the largest inconsistency may be in the estimation of heat capacity for the Fe_2O_3 melt due to difficulty in measurement. Nevertheless, the thermodynamic data provided by Ottonello et al. [178] were deemed suitable and the best available for the calculations performed in this paper.

4.2.3. Structural Equilibrium Expression. It is the opinion of the authors that the equilibrium expressed in Equation 4.3 only represents a portion of the reactions taking place in the melt. Structural changes must occur in the melt in order for there to be free oxygen anions available to reduce Fe^{3+}. These changes can be seen in the polymerization or depolymerization of the phosphate chains, or the formation of bridging or non-bridging oxygen, respectively. The structural and redox reactions must be considered concurrently to have a complete understanding of the melt equilibria.

The polymerization of the phosphate structure can be expressed by the equilibria between bridging and non-bridging oxygen given in Equation 4.11 and 4.12.

$$2(\equiv P - O^{-}) \rightarrow (\equiv P - O - P \equiv) + {O^{2-}}_{(melt)} \quad \text{(Equation 4.11)}$$

$$2(NBO^{-}) \rightarrow BO + {O^{2-}}_{(melt)} \quad \text{(Equation 4.12)}$$

The relationship described by Equation 4.12 has been established by several investigators for different glass compositions [111], [188], [202], [203].

The Gibbs free energy change for Equation 4.12, which will be designated with the subscript "str" to denote it as the "structural" reaction, is given by:

$$\Delta G_{str} = \Delta G^{o}_{str} + RT\, ln\, K_{str} \quad \text{(Equation 4.13)}$$

where the terms are similar as described above for Equation 4.6. When in equilibrium, the Gibbs free energy can be written in terms of the standard enthalpy and entropy of the reaction and can be expressed in terms of the equilibrium constant:

$$K_{str} = exp\left(-\frac{\Delta G^{o}_{str}}{RT}\right) = exp\left(-\frac{\Delta H^{o}_{str}}{RT}\right) exp\left(\frac{\Delta S^{o}_{str}}{R}\right) = \frac{(a_{BO})(a_{O^{2-}})}{(a_{NBO})^2} \quad \text{(Equation 4.14)}$$

4.2.4. Overall Equilibrium Expression. Combining Equation 4.3 and Equation 4.12 yields the overall melt equilibria:

$${2Fe^{3+}}_{(melt)} + 2(NBO^{-})_{(melt)} \rightarrow {2Fe^{2+}}_{(melt)} + BO_{(melt)} + \frac{1}{2}{O_2}_{(g)} \quad \text{(Equation 4.15)}$$

This overall reaction is described by the two-step process depicted in Figure 4.1.

The Gibbs free energy change of Equation 4.15 is simply the sum of the Gibbs free energy changes of the redox and structural reactions (Equations 4.4 and 4.13, respectively).

$$\Delta G_{eq} = \Delta G_{rdx} + \Delta G_{str} = -RTln(K_{eq}) \quad \text{(Equation 4.16)}$$

Writing the equilibrium constant expression for the overall reaction as depicted in Equation 4.15 yields:

$$K_{eq} = exp\left(-\frac{\Delta G^o_{eq}}{RT}\right) = \frac{\left(a_{Fe^{2+}}\right)^2 (a_{BO})(fO_2)^{1/2}}{\left(a_{Fe^{3+}}\right)^2 (a_{NBO})^2} \qquad \text{(Equation 4.17)}$$

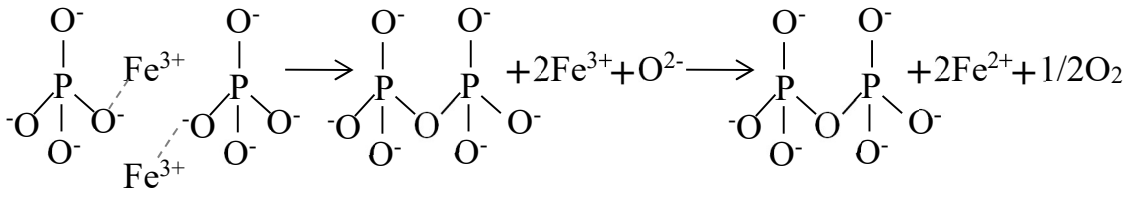

Figure 4.1. Diagram describing the two-step equilibrium reaction in iron phosphate glasses. The first step involves a structural reaction described by Equation 4.4 and the second step involves a redox reaction described by Equation 4.3.

The equilibrium expression no longer requires direct knowledge of the activity or thermochemical data of free oxygen anions, but is instead written in terms of the equilibrium glass structure and redox ratio. To further decouple the model from needing data for free oxygen anions, the Gibbs free energy expressions for both the redox and structural reactions can be rewritten as net reactions without needing to account for the free oxygen anions.

$$\Delta G^o_{rdx(net)} = 2G^o_{Fe^{2+}} + \frac{1}{2}G^o_{O_2} - 2G^o_{Fe^{3+}} \qquad \text{(Equation 4.18)}$$

$$\Delta G^o_{str(net)} = G^o_{BO} - 2G^o_{NBO^-} \qquad \text{(Equation 4.19)}$$

Substituting the equilibrium expressions described above and rearranging yields:

$$K_{eq} = exp\left(-\frac{\Delta G^o_{eq}}{RT}\right) = exp\left(-\frac{\Delta G^o_{rdx(net)}}{RT}\right) exp\left(-\frac{\Delta G^o_{str(net)}}{RT}\right)$$

$$= exp\left(-\frac{\Delta G^o_{rdx(net)}}{RT}\right) exp\left(-\frac{\Delta H^o_{str(net)}}{RT}\right) exp\left(\frac{\Delta S^o_{str(net)}}{R}\right)$$

$$= \frac{\left(a_{Fe^{2+}}\right)^2 (a_{BO})(fO_2)^{1/2}}{\left(a_{Fe^{3+}}\right)^2 (a_{NBO})^2} \quad \text{(Equation 4.20)}$$

4.2.5. Equilibrium Activity Variables. Equilibrium activity variables can be expressed in terms of composition or melt conditions as follows.

4.2.5.1. Activity of iron ions. In general terms, the activities of the iron ions are given as:

$$a_{Fe^{2+}} = \gamma_{Fe^{2+}} X_{Fe^{2+}} \quad \text{(Equation 4.21)}$$

$$a_{Fe^{3+}} = \gamma_{Fe^{3+}} X_{Fe^{3+}} \quad \text{(Equation 4.22)}$$

where $\gamma_{Fe^{n+}}$ is the activity coefficient and $X_{Fe^{n+}}$ is the mole fraction of Fe^{n+}. Ideal solution behavior would suggest that $\gamma_{Fe^{2+}} = \gamma_{Fe^{3+}} = 1$, yet some studies indicate that this may not be a very accurate assumption [204]. While activity coefficients are not assumed to be unity, the ratio of $\gamma_{Fe^{2+}}/\gamma_{Fe^{3+}}$ is assumed to be constant such that:

$$\left(\frac{a_{Fe^{2+}}}{a_{Fe^{3+}}}\right)^2 = \left(\frac{\gamma_{Fe^{2+}} X_{Fe^{2+}}}{\gamma_{Fe^{3+}} X_{Fe^{3+}}}\right)^2 = \left(\frac{\gamma_{Fe^{2+}}}{\gamma_{Fe^{3+}}}\right)^2 \left(\frac{X_{Fe^{2+}}}{X_{Fe^{3+}}}\right)^2 = k_\gamma \left(\frac{X_{Fe^{2+}}}{X_{Fe^{3+}}}\right)^2 \quad \text{(Equation 4.23)}$$

where k_γ is assumed to be constant for iron phosphate glasses in the compositional range studied here.

4.2.5.2. Fugacity of oxygen. It is generally assumed that the fugacity of oxygen in the melt can be approximated by the partial pressure of oxygen in the atmosphere [188]:

$$fO_2 = pO_{2(atmosphere)} \quad \text{(Equation 4.24)}$$

This assumption will be valid in situations which have sufficient diffusivity and are held for an adequate amount of time to reach equilibrium [188], which is more likely the case at higher melting temperatures, longer melt times and open melt atmospheres. For the purposes of this model, it will be assumed that this partition equilibrium of oxygen is achieved.

4.2.5.3. Activity of bridging and non-bridging oxygen. The activities of the bridging and non-bridging oxygen are assumed to be proportional to the molar fraction of bridging and non-bridging oxygen in the melt:

$$a_{BO} = X_{BO} \quad \text{(Equation 4.25)}$$

$$a_{NBO} = X_{NBO} \quad \text{(Equation 4.26)}$$

This proportionality has been shown in previous work and is supported by experimental results [188], [202], [203], and thus will be applied to this model. The fraction of bridging and non-bridging oxygen can be calculated with respect to the O-to-P ratio in phosphate glasses according to Equations 4.27 and 4.28, as given by Brow [3], where $R = \frac{O}{P}$:

$$X_{NBO} = \frac{2R-4}{R} \quad \text{(Equation 4.27)}$$

$$X_{BO} = \frac{4-R}{R} \quad \text{(Equation 4.28)}$$

4.2.6. Structural Assumptions. All equilibrium variables have been defined in terms of melt conditions, such as melt temperature (T) and atmosphere (pO_2), or equilibrium glass composition, such as $X_{Fe^{2+}}/X_{Fe^{3+}}$, X_{BO} and X_{NBO}, with the exception of the structural variables, $\Delta H^o_{str(net)}$ and $\Delta S^o_{str(net)}$. It will be the focus of the remainder

of this section to model these values using an atomic level bonding approach and a statistical representation of the glass structure.

It is important to note that the nature of the structural reactions will depend on the composition of the glass. Phosphate glasses are comprised on phosphate tetrahedra which are often described as "Q-units". A Q^n-unit represents a phosphate tetrahedron with n number of bridging oxygens. The pure phosphate glass composition, P_2O_5, consists of Q^3 units containing three bridging oxygens and one double-bonded, terminal oxygen, creating a three-dimensional interconnected network. As additional oxides are added to the composition, the O-to-P ratio will increase and non-bridging oxygen will be formed. Q^2 units contain two bridging oxygens resulting in phosphate chains or rings, while Q^1 units contain only one bridging oxygen and either terminate a phosphate chain or form dimers. Q^0 units are isolated phosphate tetrahedra which connect to the glass structure only through bonding with non-phosphate cations.

The proportion of Q^n-units present in a glass depends largely on the O-to-P ratio of the composition. Under ideal conditions and no site disproportionation, the fractions of each Q^n-unit can be calculated from the equations given in Table 4.1, which are derived from well-known equations for binary phosphate glasses [3].

Table 4.1. Equations describing fractions of Q-units with respect to the O-to-P ratio (R).

Phosphate	O/P = R	f(Q^3)	f(Q^2)	f(Q^1)	f(Q^0)
Ultraphosphate	2.5	1	0	0	0
Ultra → Meta	2.5 < R < 3	6 - 2R	2R - 5	0	0
Metaphosphate	3	0	1	0	0
Polyphosphate	3 < R < 3.5	0	7 - 2R	2R - 6	0
Pyrophosphate	3.5	0	0	1	0
Pyro → Ortho	3.5 < R < 4	0	0	8 - 2R	2R - 7
Orthophosphate	≥4	0	0	0	1

In actuality, some disproportionation of phosphate chains will exist within the melt, which broaden the distribution of phosphate anions and Q^n-units within a glass. For simplicity of the model, disproportionation reactions will not be considered here, but the effects of which will be discussed later in this section.

In polyphosphate glasses, the O-to-P ratio and fraction of Q^1 and Q^2 units will also impact the average chain length of phosphate anions, $\bar{n}$, which can be calculated with Equation 4.29,

$$\bar{n} = \frac{2}{\sum_j \frac{[M_j] z_j}{[P]} - 1} \qquad \text{(Equation 4.29)}$$

where $[M_j]$ is the molar concentration of metal cation j, z_j is the valence of metal cation j, and $[P]$ is the molar concentration of phosphorus. An example of such a calculation is as follows for an iron pyrophosphate glass of composition $0.4\,Fe_2O_3 \cdot 0.6P_2O_3$ $(mol\%)$:

$$\bar{n} = \frac{2}{\frac{0.8*3}{1.2} - 1} = \frac{2}{2-1} = 2 \qquad \text{(Equation 4.30)}$$

The general polymerization reaction depicted in Equation 4.9 can occur between different Q^n-units present in the glass, which may result in different enthalpies and entropies of reaction. The reactions can be categorized into five most likely situations based on the net change in Q^n-units or chain lengths, as shown in Table 4.2. The notation N_n denotes a chain of length equal to *n* phosphorus tetrahedra. Table 4.2 also lists the approximate O/P ratios expected in glasses where the Q^n-units involved in the given reaction will be predominant.

4.2.7. Statistical Analysis of Structural Reactions. A statistical distribution of the Q^n-unit reactions shown in Table 4.2 can be calculated using the fractions of Q^n-units

Table 4.2. Q-unit and chain reactions that result in a net reaction of $2(NBO^-) \rightarrow BO + O^{2-}$.

	Q-unit reaction	Chain reaction	O/P
Rxn1.)	$2Q^o \rightarrow 2Q^1 + O^{2-}$	$N_1 + N_1 \rightarrow N_2$	~4.0
Rxn2.)	$Q^o + Q^1 \rightarrow Q^1 + Q^2 + O^{2-}$	$N_1 + N_n \rightarrow N_{n+1}$ $(n \geq 2)$	3.5-4.0
Rxn3.)	$2Q^1 \rightarrow 2Q^2 + O^{2-}$	$N_n + N_m \rightarrow N_{n+m}$ $(n,m \geq 2)$	~3.5
Rxn4.)	$Q^1 + Q^2 \rightarrow Q^2 + Q^3 + O^{2-}$	$N_n + N_m \rightarrow$ 3D network $(n \geq 2, m \geq 3)$	3.0-3.5
Rxn5.)	$2Q^2 \rightarrow 2Q^3 + O^{2-}$	$N_n + N_m \rightarrow$ 3D network $(n,m \geq 3)$	~3.0

present in the melt (according to glass composition and as given by Table 4.1) to determine probabilities for reaction as shown in Equation 4.31,

$$P(Q^n \times Q^m) = p * f(Q^n) * f(Q^m) \quad \text{(Equation 4.31)}$$

$$p = 1 \ (for\ n = m)$$

$$p = 2 \ (for\ n \neq m)$$

where $P(Q^n \times Q^m)$ is the probability of a Q^n unit reacting with a Q^m unit and p is the degeneracy of the reaction. An example is given for a phosphate glass with an O-to-P ratio of R = 3.33. According to the ideal distributions given in Table 4.1,

$$f(Q^o) = f(Q^3) = 0 \quad \text{(Equation 4.32)}$$

$$f(Q^1) = 2R - 6 = 0.67 \quad \text{(Equation 4.33)}$$

$$f(Q^2) = 7 - 2R = 0.33 \quad \text{(Equation 4.34)}$$

Therefore, the probabilities of reaction are given by:

$$P(Q^1 \times Q^1) = 0.67 * 0.67 = 0.44 \quad \text{(Equation 4.35)}$$

$$P(Q^1 \times Q^2) = 2 * 0.67 * 0.33 = 0.44 \quad \text{(Equation 4.36)}$$

$$P(Q^2 \times Q^2) = 0.33 * 0.33 = 0.11 \quad \text{(Equation 4.37)}$$

However, the above equations assume equal reactivity of all Q^n-units. It is proposed by the author that reactions involving Q^n units with smaller n values will be favored to those involving Q^n units with larger n values, as they have more non-bridging oxygens available for polymerization. The probabilities of reaction as expressed in Equations 4.31 will therefore be weighted by the number of non-bridging oxygen available for polymerization for each Q^n-unit, which is equal to 3-n per Q^n. To maintain charge balance, one terminal oxygen per phosphate tetrahedra will be unavailable for structural reactions.

The fractional "reactivity", R*, of each Q^n-unit can therefore be expressed as:

$$R^*(Q^n) = \frac{(3-n)*f(Q^n)}{\sum_{n=0}^{3}[(3-n)*f(Q^n)]} \quad \text{(Equation 4.38)}$$

The probabilities for reaction can now be redistributed according to Equation 4.39.

$$P(Q^n \times Q^m) = p * R^*(Q^n) * R^*(Q^m) \quad \text{(Equation 4.39)}$$

Continuing with the example started above with a glass composition with an O-to-P ratio of 3.33, $f(Q^1) = 0.67$ and $f(Q^2) = 0.33$, the reactivity of each Q-unit is:

$$R^*(Q^1) = \frac{2*0.67}{2*0.67+\ *0.33} = 0.80 \quad \text{(Equation 4.40)}$$

$$R^*(Q^2) = \frac{1*0.33}{2*0.67+1*0.33} = 0.20 \quad \text{(Equation 4.41)}$$

The probabilities of reaction are now redistributed to favor those with more non-bridging oxygen, as shown in Equations 4.42 – 4.44.

$$P(Q^1 \times Q^1) = 0.8 * 0.8 = 0.64 \quad \text{(Equation 4.42)}$$

$$P(Q^1 \times Q^2) = 2 * 0.8 * 0.2 = 0.32 \quad \text{(Equation 4.43)}$$

$$P(Q^2 \times Q^2) = 0.2 * 0.2 = 0.04 \quad \text{(Equation 4.44)}$$

4.2.8. Statistical Distribution of Cations to Q-groups. As will be further discussed in Section 4.3.9, understanding the distribution of cations associated with the non-bridging oxygen of the Q^n-units will be necessary to calculate enthalpy of the structural reaction. A statistical distribution of these Q^n-unit arrangements will be determined based on the fraction of cations present in the melt and the fraction of non-bridging oxygens with which they are associated to maintain charge balance.

The number of ways to arrange a phosphate tetrahedral group can be represented as an unordered sampling with replacement, in that the order of cations around the central phosphorus does not affect the group (this idea will be made clearer after the introduction of group basicity in the next section) and cation species will not be "used up" after association with the group. If $\sigma_i(Q^n)$ designates each possible Q^n-unit arrangement, the total number of arrangements is given by N_σ:

$$N_{\sigma(Q^n)} = \binom{k+q-1}{q} = {}_{k+q+1}\mathrm{C}_q = \frac{(k+q-1)!}{q!(k-1)!} \qquad \text{(Equation 4.45)}$$

which represents a sample of q elements chosen from a set of k elements, with repetition allowed. Here, in terms of glass structure and Q-groups, q is equal to the number of non-bridging oxygens with which a cation can bond within the Q^n-group, and k is equal to the number of cation species in the glass compositions (not including phosphorus), such that:

$$q = 3 - n \qquad \text{(Equation 4.46)}$$

$$k = number\ of\ cation\ species\ in\ composition = N_{cat} \qquad \text{(Equation 4.47)}$$

For example, a Q^o tetrahedron in a ferric-ferrous iron phosphate melt will have 3 non-terminal, non-bridging oxygens associated with cation bonding (3 $P - O - M_j^{z_j^+}$ bonds, and thus q = 3), and will have two cation species available for bonding (Fe^{2+}

and Fe^{3+}, and thus k = 2). Therefore, there are 4 possible group arrangements, as given by Equation 4.48 and the arrangement notation that follows.

$$N_{\sigma(Q^o)} = {}_4C_3 = \frac{4!}{3!1!} = 4 \qquad \text{(Equation 4.48)}$$

$$\sigma_1(Q^o) = Q^o - Fe^{3+} - Fe^{3+} - Fe^{3+}$$

$$\sigma_2(Q^o) = Q^o - Fe^{3+} - Fe^{3+} - Fe^{2+}$$

$$\sigma_3(Q^o) = Q^o - Fe^{3+} - Fe^{2+} - Fe^{2+}$$

$$\sigma_4(Q^o) = Q^o - Fe^{2+} - Fe^{2+} - Fe^{2+}$$

Another example would be for a Q^l-unit in a sodium-aluminum-iron phosphate glass. In this case, q = 2 and k = 4 (Na^+, Al^{3+}, Fe^{2+} and Fe^{3+}), and therefore there are 10 possible group arrangements as represented by Equation 4.49.

$$N_{\sigma(Q^1)} = {}_5C_2 = \frac{5!}{2!3!} = 10 \qquad \text{(Equation 4.49)}$$

$$\sigma_1(Q^1) = Q^1 - Fe^{3+} - Fe^{3+}$$

$$\sigma_2(Q^1) = Q^1 - Fe^{3+} - Fe^{2+}$$

$$\sigma_3(Q^1) = Q^1 - Fe^{3+} - Al^{3+}$$

$$\sigma_4(Q^1) = Q^1 - Fe^{3+} - Na^{+}$$

$$\sigma_5(Q^1) = Q^1 - Fe^{2+} - Fe^{2+}$$

$$\sigma_6(Q^1) = Q^1 - Fe^{2+} - Al^{3+}$$

$$\sigma_7(Q^1) = Q^1 - Fe^{2+} - Na^{+}$$

$$\sigma_8(Q^1) = Q^1 - Al^{3+} - Al^{3+}$$

$$\sigma_9(Q^1) = Q^1 - Al^{3+} - Na^{+}$$

$$\sigma_{10}(Q^1) = Q^1 - Na^{+} - Na^{+}$$

Now that possible arrangements of Q^n-units in a composition have been defined, the statistical probability of each arrangement occurring can be determined. The fraction of available non-bridging oxygen bonds associated with a cation $M_j^{z_j^+}$ is given by:

$$X_{P-O-M_j^{z_j^+}} = \frac{\left[M_j^{z_j^+}\right] z_j^+}{\Sigma\left[M_j^{z_j^+}\right] z_j^+} \qquad \text{(Equation 4.50)}$$

where $\left[M_j^{z_j^+}\right]$ is the molar concentration and z_j^+ is the valence of cation $M_j^{z_j^+}$. For example, in a glass of composition $0.3Fe_2O_3 \cdot 0.1FeO \cdot 0.6P_2O_5$, the fraction of $P - O - M_j^{z_j^+}$ bonds would be given by Equations 4.51 and 4.52.

$$X_{P-O-Fe^{3+}} = \frac{(2*0.3)*3}{(2*0.3)*3+(1*0.1)*2} = 0.9 \qquad \text{(Equation 4.51)}$$

$$X_{P-O-F^{2+}} = \frac{(1*0.1)*2}{(2*0.3)*3+(1*0.1)*2} = 0.1 \qquad \text{(Equation 4.52)}$$

The probability of a specific Q^n-unit arrangement, σ_i, is therefore given by Equation 4.53,

$$P(\sigma_i) = p \prod_{j=1}^{3-n} X_{P-O-M_j^{z_j^+}} \qquad \text{(Equation 4.53)}$$

where p is again the degeneracy of the Q^n-unit arrangement, or the number of different ways in which the given arrangement can exist. p will be equal to the permutation of a multiset with 3-n components, or

$$p = \frac{(3-n)!}{m_j!\ldots m_{(3-n)!}} \qquad \text{(Equation 4.54)}$$

where m_j are the number of similar cations of type $M_j^{z_j^+}$ bonded to the Q^n-unit.

In the example given above for a glass of composition $0.3Fe_2O_3 \cdot 0.1FeO \cdot 0.6P_2O_5$ and fraction of $P-O-M_j^{z_j^+}$ bonds as given by Equations 4.51 and 4.52, we know from Equation 4.48 that there are 4 bonding arrangements for Q^o-units which can be expressed as:

$$\sigma_1(Q^o) = Q^o - Fe^{3+} - Fe^{3+} - Fe^{3+} \qquad \text{(Equation 4.55)}$$

$$\sigma_2(Q^o) = Q^o - Fe^{3+} - Fe^{3+} - Fe^{2+}$$

$$\sigma_3(Q^o) = Q^o - Fe^{3+} - Fe^{2+} - Fe^{2+}$$

$$\sigma_4(Q^o) = Q^o - Fe^{2+} - Fe^{2+} - Fe^{2+}$$

p calculations for these arrangements are as follows:

$$p(\sigma_1) = \frac{3!}{3!0!} = 1 \qquad \text{(Equation 4.56)}$$

$$p(\sigma_2) = \frac{3!}{2!\,1!} = 3$$

$$p(\sigma_3) = \frac{3!}{1!\,2!} = 3$$

$$p(\sigma_4) = \frac{3!}{0!\,3!} = 1$$

The probability of each of these arrangements are therefore given in Equation 4.57.

$$P(\sigma_1) = 1 * (0.9) * (0.9) * (0.9) = 0.729 \qquad \text{(Equation 4.57)}$$

$$P(\sigma_2) = 3 * (0.9) * (0.9) * (0.1) = 0.243$$

$$P(\sigma_3) = 3 * (0.9) * (0.1) * (0.1) = 0.027$$

$$P(\sigma_4) = 1 * (0.1) * (0.1) * (0.1) = 0.001$$

This statistical distribution of Q-units, Q-reactions and Q-group arrangements will now allow for the calculation of structural changes upon polymerization once enthalpies and entropies are assigned to the reacting Q-groups.

4.2.9. Optical Basicity and Enthalpy of Structural Reaction. Optical basicity is a concept established by Duffy and Ingram [129], [130] to provide a measure of the electron donor power of the oxides in a glass or melt. It provides a means to consider acid-base properties within a melt, which is vital to controlling redox equilibria. Ionic oxides are associated with basic properties and yield a larger overall negative charge borne by the oxygen atoms in the system, while covalent oxides yield a lesser negative charge borne by the oxygen and are associated with acidic properties in a glass melt [170]. The optical basicity of an oxide is related to many other properties, such as polarizability and electronegativity, and can affect many other properties of a glass, including refractive index [133], [141], [142], [205], [206].

Although the optical basicity of a glass is an experimentally determined property, it can be theoretically approximated using Duffy's approach and constants, as described in detail elsewhere [207]–[209]. The bulk optical basicity of a glass is approximated from the optical basicity of each melt component using the following equation [193], [210]:

$$\Lambda_{bulk} = X_{AO_{a/2}}\Lambda_{AO_{a/2}} + X_{BO_{b/2}}\Lambda_{BO_{b/2}} + \ldots \qquad \text{(Equation 4.58)}$$

where $X_{nO_{n/2}}$ is the equivalent proportion of oxygen that each component contributes and $\Lambda_{nO_{n/2}}$ is the optical basicity of that component. For any oxide, $\Lambda = 1/\gamma$, where γ is the corresponding basicity modifying parameter. The optical basicity and basicity modifying parameter values for the individual oxides which were used in this study, including values used to fit the model to ternary and quaternary glass systems from literature, are given in Table 4.3 [208].

It has been shown [211] that using Duffy's theoretical approach to calculate bulk optical basicity is valid for most phosphate glasses, and results in values which are just

slightly higher than the observed experimental values. It should be noted that studies have shown that there tends to be a balancing effect between different oxides such that the bulk basicity of the glass does not change with temperature [212]. For this reason, temperature was not considered here in the basicity calculations.

Table 4.3. Optical basicity of melt components.

Element	Valence	Oxide	Basicity Modifying Parameter, γ	Optical Basicity, Λ	References
P	5	P_2O_5	3.00	0.33	Duffy 2004
Fe	3	Fe_2O_3	1.30	0.77	Duffy 1976
Fe	2	FeO	1.00	1.00	Duffy 2001
Li	1	Li_2O	1.00	1.00	Duffy 2004
Na	1	Na_2O	0.87	1.15	Duffy 2004
K	1	K_2O	0.73	1.40	Duffy 2004
Mg	2	MgO	1.28	0.78	Duffy 2004
Ca	2	CaO	1.00	1.00	Duffy 2004
Ba	2	BaO	0.87	1.15	Duffy 2004
Al	3	Al_2O_3	1.66	0.60	Duffy 2004
Mn	2	MnO	1.00	1.00	Duffy 2001

While the bulk basicity of the glass provides useful information concerning the bulk behavior and properties of the melt, it is more useful in this case to look at the microscopic and group basicities of the individual oxygens and Q^n-units that are involved in the structural reactions of interests. Duffy and Ingram [130] proposed that the microscopic optical basicity, λ, of an individual oxygen atom bonded to cations A and B can be calculated using Equation 4.59,

$$\lambda = 1 - \left\{\left(\frac{z_A r_A}{2}\right)\left(1 - \frac{1}{\gamma_A}\right) + \left(\frac{z_B r_B}{2}\right)\left(1 - \frac{1}{\gamma_B}\right)\right\} \qquad \text{(Equation 4.59)}$$

where z_A is the valence of cation A, r_A is the ionic ratio of cation A with respect to the total number of oxides (r_A = 1/(coordination number)$_A$), and γ_A is the basicity modifying parameter of cation A. For example, an oxygen that bridges a phosphorus atom and an octahedrally coordinated ferric iron atom will have a microscopic basicity of:

$$\lambda_{P-O-F^{3+}} = 1 - \left\{\left(\frac{5*1/4}{2}\right)\left(1 - \frac{1}{3}\right) + \left(\frac{3*1/6}{2}\right)\left(1 - \frac{1}{1.3}\right)\right\} = 0.526 \quad \text{(Equation 4.60)}$$

Duffy used this same concept to calculate group basicities (noted here as λ_g to differentiate from microscopic basicities, although Duffy uses the symbol λ for both microscopic and group basicities) for oxyanion units, such that

$$\lambda_g = 1 - \left\{\left(\frac{z_A r_A}{2}\right)\left(1 - \frac{1}{\gamma_A}\right)\right\} \quad \text{(Equation 4.61)}$$

where r_A is now taken as the inverse of the number of oxygens "owned" by the central cation in the group. For example, a Q^2 phosphate tetrahedral unit consists of two bridging oxygens, which are each half "owned" by the central phosphate, and two non-bridging oxygens, both of which are fully "owned" by the central phosphate. The central phosphate therefore is associated with 3 total oxygens, and r_{Q2} = 1/3. The group basicity of a Q^2-unit is therefore:

$$\lambda_{Q2} = 1 - \left\{\left(\frac{5*\left(\frac{1}{3}\right)}{2}\right)\left(1 - \frac{1}{3}\right)\right\} = 1 - \frac{5}{9} = 0.444 \quad \text{(Equation 4.62)}$$

Duffy's consideration of group basicity assumes complete neutralization within the oxyanion units, which is an approximation of the conditions in basic, ionic melts (in general, components with $\Lambda \geq 1$). Ferric iron has a basicity of 0.77 and will not follow the assumption of complete neutralization. Therefore, the calculations for group basicity were taken a step further in this model and modified to account for the individual microscopic basicities of each oxygen within a given Q^n-unit.

Each Q^n-unit is considered in ownership of $4-\frac{1}{2}n$ oxygen, with n bridging oxygen, 1 terminal oxygen, and $3-n$ non-bridging oxygen which are each associated with a cation, $M_j^{z_j+}$, in the melt. The group basicity of that Q^n unit will be taken as a weighted average of the microscopic basicity contributions of each oxygen according to Equation 4.63:

$$\lambda_{Q^n} = \frac{1}{4-\frac{n}{2}}\sum r\lambda = \frac{1}{4-\frac{n}{2}} * \left(\frac{1}{2} * n * \frac{1}{6} + \frac{7}{12} + \sum_j \lambda_{P-O-M_j^{z_j+}}\right) \text{(Equation 4.63)}$$

where n is the number of bridging oxygen, r is the number of oxygen "owned" in a bond (r = 0.5 for BO and 1 for NBO), $\frac{1}{6}$ is the microscopy basicity of each bridging oxygen, $\frac{7}{12}$ is the microscopy basicity of the terminal oxygen, and $\sum_j \lambda_{P-O-M_j^{z_j+}}$ is the sum of microscopic basicities for all non-bridging oxygens with associated cations $M_j^{z_j+}$. For example, in a ferric phosphate glass, a Q^2-unit will consist of two bridging oxygen, one terminal oxygen, and one non-bridging oxygen that is bonded to an octahedrally coordinated Fe^{3+} cation. The group basicity of that Q^2-unit can be calculated as follows, and yields a result that is between the microscopic basicity of the $P-O-Fe^{3+}$ bond calculated in Equation 4.60 and the group basicity of a completely neutralized phosphate Q^2-unit as calculated in Equation 4.62:

$$\lambda_{Q^2(Fe^{3+})} = \frac{1}{4-1} * \left(2 * \frac{1}{6} + \frac{7}{12} + 0.526\right) = 0.481 \qquad \text{(Equation 4.64)}$$

Using relationships between electronegativity and basicity and applying Pauling's treatment of electronegativity to calculate bond energies [213], Duffy [134] determined

the following empirical relationship between bond energies per oxygen atom, Q/b, of simple oxides, M_aO_b, as a function of bulk basicity:

$$\frac{Q}{b} = 2 * \left[3.85 - 1.16\Lambda(M_aO_b) - \frac{0.75}{\Lambda(M_aO_b)}\right]^2 - 1.13 \text{ (eV)} \quad \text{(Equation 4.65)}$$

Converting this relationship to heat of formation yields Equation 4.66:

$$\Delta H_f^o = -192.96b * \left[3.85 - 1.16\Lambda(M_aO_b) - \frac{0.75}{\Lambda(M_aO_b)}\right]^2 + 109.02b \text{ (kJ/mol)} \quad \text{(Equation 4.66)}$$

This study will extend this concept of using basicity to determine heats of formation to more complex oxide compositions by using the group basicity calculations introduced in this work.

Phosphate group basicities were calculated using Equation 4.63 for metaphosphate (Q^2), pyrophosphate (Q^1) and orthophosphate (Q^o) groups with different cations bonding to the available non-bridging oxygens, and thus different microscopic basicities for each non-bridging oxygen. These group basicities were used to calculate heats of formation of each arrangement of meta-, pyro- or orthophosphate unit according to Equation 4.67, which was derived from Equation 4.66:

$$\Delta H_f^o(\sigma(Q^n)) = -192.96b * \left[3.85 - 1.16\lambda_{\sigma(Q^n)} - \frac{0.75}{\lambda_{\sigma(Q^n)}}\right]^2 + 109.02b \text{ (kJ/mol)} \quad \text{(Equation 4.67)}$$

These heats of formation for Q-groups, including some with mixed cations, were then compared to heats of formation for crystalline compounds of the same molar composition at both 298K and 1500K, which is a temperature corresponding to the typical batch melting temperature range of many iron phosphate compositions. Figure 4.2 shows a clear linear correspondence exists between the two values for most compounds, and that the temperature at which the heat of formation of the crystalline compound is taken does not change the correspondence between enthalpy values. However, Figure 4.2

also shows that transition metal phosphates do not follow the trend observed for other phosphate compounds.

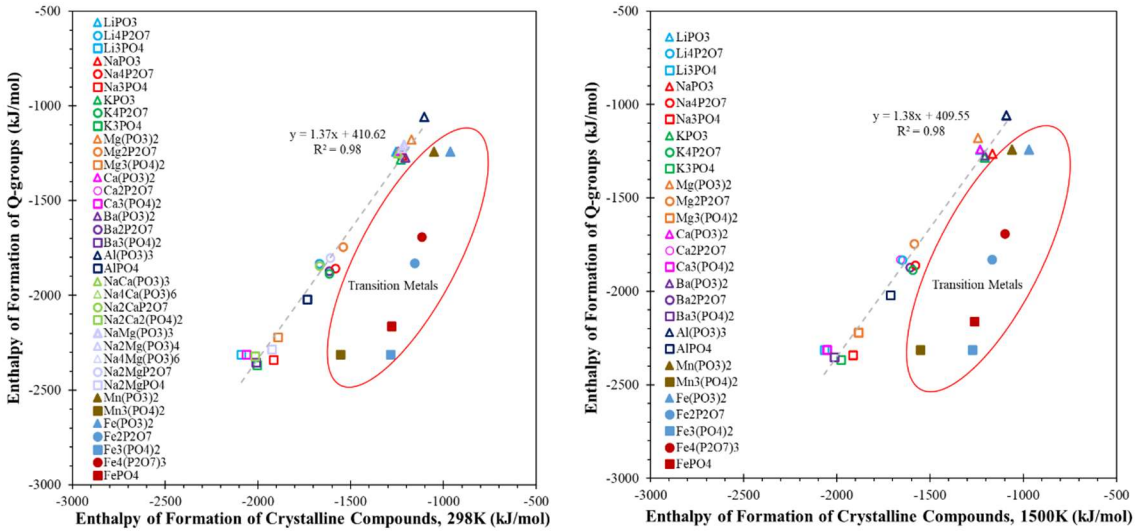

Figure 4.2. Enthalpy of formation of phosphate Q-units calculated using Equations 4.63 and 4.67 versus enthalpy of formation of phosphate crystalline compounds with the same stoichiometric ratios (per mole of phosphorus).

This noncompliance of transition metals to the observed behavior of other compounds was also observed by Duffy [134], [214]. Equation 4.65 is derived from the relationship between the bond energy and the electronegativity difference between the oxygen and the cation it is bonded with. Most oxides follow the same relationship between electronegativity difference and basicity, but transition metal oxides exhibit higher than expected oxygen electronegativities for a given oxide basicity [214]. This larger electronegativity was determined to arise from an additional contribution of *d-d* orbital overlapping between adjacent metal ions to the heat of formation. Binks and Duffy [214] were able to calculate a "correction" to the oxygen electronegativity and thus

the heat of formation of simple transition metal oxides by measuring the difference between experimental values and those expected based on basicity of the oxide. This correction to the heat of formation was attributed to the enthalpy contribution of the *d-d* orbital bonding.

Using a similar approach, a correction to the heat of formation contribution of the $P-O-M_j^{z_j^+}$ bonds in a Q-group can be calculated by measuring the difference between expected and observed values for the enthalpy of formation based on the relationship shown in Figure 4.2. Such a calculation yields corrections (per $P-O-M_j^{z_j^+}$ bond) to the total enthalpy of formation of a Q-group of roughly -328 kJ/mol, -280 kJ/mol, and -203 kJ/mol for $M_j^{z_j^+}$ = Fe^{2+}, Fe^{3+}, and Mn^{2+}, respectively. Results here correspond well to the corrections assigned by Binks and Duffy [214] to FeO and MnO (Fe_2O_3 was not included in their study). While Binks and Duffy were studying simple transition metal oxides, they found the enthalpy of formation correction for Mn^{2+} orbital overlap to be roughly two-thirds that of Fe^{2+}, which is similar to the contribution ratio found here. Differences in the contribution of the orbital overlap to enthalpy were attributed to differences in electron configurations and spin states of the cations, with the larger contribution in Fe^{2+} resulting from the smaller exchange energy of the high spin d^6 electron configuration compared to the high spin d^5 configuration of Mn^{2+}. Exchange energies will increase with increasing oxidation number, so Fe^{3+} is also expected to have a larger exchange energy and therefore smaller contribution to the enthalpy of formation compared to Fe^{2+}, which agrees with the contribution results calculated here.

Taking the calculated *d-d* contributions into account and recalculating the enthalpy of formation of Q-groups for the transition metal phosphates yields the corrected values shown in Figure 4.3. The results here suggest that enthalpies of formation of Q-groups as described herein provide consistent and reliable values to describe the enthalpy change of Q-group reactions.

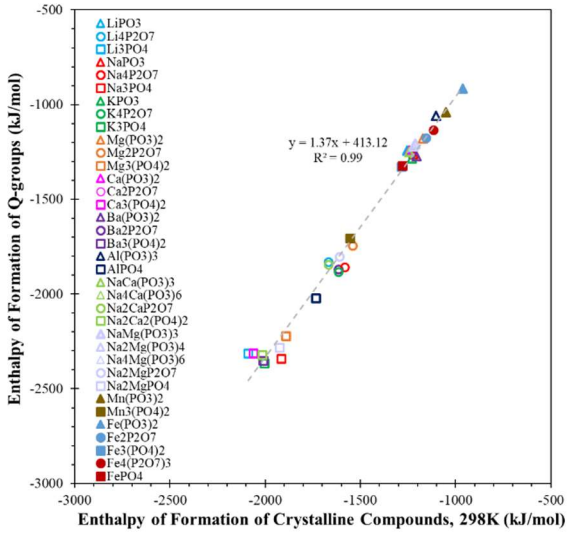

Figure 4.3. Enthalpy of formation of phosphate Q-units versus enthalpy of formation of phosphate crystalline compounds with the same stoichiometric ratios (per mole of phosphorus). Q-group enthalpies are calculated using Equations 4.58 and 4.62 and include corrections to the enthalpy contribution of transition metal cations to account for d-d orbital bonding.

4.2.10. Enthalpy of Structural Reaction. The structural polymerization reactions taking place upon iron reduction in the melt can be described by the *Q*-unit reactions given in Table 4.2. The oxygen anion can be disregarded in the reactions because only the net reactions are being considered, as described in Section 4.3.4.

The enthalpy of reaction can be written as the enthalpy difference between the products and reactants:

$$\Delta H^o_{str} = H^o_{f(products)} - H^o_{f(\ reactants)} \quad \text{(Equation 4.68)}$$

$$\Delta H^o_{str}(Q_{rxn}) = H^o_f(Q^{n+1}) + H^o_f(Q^{m+1}) - H^o_f(Q^n) - H^o_f(Q^m) \quad \text{(Equation 4.69)}$$

The overall enthalpies of formations of the Q^n-units were calculated using the fractional contributions of each possible arrangement,

$$H^o_f(Q^n) = \sum_{i=1}^{N_\sigma} H^o_f(\sigma_i(Q^n)) * P(\sigma_i(Q^n)) \quad \text{(Equation 4.70)}$$

where $H^o_f(\sigma_i(Q^n))$ is given by Equation 4.67, $P(\sigma_i(Q^n))$ is given by Equation 4.53, and N_σ is given by Equation 4.45. The change in enthalpy for each of the Q-reactions described in Table 4.2 can now be calculated using Equation 4.69 and Equation 4.70. The overall ΔH^o_{str} will be a sum of contributions of these reactions,

$$\Delta H^o_{str} = \sum_{n,m=0}^{2} \Delta H^o_{str}(Q_{rxn}) * P(Q^n x Q^m) \quad \text{(Equation 4.71)}$$

where $\Delta H^o_{str}(Q_{rxn})$ is given by Equation 4.69 and $P(Q^n x Q^m)$ is given by Equation 4.39.

4.2.11. Entropy of Structural Reaction. As stated earlier, phosphate glasses are generally described as polymeric in that they consist of phosphate anion chains of average length determined by the O-to-P ratio, as given in Equation 4.29. The entropy changes within the melt resulting from polymerization reactions are suggested here to be largely due to changes in the configurational entropy of these phosphate chains.

Adam and Gibbs [215] suggested a viscosity-temperature dependence involving the configurational entropy of a system, which assumes the flow of a melt to be dependent on the rearrangement of structural units:

$$\eta = \eta_o exp\left(\frac{A}{TS_c}\right) \quad \text{(Equation 4.72)}$$

where η is the viscosity, η_o is a pre-exponential constant, and S_c is the configurational entropy. A is given by Equation 4.73,

$$A = \frac{\Delta\mu S_c^*}{R} \qquad \text{(Equation 4.73)}$$

where $\Delta\mu$ is the potential barrier hindering rearrangement and S_c^* is the configurational entropy of the smallest group of molecules that can undergo rearrangement and is given by $S_c^* = Rln(W^*)$, where W^* is assumed to be about 2. Rearranging in terms of S_c yields:

$$S_c = \frac{A}{Tln\left(\frac{\eta}{\eta_o}\right)} = \frac{\Delta\mu ln(2)}{Tln\left(\frac{\eta}{\eta_o}\right)} \qquad \text{(Equation 4.74)}$$

The relationship given by Equation 4.74 serves as a basis for the relationship of used here to describe the configurational entropy of Q-groups for this model. The potential barrier for rearrangement of a Q-group is taken as the bond energy or heat of formation of that Q-group, as calculated by Equation 4.67 and described in Section 4.3.9,

$$\Delta\mu(\sigma(Q^n)) = \Delta H_f^o(\sigma(Q^n)) \qquad \text{(Equation 4.75)}$$

The viscosity term, $ln\left(\frac{\eta}{\eta_o}\right)$, will be redefined as k_η and represents the dependence of the configurational entropy on flow of the phosphate chains. This term will be further explored in Section 4.3.13.

The configurational entropy of a Q-group arrangement can now be written as in Equation 4.76.

$$S_c(\sigma(Q^n)) = \frac{\ln(2)}{k_\eta T}\Delta H_f^o(\sigma(Q^n)) \qquad \text{(Equation 4.76)}$$

The same statistical analysis that was performed for enthalpies of Q-groups and reactions in Equations 4.69 – 4.71 can now be applied to entropy calculations,

$$S_c(Q^n) = \sum_{i=1}^{N_\sigma} S_c(\sigma_i(Q^n)) * P(\sigma_i(Q^n)) \qquad \text{(Equation 4.77)}$$

$$\Delta S_c(Q_{rxn}) = S_c(Q^{n+1}) + S_c(Q^{m+1}) - S_c(Q^n) - S_c(Q^m) \quad \text{(Equation 4.78)}$$

$$\Delta S^o_{str(net)} = \sum_{n,m=0}^{2} \Delta S_c(Q_{rxn}) * P(Q^n x Q^m) \quad \text{(Equation 4.79)}$$

where $P(\sigma_i(Q^n))$ and $P(Q^n x Q^m)$ are as previously described by Equations 4.53 and 4.39.

4.2.12. Equilibrium Variable Equations. Equations developed for equilibrium variables can be incorporated into Equation 4.20 to yield the following expression:

$$K_{rdx(net)} exp\left(\frac{-\Delta H^o_{str(net)}}{RT}\right) exp\left(\frac{\Delta S^o_{str(net)}}{R}\right) = \left(\frac{X_{Fe^{2+}}}{X_{Fe^{3+}}}\right)^2 \left(\frac{X_{BO}}{X^2_{NBO}}\right) (pO_2)^{1/2} \quad \text{(Equation 4.80)}$$

Rearranging to put experimental condition variables (*T, pO_2*) on the left side and composition dependent variables on the right side yields:

$$K_{rdx(net)} (pO_2)^{-1/2} = \left(\frac{X_{Fe^{2+}}}{X_{Fe^{3+}}}\right)^2 \left(\frac{X_{BO}}{X^2_{NBO}}\right) exp\left(\frac{\Delta H^o_{str(net)}}{RT}\right) exp\left(\frac{-\Delta S^o_{str(net)}}{R}\right) \quad \text{(Equation 4.81)}$$

To solve for the iron redox ratio, all variables need to be expressed in terms of experimental melt conditions and known starting composition. Examples for different batch compositions are given in Appendix B, but examples of these variables for the melts made in this study are shown here.

Most glasses made in this work had initial compositions given by:

$$yFe_2O_3 \cdot (1-y)P_2O_5 \ (mol\%) \quad \text{(Equation 4.82)}$$

Final reduced compositions therefore have the form:

$$\left(\frac{y-2x}{1+x}\right) Fe_2O_3 \cdot \left(\frac{2x}{1+x}\right) FeO \cdot \left(\frac{1-y}{1+x}\right) P_2O_5 \ (mol\%) \quad \text{(Equation 4.83)}$$

Equations for equilibrium variables can be developed from relationships given in this section and are shown below:

$$\frac{X_{Fe^{2+}}}{X_{Fe^{3+}}} = \frac{x}{y-x} \quad \text{(Equation 4.84)}$$

$$\frac{X_{Fe^{2+}}}{\Sigma Fe} = \frac{x}{y} \quad \text{(Equation 4.85)}$$

$$\frac{O}{P} = R = \frac{5-2y-x}{2(1-y)} \quad \text{(Equation 4.86)}$$

$$X_{BO} = \frac{4-R}{R} = \frac{3-6y+x}{5-2y-x} \quad \text{(Equation 4.87)}$$

$$X_{NBO} = \frac{2R-4}{R} = \frac{2(1+2y-x)}{5-2y-x} \quad \text{(Equation 4.88)}$$

$$\frac{X_{BO}}{X_{NBO}^2} = \frac{(3-6y+x)(5-2y-x)}{4*(1+2y-x)^2} \quad \text{(Equation 4.89)}$$

$$\Lambda_{bulk} = \frac{0.77*3(y-x)+1.0(2x)+0.40*5(1-y)}{5-2y-x} \quad \text{(Equation 4.90)}$$

Equations for the thermochemical variables are much more complex and will not be written out in this section. However, equations and thermochemical data used to calculate $K_{rdx(net)}$ are given in Appendix A. Equations for $\Delta H^o_{str(net)}$ and $\Delta S^o_{str(net)}$ are developed as described above. Although there are too many factors and embedded calculation steps for these variables to be expressed here in a single, succinct equation, the factors and equations are easy to input into a spreadsheet to perform all necessary calculations. It is worth noting that the ultimate goal of these calculations is to determine the iron redox ratio, as expressed in Equation 4.85, as a function of batch composition and melting conditions. Therefore, only the value of *x* needs to be determined, and Solver in Excel can be set up to solve for *x* as the objective cell once experimental and batch variables are entered.

4.2.13. Dependencies of the Structural Entropy Variable. Fitting the behavior for the entropy of the structural reaction has proven to be exceptionally challenging. Recent studies of configuration entropy of glass forming melts imply that the complex

calculations necessary to model configurational entropy can only be accomplished with computational methods [216].

All variables used in the equilibria expressions above have been defined in terms of melting conditions or melt composition with the exception of the only unknown variable, k_η, as introduced in Equation 4.76. Using experimental redox data from this study as well as literature, expected values of k_η can be calculated for known glass compositions and melt conditions. As it relates to the Adam-Gibbs equation, there is expected to be viscosity dependent term that correlates to k_η through an exponential dependence, such that:

$$k_o = \exp(k_\eta) \propto \eta \qquad \text{(Equation 4.91)}$$

A summary of glasses considered in this study is given in Table 4.4, which includes the values calculated for ΔH_{str} using Equation 4.71 and the values for ΔS_{str} expected from back-calculating with experimental values for iron redox ratio. Values for k_η and k_o are also provided, and were determined using the provided values for ΔS_{str} and Equations 4.76 – 4.79.

The relationship proposed for the configurational entropy as given by Equation 4.76 implies a linearity between the structural entropy term and 1/T, as well as a linearity between ΔS_{str} and $\Delta H_{str.}$ Both of these relationships are indeed observed for data in Table 4.4, as seen in Figure 4.4 (for data sets with temperature variations) and Figure 4.5 (for all data sets).

Qualitative analysis of the calculated values for k_η reveal trends that scale with those expected for viscosity. Increasing O-to-P decreases the connectivity of the structure and is expected to decrease viscosity. For the glasses in this work, k_η decreases with

increasing O-to-P ratios for both the Fe(III) and Fe(II/III) series, as well as for the glasses reported by Griscom (1998) [89].

Table 4.4. Calculated enthalpies and entropies of structural reactions for glass compositions found in literature, as well as corresponding k_η and k_o values.

Batch Composition (mol%)	Melt Temp (°C)	pO_2 (atm)	$\%Fe^{2+}$	H_f (J/mol)	S_f (J/mol·K)	k_η	k_o	Reference
$0.25Fe_2O_3{\cdot}0.75P_2O_5$	1250	0.21	32	2014339	1146	-0.800	0.449	Schmitt (this work)
	1300		35	1997595	1094	-0.805	0.447	
	1350		36	1972867	1039	-0.811	0.444	
$0.33Fe_2O_3{\cdot}0.67P_2O_5$	1200	0.21	17	1817983	1041	-0.822	0.440	
	1250		19	1825027	1006	-0.826	0.438	
	1300		24	1843449	984	-0.826	0.438	
	1350		35	1884494	981	-0.820	0.440	
$0.40Fe_2O_3{\cdot}0.60P_2O_5$	1200	0.21	25	1725505	981	-0.827	0.437	
	1250		31	1743726	959	-0.827	0.437	
	1300		32	1746721	924	-0.833	0.435	
	1350		38	1765318	905	-0.833	0.435	
	1400		44	1785067	888	-0.833	0.435	
$0.237Fe_3O_4{\cdot}0.763P_2O_5$	1200	0.21	21	1901092	1112	-0.805	0.447	
	1250		32	1934589	1096	-0.803	0.448	
	1300		37	1952417	1069	-0.805	0.447	
	1350		39	1966297	1040	-0.807	0.446	
$0.293Fe_3O_4{\cdot}0.707P_2O_5$	1200	0.21	29	1790646	1038	-0.812	0.444	
	1350		49	1845112	966	-0.816	0.442	
$0.318Fe_3O_4{\cdot}0.682P_2O_5$	1200	0.21	14	1697046	956	-0.835	0.434	
	1350		32	1747798	894	-0.835	0.434	
$0.40Fe_2O_3{\cdot}0.60P_2O_5$	1150	0.21	17	1704647	1001	-0.830	0.436	Ray (1999)
	1200		19	1709924	965	-0.834	0.434	
	1250		29	1737822	954	-0.829	0.436	
	1300		35	1755882	933	-0.830	0.436	
	1350		42	1778350	916	-0.829	0.437	
	1400		50	1806077	905	-0.827	0.437	
	1450		57	1832348	893	-0.825	0.438	
$0.40Fe_2O_3{\cdot}0.60P_2O_5$	1150	0.21	13	1696909	991	-0.834	0.4345	Bingham (2006)
$0.40Fe_2O_3{\cdot}0.60P_2O_5$	1150	0.21	15	1700237	996	-0.832	0.435	Ghussn (2007)
	1200		18	1706483	961	-0.836	0.434	
	1250		25	1726912	943	-0.833	0.435	
$0.40Fe_2O_3{\cdot}0.60P_2O_5$	1150	0.21	18	1707273	1004	-0.828	0.437	Karabulut (2002)
	1200		20	1712598	968	-0.833	0.435	
	1350		48	1798926	934	-0.823	0.439	
	1450		59	1840231	899	-0.823	0.439	
$0.40Fe_2O_3{\cdot}0.60P_2O_5$	1200	10^{-6*}	80	1935014	1118	-0.814	0.443	
$0.29Fe_2O_3{\cdot}0.71P_2O_5$	1250	0.21	27	1961161	1106	-0.807	0.446	Griscom (1998)
	1450		51	2080476	1040	-0.805	0.447	
$0.40Fe_2O_3{\cdot}0.60P_2O_5$	1100	0.21	19	1709924	1052	-0.820	0.440	
	1450		57	1832348	893	-0.825	0.438	
	1200	1	21	1715298	977	-0.826	0.4378	

Table 4.4. Calculated enthalpies and entropies of structural reactions for glass compositions found in literature, as well as corresponding k_η and k_o values. (continued)

Batch Composition (mol%)	Melt Temperature (°C)	pO_2 (atm)	$\%Fe^{2+}$	Hf	Sf	k_η	k_o	Reference
$0.40Fe_2O_3 \cdot 0.60P_2O_5$	1200	0.21	19	1709924	965	-0.834	0.4343	Marasinghe (1997)
$0.31Fe_3O_4 \cdot 0.69P_2O_5$			24	1719680	977	-0.829	0.4366	
$0.24Fe_2O_3 \cdot 0.24FeO \cdot 0.52P_2O_5$			34	1738896	998	-0.82	0.4405	
$0.40Fe_2O_3 \cdot 0.60P_2O_5$		10^{-3*}	22	1718022	951	-0.85	0.4275	
		1	21	1715298	977	-0.826	0.4378	
$0.05FeO \cdot 0.95P_2O_5$	1100	$1.6x10^{-7*}$	85	2206000	1430	-0.779	0.459	Karabulut (2003)
$0.10FeO \cdot 0.90P_2O_5$			85	2206000	1429	-0.779	0.459	
$0.15FeO \cdot 0.85P_2O_5$			87	2213812	1437	-0.778	0.459	
$0.20FeO \cdot 0.80P_2O_5$			82	2194550	1415	-0.783	0.457	
$0.25FeO \cdot 0.75P_2O_5$			85	2206000	1426	-0.781	0.458	
$0.30FeO \cdot 0.70P_2O_5$			88	2217774	1437	-0.779	0.459	
$0.35FeO \cdot 0.65P_2O_5$			90	2225810	1445	-0.778	0.460	
$0.40FeO \cdot 0.60P_2O_5$			95	2246586	1471	-0.771	0.463	
$0.45FeO \cdot 0.55P_2O_5$			91	2229886	1446	-0.778	0.459	
$0.50FeO \cdot 0.50P_2O_5$			94	2217826	1443	-0.776	0.460	
$0.333Fe_2O_3 \cdot 0.667P_2O_5$	1100	0.21	13	1805585	1120	-0.814	0.443	Zhang (2010)
	1200		21	1769176	1093	-0.817	0.442	
$0.354Fe_2O_3 \cdot 0.646P_2O_5$	1100		14	1741585	1073	-0.819	0.441	
	1200		25	1702045	1043	-0.824	0.439	
$0.372Fe_2O_3 \cdot 0.628P_2O_5$	1100		15	1832214	1055	-0.817	0.442	
	1200		27	1803826	1039	-0.817	0.442	
$0.40Fe_2O_3 \cdot 0.60P_2O_5$	1100		16	1777499	1021	-0.819	0.441	
	1200		31	1743726	1000	-0.821	0.440	
$0.032Fe_2O_3 \cdot 0.387BaO \cdot 0.581P_2O_5$	1000	0.21	1.4	1733495	1137	-0.83	0.436	Bergo (2004)
$0.064Fe_2O_3 \cdot 0.374BaO \cdot 0.562P_2O_5$			4	1773329	1185	-0.815	0.443	
$0.090Fe_2O_3 \cdot 0.364BaO \cdot 0.546P_2O_5$			5	1697287	1128	-0.819	0.441	
$0.110Fe_2O_3 \cdot 0.356BaO \cdot 0.534P_2O_5$			6	1653061	1095	-0.822	0.440	
$0.135Fe_2O_3 \cdot 0.346BaO \cdot 0.519P_2O_5$			9	1611752	1067	-0.823	0.439	
$0.155Fe_2O_3 \cdot 0.338BaO \cdot 0.507P_2O_5$			10	1585046	1048	-0.824	0.439	
$0.36Fe_2O_3 \cdot 0.10Na_2O \cdot 0.54P_2O_5$	1200	0.21	28	1655016	934	-0.833	0.4345	Marasinghe (2000)
$0.32Fe_2O_3 \cdot 0.20Na_2O \cdot 0.48P_2O_5$			32	1559919	870	-0.843	0.4302	
$0.36Fe_2O_3 \cdot 0.10Cs_2O \cdot 0.54P_2O_5$			32	1666400	946	-0.829	0.4364	
$0.28Fe_2O_3 \cdot 0.30Cs_2O \cdot 0.42P_2O_5$			29	1446321	785	-0.867	0.4204	
$0.38Fe_2O_3 \cdot 0.05Cs_2O \cdot 0.57P_2O_5$	1250	0.21	32	1707105	935	-0.831	0.4357	Karabulut (1999)
$0.36Fe_2O_3 \cdot 0.10Cs_2O \cdot 0.54P_2O_5$	1250		34	1671214	912	-0.834	0.4343	
$0.339Fe_2O_3 \cdot 0.156Cs_2O \cdot 0.505P_2O_5$	1250		33	1610062	869	-0.843	0.4304	
$0.24Fe_2O_3 \cdot 0.16Na_2O \cdot 0.60P_2O_5$	1200	0.21	11	1727037	971	-0.837	0.433	Al Shahrani (2005)
$0.24Fe_2O_3 \cdot 0.12Na_2O \cdot 0.04Li_2O \cdot 0.60P_2O_5$			4.3	1709860	942	-0.854	0.426	
$0.24Fe_2O_3 \cdot 0.08Na_2O \cdot 0.08Li_2O \cdot 0.60P_2O_5$			3.5	1706807	936	-0.858	0.424	
$0.24Fe_2O_3 \cdot 0.04Na_2O \cdot 0.12Li_2O \cdot 0.60P_2O_5$			6.4	1712308	951	-0.847	0.429	
$0.24Fe_2O_3 \cdot 0.16Li_2O \cdot 0.60P_2O_5$			6.0	1710147	948	-0.849	0.428	

Table 4.4. Calculated enthalpies and entropies of structural reactions for glass compositions found in literature, as well as corresponding k_η and k_o values. (continued)

Batch Composition (mol%)	Melt Temperature (°C)	pO_2 (atm)	$\%Fe^{2+}$	Hf	Sf	k_η	k_o	Reference
$0.20Fe_2O_3{\cdot}0.20K_2O{\cdot}0.60P_2O_5$			26	1789120	1032	-0.816	0.442	
$0.20Fe_2O_3{\cdot}0.05Na_2O{\cdot}0.15K_2O{\cdot}0.60P_2O_5$			24	1782923	1026	-0.818	0.442	
$0.20Fe_2O_3{\cdot}0.10Na_2O{\cdot}0.10K_2O{\cdot}0.60P_2O_5$	1200	0.21	25	1784543	1028	-0.817	0.442	
$0.20Fe_2O_3{\cdot}0.15Na_2O{\cdot}0.05K_2O{\cdot}0.60P_2O_5$			26	1785775	1030	-0.816	0.442	
$0.20Fe_2O_3{\cdot}0.20Na_2O{\cdot}0.60P_2O_5$			24	1778541	1023	-0.818	0.441	
$0.32Fe_2O_3{\cdot}0.20K_2O{\cdot}0.48P_2O_5$			17	1527627	833	-0.863	0.422	
$0.32Fe_2O_3{\cdot}0.05Na_2O{\cdot}0.15K_2O{\cdot}0.48P_2O_5$			13	1519824	822	-0.870	0.419	
$0.32Fe_2O_3{\cdot}0.10Na_2O{\cdot}0.10K_2O{\cdot}0.48P_2O_5$	1200	0.21	14	1521820	825	-0.868	0.420	Fang (2000, 2003)
$0.32Fe_2O_3{\cdot}0.15Na_2O{\cdot}0.05K_2O{\cdot}0.48P_2O_5$			14	1521604	825	-0.868	0.420	
$0.32Fe_2O_3{\cdot}0.20Na_2O{\cdot}0.48P_2O_5$			16	1525212	830	-0.865	0.421	
$0.32Fe_2O_3{\cdot}0.20Cs_2O{\cdot}0.48P_2O_5$			20	1536450	843	-0.858	0.424	
$0.32Fe_2O_3{\cdot}0.05Na_2O{\cdot}0.15Cs_2O{\cdot}0.48P_2O_5$			20	1535715	842	-0.858	0.424	
$0.32Fe_2O_3{\cdot}0.10Na_2O{\cdot}0.10Cs_2O{\cdot}0.48P_2O_5$	1200	0.21	20	1534976	842	-0.858	0.424	
$0.32Fe_2O_3{\cdot}0.15Na_2O{\cdot}0.05Cs_2O{\cdot}0.48P_2O_5$			25	1544965	854	-0.852	0.427	
$0.32Fe_2O_3{\cdot}0.20Na_2O{\cdot}0.48P_2O_5$			16	1525212	830	-0.865	0.421	

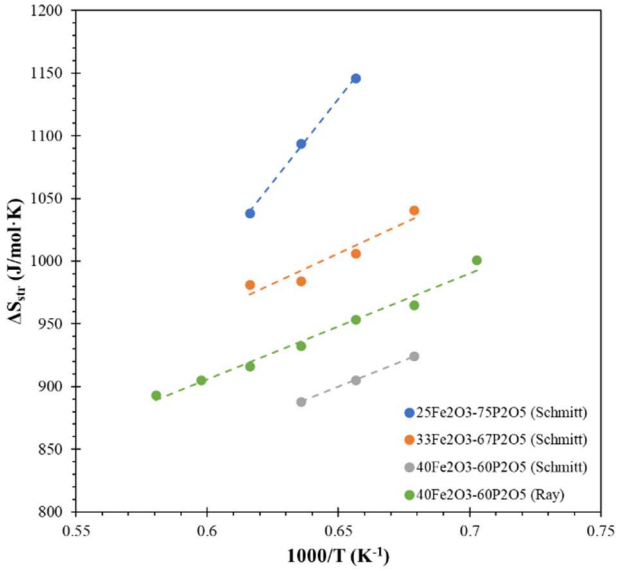

Figure 4.4. Calculated entropy of the structural reaction as a function of temperature, using experimental data from this dissertation and Ray et al. [83].

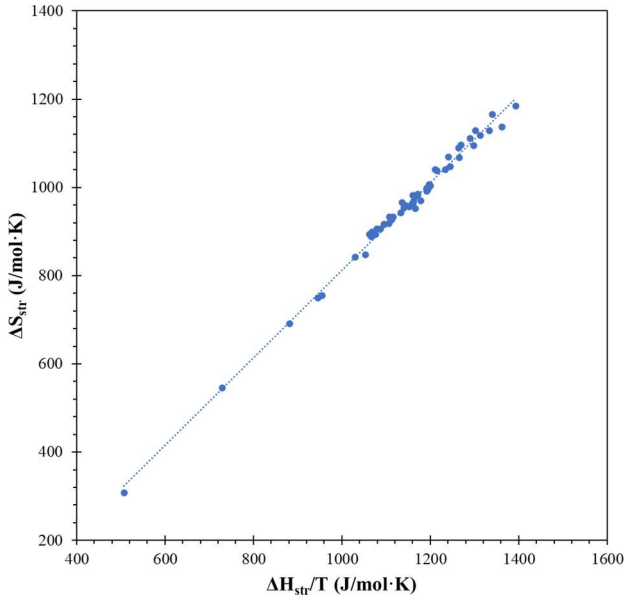

Figure 4.5. Calculated entropy versus enthalpy of the structural reaction for all glasses in Table 4.4.

Interesting trends are also seen in the results for Al Shahrani (2005) [217]. Al Shahrani et al. reported a mixed alkali effect in the Na_2O-Li_2O-Fe_2O_3-P_2O_5 series investigated. A minimum in calculated k_η values corresponds with the composition where the minimum viscosity is expected (Na/Li = 1) (Figure 4.6). Fang [218], [219] did not observe a mixed alkali effect in any of his glass series, and k_η is constant within each of his glass series. However, a decrease in k_η is seen for the Na_2O-K_2O-Fe_2O_3-P_2O_5 glasses in Fang's study when the O-to-P ratio is increased from 3.17 to 3.7. It is also worthwhile to note that the highest k_η values in Table 4.4 are seen for the FeO-P_2O_5 series reported by Karabulut (2003) [121], which are ultraphosphates and are expected to have higher viscosities than glasses in the meta- to pyrophosphate compositional ranges. Results suggest that the ability to model the structural entropy term are contingent on the ability to model trends in k_η based on structural contributions to viscosity.

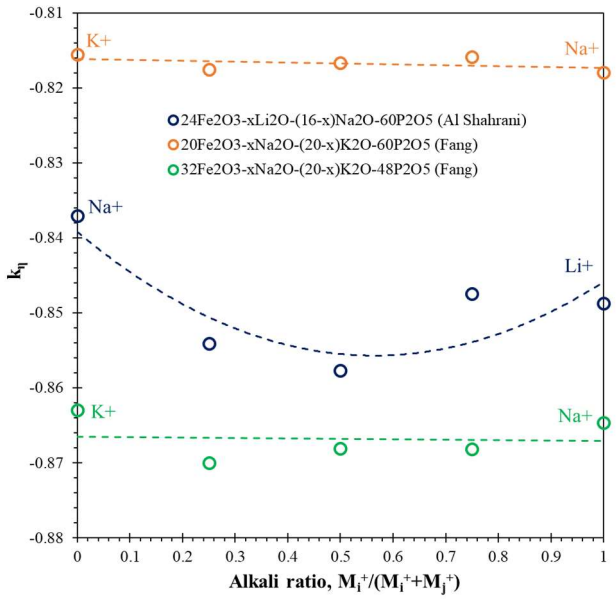

Figure 4.6. Trends in viscosity term k_η with degree of mixing for mixed alkali iron phosphate glasses.

Research has shown a dependence of viscosity on bulk basicity of a glass [135], [144]. Ray and Pal [144] developed equations to approximate the viscosity of silicate slags and reported the viscosity relationship given in Equation 4.92, where A and B are dependent on optical basicity and are given in Equations 4.93 – 4.94.

$$\ln(\eta) = \ln(AT) + \frac{1000B}{T} \qquad \text{(Equation 4.92)}$$

$$B = 297.14\Lambda^2 - 466.69\Lambda + 196.22 \qquad \text{(Equation 4.93)}$$

$$-\ln(A) = 0.2056B + 12.492 \qquad \text{(Equation 4.94)}$$

Choudhury et al. [135] investigated lead silicate slags and reported the relationship in Equation 4.95.

$$\log\eta = -4.600 + \frac{-8.00\Lambda + 7.78}{\log T - .715} \qquad \text{(Equation 4.95)}$$

While these specific relationships and fitting constants are not expected to hold for the glasses investigated here, it is worthwhile to observe the changes in k_η with bulk basicity. Figure 4.7 includes select glass series ranging from meta- to pyrophosphates melted at temperatures ranging from 1000 – 1350°C and with compositions including binary (ternary) iron phosphates, alkali iron phosphates, and alkaline earth iron phosphates. Results shows a general decrease in k_η with increasing basicity. Decreasing temperature also appears to increase k_η.

Empirical evidence shows a dependence of viscosity on chain length in phosphate glasses, the details of which are complicated by the abrupt increase in chain length as glass compositions approach the metaphosphate O-to-P ratio of 3.0 and then begin to form an interconnected, 3-D network. In order to constrain the value of chain length, it can be expressed as $1 - \frac{1}{\bar{n}}$, where $\bar{n}$ is equal to the average chain length as defined in Equation 4.29. This constrained value will approach 1 when $\bar{n}$ approaches infinite lengths (O/P = 3.0) and will approach 0 as $\bar{n}$ approaches 1 (O/P = 4.0). Figure 4.8 shows the relationship between k_η and $1 - \frac{1}{\bar{n}}$ for select glasses.

A second order polynomial fit between k_η and $1 - \frac{1}{\bar{n}}$ for the Fe(III) glasses prepared in this study is given in Equation 4.96. When this relationship is used in the model presented here, the iron redox ratio can be calculated. Comparison between experimental iron redox ratios and those predicted using the model are shown in Figure 4.9. The dashed line corresponds to perfect agreement and the dashed lines represent a typical experimental error of ± 5%.

$$k_\eta = 0.231\left(1 - \frac{1}{\bar{n}}\right)^2 - 0.283\left(1 - \frac{1}{\bar{n}}\right) - 0.746 \qquad \text{(Equation 4.96)}$$

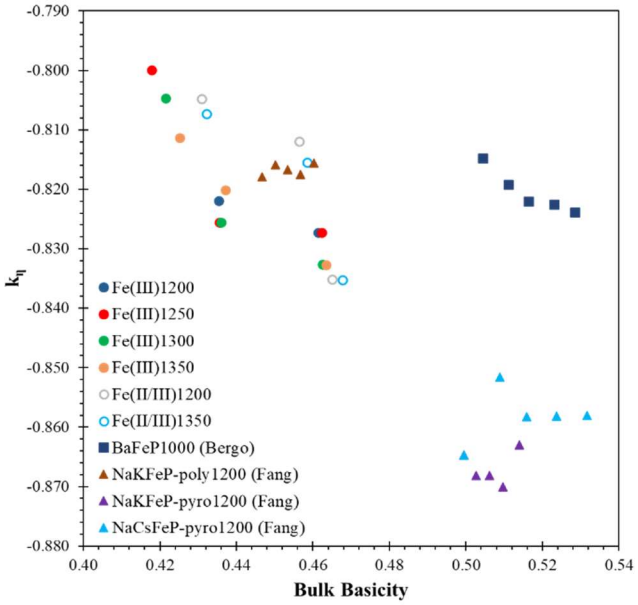

Figure 4.7. Variable k_η as a function of bulk basicity for select glasses from Table 4.4.

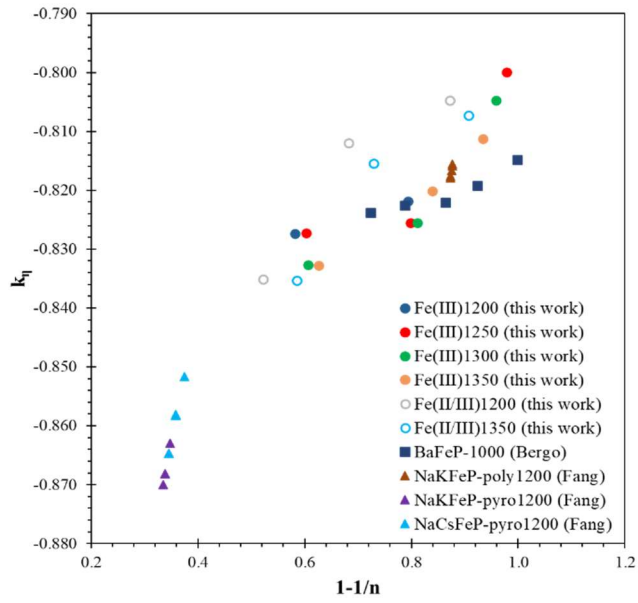

Figure 4.8. Variable k_η as a function of 1-1/n for select glasses from Table 4.4, where n equals average chain length.

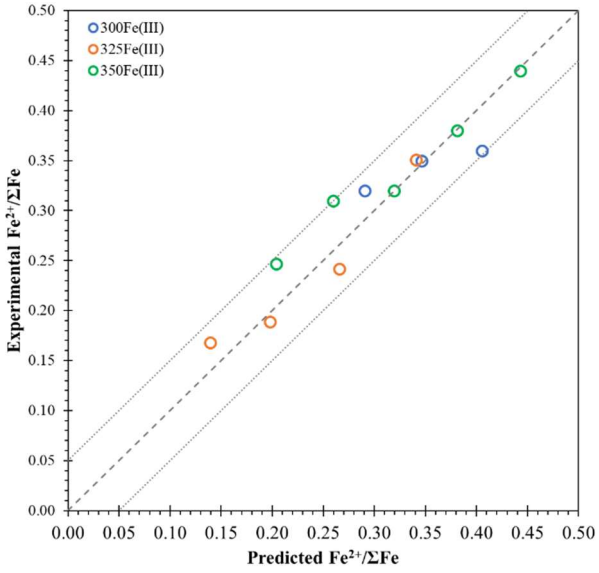

Figure 4.9. Comparison of experimental and predicted iron redox ratios for the Fe(III) series prepared in this study.

Additional work must be completed to develop an equation that fits the k_η viscosity variable to all phosphate glass systems, and that work will likely require computational methods that are beyond the capabilities of Excel and Solver. However, bulk basicity and chain length are likely to be factors considered in future work to complete this model.

4.3. DISCUSSION

While the purpose of this research was to develop a model to predict the iron redox ratio in phosphate glasses based on batch composition and melting conditions, it has been taken as far as it can without more powerful computational tools than are currently available. The entropy of the structural reaction is a function of many variables and likely is greatly affected by the viscosity of the melt, in addition to the bulk basicity

and phosphate chain lengths and distribution. Fitting the entropy of the structural reaction with multiple variables to empirical results will require additional computational tools and time.

The accuracy of this model is only as good as the data to which it is fit. There is notable spread in the reported iron redox ratio found in literature for glasses with the same batch composition and experimental conditions. Figure 4.10 shows reported iron redox ratios for glasses with a $0.40Fe_2O_3 \cdot 0.60P_2O_5$ $(mol\%)$ batch composition melted in air for 1-2 hrs. While all series show a trend of increasing ferrous iron content with increasing melting temperature, the iron redox ratio varies by a spread of over 10% for some melting temperature. It is unclear whether these discrepancies are due to actual differences in glass compositions or due to measurement errors. Redox ratios reported in literature are almost exclusively measured by Mössbauer. As mentioned in Section 3 of this dissertation, choices concerning coordination environments and absorption efficiencies of the iron ions will affect how the spectra are fit and the resulting redox ratio.

Inconsistencies were also seen in equivalent compositions melted with different raw materials. Marasinghe et al. [82] melted mixed valency iron phosphate glasses of the same batch composition (Fe/P = 0.67-0.69, Fe^{2+}/Fe^{3+} = 0.5) but one glass was batched with Fe_3O_4 and the other was batched with FeO and Fe_2O_3. Both glasses were melted at 1200°C in air but the glass batched with Fe_3O_4 resulted in a glass with 24% Fe^{2+}, while the glass batched with FeO and Fe_2O_3 resulted in a glass with 34% Fe^{2+}. This difference in iron redox ratio is outside of typical measurement error. Even larger inconsistencies were seen in alkali iron phosphate glasses. Glasses of batch composition $0.32Fe_2O_3 \cdot$

$0.20Na_2O \cdot 0.48P_2O_5$ $(mol\%)$ were melted in air at 1200°C by Marasinghe et al. [75] and Fang et al. [218], and both studies used Mössbauer to measure the iron redox ratio. While Marasinghe reported an iron redox ratio of 32% Fe^{2+}, Fang reported just half that amount at 16% Fe^{2+}.

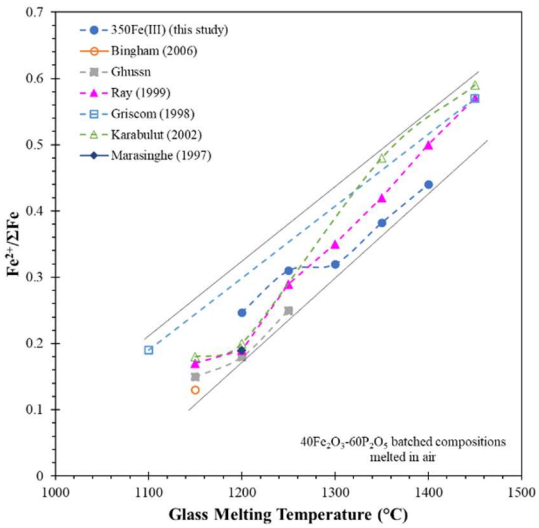

Figure 4.10. Iron redox ratios reported for $40Fe_2O_3 \cdot 60P_2O_5$ $(mol\%)$ batched compositions melted in air. Solid lines are guides to the eye to show spread in data.

The effect of melting atmosphere is also a point of contention. One study [220] found no change in the Fe^{2+} content for glasses which were melted in air and for those that were prepared by bubbling oxygen through the melt. Another study [6] found relatively little change in Fe^{2+} content for glasses with the same initial batch compositions which were melted at the same temperature under air, bubbled nitrogen and bubbled oxygen. These results seem inconsistent with the expectations of Equation 4.3.

It is worth noting experiments performed under closed environments (sealed under vacuum in an ampoule) [221] or flowing gases (argon) [185] reported expected

trends in iron redox ratios, while those which bubbled gases through the melt [6], [220] saw little to no change. This finding may suggest that bubbling gases is not adequate to change the fugacity of oxygen in the melt and thus is not an efficient way to alter the iron redox ratio of a melt. Also, studies of iron redox equilibria in silicate glasses melted under variable oxygen fugacity do show the expected trend of linearly increasing $\ln(Fe^{3+}/Fe^{2+})$ with increasing $\ln(fO_2)$ [196]. Unlike studies where gases are bubbled into melts, the oxygen fugacity in this study was precisely controlled with a CO-CO_2 gas mixture and was monitored.

It is interesting to note the observed change in iron redox ratio in mixed alkali iron phosphate glasses. Fang [219] observed no traditional mixed alkali effect in iron phosphate glasses when sodium ions are exchanged for potassium or cesium, and also no significant change in iron redox ratio within the same alkali iron phosphate glass series. Melting temperature, Fe-to-P ratio and O-to-P ratio were held constant within the series, and only the proportions of the two alkali oxides are changed. However, Al Shahrani et al. [217] did observe a mixed alkali effect in iron phosphate glasses of composition $0.24Fe_2O_3 \cdot (0.16 - x)Na_2O \cdot xLi_2O \cdot 0.60P_2O_5$ $(mol\%)$ when sodium was exchanged for lithium, where melting temperature, Fe-to-P ratio and O-to-P ratio are also kept consistent. In this case, the iron redox ratio did change as the proportions of alkali ions changed, reaching a minimum when the Na-to-Li ratio was equal to 1. It is also interesting to note that the composition with all sodium alkali ions ($x = 0$) yielded a higher iron redox ratio in the glass than the melt with all lithium alkali ions ($x = 0.16$), as would be expected based on the higher basicity of sodium as compared to lithium. However, the minimum observed in the iron redox ratio upon mixing of the alkali is not

anticipated based solely on basicity changes. This suggests that the lower ferrous iron content observed in compositions with mixed alkali could be a result of the lower melt viscosity associated with the mixed alkali effect. This lower viscosity could affect the structural entropy term in the thermodynamic equilibrium expression as it would be incorporated into the k_o fitting parameter, or could potentially affect the diffusivity of oxygen gas in the melt. Lower melt viscosity may result in increased oxygen diffusivity, which could increase the fugacity of oxygen and shift the equilibrium reaction shown in Equation 4.3 to the left, resulting in higher concentrations of Fe^{3+} and lower concentrations of Fe^{2+}.

The reliability of reported experimental conditions and of the redox measurements must be questioned. For example, most of the Fe^{2+} concentration data in the literature was collected via Mössbauer, with only a few values obtained via chemical titration techniques. Mössbauer results have been shown to overestimate the amount of Fe^{3+} in glasses [178] unless corrections are made to account for the different coordination states of Fe^{2+}. Wet chemistry is usually favored by geologists when investigating the iron contained in volcanic rocks due to its greater accuracy and precision when used with glassy materials as compared to Mössbauer or other physical methods [222]–[224].

In addition, most melts were only held for 1 – 2 hours, which may not be sufficient to reach equilibrium, especially at lower melt temperatures. It has been shown for iron-alkali-silicate melts that times as long as 19 – 24 hours were needed for very viscous melts (SiO_2 > 65 wt%) to attain redox equilibria at temperatures of 1100 – 1200ºC, and more fluid melts (SiO_2 < 50 wt%) required times as long as 5 hours at these temperatures [189]. While longer melt times and higher melt temperatures may ensure

sufficient time and fluidity such that iron redox equilibrium is attained, they may also result in larger amounts of unwanted phosphate volatilization and greater contamination from the crucible, which will also affect melt equilibrium. Some literature data was taken from experiments which were held in closed environments and may not have reached the equilibrium partition of oxygen, resulting in errors in the pO_2 values used to fit the data. Zhang et al. [225] showed that melting times of over 2 hours are needed for the redox ratio to equilibrate in iron orthophosphate compositions (see Figure 4.11) at melting temperatures of 1150ºC and 1300ºC for small melts (5-10 g). Ray et al. [184] showed a gradual increase in redox ratio in iron pyrophosphate as melting time increased from 1 to 24 hours at a melting temperature of 1200 ºC (19% Fe^{2+} at 1 hour to 26% Fe^{2+} at 24 hours).

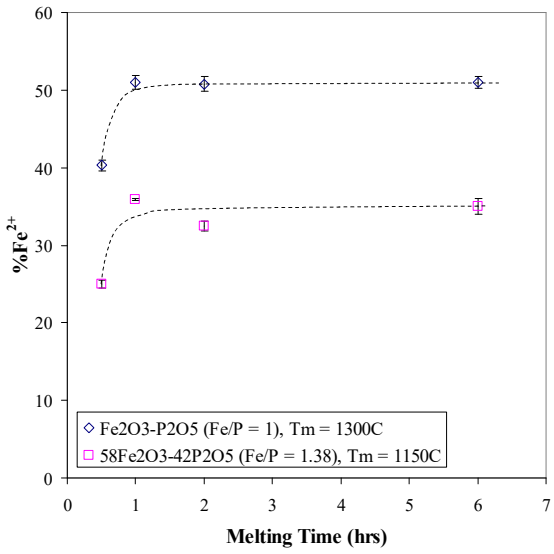

Figure 4.11. Ferrous iron content as a function of melting time for iron orthophosphate glass showing that melt times must exceed 2 hours for equilibrium to be reached [Zhang et al. [120]].

It can be seen in Table 3.3 that the amount of phosphate loss in this study for glass melts held in air for only 2 hours is not insignificant, especially at higher melting temperature and for less stable compositions (metaphosphates). Phosphate loss may be even larger for melts with larger initial phosphate content and melts which are brought to higher temperatures or held for longer times. Large phosphate losses will affect calculations used in this model, such as basicity calculations and all calculations based on the assumed final glass composition. Although phosphate volatilization is expected for glasses which are melted in the temperature range used for most iron phosphates (1100 – 1400 ºC), it is not worthwhile to factor this phosphate loss into the general model. Numerous conditions will contribute to the amount of phosphate loss, such as melting temperature, melting time, initial phosphate content, and whether a closed or open atmosphere is used, and not enough data exists in the literature to predict the amount of loss which will result from a given set of conditions. All of the calculations which are completed here assume no phosphate volatilization, so that the final glass composition can be expressed with respect to our initial batch composition.

Other assumptions made in developing the model must also be considered. For example, it was assumed that the iron redox ratio does not change upon quenching of the melt. Some data used in fitting the model may be taken from glasses which had not be quenched sufficiently fast. Resulting Fe^{2+} content may represent a glass melt at a temperature slightly lower than the reported melt temperature, and thus may be underestimating the effect of temperature on iron reduction. Also, all thermodynamic data used in calculating the Gibbs free energy of reaction were based on a study involving silicate melts, not phosphate melts. Ideally, similar studies to those by

Ottonello [226] would be completed on phosphate glasses to better approximate the value of ΔG_{rdx}.

The effect of melt basicity on the equilibrium reaction also needs to be considered. As the melt becomes more basic, the redox equilibria reaction has been reported to switch from that given in Equation 4.3 to that given in Equation 4.97 [194]:

$$FeO_2{}^{-}{}_{(melt)} = Fe^{2+}{}_{(melt)} + \frac{1}{4}O_{2(g)} + \frac{3}{2}O^{2-}{}_{(melt)} \qquad \text{(Equation 4.97)}$$

As can be seen from the corresponding thermodynamic equilibrium constant (Equation 4.98), increased melt basicity (represented by $a_{O^{2-}}$) results in decreased Fe^{2+} content, which is opposite of the behavior observed in acidic glass melts.

$$K_{eq} = exp\left(-\frac{\Delta G_{Rxn}}{RT}\right) = \frac{(a_{Fe^{2+}})(a_{O^{2-}})^{3/2}(pO_2)^{1/4}}{\left(a_{FeO_2{}^{-}}\right)} \qquad \text{(Equation 4.98)}$$

This change in behavior has been reportedly observed at a bulk optical basicity of approximately $\Lambda \approx 0.50$ [194], [211], where increasing the optical basicity results in increased Fe^{2+} content for $\Lambda < 0.50$ but results in decreased Fe^{2+} content for $\Lambda > 0.50$. This suggestion is supported by the experimental results observed for iron phosphate glasses in the literature reviewed here. Iron phosphates in the metaphosphate composition range have optical basicities of ~0.42, whereas those in the pyrophosphate composition range have optical basicities of ~0.46. All of the glasses made in this study show an increase in Fe^{2+} content with increasing basicity and therefore are assumed to follow the reduction reaction shown in Equation 4.3 where increases in optical basicity favor the reduced oxidation state. However, the addition of alkali to iron phosphate glasses can increase the basicity to or above $\Lambda = 0.50$. This change in dependence of iron redox ratio on basicity is most readily seen in compositions with cesium oxide, which has a

comparatively high optical basicity of $\Lambda_{Cs_2O} = 1.7$. In a series of cesium iron phosphates reported by Karabulut et al. [55], the Fe-to-P ratio is kept constant and the amount of cesium oxide is increased, resulting in bulk basicities of the glasses ranges from 0.48 – 0.52. The resulting ferrous iron content is highest for the composition with a bulk basicity of 0.50. The same trend is observed for cesium iron phosphate glasses made by Marasinghe et al. [75], where glasses with constant Fe-to-P ratios and increasing cesium oxide content yielded a decrease in measured ferrous iron content as the bulk basicity of the glass was increased from 0.50 to 0.58.

The statistical approach to determining bond arrangements and Q-unit distributions will be less accurate for glasses where preferential bonding occurs or glasses with large amounts of disproportionation, which refers to the redistribution of phosphate anions. Phosphate glasses can be described by the Flory distribution model [227],

$$2(P_nO_{3n+1})^{-(n+2)} \leftrightarrow (P_{n+1}O_{3n+4})^{-(n+3)} + (P_{n-1}O_{3n-2})^{-(n+1)} \quad \text{(Equation 4.99)}$$

with an equilibrium constant given by:

$$K_{P_n} = \frac{[P_{n+1}][P_{n-1}]}{[P_n]^2} \quad \text{(Equation 4.100)}$$

Cations with greater field strengths generally result in broader distributions of phosphate anions, or larger values of K_{P_n}. An ideal distribution is considered one in which $K_{P_n} = 1$, and the mole fraction of phosphate anions can be described by

$$N_{(P_nO_{3n+1})} = \frac{1}{\bar{n}}\left(\frac{\bar{n}-1}{\bar{n}}\right)^{n-1} \quad \text{(Equation 4.101)}$$

Assuming an ideal distribution as described above,

$$N_{(PO_4)} = N_{(Q^o)} = \frac{1}{2}\left(\frac{1}{2}\right)^0 = \frac{1}{2} \quad \text{(Equation 4.102)}$$

$$N_{(P_2O_7)} = \frac{1}{2}\left(\frac{1}{2}\right)^1 = \frac{1}{4}$$

$$N_{(P_3O_9)} = \frac{1}{2}\left(\frac{1}{2}\right)^2 = \frac{1}{8}$$

and so forth. High-performance liquid chromatography investigations have shown that larger field strengths and lower energies of formation associated with the metal oxide additions will result in larger distributions of anion chains in phosphate glasses [228]. Structural studies can be used in conjunction with the model to redistribute bond arrangements or Q-unit proportions and improve accuracy of calculations.

4.4. SUMMARY

The iron redox ratio within the iron phosphate glass system yields considerable ranges in reported experimental values for nearly identical glasses and melting conditions. Unexpected results with changes in melt atmosphere suggest the fugacity of oxygen may not be equal to the partial pressure of oxygen above the melt or bubbled through the melt, and may be a more complicated experimental variable to control. Results from mixed alkali iron phosphate glasses imply the viscosity of the glass alone can affect the iron redox ratio, even when all other conditions such as melt temperature, O-to-P ratio and Fe-to-P ratio are keep constant. This may suggest either an effect of viscosity on the entropy of the structural reaction or on the diffusivity of oxygen gas in the melt. The effect of viscosity on redox ratio may imply that other factors not considered here, such as the water content in the glass or humidity of the melt environment, could be a factor in the spread of redox ratios reported for glasses of identical batch compositions melted under similar conditions.

Results also indicate that raw materials used in the batching of the glass, as well as the valency of the iron in the batch materials, may affect the final iron redox ratio of the glass. This may suggest that the typical melting time of ~2hrs is not enough to reach equilibrium, or that the raw materials affect the viscosity of the melt, and likewise affect the iron redox ratio, as discussed previously.

Modeling the composition and reactions within the melt based on a statistical distribution of glass components allows for interesting comparisons of compositions and equilibria. Modifying the idea of group basicity as introduced by Duffy to account for situations where complete neutralization does not occur provides a way to calculate heats of formation of phosphorus oxides containing one or two additional cations and results in a high correlation to known heats of formation for equivalent compounds. The most difficult parameter to approximate is the entropy of the structural equilibrium reaction. Entropy of glass melts has historically been an extremely difficult property to predict and characterize. Many modern investigations use computational approaches and computer simulations [216] which were not available for this research. Future modifications of the bonding approach model developed here may rely on these computational techniques to accurately model the entropy or viscosity of the system, and thus the final redox ratio. It is likely that the chain length and distribution and potentially the melt basicity will factor into the entropy of the structural reaction.

In summary, future improvement of the model relies on better understanding of oxygen fugacity in phosphate melts, effect of melt viscosity on oxygen diffusion, effect of water in the melt or melt atmosphere, effect of raw materials (which may relate to melt basicity and viscosity), and ability to predict configurational entropy changes resulting

from polymerization reactions with computational methods. However, the bonding-level approach developed here has been validated by high correlation between calculated heats of formation of phosphate Q-groups with reported heats of formation of equivalent crystalline compounds, as well as predicting trends in the melt entropy and viscosity that correspond well with those expected based on O-to-P ratios and melt basicities.

5. AQUEOUS DISSOLUTION OF PHOSPHATE GLASSES: A NEW THEORETICAL MODEL OF BOND HYDRATION BASED ON OPTICAL BASICITY

Previously established glass dissolution models rely on the availability of thermodynamic data and phase diagrams of the glass compositional systems to be able to calculate free energy of hydration for structural components. This information is not readily available for many phosphate glass systems, so efforts are made here to establish a new approach to calculate free energies of hydration for phosphate glasses. The model proposed here uses microscopic basicities of non-bridging oxygen bonds to approximate hydration energies for those bonds. The total hydration energy for the glass is suggested to be a weighted sum of the bond hydration energies. Efforts to model the hydration energy with group basicity calculations were not successful and largely overestimated the bond hydration energies on Q^2 units. Results from microscopic basicity calculations yield the expected trends between dissolution rate and free energy of hydration, but significant scatter exists in the data. Deviations from linearity are observed for many glass systems and are often dependent on the concentration and size of divalent cations in the glass composition, suggesting the deviation is partially due to the slowing of water diffusion into the glass structure, which is not accounted for with this bonding model. The approach taken here shows potential and requires further investigation to quantitatively describe deviations from linearity in order to produce a model which can accurately predict dissolution rates based solely on glass compositions, without the need for thermochemical data.

5.1. GENERAL PRINCIPLES

Iron phosphates are distinctive among phosphate glasses due to their exceptional chemical durability. Many studies have investigated the chemical durability of binary iron phosphates as well as iron phosphate glasses with many other oxide additions, such as Li_2O, Na_2O, K_2O, MgO, CaO, BaO, ZnO and PbO [60], [229]–[233]. It is important for future applications of iron phosphate glasses to understand how compositional changes will affect dissolution rates. Current dissolution models lack the necessary thermochemical data to accurately predict the chemical durability of iron phosphate glasses, or phosphate glasses in general. The utility of a model that can approximate dissolution rates for phosphate glasses is apparent, and development of such a model will first focus on alkali and alkaline earth phosphate compositions to substantiate the new approach.

Many factors influence glass dissolution rate, including temperature, solution pH and chemistry, and the ratio of the surface area of the glass to the volume of the solution. In addition, solution stirring or replenishing throughout the experiment may impact dissolution [234], [235]. Dissolution rate is also significantly affected by glass composition, including structural factors such as Q-units that are present, chain lengths and distributions, presence of rings, and cation coordination numbers [234], [236].

Dissolution of most phosphate glasses have been shown to follow a three-step process. First, water diffuses into the glass. Elemental depth profiles have shown that most of the hydrogen which enters glass is in the form of water [234]. Next, modifier cations are hydrated, as depicted in Equation 5.1. Lastly, the $P - O - P$ bonds hydrolyze, as depicted in Equation 5.2.

$$\equiv P - O^{-}Na^{+} + H_2O \rightarrow \equiv P - OH + Na^{+}OH^{-}_{(aq)} \qquad \text{(Equation 5.1)}$$

$$\equiv P - O - P \equiv + H_2O \rightarrow \equiv P - OH + HO - P \equiv \qquad \text{(Equation 5.2)}$$

Phosphates are most durable in neutral pH (pH5 to pH9), where glass dissolution rates exceed hydrolysis rates and no selective alkali leaching is observed [234]. In this pH range, research shows that phosphate glasses dissolve congruently via bond hydration, and that activation energies of hydrolysis are almost twice that for glass dissolution. Surface phosphate chains are surrounded by water, hydrated and "disentangled", and then are released intact into the solution. Hydrolysis of the chains occurs after they are released into solution. Dissolution rates increase considerably at lower pH (pH<4), where hydrolysis of the $P - O - P$ bonds becomes the dominant dissolution mechanism [234], [236].

Gao et al. [237] demonstrated that the phosphate dissolution rate takes time to reach steady state. The presence of a pre-hydrated layer will result in very fast initial dissolution, while slow diffusion of water may result in slow initial dissolution. The dissolution kinetics follow those of a polymer hydration model, with an initial stage dependent on the rate of water diffusion and weight loss following a $t^{1/2}$ dependence [234]. This stage can require several minutes to several days depending on the glass composition. The dissolution rate will eventually reach steady state and the thickness of the hydrated layer will remain constant. Weight loss will follow a linear t^{1} dependence during this second stage of dissolution [234].

Many glass dissolution models already exist, although the two most widely used models are perhaps those proposed by Paul [238] and Conradt [235]. Paul's approach [238] relates chemical durability to the sum of free energies of hydration of structural

components. The free energies of the metaphosphate or oxide constituents are typically used in these calculations. Jantzen et al. and Plodinec et al. [239]–[242] used Paul's approach to model the durability of natural, medieval and nuclear waste glass. There is an apparent linear dependence of dissolution rate on the free energy of hydration for many silicate and borosilicate compositions, but there is a good deal of scatter in the data. Also, different glass sub-systems showed different optimized fitting parameters.

Conradt [235], [243], [244] greatly improved the fit of the dissolution model for silicate glasses by using Paul's approach but with thermodynamic data for constitutional phases rather than oxide data. The glass compositions are put in terms of the crystalline equilibrium reference state and a small amount of vitrification energy is added. While the methods and models proposed by Conradt have been shown to accurately describe and predict experimental dissolution data, the model relies on the availability of thermodynamic data and phase diagrams for the glass compositional systems. While this data is readily available for silicate and borate systems, there are few literature studies or reference materials available for phosphate systems. Not enough data currently exist to use either the constitutional or free energy approach to model the dissolution of phosphate glasses.

A new approach to dissolution modeling is proposed which is based on individual bonds instead of bulk compositions. This approach will eliminate the necessity of phase diagrams for modeling dissolution in complex glass systems and will allow for many structural factors to be accounted for which current models overlook, such as cation coordination changes. An example where this approach may be beneficial is for the glass compositional series $xAl_2O_3 \cdot (1-x)NaPO_3$. Increasing alumina content will increase

the valency and average field strength of the cations in the glass, thereby increasing connectivity and decreasing dissolution rates. However, experimental data has shown [245] that with increasing Al_2O_3, dissolution rate (K) eventually ceases to decrease near an O-to-P ratio of 3.5 (Figure 5.1). This O-to-P ratio corresponds to both the formation of Q^0 units as well as a change from octahedrally to tetrahedrally bonded Al. A bonding approach model will be able to account for both the coordination changes and Q-unit changes within the glass.

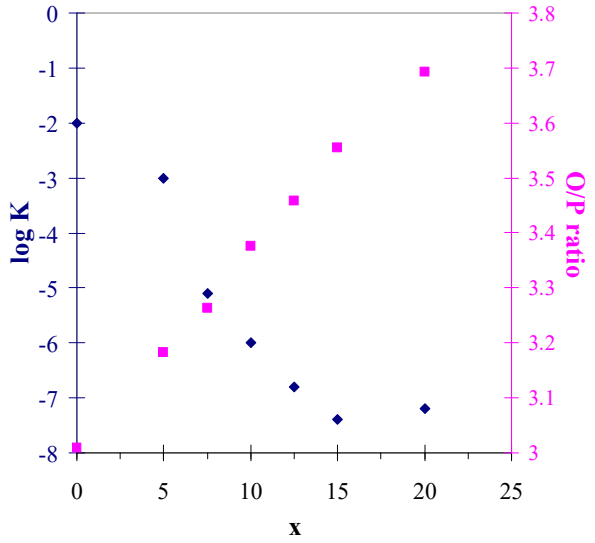

Figure 5.1. Dissolution rate and O/P ratio as a function of x for $xAl_2O_3 \cdot (100 - x)NaPO_3$ glasses (data from [245]).

The concept of breaking down dissolution behavior to individual bonds will also help explain other observed trends in phosphate glass dissolution which cannot be explained by bulk glass compositions. For example, phosphate chain distributions are reported to affect dissolution [246]. In the example shown in Figure 5.2, both cases have the same O/P ratio (= 3.5) and the same average chain length (= 2). However, since they

have different distributions of chain lengths, the dissolution rates for the two situations may be different. This difference can be accounted for with a bonding approach model, as seen in the disparity of the two corresponding dissolution equations, where K_{bulk} is the bulk dissolution rate and $K_{Q^n-M_j^{z+}}$ is the dissolution rate of a specific $Q^n - M_j^{z_j^+}$ bond:

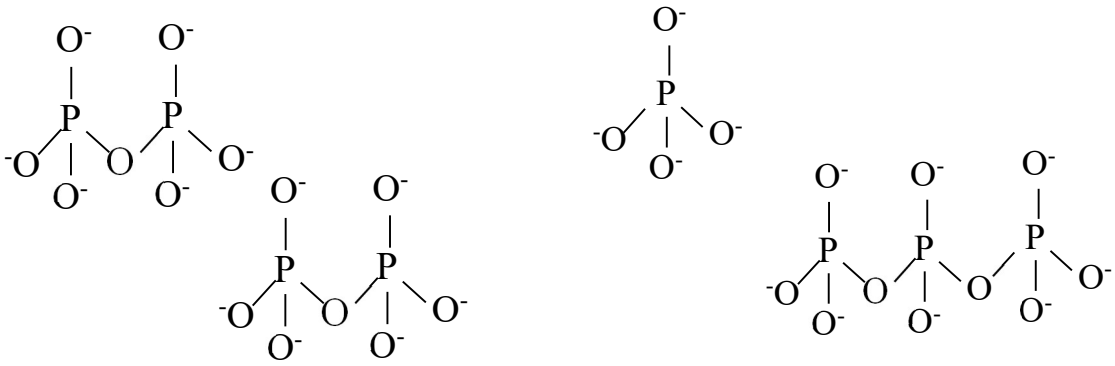

$K_{bulk} = K_{Q^1-M_j^{z+}}$

$K_{bulk} = 0.25 * K_{Q^0-M_j^{z+}} + 0.5 * K_{Q^1-M_j^{z+}} + 0.25 * K_{Q^2-M_j^{z+}}$

Figure 5.2. Schematic depicting two situations with the same average chain lengths but different chain length distributions.

5.2. DEVELOPING THE MODEL

The new model concept and development are described below.

5.2.1. Concept and Assumptions. For the purposes of this model, we will assume that dissolution is independent of stirring, which is supported by the results of Gao et al [237]. Also, it is assumed that the system is open or the solution is replenished, and the system is large enough such that the surface area-to-volume ratio will not affect the dissolution rate. Studies have shown that this ratio is generally unimportant for the dissolution of phosphate glasses due to the lack of selective leaching and solution saturation effects associated with phosphate systems [234]. The final assumption is that

of a solution of water with neutral pH. The dissolution rate will therefore be dependent only on temperature, glass composition and structure.

As previously discussed and shown in Figure 2.1, the structure of phosphate glasses is largely dependent on the O-to-P ratio, which results in different Q^n-units throughout the glass. Phosphate glasses are therefore composed of a distribution of different $Q^n - M_j^{z_j^+}$ bonds, where $M_j^{z_j^+}$ represents cation species in the glass composition. This model proposes that the bulk dissolution rate of a glass that dissolves congruently via hydration of oxygen-cation bonds is a weighted sum of the dissolution rates of these bonds.

Similar to previous dissolution models, the rate of dissolution is assumed to be dependent on the free energy of hydration. However, instead of approximating the free energy of hydration of the glass using molar fractions of oxides or constitutional phases, this model will explore the concept of using molar fractions of specific Q^n arrangements (for the group basicity approach) and fractions of oxygen (for the microscopic basicity approach) associated with specific $Q^n - M_j^{z_j^+}$ bonds. The fraction of Q-units and distribution of cations among available NBO would preferably be known from structural experiments. However, if this data is not known, an ideal statistical distribution of Q-units and cations can be calculated based on the composition and O-to-P ratio. Details and equations for these calculations are given in Table 4.1 and Section 4.3.8 and will not be discussed again here.

Using this concept, the glass structure can be described as a distribution of Q-unit arrangements, such that:

$$X\left(\sigma_i(Q^n)\right) = f(Q^n) * P\left(\sigma_i(Q^n)\right) \quad \text{(Equation 5.3)}$$

where $X\left(\sigma_i(Q^n)\right)$ is the molar fraction of a specific Q-unit arrangement, $f(Q^n)$ is the fraction of Q^n units as given in Table 4.1, and $P\left(\sigma_i(Q^n)\right)$ is the probability of an arrangement of Q^n as given by Equation 4.53. As the given fractions relate to one mole of phosphate atoms, the free energy of hydration for a mole of glass can be expressed as a sum of contributions of free energies of hydration of all Q-unit arrangements, multiplied by the number of phosphate atoms per mole of glass:

$$\Delta G_{hyd} = \left(\frac{\#P}{mol\ glass}\right) \sum_{n,i} \Delta G_{hyd}\left(\sigma_i(Q^n)\right) * X\left(\sigma_i(Q^n)\right) \quad \text{(Equation 5.4)}$$

5.2.2. Hydration Dependence on Basicity. Chemical durability of phosphate glasses has been shown to be a function of both O-to-P ratio and cation identity [69], [229], [234], [236]. Both of these factors are introduced when considering optical basicity, or the electron donor power of oxygen, as discussed in Section 4.3.9. Duffy [130] suggests that high local basicity, which represents high electron density on oxygen, attracts the positive ends of water molecules. If greater local basicity attracts water molecules, it reasons that greater basicity will cause faster dissolution rates. This idea is supported by studies of alkali phosphate glasses which show increasing dissolution rates when lithium ($\Lambda_{Li} = 1.0$) is replaced with sodium ($\Lambda_{Na} = 1.15$) [234], or when potassium ($\Lambda_{K} = 1.4$) is replaced with cesium ($\Lambda_{Cs} = 1.7$) [247].

Duffy et al. [248] has shown a relationship between the group basicity of a phosphate anion (represented by A^- in Equation 5.5) and the corresponding acid-base dissociation constant (pK as given by Equation 5.7), as seen in Figure 5.3.

$$A^- + H^+ = AH \quad \text{(Equation 5.5)}$$

$$K' = \frac{[AH]}{[A^-][H^+]} \quad \text{(Equation 5.6)}$$

$$pK = logK' \quad \text{(Equation 5.7)}$$

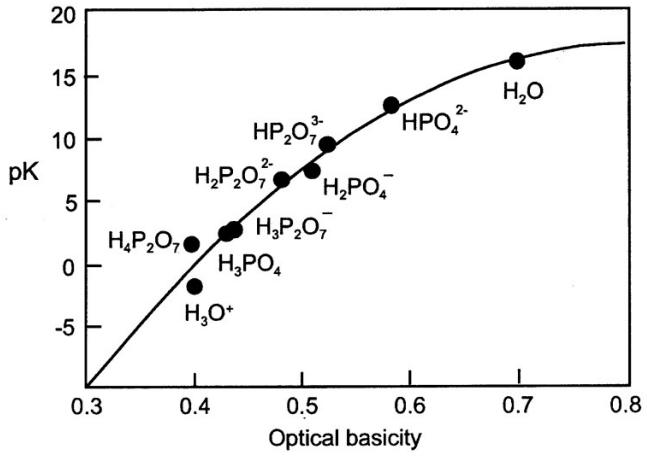

Figure 5.3. Plot of pK of acidic species denoted versus optical basicity of corresponding anion (conjugate base). Figure taken from Duffy et al. [248].

Group basicity calculations used in Figure 5.3 assume complete neutralization of the phosphate anions, which is equivalent to assuming non-bridging oxygens bonding with cations of basicity equal to unity. Although the line drawn through the data is guided by the pK values for the dissociations of H_3O^+ and H_2O, the reasoning for this is not obvious to the work here. Further inquiry into the relationship between pK and group basicity of the phosphate conjugate base was deemed necessary.

Data for the pK values were obtained using FactSage and group basicities were again calculated assuming complete neutralization, the values for which are given in Table 5.1. The relationship between pK and optical basicity was replotted for only the phosphate anions, as shown in Figure 5.4. A linear relationship is exhibited with an R^2 =

0.9613. However, if the data are split into two series, one for the orthophosphate anions and one for the pyrophosphate anions, the linear fit nears $R^2 = 1$ for each series, excluding the one outlier point for the $H_2P_2O_7^{2-} + H^+ = H_3P_2O_7^-$ reaction. These results call into question the accuracy of available thermochemical data, especially considering FactSage reports having limited data specifically for $H_2P_2O_7^{2-}$. Thermochemical data is not available for equivalent reactions of any metaphosphate compositions, although it would reason that a similar linear relationship exists.

Table 5.1. pK_a and group basicity values for phosphate anions.

Base (A-)	Acid (A)	K_{eq}	pK_a	Group Basicity (Base)
PO_4^{3-}	HPO_4^{2-}	2.65E+12	12.423	0.583
HPO_4^{2-}	$H_2PO_4^-$	1.57E+07	7.195	0.508
$H_2PO_4^-$	H_3PO_4	1.41E+02	2.150	0.433
$P_2O_7^{4-}$	$HP_2O_7^{3-}$	1.81E+09	9.257	0.524
$HP_2O_7^{3-}$	$H_2P_2O_7^{2-}$	6.01E+06	6.779	0.481
$H_2P_2O_7^{2-}$	$H_3P_2O_7^-$	1.52E+02	2.183	0.438
$H_3P_2O_7^-$	$H_4P_2O_7$	3.32E+01	1.521	0.395

This relationship implies that the change in free energy associated with the hydration of one non-bridging oxygen bond on a given Q-unit can be expressed as,

$$\Delta G_H(Q^n - O^-) = -RTlnK' = -2.303RTlogK' = -2.303RTpK$$

$$\therefore \Delta G_H(Q^n - O^-) = -2.303RT\left(m_{Qn}\lambda_g - b_{Qn}\right) \qquad \text{(Equation 5.8)}$$

where λ_g is the group basicity of the Q^n-unit and m_{Qn} and b_{Qn} are the linear fitting parameters for the type of Q^n-unit being considered.

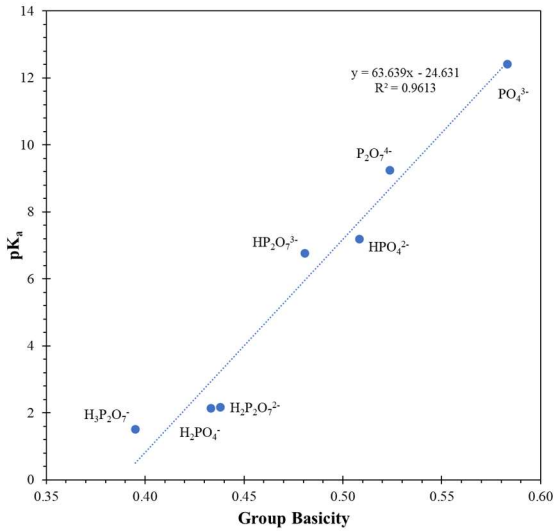

Figure 5.4. Replotting of pK_a of acidic species corresponding to the denoted conjugate bases versus optical basicity of the ortho- and pyrophosphate anion bases.

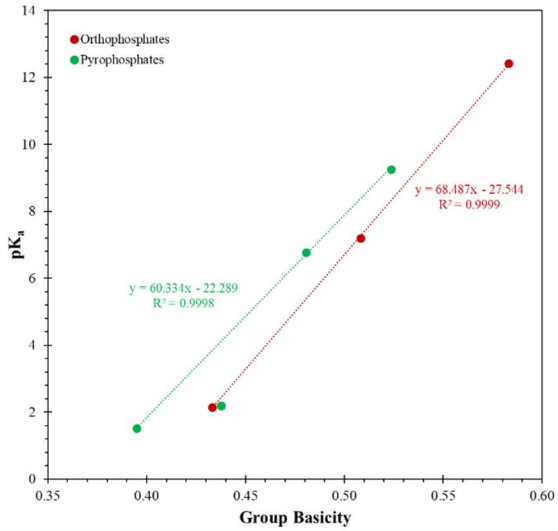

Figure 5.5. Linear fits for relationship between pK_a and group basicity of corresponding conjugate base for ortho- and pyrophosphates (omitting data for outlier $H_2P_2O_7^{2-}$).

5.2.3. Application of Group Basicity Calculation to Experimental Data.

Literature data for dissolution rates of phosphate glasses are compiled in Table 5.2.

Although a large set of data exists, the majority of published data is for metaphosphate

(O/P = 3) and ultraphosphate (O/P < 3) compositions. As thermochemical data for metaphosphate anions are missing from the analyses plotted in Figure 5.4 and Figure 5.5, this complicates the analysis performed here. This study largely aims to model the dissolution behavior of glasses in the poly- and pyrophosphate composition ranges, with O-to-P ratios between 3.0 – 4.0. Glasses with interconnected networks consisting of Q^3 units are expected to corrode at least partially via hydrolysis of the $P-O-P$ bonds, not solely due to hydration of the $P-O-M_j^{z_j^+}$ bonds as considered here. Also, glasses with O-to-P ratios near or greater than 4.0 will exhibit an invert glass structure and consist of $M_j^{z_j^+}-O-M_j^{z_j^+}$ bonds, which again will exhibit different dissolution mechanisms than those considered here of $P-O-M_j^{z_j^+}$ bonds. Future investigations will rely of the availability of dissolution data for congruently dissolving phosphate glasses in the poly- to pyrophosphate range.

Extensive effort was made to use the relationship given in Equation 5.8 to explain experimental measurements of dissolution rates for phosphate glasses. Q-unit arrangements and relative fractions were calculated as described earlier in Section 5.2, and group basicities for each Q-unit arrangement were calculated using Equation 4.63. It is important to note that the group basicity of the arrangement will change as the bonds are hydrated. Just as the optical basicity, and thus the pK values, change for an orthophosphate group as PO_4^{3-} hydrates to form HPO_4^{2-} and then $H_2PO_4^-$ and H_3PO_4 (see Table 5.1), so will the group basicity change for the phosphate Q-units considered here as cation bonds are replaced with hydrogen bonds. It is assumed here that the $Q^n-M_j^{z_j^+}$ bond with the highest microscopic basicity will preferentially hydrate, and the group

basicity of a Q-unit was recalculated between each bond hydration according to these assumptions.

The total free energy of hydration for a Q-unit arrangement is the sum of free energies for all $Q^n - M_j^{z_j+}$ bonds on the arrangement, of which there will be *3-n*.

$$\Delta G_H\left(\sigma_i(Q^n)\right) = \sum_{3-n} \Delta G_H(Q^n - O^-) \qquad \text{(Equation 5.9)}$$

$\Delta G_H(Q^n - O^-)$ was calculated using Equation 5.8 using both the average linear fitting constants in Figure 5.4 for all Q-units, and also using the different fitting constant for separate Q-units as in Figure 5.5. Neither method yielded results that were consistent with expected behavior.

Of the literature data compiled in Table 5.2, the most complete set with varying O-to-P ratio (and consistent temperature) are the sodium-aluminophosphate glasses reported by Brow et al. [245]. Figure 5.6(A) shows the relationship between the experimental dissolution rate of the glasses and the G_H value calculated using the basicity approach detailed above. The four compositional series investigated and shown in Figure 5.6(A) were Series 1: $xAl(PO_3)_3 \cdot (1-x)NaPO_3$, Series 2: $xAlPO_4 \cdot (1-x)NaPO_3$, Series 3: $xAl_2O_3 \cdot (1-x)NaPO_3$, and Series 4: $xNaAlO_2 \cdot (1-x)NaPO_3$, as shown in Figure 5.6(B) (phase diagram taken from Brow et al. [245]). O-to-P ratios range from 3.0 to 3.7.

While the linearity of the calculated relationship is encouraging and the range of values for G_H are in the general range that would be expected, the first obvious inconsistency is the direction of the relationship observed. Results show dissolution rate increasing with increasing free energy of reaction, while the opposite is expected. Also, the slope of the dependency changes with compositional series, increasing with

increasing phosphorus content of the series. Results from calculations for other glass series suggests that this method underestimates the dissolution rates associated with Q^2-units in particular, and also underestimates the effect of changes in cation identities.

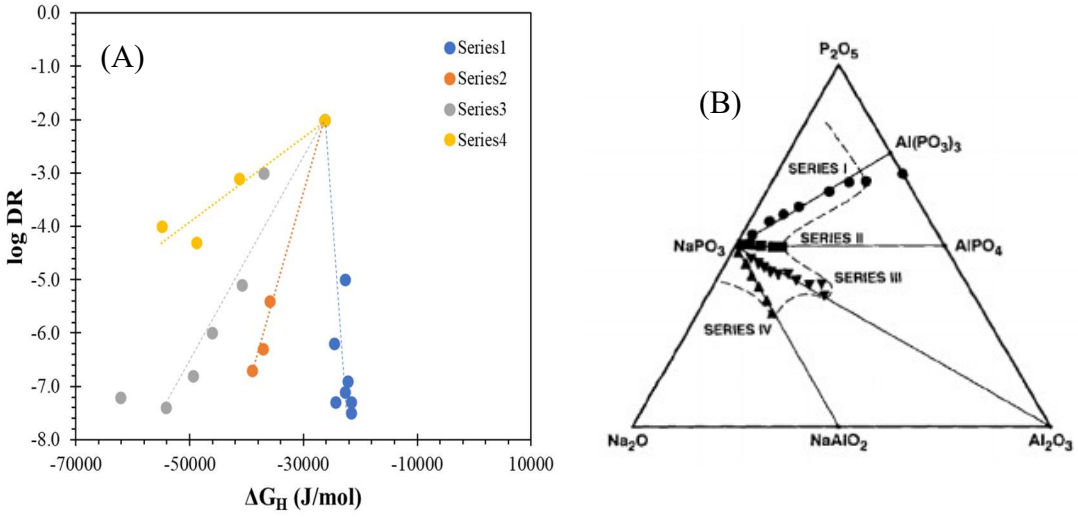

Figure 5.6. (A) Experimental dissolution rates versus ΔG_H values calculated using Equations 5.4 and 5.8, and the linear fitting parameters from Figure 5.4. (B) Compositional glass series shown in part (A) (phase diagram taken from Brow et al. [245]).

5.2.4. Application of Microscopic Basicity Calculations. It is clear that the acid-base reaction for phosphate anions as described by Equation 5.5 does not fully describe the hydration reaction occurring in the glass, particularly in that the cation identities associated with the non-bridging oxygens are not taken into account. The hydration reaction for a specific bond is more accurately described as a two-step process as given by the reactions and equilibrium constants in Equations 5.10 – 5.13.

Table 5.2. Literature survey of phosphate glass dissolution rates.

Glass Compositional Family	Composition (mol%)	O/P ratio	Dissolution Temp. (K)	Dissolution rate, K (g/cm^2-min unless specified)	log K (K in g/cm^2-min)	Reference
Na-Al-P	$0.5Na_2O$ - $0.5P_2O_5$	3.00	303	20000 mg/cm^2-day	-1.86	Gao (2004)
	$0.4Na_2O$ - $0.6P_2O_5$	2.83		2.2 mg/cm^2-day	-5.82	
	$0.4Na_2O$ - $0.025Al_2O_3$ - $0.525P_2O_5$	2.95		0.6 mg/cm^2-day	-6.38	
	$0.4Na_2O$ - $0.05Al_2O_3$ - $0.55P_2O_5$	3.00		0.1333 mg/cm^2-day	-7.03	
	$0.4Na_2O$ - $0.075Al_2O_3$ - $0.525P_2O_5$	3.10		0.0667 mg/cm^2-day	-7.33	
	$0.4Na_2O$ - $0.1Al_2O_3$ - $0.5P_2O_5$	3.20		0.0667 mg/cm^2-day	-7.33	
	$0.4Na_2O$ - $0.125Al_2O_3$ - $0.475P_2O_5$	3.32		0.2 mg/cm^2-day	-6.86	
Na-Al-P	$0.504Na_2O$ - $0.496P_2O_5$	3.01	343	reported as logK	-2.00	Brow (1993)
	$0.383Na_2O$ - $0.051Al_2O_3$ - $0.566P_2O_5$	2.97			-5.00	
	$0.363Na_2O$ - $0.076Al_2O_3$ - $0.561P_2O_5$	3.03			-6.20	
	$0.296Na_2O$ - $0.106Al_2O_3$ - $0.598P_2O_5$	3.01			-6.90	
	$0.248Na_2O$ - $0.136Al_2O_3$ - $0.616P_2O_5$	3.03			-7.10	
	$0.20Na_2O$ - $0.16Al_2O_3$ - $0.64P_2O_5$	3.03			-7.30	
	$0.158Na_2O$ - $0.185Al_2O_3$ - $0.657P_2O_5$	3.04			-7.50	
	$0.106Na_2O$ - $0.227Al_2O_3$ - $0.667P_2O_5$	3.09			-7.30	
	$0.453Na_2O$ - $0.066Al_2O_3$ - $0.481P_2O_5$	3.18			-5.40	
	$0.444Na_2O$ - $0.075Al_2O_3$ - $0.475P_2O_5$	3.20			-6.30	
	$0.417Na_2O$ - $0.101Al_2O_3$ - $0.482P_2O_5$	3.25			-6.70	
	$0.483Na_2O$ - $0.051Al_2O_3$ - $0.465P_2O_5$	3.18			-3.00	
	$0.468Na_2O$ - $0.076Al_2O_3$ - $0.456P_2O_5$	3.26			-5.10	
	$0.464Na_2O$ - $0.10Al_2O_3$ - $0.436P_2O_5$	3.38			-6.00	
	$0.448Na_2O$ - $0.124Al_2O_3$ - $0.426P_2O_5$	3.46			-6.80	
	$0.437Na_2O$ - $0.147Al_2O_3$ - $0.416P_2O_5$	3.56			-7.40	
	$0.404Na_2O$ - $0.189Al_2O_3$ - $0.406P_2O_5$	3.70			-7.20	
	$0.504Na_2O$ - $0.055Al_2O_3$ - $0.441P_2O_5$	3.26			-3.10	
	$0.506Na_2O$ - $0.084Al_2O_3$ - $0.41P_2O_5$	3.42			-4.30	
	$0.496Na_2O$ - $0.112Al_2O_3$ - $0.392P_2O_5$	3.56			-4.00	
	$0.513Na_2O$ - $0.191Al_2O_3$ - $0.296P_2O_5$	4.33			-5.20	
Na-Ca-P	$0.4Na_2O$ - $0.1CaO$ - $0.5P_2O_5$	3.00	293	5.00E-05	-4.30	Bunker (1984)
	$0.3Na_2O$ - $0.2CaO$ - $0.5P_2O_5$	3.00		3.00E-06	-5.52	
Li-Ca-P	$0.4Li_2O$ - $0.1CaO$ - $0.5P_2O_5$	3.00		6.00E-06	-5.22	
	$0.3Li_2O$ - $0.2CaO$ - $0.5P_2O_5$	3.00		3.00E-07	-6.52	
Na-Ca-P	$0.25Na_2O$ - $0.30CaO$ - $0.45P_2O_5$	3.11	310	12.68E-4 mg/cm^2-h	-7.68	Ahmed (2004)
	$0.20Na_2O$ - $0.35CaO$ - $0.45P_2O_5$	3.11		2.038E-4 mg/cm^2-h	-8.47	
	$0.15Na_2O$ - $0.40CaO$ - $0.45P_2O_5$	3.11		1.557E-4 mg/cm^2-h	-8.59	
	$0.20Na_2O$ - $0.30CaO$ - $0.50P_2O_5$	3.00		2.833E-3 mg/cm^2-h	-7.33	
	$0.15Na_2O$ - $0.35CaO$ - $0.50P_2O_5$	3.00		1.26E-3 mg/cm^2-h	-7.68	
	$0.10Na_2O$ - $0.40CaO$ - $0.50P_2O_5$	3.00		5.883E-4 mg/cm^2-h	-8.01	
	$0.15Na_2O$ - $0.30CaO$ - $0.55P_2O_5$	2.91		3.455E-4 mg/cm^2-h	-8.24	
	$0.10Na_2O$ - $0.35CaO$ - $0.55P_2O_5$	2.91		2.94E-4 mg/cm^2-h	-8.31	
	$0.05Na_2O$ - $0.40CaO$ - $0.55P_2O_5$	2.91		3.125E-4 mg/cm^2-h	-8.28	
K-Al-P	$0.30K_2O$ - $0.10Al_2O_3$ - $0.60P_2O_5$	3.00	343	reported as logK	-5.50	Metwalli (2001)
	$0.25K_2O$ - $0.125Al_2O_3$ - $0.625P_2O_5$	3.00			-5.90	
	$0.20K_2O$ - $0.15Al_2O_3$ - $0.65P_2O_5$	3.00			-6.80	
	$0.10K_2O$ - $0.20Al_2O_3$ - $0.70P_2O_5$	3.00			-7.80	
Mg-Al-P	$0.40MgO$ - $0.05Al_2O_3$ - $0.55P_2O_5$	3.00	343	reported as logK	-6.80	
	$0.30MgO$ - $0.10Al_2O_3$ - $0.60P_2O_5$	3.00			-7.30	
	$0.25MgO$ - $0.125Al_2O_3$ - $0.625P_2O_5$	3.00			-7.70	
	$0.20MgO$ - $0.15Al_2O_3$ - $0.65P_2O_5$	3.00			-8.00	
	$0.10MgO$ - $0.20Al_2O_3$ - $0.70P_2O_5$	3.00			-8.30	

Table 5.2. Literature survey of phosphate glass dissolution rates (continued).

Glass Compositional Family	Composition (mol%)	O/P ratio	Dissolution Temp. (K)	Dissolution rate, K (g/cm^2-min unless specified)	log K (K in g/cm^2-min)	Reference
K-Al-P	$0.30K_2O$ - $0.10Al_2O_3$ - $0.60P_2O_5$	3.00	323	1.26E-07	-6.90	Tischendorf (2005)
	$0.40K_2O$ - $0.20Al_2O_3$ - $0.40P_2O_5$	3.75		1.53E-07	-6.82	
Mg-Al-P	$0.30MgO$ - $0.10Al_2O_3$ - $0.60P_2O_5$	3.00		1.30E-08	-7.89	
Ba-Al-P	$0.30BaO$ - $0.10Al_2O_3$ - $0.60P_2O_5$	3.00		5.00E-09	-8.30	
K-Mg-P	$0.25K_2O$ - $0.25MgO$ - $0.50P_2O_5$	3.00		7.94E-07	-6.10	
K-Mg-Al-P	$0.15K_2O$ - $0.15MgO$ - $0.10Al_2O_3$ - $0.60P_2O_5$	3.00		1.30E-08	-7.89	
	$0.20K_2O$ - $0.20MgO$ - $0.10Al_2O_3$ - $0.50P_2O_5$	3.20		3.60E-08	-7.44	
	$0.25K_2O$ - $0.25MgO$ - $0.10Al_2O_3$ - $0.40P_2O_5$	3.50		1.58E-07	-6.80	
K-Ba-Al-P	$0.15K_2O$ - $0.15BaO$ - $0.10Al_2O_3$ - $0.60P_2O_5$	3.00		1.30E-08	-7.89	
K-Mn-P	$0.20K_2O$ - $0.15MnO$ - $0.65P_2O_5$	2.77	298	1.23E-05	-4.91	Ahmina (2018)
	$0.20K_2O$ - $0.20MnO$ - $0.60P_2O_5$	2.83		9.54E-06	-5.02	
	$0.20K_2O$ - $0.25MnO$ - $0.55P_2O_5$	2.91		6.30E-06	-5.20	
	$0.20K_2O$ - $0.30MnO$ - $0.50P_2O_5$	3.00		2.29E-06	-5.64	
Na-P	$0.50Na_2O$ - $0.50P_2O_5$	3.00	303	20000 mg/cm^2-day	-1.86	Gao (2004)
	$0.45Na_2O$ - $0.55P_2O_5$	2.91		100 mg/cm^2-day	-4.16	
	$0.40Na_2O$ - $0.60P_2O_5$	2.83		2.2 mg/cm^2-day	-5.82	
	$0.35Na_2O$ - $0.65P_2O_5$	2.77		2 mg/cm^2-day	-5.86	
	$0.30Na_2O$ - $0.70P_2O_5$	2.71		3 mg/cm^2-day	-5.68	
	$0.25Na_2O$ - $0.75P_2O_5$	2.67		4 mg/cm^2-day	-5.56	
Na-Ca-P	$0.40Na_2O$ - $0.60P_2O_5$	2.83	303	2.2 mg/cm^2-day	-5.82	
	$0.35Na_2O$ - $0.05CaO$ - $0.60P_2O_5$	2.83		0.72 mg/cm^2-day	-6.30	
	$0.30Na_2O$ - $0.10CaO$ - $0.60P_2O_5$	2.83		0.15 mg/cm^2-day	-6.98	
	$0.25Na_2O$ - $0.15CaO$ - $0.60P_2O_5$	2.83		0.09 mg/cm^2-day	-7.20	
	$0.20Na_2O$ - $0.20CaO$ - $0.60P_2O_5$	2.83		0.08 mg/cm^2-day	-7.26	
	$0.15Na_2O$ - $0.25CaO$ - $0.60P_2O_5$	2.83		0.07 mg/cm^2-day	-7.31	
Na-Mg-P	$0.40Na_2O$ - $0.60P_2O_5$	2.83	303	2.2 mg/cm^2-day	-5.82	
	$0.35Na_2O$ - $0.05MgO$ - $0.60P_2O_5$	2.83		1.0 mg/cm^2-day	-6.16	
	$0.30Na_2O$ - $0.10MgO$ - $0.60P_2O_5$	2.83		0.35 mg/cm^2-day	-6.61	
	$0.25Na_2O$ - $0.15MgO$ - $0.60P_2O_5$	2.83		0.19 mg/cm^2-day	-6.88	
	$0.20Na_2O$ - $0.20MgO$ - $0.60P_2O_5$	2.83		0.10 mg/cm^2-day	-7.16	
	$0.15Na_2O$ - $0.25MgO$ - $0.60P_2O_5$	2.83		0.08 mg/cm^2-day	-7.26	
Na-Zn-P	$0.40Na_2O$ - $0.60P_2O_5$	2.83	303	2.2 mg/cm^2-day	-5.82	
	$0.35Na_2O$ - $0.05ZnO$ - $0.60P_2O_5$	2.83		1.2 mg/cm^2-day	-6.08	
	$0.30Na_2O$ - $0.10ZnO$ - $0.60P_2O_5$	2.83		0.52 mg/cm^2-day	-6.44	
	$0.25Na_2O$ - $0.15ZnO$ - $0.60P_2O_5$	2.83		0.32 mg/cm^2-day	-6.65	
	$0.20Na_2O$ - $0.20ZnO$ - $0.60P_2O_5$	2.83		0.25 mg/cm^2-day	-6.76	
	$0.15Na_2O$ - $0.25ZnO$ - $0.60P_2O_5$	2.83		0.19 mg/cm^2-day	-6.88	
Zn-P	$0.55ZnO$ - $0.45P_2O_5$	3.11	303	1.667E-8 kg/mm^2-hr	-4.56	Takebe (2006)
	$0.60ZnO$ - $0.40P_2O_5$	3.25		4.583E-9 kg/mm^2-hr	-5.12	
	$0.65ZnO$ - $0.35P_2O_5$	3.43		8.75E-11 kg/mm^2-hr	-6.84	
	$0.70ZnO$ - $0.30P_2O_5$	3.67		2.50E-11 kg/mm^2-hr	-7.38	
K-Zn-Al-P	$0.41K_2O$ - $0.025ZnO$ - $0.015Al_2O_3$ - $0.55P_2O_5$	2.94	293	3.30E-04	-3.48	Minami (1977)
K-Al-P	$0.37K_2O$ - $0.045Al_2O_3$ - $0.585P_2O_5$	2.93		4.70E-07	-6.33	
	$0.33K_2O$ - $0.07Al_2O_3$ - $0.60P_2O_5$	2.95		2.50E-07	-6.60	
Cs-Al-P	$0.33K_2O$ - $0.07Al_2O_3$ - $0.60P_2O_5$	2.95		2.50E-04	-3.60	

$$\text{Rxn1: } Q^n - O - M_j^{z_j+} \rightarrow Q^n - O^- + M_j^{z_j+} \qquad \text{(Equation 5.10)}$$

$$K_1 = \frac{[Q^n - O^-]\left[M_j^{z_j+}\right]}{\left[Q^n - O - M_j^{z_j+}\right]} \qquad \text{(Equation 5.11)}$$

$$\text{Rxn2: } Q^n - O^- + H^+ \rightarrow Q^n - O - H \qquad \text{(Equation 5.12)}$$

$$K_2 = \frac{[Q^n - O - H]}{[Q^n - O^-][H^+]} \qquad \text{(Equation 5.13)}$$

The total hydration reaction is the sum of Equation 5.10 and 5.12, as given by Equations 5.14 – 5.16,

$$Q^n - O - M_j^{z_j+} + H^+ \rightarrow Q^n - O - H + M_j^{z_j+} \qquad \text{(Equation 5.14)}$$

$$K_{hyd(bond)} = K_1 K_2 = \frac{[Q^n - O - H]\left[M_j^{z_j+}\right]}{\left[Q^n - O - M_j^{z_j+}\right][H^+]} \qquad \text{(Equation 5.15)}$$

$$\Delta G_{hyd(bond)} = \Delta G_{diss} + \Delta G_H = \Delta G_{diss} - 2.303RT * \left(m_{Qn}\lambda - b_{Qn}\right) \text{ (Equation 5.16)}$$

where ΔG_{diss} is the free energy associated with the dissociation of the $Q^n - O - M_j^{z_j+}$ bond (Equation 5.10). The free energy of dissociation is expected to be a function of the bond strength, and it is clear that the cation identities associated with specific bonds need to be accounted for in a more discrete way than using group basicity values.

Although the relationships shown in Figure 5.5 may not tell the whole story behind bond hydration, important information is still implied. Firstly, increasing basicity yields larger pK values, which corresponds to lower values of ΔG_{hyd}, and the relationship may be linear. Secondly, for a given basicity, Q^1 units have larger pK (lower ΔG_{hyd}) values that Q^0 units. This suggestion supports experimental evidence that dissolution rates decrease with decreasing chain lengths.

These aspects are applied to the new model of dissolution. Instead of using group basicities of the phosphate anion, the free energy of bond hydration was calculated using microscopic basicities of the oxygen involved in the reaction and the assumption of a linear relationship between pK and optical basicity. The effects of Q-groups are taken

into account in regards to the linear fitting parameters, m_{Qn} and b_{Qn}. Due to unavailability of thermochemical data for aqueous metaphosphate anions, values for m_{Q2} and b_{Q2} were inferred using group basicity values and relationships observed for Q^1 and Q^0 units in Figure 5.5.

The free energy of hydration of a specific $Q^n - M_j^{z_j^+}$ bond is given by Equation 5.17,

$$\Delta G_{hyd}\left(Q^n - M_j^{z_j^+}\right) = \Delta G_{diss}\left(P - O - M_j^{z_j^+}\right) - 2.303RT * \left(m_{Qn}\lambda_{P-O-M} - b_{Qn}\right) \quad \text{(Equation 5.17)}$$

where $\Delta G_{diss}\left(P - O - M_j^{z_j^+}\right)$ is the dissociation energy of the $P - O - M_j^{z_j^+}$ bond, λ_{P-O-M} is the microbasicity of the $P - O - M_j^{z_j^+}$ bond and m_{Qn} and b_{Qn} are the linear fitting parameters for the pK – basicity relationship for a Q^n species.

The dissociation energy of a cation-oxygen bound is assumed to be proportional to the bond energy per oxygen of the metal oxide as calculated from the oxide basicity, given by Equation 4.65 and again here:

$$\frac{Q}{b} = 2 * \left[3.85 - 1.16\Lambda(M_aO_b) - \frac{0.75}{\Lambda(M_aO_b)}\right]^2 - 1.13 \text{ (eV)} \quad \text{(Equation 5.18)}$$

Converting to joules per mole and adding a constant multiplier, k_o, yields Equation 5.19:

$$\Delta G_{diss}\left(P - O - M_j^{z_j^+}\right) = k_o * \left(192.96 * \left[3.85 - 1.16\Lambda(M_aO_b) - \frac{0.75}{\Lambda(M_aO_b)}\right]^2 - 109.02\right) \text{ (J/mol)} \quad \text{(Equation 5.19)}$$

The microbasicity of the bond, λ_{P-O-M}, is given in Equation 5.20 and is explained in more detail in Section 4.3.9,

$$\lambda_{P-O-M} = 1 - \left\{\left(\frac{z_P r_P}{2}\right)(1 - \Lambda_P) + \left(\frac{z_M r_M}{2}\right)(1 - \Lambda_M)\right\} \quad \text{(Equation 5.20)}$$

where z_p and z_M are the valences of phosphorus ($z_p = 5$) and cation M, r_p and r_M are equal to the inverse of the coordination number of P and M with respect to oxygen ($r_p = 1/4$), and Λ_P and Λ_M are the optical basicities of P and M ($\Lambda_P = 0.333$).

Values used for m_{Qn} and b_{Qn} are given in Table 5.3. Values were derived from the linear fits in Figure 5.5 for Q^1 and Q^0 units and were inferred by the author from basicity relationships for Q^2 units.

Table 5.3. Linear fitting parameters between pK and optical basicity for Q-species as it applies to Equation 5.17.

Q-unit	m_{Qn}	b_{Qn}
Q^0 (PO_4^{3-})	68.5	27.5
Q^1 ($PO_{3.5}^{2-}$)	60.3	22.3
Q^2 (PO_3^-)	52.0	17.1

The total free energy of hydration of a mole of glass is then equal to the sum of fractional contributions of free energy for all oxygen bonds, multiplied by the number of oxygen atoms in a mole of glass, $[\#O]$.

$$\Delta G_{hy} = [\#O] \sum_j \Delta G_{hy} \left(Q^n - M_j^{z_j^+}\right) * f\left(Q^n - M_j^{z_j^+}\right) \quad \text{(Equation 5.21)}$$

5.2.5. Calculating the Fraction of Oxygen Bond Arrangements. The fraction of bonding, non-bridging oxygen (NBO(B)) associated with a cation $M_j^{z_j^+}$ is given by:

$$X_{P-O-M_j^{z_j^+}} = \frac{\left[M_j^{z_j^+}\right] z_j^+}{\sum \left[M_j^{z_j^+}\right] z_j^+} \quad \text{(Equation 5.22)}$$

where $\left[M_j^{z_j^+}\right]$ is the molar concentration and z_j^+ is the valence of cation $M_j^{z_j^+}$. The fraction of *total oxygen* associated with a $P-O-M_j^{z_j^+}$ bond is therefore,

$$f\left(P-O-M_j^{z_j^+}\right) = X_{NBO(B)} * X_{P-O-M_j^{z_j^+}} \qquad \text{(Equation 5.23)}$$

where $X_{NBO(B)}$ is the fraction of bonding, non-bridging oxygen and is given in Equation 5.24:

$$X_{NBO(B)} = X_{NBO} - X_{NBO(T)} \qquad \text{(Equation 5.24)}$$

X_{NBO} represents the fraction of all non-bridging oxygen relative to total oxygen and can be calculated from the O-to-P ratio using Equation 4.27. $X_{NBO(T)}$ is the fraction of non-bridging oxygen that are double-bonded, terminal oxygen. There will be one terminal oxygen per phosphate tetrahedra, and thus $X_{NBO(T)}$ can be calculated,

$$X_{NBO(T)} = \frac{[\#P]}{[\#O]} \qquad \text{(Equation 5.25)}$$

where $[\#P]$ and $[\#O]$ are the molar concentrations of P and O per mole of glass.

The fraction of $P-O-M_j^{z_j^+}$ associated with specific Q-units can now be calculated:

$$f\left(Q^n-M_j^{z_j^+}\right) = f\left(P-O-M_j^{z_j^+}\right) * f(Q^n-NBO(B)) \qquad \text{(Equation 5.26)}$$

where $f\left(P-O-M_j^{z_j^+}\right)$ is given by Equation 5.23 and $f(Q^n-NBO(B))$ is the fraction of NBO(B) associated with a given Q^n-unit and is calculated using Equation 5.27. If not empirically known, $f(Q^n)$ can be approximated using the equations in Table 4.1 and the O-to-P ratio.

$$f(Q^n - NBO(B)) = \frac{f(Q^n)*(3-n)}{\sum_{n=0-3} f(Q^n)*(3-n)} \qquad \text{(Equation 5.27)}$$

Equations 5.27 and 5.17 can be used with Equation 5.21 to calculate the free energy of hydration of a glass composition.

5.2.6. Fitting the Model with Experimental Data. Figure 5.7 shows experimental log(DR) versus hydration energy as calculated by Equation 5.21 for glasses in Table 5.2 and k_o = 117.4 (Equation 5.19), which was optimized using Solver in Excel.

In Figure 5.7, circles indicate compositions with monovalent modifiers only, squares are divalent modifiers only, and triangles indicate compositions with both monovalent and divalent modifiers. Filled markers are glasses with compositions containing alumina, open markers are glasses that do not contain alumina. The legend notes the glass family, O-to-P ratio of the series (denoted as ultra, meta, poly, pyro or ortho), and the dissolution temperatures in kelvin. O-to-P ratios range from 2.67 – 3.75, and glass compositional components include Li_2O, Na_2O, K_2O, MgO, CaO, BaO, ZnO, and Al_2O_3. Glasses are mostly trinary compositions, but binary and quaternary compositions are also included.

It is worthwhile to note that by allowing k_o to be optimized separately for the ultraphosphate series, a value of k_o = 142.0 results in much better alignment of the ultraphosphate series with the rest of the data, as seen in Figure 5.8. This may imply that ΔG_{diss} plays a more significant role in the total hydration for ultraphosphates than in less connected structures with shorter chain lengths.

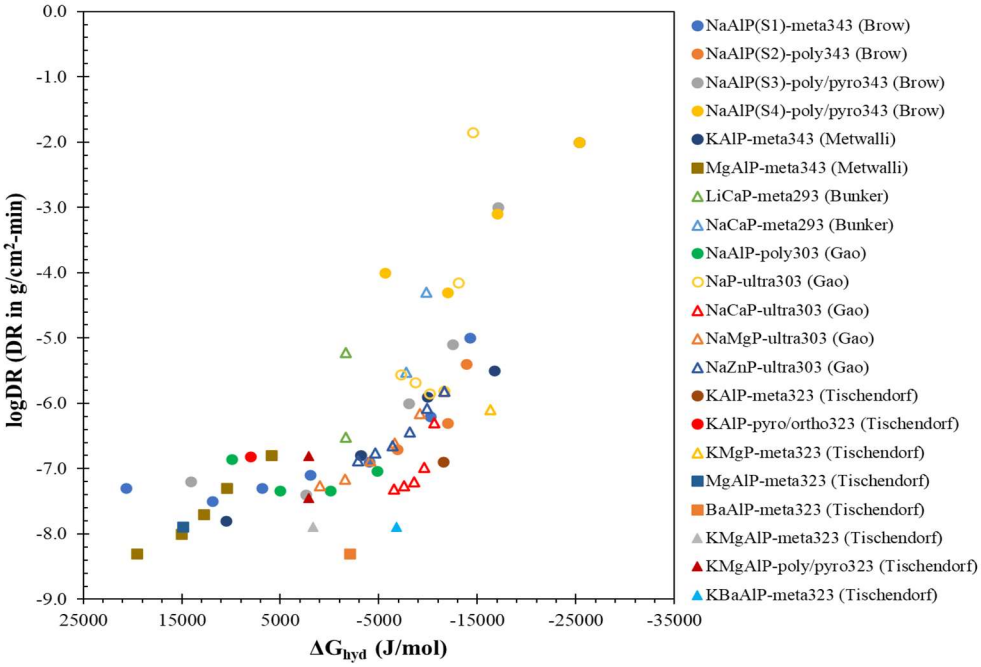

Figure 5.7. Dissolution rate (as logDR with DR in g/cm^2-min) versus ΔG_{hyd} calculated using Equation 5.21 with k_o = 117.4.

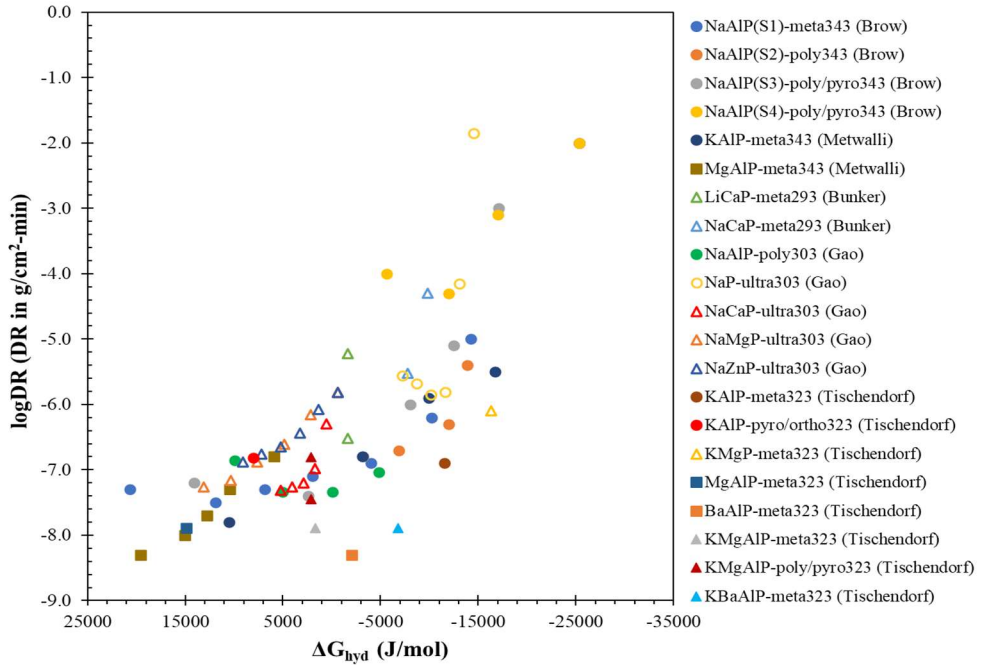

Figure 5.8. Dissolution rate versus ΔG_{hyd} calculated using Equation 5.21 with k_o = 142.0 for the ultraphosphate series and k_o = 117.4 for all other series.

5.3. DISCUSSION

Calculation of free energy of hydration using microscopic basicities of individual bonds in the glass appears to provide results that follow expected trends with experimentally determined dissolution rates. However, there is a good amount of scatter to the data and additional considerations should be included in future work.

While increasing field strength and decreasing basicity of monovalent cations result in lower dissolution rates, the opposite effect is observed with divalent cation additions. Numerous studies [236], [249]–[251] observed an increase in dissolution rate when lower basicity (higher field strength) divalent ion replaced those with higher basicity (lower field strength). This observation is explained by the increasing size of the divalent cations. When forming a chelated crosslink between phosphate chains, the divalent cations will fill interstices. Cations with larger radii will effectively block the pathways of the water molecules, slowing their diffusion through the leached layer and decreasing the corrosion rate [250].

As seen in Figure 5.7, compositions which include barium, the largest divalent cation considered here, fall farthest from linearity. Also, in the three Na_2O-MO-ultraphosphate series reported by Gao [236], Figure 5.7 shows nearly the same deviation from linearity for series where MO = ZnO and MgO. While these oxides have different basicities ($\Lambda_{ZnO} = 0.91$, $\Lambda_{MgO} = 0.78$) which were used in ΔG_{hyd} calculations, they have nearly identical ionic radii ($r_{Zn2+} = 0.74$Å, $r_{Mg2+} = 0.72$ Å), and their dissolution curves fall practically on top of each other. In contrast, the series with MO = CaO yields a larger deviation from linearity, which is consistent with calcium having a larger radius (r_{Ca2+} =

1.00 Å). Adjustments to the model which account for decreases in the dissolution rate as a function of concentration and size of the divalent cations in the glass may be possible.

Future work should also consider the effect of crosslinking by divalent and trivalent cations. The current model is unable to account for changes in crosslinking when basicity is unchanged. For example, Bunker [234] reported dissolution rates for glasses in the Li_2O-CaO-P_2O_5 family, where Li_2O is replaced by CaO. The two metal oxides have the same optical basicity ($\Lambda_{Li2O} = \Lambda_{CaO} = 1.0$) and contribute the same number of oxygens per mole of oxide, and therefore no change in ΔG_{hyd} will be calculated for the changing compositions according to the model presented here. This clearly is not consistent with experimental observations, as replacing monovalent Li_2O with divalent CaO results in a decrease in dissolution rate. The contribution of chelate structures to the dissolution behavior must be considered in the next version of the model.

Although lacking structural data permits many assumptions concerning ideal distributions of cation bonding, it is highly unlikely that many glasses will take on such an idealized configuration. Disproportionation of Q-units will occur for many glasses, the extent of which is related to free energy of formation and field strength of the cations present in the composition [228]. Studies have also suggested preferential bonding of divalent cations to chain-ending Q^1 units as opposed to Q^2 units [250]. Further work can be done to improve the model with more specific structural knowledge of glass families and compositions.

5.4. SUMMARY

A bonding approach to dissolution modeling was proposed using microscopic optical basicity of bonds to calculate hydration energies, and assuming the total free energy of hydration for the glass is a sum of contributions of bond hydration energies. It is important to note that no thermochemical data was used in these calculations, and the only information necessary was the glass composition and optical basicity values for glass components. Structural information concerning coordination environments and fractions of Q units will improve accuracy of the model, although approximations can be made using common coordination environments and idealized structural units as done here.

Preliminary results show that the model can predict general trends in dissolution rate with hydration energy calculations, although future work is needed to incorporate additional factors which effect dissolution rate, such as crosslinking of phosphate chains due to divalent and trivalent cations, and the reduction of dissolution rate caused by divalent cations blocking the pathways of water diffusion. Also, results suggest that certain compositional regions (ie. ultraphosphates) may have different fitting parameters, k_o, indicating a changing dependence of ΔG_{hyd} on ΔG_{diss} of the cation-oxygen bond for different structural features. Further investigations are needed to be able to computationally account for these factors in order to ultimately establish a model which can predict dissolution rates based solely on composition, with no need for thermochemical data.

6. CRYSTALLIZATION OF IRON PHOSPHATE GLASSES: COMPOSITIONAL AND ATMOSPHERIC EFFECTS ON GLASS STABILITY, CRYSTALLIZATION KINETICS AND CRYSTAL PHASE FORMATION

Iron phosphate glasses with compositions ranging from metaphosphates to pyrophosphates (with Fe/P ratios of 0.33 – 0.67) were prepared at melting temperatures between 1200°C and 1350°C to vary the Fe^{2+}/Fe^{3+} ratio. The polyphosphate series with Fe/P ratios of 0.5 and intermediate chain lengths was most comprehensively studied. Crystallization behavior was studied using DTA and crystalline phases were identified using Raman spectroscopy and XRD. Activation energies of crystallization were calculated via the Kissinger method using both the onset and peak crystallization temperatures, and glass stabilities were calculated using multiple parameters. Results indicate an increase in the Fe^{2+}/Fe^{3+} ratio and a decrease in glass transition and crystallization temperatures with increasing melt temperature, and the formation of multiple crystalline phases for all samples, including $FePO_4$, $Fe_4(P_2O_7)_3$, $Fe(PO_3)_3$ and $Fe_3(P_2O_7)_2$. The iron polyphosphate series exhibited the greatest glass stability of those studied, with greater stability in air than nitrogen. Measurement of mass changes suggest oxidation of Fe^{2+} to Fe^{3+} upon heating, the extent of which is greatly dependent on the oxygen available in the environment and the average sample particle size. All samples exhibit predominant surface crystallization, with glass stability increasing with increasing particle size.

6.1. GENERAL PRINCIPLES

Radioactive decay of encapsulated nuclear wastes may heat the host glass matrices during long storage periods [252]. Glass stability and crystallization upon heating, the occurrence of which may affect the glass durability, viscous flow, strength, and response to radiation, are therefore among the most critical properties of iron phosphate glasses to be better understood for future applications in HLW encapsulation. Crystallization may also result upon quenching, resulting in large volume changes which can cause glass monoliths to crack, and precipitation of dense crystals in the glass melt may result in adverse consequences to the melt tanks.

Glass stability refers to the tendency of a melt to avoid devitrification upon reheating, whereas glass forming ability refers to the tendency of a melt to avoid crystallization upon cooling. Many parameters exist from which glass stability can be evaluated, and Jiusti et al. [253] have determined which of these parameters can also best predict glass forming tendency. Glass stability parameters used here can be quickly and easily calculated using thermal analysis scans. Data acquired from thermal analysis can also be used to calculate crystallization activation energies and to determine whether devitrification is occurring via homogeneous or heterogeneous (in this case surface) crystallization.

Many parameters that affect crystallization kinetics, such as melt viscosity and liquidus temperature, are functions of composition and will be contingent on the Fe/P and O/P ratios of the melt. Seeing as changes in the iron redox ratio (Fe^{2+}/Fe^{3+}) will change the O/P ratio and chain length within the melt, understanding how to control the iron redox ratio is also important to controlling crystallization behavior in iron phosphate

glasses. In addition, it is vital to investigate how the iron redox ratio within the glass and particularly on the glass surface may change upon heating, thus affecting crystallization tendency.

Unexpected glass stability has been shown for the iron phosphate glasses in the polyphosphate composition range, which exhibit average chain lengths between the dimers primarily seen in pyrophosphate compositions and long chain lengths seen in metaphosphate compositions. This observation suggests that average and distribution of chain lengths may play an important role in controlling parameters, such as melt viscosity and liquidus temperature, that affect crystallization kinetics.

Identification of the crystalline phases which form under specific conditions is important to fully understanding the crystallization behavior of a glass. Knowledge of the applicable phase diagrams and liquidus temperatures are valuable to this understanding, as well, and can help explain how composition and heat treatment conditions affect crystallization behavior.

Glasses in the metaphosphate, polyphosphate and pyrophosphate compositional ranges have been prepared in this study, with a primary focus on glasses in the polyphosphate range with Fe/P ~ 0.5 and O/P ~ 3.25. Only glasses from the Fe(III) and FPP series were used in crystallization experiments. The effects of Fe/P ratio, iron redox ratio, particle size and atmosphere on crystallization and glass stability will be discussed, as well as identification of crystalline phase formation and associated crystallization temperatures.

6.2. EXPERIMENTAL PROCEDURES

See Section 3 for glass preparation procedures and compositional analyses.

Glass powder was prepared by crushing bulk glass pieces with a steel mortar and pestle and then grinding them with a silica mortar and pestle. Powders were then sieved to several particle size ranges, including fine and coarse grains, of 45 – 63 μm, 75 – 106 μm, 250 – 300 μm, and 425 – 500 μm.

Differential thermal analysis experiments were conducted using a Perkin Elmer DTA 7. Powdered and bulk samples of masses ~50 mg were placed in alumina crucibles and powdered alumina was used as the reference sample. All experiments were performed under a nitrogen environment. Heating and cooling rates ranged from 1 – 30 K/min and samples were heated to temperatures up to 1200ºC.

Differential scanning calorimetry experiments were conducted using a Netzsch STA 409 DSC/TGA. Alumina crucibles and alumina reference samples were used and experiments were performed in both air and nitrogen environments. Samples of mass ~50 mg were heated to 1200ºC at a rate of 10 K/min.

X-ray diffraction was performed using a Philips X-Pert Diffractometer with Cu K_α radiation. Spectra were recorded using a step size of 0.03 and a step time of 2 seconds between angles of 10 – 70 º2Θ.

Raman spectroscopy was carried out using a LabRAM ARAMIS spectrometer with a 632.81 nm HeNe laser and 5 second exposition time. Results were analyzed with LabSpec5 software.

Optical microscopy was performed using a Leica DMRX optical microscope with objectives from 2.5 up to 100×. A CCD camera and freeware *ImageJ* were used to observe the crystalline phases.

6.3. RESULTS AND DISCUSSION

Thermal analysis and crystallization results are discussed below.

6.3.1. Compositional Effects on Characteristic Temperatures. DTA scans in a nitrogen environment for all glass series at various melting temperatures are shown in Figure 6.1, while Figure 6.2 shows the change in characteristic temperatures with increasing glass melt temperature and ferrous iron content. Values of characteristic temperatures as well as important compositional parameters are given in Table 6.1, where T_g is the glass transition temperature, T_x is the onset crystallization temperature, T_p is the peak crystallization temperature, and T_m is the onset melting temperature.

The general decrease in glass transition and crystallization temperatures with increasing melting temperature can be explained in terms of the change in iron redox ratio. As the fraction of Fe^{2+} relative to Fe^{3+} increases, the connectivity of the glass structure will decrease due to the replacement of trivalent bonds with weaker divalent bonds. Similar results have been reported for other iron oxide systems [254]. According to the results shown in Figure 6.3 [117], this effect results in a lowering of viscosity and greater ease of bond rearrangement necessary for crystallization, allowing for crystallization at lower temperatures. As the temperature increases towards the melting point, glasses with different Fe^{2+}/Fe^{3+} ratios present similar viscosity. Thermal analysis results of Fe(III) series reveal a decrease in glass transition temperature with increasing

Fe/P and O/P ratios, which follows with the decrease in viscosity with increase in Fe/P seen in Figure 6.3.

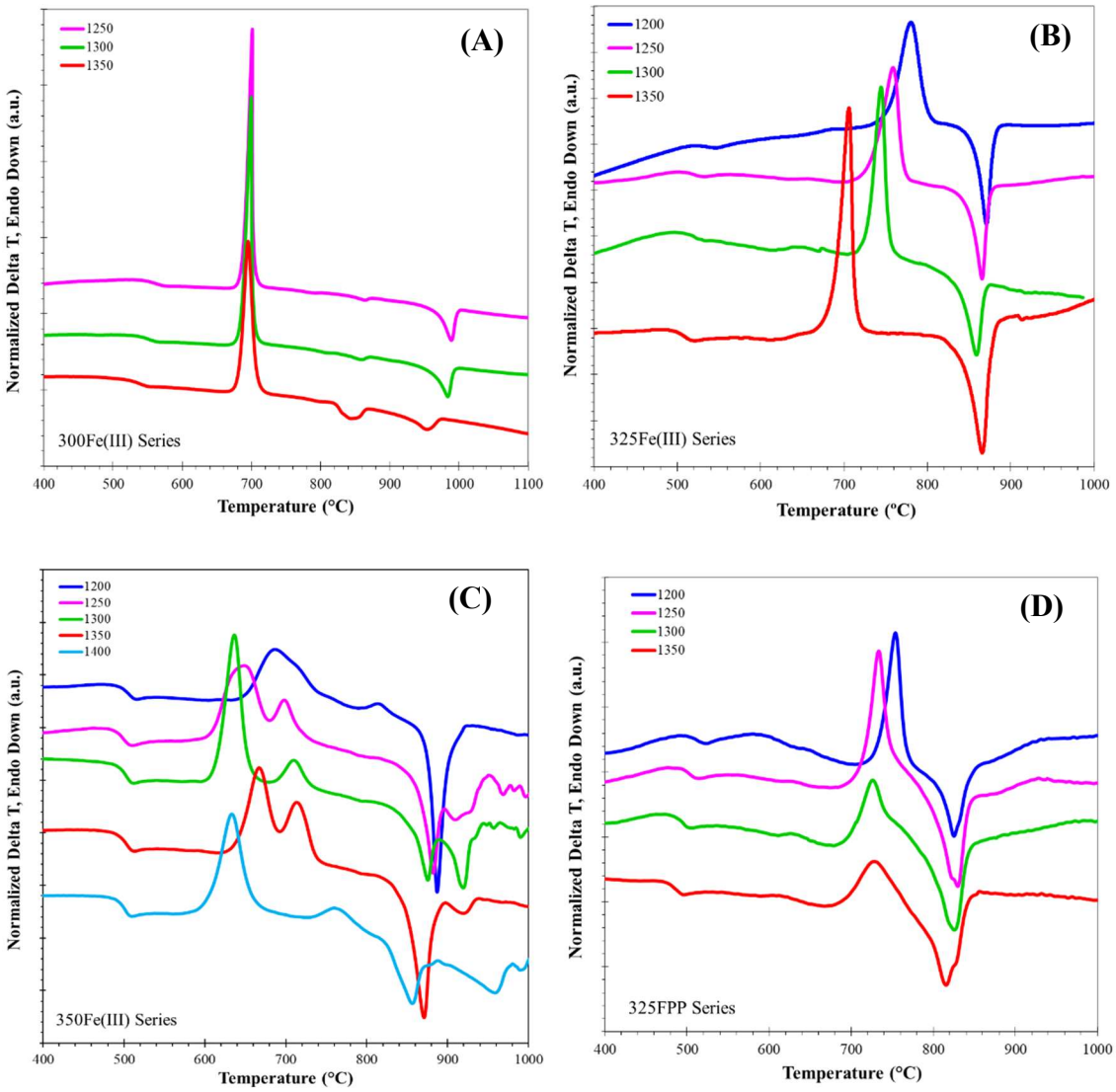

Figure 6.1. DTA scans in a nitrogen environment with 10 K/min heating rate and 75 – 106 μm particle size for (A) 300Fe(III), (B) 325Fe(III), (C) 350Fe(III) and (D) 325FPP glass series.

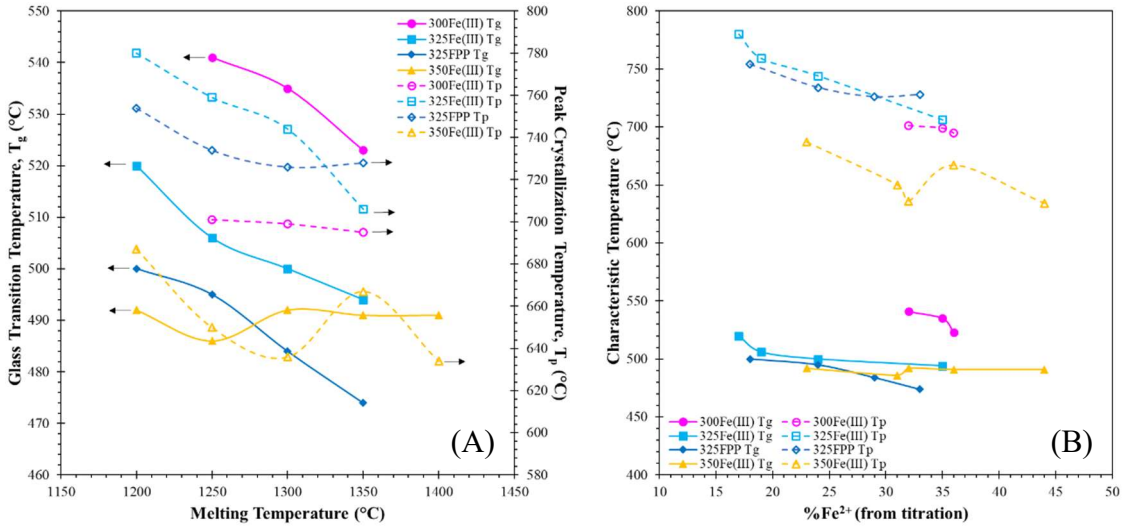

Figure 6.2. Glass transition and peak crystallization temperatures for all iron phosphate glass series (measured in nitrogen environment with 10 K/min heating rate and 75 – 106 µm particle size) plotted versus (A) glass melting temperature and (B) ferrous iron content.

Table 6.1. Characteristic temperatures of glass series at various melt temperatures measured with a 10 K/min heating rate in nitrogen for 75-106 µm particle sizes.

Glass Series	Melting Temp (°C)	%Fe^{2+}	O/P	T_g (°C)	T_x (°C)	T_p (°C)	T_m (°C)
300Fe(III)	1250	32	3.04	541	687	701	838
	1300	35	3.09	535	685	699	823
	1350	36	3.15	523	679	695	821
325Fe(III)	1200	17	3.28	520	751	780	856
	1250	19	3.34	506	728	759	846
	1300	24	3.21	500	726	744	840
	1350	35	3.28	494	687	706	841
325FPP	1200	18	3.25	500	733	754	809
	1250	24	3.24	495	713	734	808
	1300	29	3.24	484	693	726	804
	1350	33	3.24	474	689	728	800
350Fe(III)	1200	23	3.42	492	650	687	876
	1250	31	3.45	486	610	650	862
	1300	32	3.41	492	612	636	855
	1350	36	3.41	491	638	667	847
	1400	44	3.48	491	603	634	824

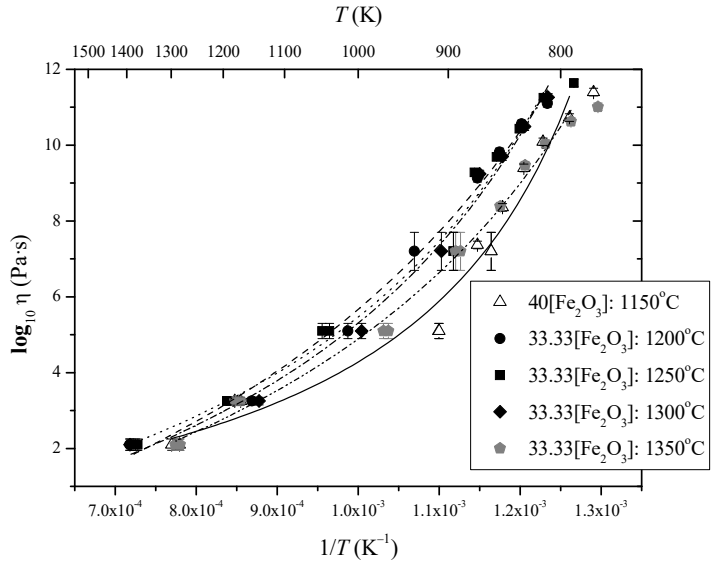

Figure 6.3. Viscosity versus 1/T (in air) for 325Fe(III) and 350Fe(III) glasses: full line, 350Fe(III)1150 (from other work); dashed line, 325Fe(III)1200; dotted line: 325Fe(III)1250; dashed-dotted line: 325Fe(III)1300; dashed-dotted-dashed line: 325Fe(III)1350 [taken from Ghussn et al, 2007] [117].

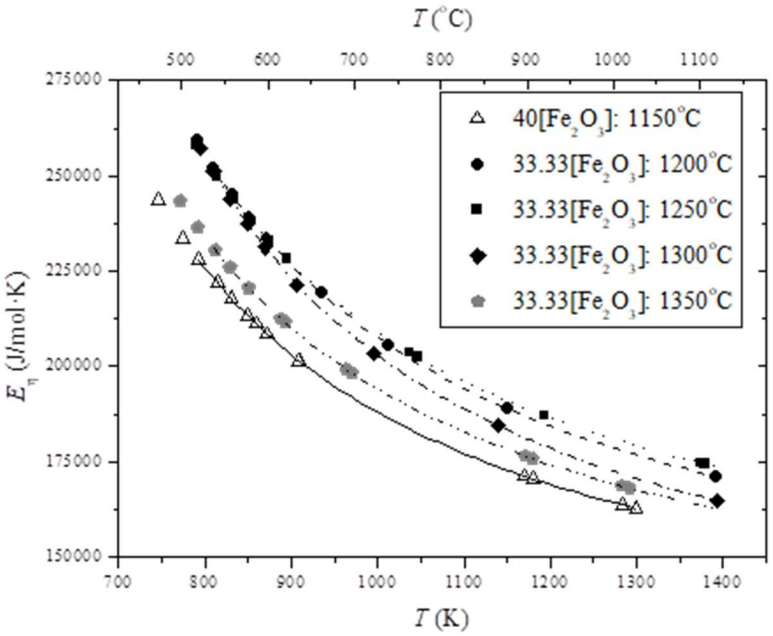

Figure 6.4. Activation energy for viscous flow, E_η, for the 325Fe(III) series. [taken from Ghussn et al, 2007] [117]

The activation energies of viscous flow for these glasses were reported elsewhere [117] and are shown in Figure 6.4, supporting the viscosity results shown above. Results show a higher activation energy for the more polymerized network of the polyphosphate 325Fe(III) series as compared to the pyrophosphate 350Fe(III) glass, and a higher activation energy associated with lower glass melting temperatures within the 325Fe(III) series, which correlate to higher connectivity within the structure due to greater proportions of trivalent Fe^{3+} relative to divalent Fe^{2+}.

The 300Fe(III) metaphosphate series exhibits the highest glass transition temperature, likely due to having the lowest O-to-P ratio and most highly polymerized structure. Although the iron redox ratio changes the least of the glass series studied, the O-to-P ratio increases the most due to phosphate volatilization, which is expected to decrease both viscosity and T_g. The metaphosphate series exhibits a sharp crystallization peak with onset and peak temperatures which do not change much with glass melting temperature. Although sharp, the peaks are asymmetric (as seen in Figure 6.5) and multiple crystal melt peaks are observed, suggesting the formation of multiple crystalline phases.

The 350Fe(III) pyrophosphate series exhibits no significant change in glass transition temperature with changes in melting temperature, despite notable changes in iron redox ratio. This observation suggests that as ferric iron is further reduced to ferrous iron, presumably decreasing the connectivity of the glass, other structural changes with an opposing effect on the glass connectivity and viscosity may be occurring. The reduction of iron is coupled with polymerization of the glass structure as explored in Section 4 of this dissertation. The increased connectivity of the structure with

replacement of Q^1 dimer units (and potentially Q^0-units assuming some disproportionation within the structure) by longer, Q^2-containing chains may counteract the effect of replacing trivalent Fe^{3+} with divalent Fe^{2+} on the glass transition temperature. Multiple crystallization and melt peaks are observed for all glasses in the series and the identity of the phases formed may be correlated to both the composition and short-range structure of the glass.

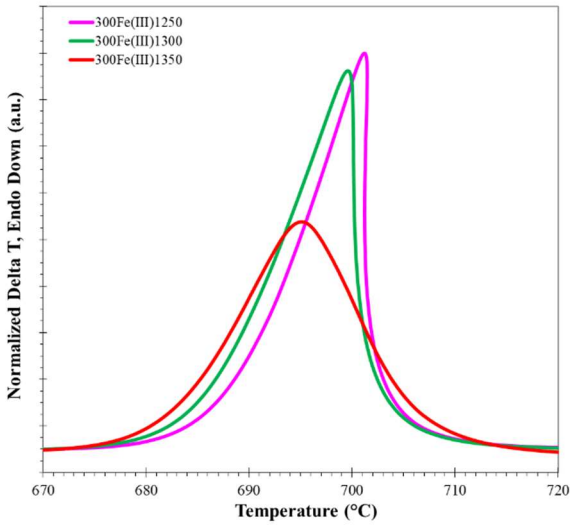

Figure 6.5. Crystallization peaks of 300Fe(III) series.

Despite the similar compositions of the 325Fe(III) and 325FPP polyphosphate series, differences are observed in their glass transition temperatures and crystallization behavior. Both series exhibit a decrease in T_g and T_x with increasing melt temperature although all characteristic temperatures are lower for the 325FPP series than those of the 325Fe(III) series. While slight differences may be expected due to the lower Fe/P ratio and higher Fe^{2+} content, the compositional differences seem too insignificant to cause

such a drastic disparity. In addition, instead of the systematic shift in onset and peak crystallization temperatures observed with increasing melt temperature in the 325Fe(III) series, the crystallization peak for the 325FPP series initially shifts to lower temperatures but then broadens, such that the onset crystallization temperature does not significantly change at higher melt temperatures. The broadening and asymmetry of the crystallization peak suggests that not only may the melt be crystallizing at lower temperatures due to decreased viscosity, but that additional crystalline phases may be forming when larger proportions of Fe^{2+} are available in the melt. This conclusion is supported by the appearance of a second melt peak at slightly lower temperatures for the higher melt glasses.

The differences in glass transition temperature and crystallization behavior of the two iron polyphosphate series suggest that there may be structural and intermediate range order differences between the glasses which affect these properties. Using iron pyrophosphate as a raw material may result in different chain length or ring distributions within the glass structure, which may favor the crystallization of certain phases or affect the way the glass rearranges during crystallization or annealing. Additional differences between the two polyphosphate series are explored in Section 7 and further investigation of effects of raw materials is suggested as future work.

6.3.2. Compositional Effects on Glass Stability. Glass stability is defined as the resistance of a glass against crystallization upon reheating after glass formation and can be measured using many different parameters [253], [255]–[257]. Nascimento et al. [255] evaluated and compared numerous parameters using fourteen different methods to determine which glass stability parameters have the best empirical correlations with glass

forming ability. Among those parameters considered, the Weinberg (K_W), Hrüby (K_H) and Lu and Liu (K_{LL}) stability parameters provided the best measure of relative vitrification tendencies of different glass forming systems. Higher K values indicate greater stability against crystallization on heating.

While traditionally onset crystallization temperatures are used in K_W and K_H stability calculations, it was recently determined by Jiusti et al [253] that using peak crystallization instead of onset crystallization temperatures improves the predictive power of the stability parameters and that K_W values were considered most predictive of those investigated. For comparison purposes, stability calculations were performed here using both crystallization temperatures and both the Weinberg [258] and Hrüby [259] parameters (according to Equation 6.1 and 6.2) and are given in Table 6.2.

$$K_W = \frac{T_{(x,p)} - T_g}{T_m} \qquad \text{(Equation 6.1)}$$

$$K_H = \frac{T_{(x,p)} - T_g}{T_m - T_{(x,p)}} \qquad \text{(Equation 6.2)}$$

Figure 6.6 shows the change in K_W and K_H stability parameters using peak crystallization temperatures as a function of both glass melting temperature and ferrous iron content. Results show that the pyrophosphate and metaphosphate series have comparable glass stabilities. The two iron polyphosphate series have similar glass stabilities and are the most stable glasses of the compositional series investigated in this study. There is no consistent trend of glass stability with ferrous iron content between the glass series, with the stability increasing and decreasing in different compositional ranges within the series.

Table 6.2. Weinberg and Hrüby glass stability parameters calculated from the characteristic temperatures in Table 6.1.

Glass Series	Melting Temp (°C)	$K_w(T_p)$	$K_H(T_p)$	$K_w(T_x)$	$K_H(T_x)$
300Fe(III)	1250	0.144	1.168	0.131	0.967
	1300	0.150	1.323	0.137	1.087
	1350	0.157	1.365	0.143	1.099
325Fe(III)	1200	0.230	3.421	0.205	2.200
	1250	0.226	2.908	0.198	1.881
	1300	0.219	2.542	0.203	1.982
	1350	0.190	1.570	0.173	1.253
325FPP	1200	0.235	4.618	0.215	3.066
	1250	0.221	3.230	0.202	2.295
	1300	0.225	3.103	0.194	1.883
	1350	0.237	3.528	0.200	1.937
350Fe(III)	1200	0.170	1.032	0.138	0.699
	1250	0.144	0.774	0.109	0.492
	1300	0.128	0.658	0.106	0.494
	1350	0.157	0.978	0.131	0.703
	1400	0.130	0.753	0.102	0.507

The 325FPP series exhibits an apparent stability minimum near a melt temperature of 1300ºC. This minimum may not be a real compositional effect on crystallization tendency but rather an artificial result of DSC data. As seen in Figure 6.1D, the crystallization peak and melt peak begin to overlap for samples 325Fe(III)1300 and 325Fe(III)1350, obscuring and causing an apparent shift in the onset melting temperature. The true onset temperature of the crystal melt peak, unaffected by any endothermic contribution from crystallization, would need to be determined in order to calculate a more accurate measure of glass stability. The stability of the 325Fe(III) series

exhibits the most consistent trend, showing a greater devitrification tendency with increasing ferrous iron content.

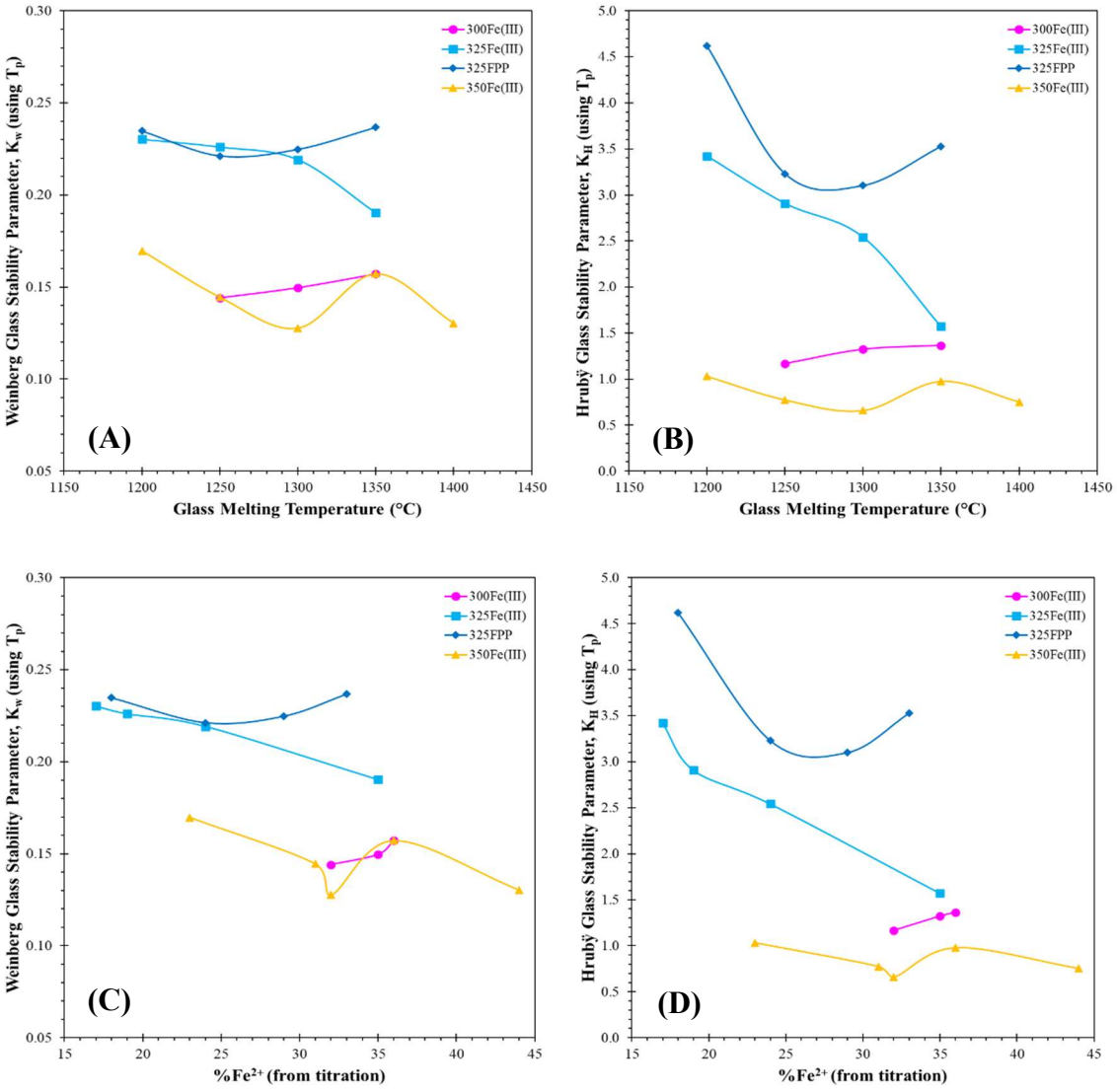

Figure 6.6. Weinberg and Hrubÿ glass stability parameters for all glass series as a function of glass melting temperature (A and B) and ferrous iron content (C and D). All calculations use peak crystallization temperatures and are measured in nitrogen at 10 K/min heating rates.

6.3.3. Activation Energy Calculations. Figure 6.7 – Figure 6.9 show DTA results for glasses with a 75 – 106 μm particle size but varying heating rate for all glass series. Characteristic temperatures are summarized in Table 6.3.

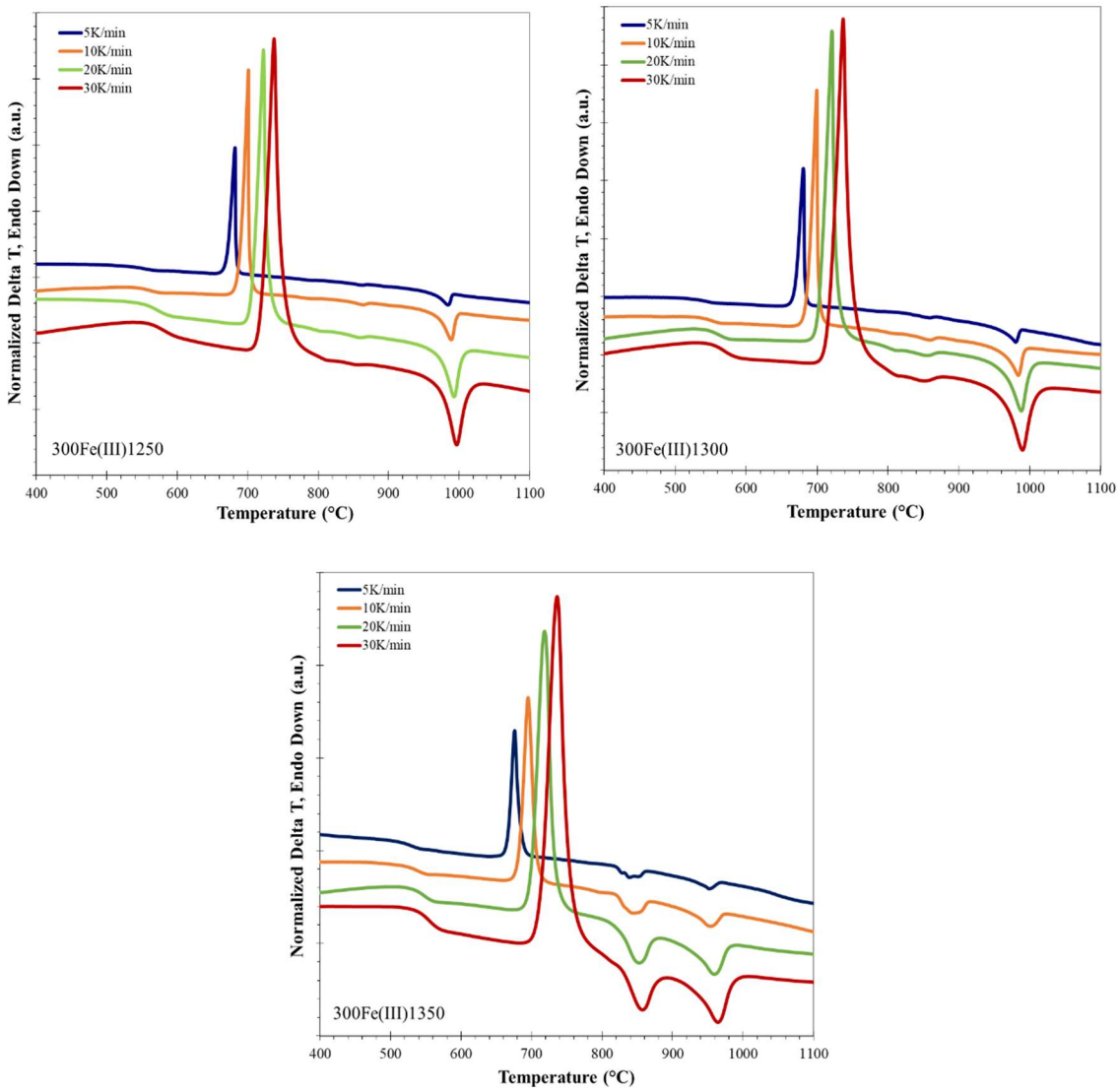

Figure 6.7. DTA scans for 300Fe(III) series at various heating rates for 75 – 106μm particles in a nitrogen environment.

The glass transition temperature and peak crystallization temperature increase with increasing heating rate. This increase may have a kinetic basis, as the glass will have less time to relax and less time at nucleation and growth temperatures with faster heating rates. This variation of characteristic temperatures with heating rate can be used in activation energy calculations for structural relaxation and crystallization [260], [261].

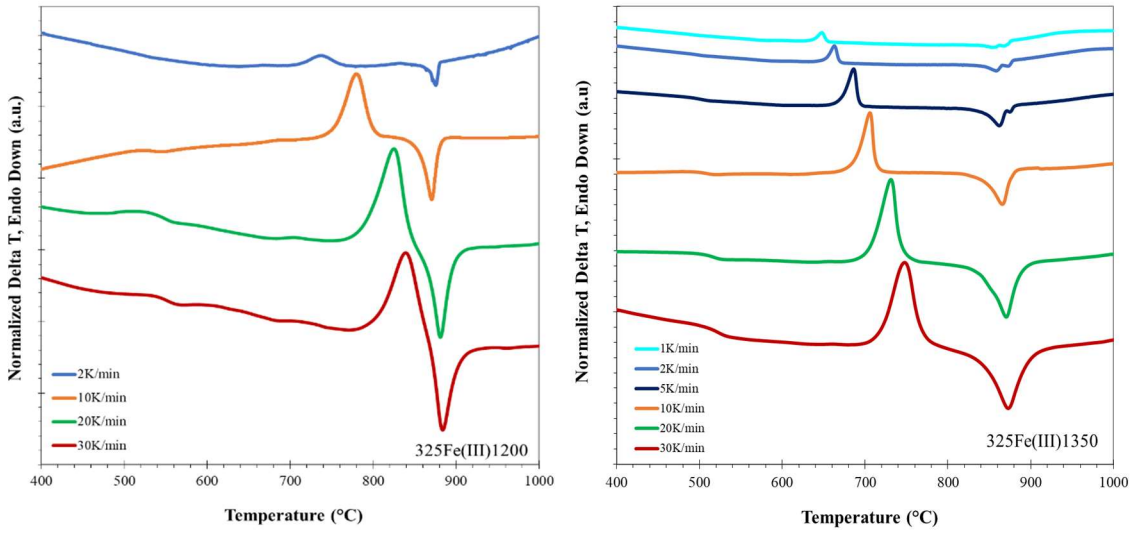

Figure 6.8. DTA scans for 325Fe(III)1200 and 325Fe(III)1350 series at various heating rates for 75 – 106μm particles in a nitrogen environment.

Activation energies of crystallization are calculated using the Kissinger method [2], where Φ is the heating rate, T_p is the peak crystallization temperature, A is a constant, E is the activation energy of crystallization and R is the universal gas constant:

$$ln\left(\frac{\Phi}{{T_p}^2}\right) = A - \frac{E}{RT_p} \qquad \text{(Equation 6.3)}$$

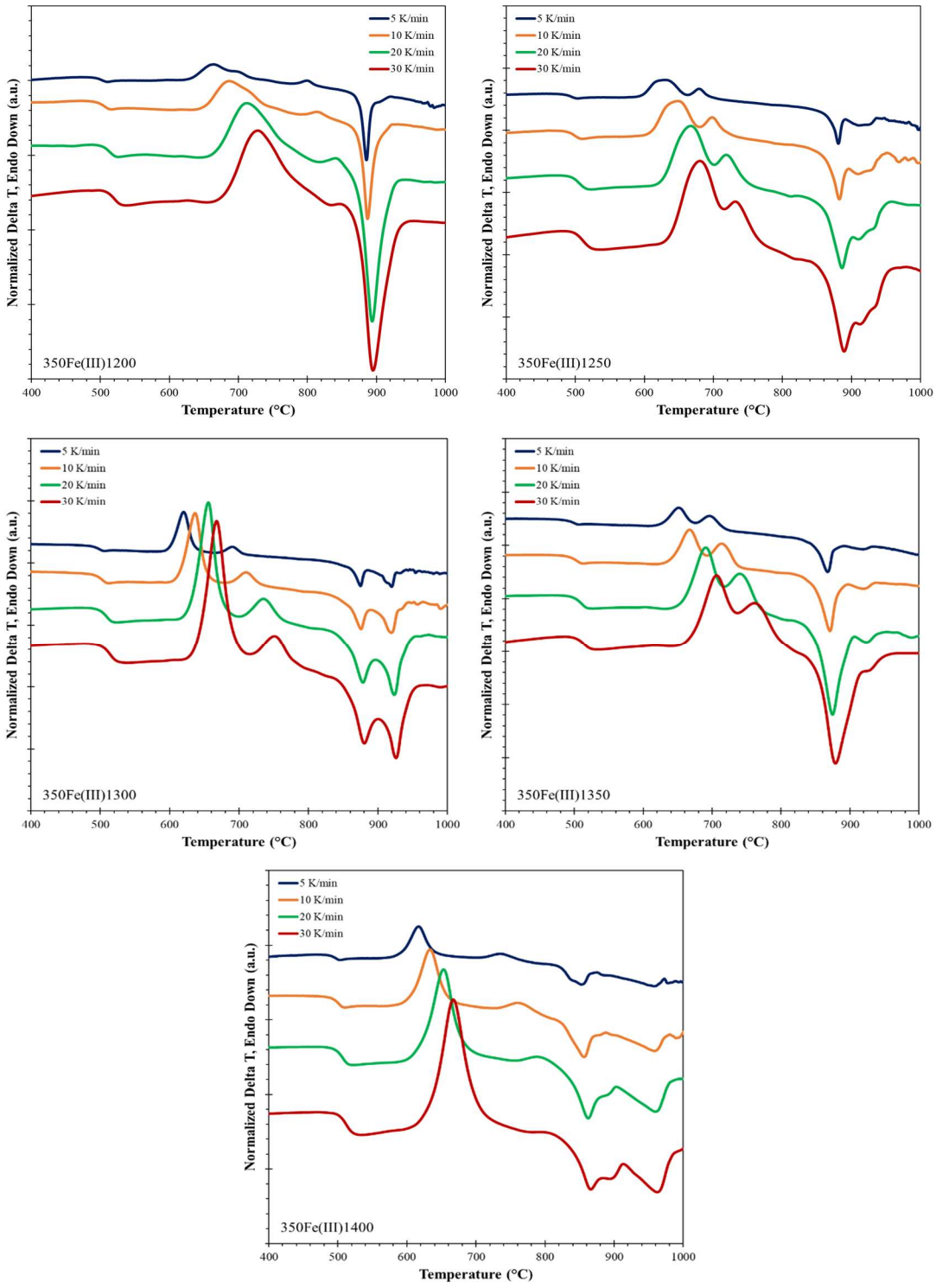

Figure 6.9. DTA scans for 350Fe(III) series at various heating rates for 75 – 106μm particles in a nitrogen environment.

Table 6.3. Characteristic temperatures for all Fe(III) series at various heating rates.

Glass Series	Melting Temp (°C)	Heating Rate (K/min)	T_g (°C)	T_x (°C)	T_p (°C)	T_m (°C)
300Fe(III)	1250	5	532	670	682	836
		10	541	687	701	838
		20	550	705	722	830
		30	555	717	738	830
	1300	5	521	668	681	826
		10	535	685	699	823
		20	540	700	721	826
		30	547	714	737	827
	1350	5	511	665	676	820
		10	514	680	695	821
		20	528	698	719	824
		30	535	712	736	830
325Fe(III)	1200	2	514	707	737	859
		10	520	751	780	856
		20	530	787	825	868
		30	537	801	840	872
	1250	10	506	728	759	846
	1300	10	500	726	744	840
	1350	1	493	636	648	840
		2	490	651	663	842
		5	489	670	686	841
		10	494	687	706	841
		20	503	704	731	844
		30	508	717	748	845
350Fe(III)	1200	5	490	629	664	876
		10	492	650	687	876
		20	501	667	712	877
		30	509	679	728	875
	1250	5	484	596	630	861
		10	486	610	650	862
		20	492	625	667	860
		30	497	636	680	862
	1300	5	490	599	620	863
		10	492	612	636	855
		20	498	629	656	855
		30	502	638	667	857
	1350	5	486	623	651	848
		10	491	638	667	847
		20	498	655	691	850
		30	501	667	707	856
	1400	5	486	589	617	822
		10	491	603	634	824
		20	496	616	653	836
		30	502	630	667	833

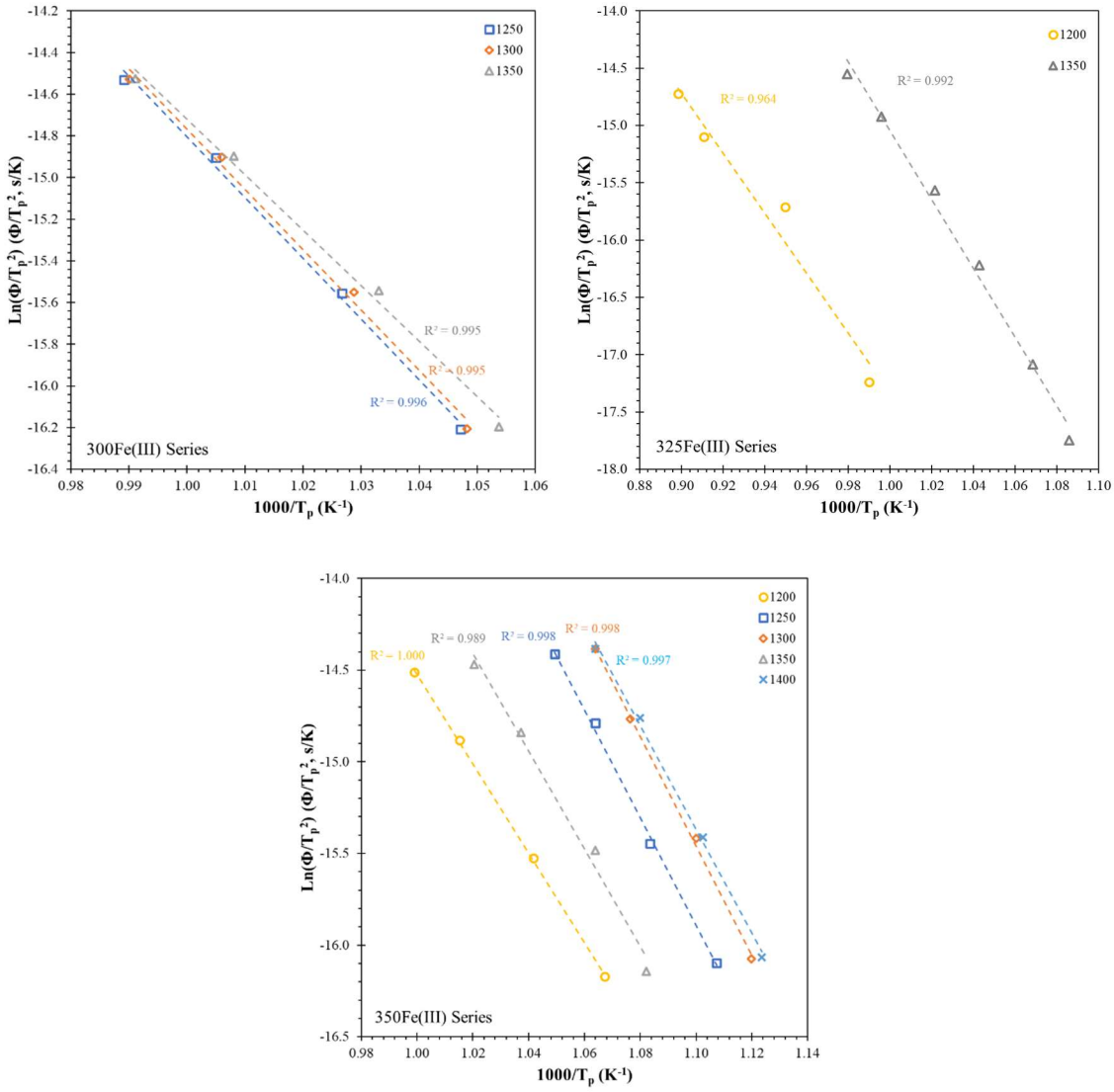

Figure 6.10. Kissinger plots of all glass series and linear fits used to calculate crystallization activation energies.

Figure 6.10 shows Kissinger plots for all Fe(III) glasses in nitrogen. Values for calculated crystallization activation energies are given in Table 6.4 and are shown as a function of glass melt temperature and ferrous iron content in Figure 6.11. Similar to glass stability calculations, there is no consistent trend in crystallization activation energy with increasing ferrous iron content within or between the series. This inconsistency is

likely due to changes in which crystalline phases are forming as the ferrous iron content increases in the melt. The polyphosphate series appears to have the highest activation energy of the glasses studied here, which is consistent with having the highest calculated glass stability. Potential reasons for this higher observed stability will be discussed later in the section.

Table 6.4. Crystallization activation energies for glass series with 75 – 106 μm particle size range.

Glass Series	Melting Temp (°C)	$\%Fe^{2+}$	Slope	E (kJ/mole)
300Fe(III)	1250	32	-29.148	242
	1300	35	-28.895	240
	1350	36	-26.594	221
325Fe(III)	1200	17	-27.106	225
	1350	35	-30.024	250
350Fe(III)	1200	23	-24.354	202
	1250	31	-29.436	245
	1300	32	-29.814	248
	1350	36	-26.676	222
	1400	44	-28.318	235

All glasses exhibit an increase in glass stability with increasing heating rate, again likely due to having less time at nucleation and growth temperatures with faster heating rates. Figure 6.12 shows the Weinberg stability parameter calculated using Equation 6.1 and peak crystallization temperatures as a function of heating rate. All data exhibit a logarithmic dependence between stability and heat rate.

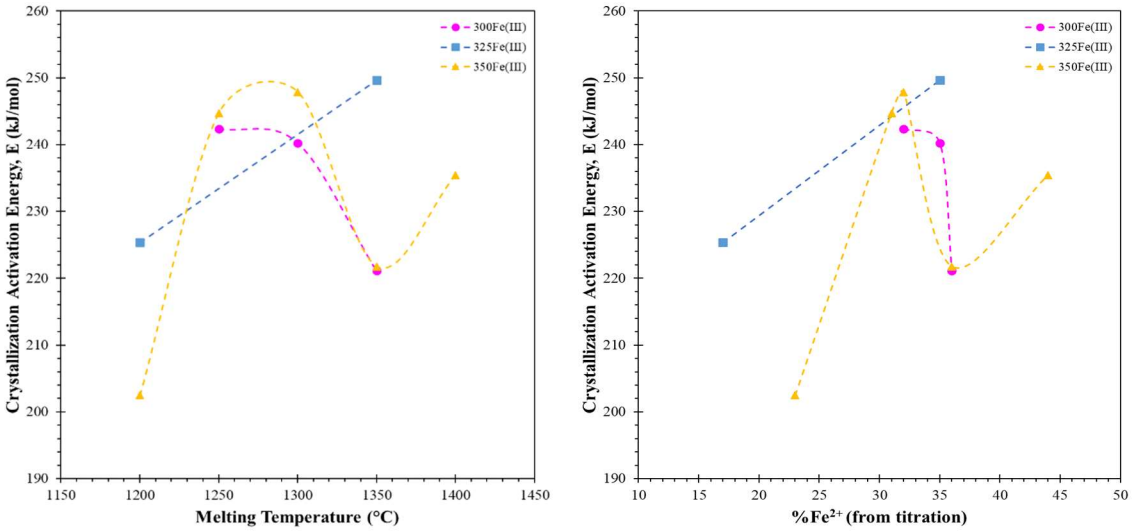

Figure 6.11. Crystallization activation energies as a function of melting temperature for all Fe(III) melt series.

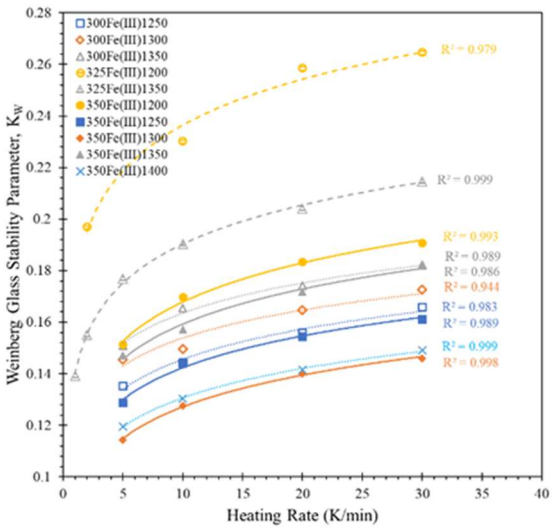

Figure 6.12. Dependence of the Weinberg stability parameter (using peak crystallization temperatures) on heating rate for all glass samples.

6.3.4. Particle Size Effects. The 325Fe(III) series was chosen for further analysis due to the higher glass stability of the polyphosphate series as compared to the meta- and pyrophosphate series. The effect of particle size on stability and crystallization was

studied. Thermal analysis results are shown for consistent heating rates but changing particle size (Figure 6.13 – Figure 6.16) as well as for consistent particle size but increasing heating rate (Figure 6.17 – Figure 6.20). Characteristic temperatures are summarized in Table 6.5. Values listed in gray italics have additional uncertainty due to the overlap of the crystallization and melt features (concerning T_m values) or difficulty in distinguishing the endothermic glass transition feature for slower heating rates.

For all cases, increasing particle size with a consistent heating rate results in constant glass transition temperatures and increasing onset crystallization temperatures, showing a clear dependence of crystallization kinetics on surface area. The increase in crystallization temperature with increasing particle size is indicative of predominant surface crystallization [262]. Homogeneous crystallization occurs throughout the bulk of the glass, such that the size of the individual particles will not affect the overall crystallization rate. Heterogeneous crystallization, however, depends on the availability of nucleation sites. For surface crystallization, the sample surface provides many nucleation sites (solid contaminants, cracks, scratches, etc.) and thus greater surface area facilitates crystallization. Therefore, for an equal mass of glass, smaller particles will have a greater surface area, often resulting in faster crystallization at lower temperatures, with more intense and narrower crystallization peaks, as seen for the 325Fe(III) series.

This effect can be quantified by plotting the ratio $T_p^2/(\Delta T)_p$ versus particle size, where $(\Delta T)_p$ is the crystallization peak half width [262]. A decrease in $T_p^2/(\Delta T)_p$ with increasing particle size, as seen in Figure 6.21, is indicative of surface crystallization. Figure 6.22 shows an image of a sample of 325Fe(III)1200 heat treated at 800°C for 30 minutes, clearly indicating predominant surface crystallization.

Table 6.5. Characteristic temperatures and calculated glass stabilities for glasses with varying particle sizes.

Glass Series	Melting Temp (°C)	Particle Size Range (μm)	Heating Rate (K/min)	T_g (°C)	T_x (°C)	T_p (°C)	T_m (°C)	K_W (T_x)	K_W (T_p)	K_H (T_x)	K_H (T_p)
325Fe(III)	1200	45-63	2	*493*	694	718	852	0.179	0.200	1.272	1.679
			5	514	720	745	852	0.183	0.205	1.561	2.159
			10	517	744	770	*852*	0.202	0.225	2.102	3.085
			20	523	769	807	*858*	0.218	0.251	2.764	5.569
			30	527	789	825	*862*	0.231	0.263	3.589	8.054
		75-106	2	*514*	707	737	859	0.170	0.197	1.270	1.828
			10	520	751	780	856	0.205	0.230	2.200	3.421
			20	530	787	825	*868*	0.225	0.259	3.173	6.860
			30	537	801	840	*872*	0.231	0.265	3.718	9.469
		250-300	2	*514*	724	761	864	0.185	0.217	1.500	2.398
			10	518	780	827	*867*	0.230	0.271	3.011	7.725
			20	531	808	847	*873*	0.242	0.276	4.262	12.154
			25	534	819	858	*876*	0.248	0.282	5.000	18.000
			30	538	822	867	-	-	-	-	-
		425-500	2	-	729	774	867	-	-	-	-
			5	512	759	808	856	0.219	0.262	2.546	6.167
			10	520	800	837	*863*	0.246	0.279	4.444	12.192
			20	529	812	843	-	-	-	-	-
			30	533	823	866	-	-	-	-	-
	1250	45-63	2	*496*	690	709	863	0.171	0.188	1.121	1.383
			5	499	699	721	846	0.179	0.198	1.361	1.776
			10	508	718	745	846	0.188	0.212	1.641	2.347
		75-106	10	506	728	759	846	0.198	0.226	1.881	2.908
		425-500	5	505	726	770	849	0.197	0.236	1.797	3.354
			10	508	754	804	*852*	0.219	0.263	2.510	6.167
			20	517	766	821	*857*	0.220	0.269	2.736	8.444
			30	523	785	849	*869*	0.229	0.285	3.119	16.300
	1300	45-63	20	514	737	760	837	0.201	0.222	2.230	3.195
		75-106	10	500	726	744	840	0.203	0.219	1.982	2.542
		425-500	2	*497*	693	705	851	0.174	0.185	1.241	1.425
			5	501	708	729	841	0.186	0.205	1.556	2.036
			10	509	738	765	841	0.206	0.230	2.223	3.368
			20	516	762	800	*849*	0.219	0.253	2.828	5.796
			30	529	785	825	*866*	0.225	0.260	3.160	7.220
		bulk	10	514	743	791	*856*	0.203	0.245	2.027	4.262
			20	517	766	814	*846*	0.223	0.265	3.113	9.281
	1350	45-63	2	*478*	637	649	831	0.144	0.155	0.820	0.940
			20	498	690	711	830	0.174	0.193	1.371	1.790
		75-106	1	*493*	636	648	840	0.128	0.139	0.701	0.807
			2	*490*	651	663	842	0.144	0.155	0.843	0.966
			5	489	670	686	841	0.162	0.177	1.058	1.271
			10	494	687	706	841	0.173	0.190	1.253	1.570
			20	503	704	731	844	0.180	0.204	1.436	2.018
			30	508	717	748	845	0.187	0.215	1.633	2.474
		250-300	10	498	699	728	842	0.180	0.206	1.406	2.018
			20	504	717	757	847	0.190	0.226	1.638	2.811
			30	506	720	762	*841*	0.192	0.230	1.769	3.241
		425-500	2	*481*	659	681	833	0.161	0.181	1.023	1.316
			5	488	672	698	833	0.166	0.190	1.143	1.556
			10	492	698	734	831	0.187	0.219	1.549	2.495
			15	495	707	745	836	0.191	0.225	1.643	2.747
			30	503	726	772	*831*	0.202	0.244	2.124	4.559

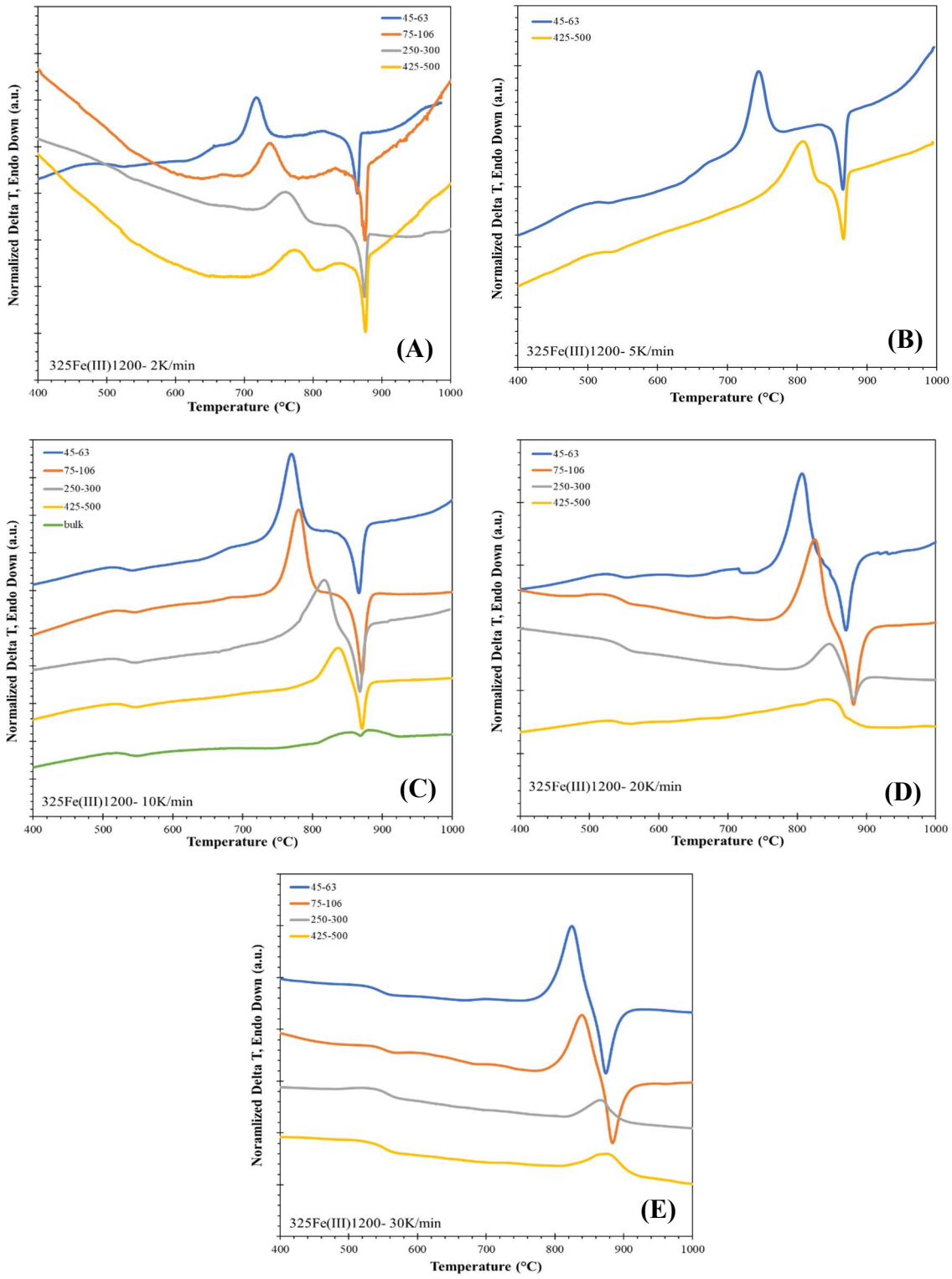

Figure 6.13. Effect of particle size on DTA spectra for 325Fe(III)1200 glass at (A) 2 K/min, (B) 5 K/min, (C) 10 K/min, (D) 20 K/min, and (E) 30 K/min.

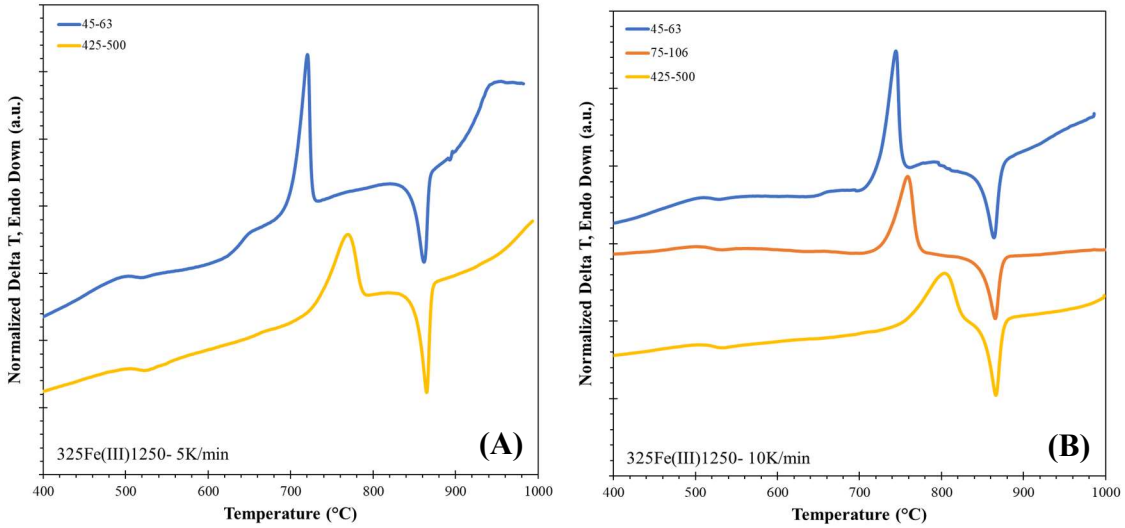

Figure 6.14. Effect of particle size on DTA spectra for 325Fe(III)1250 glass at (A) 5 K/min and (B) 10 K/min.

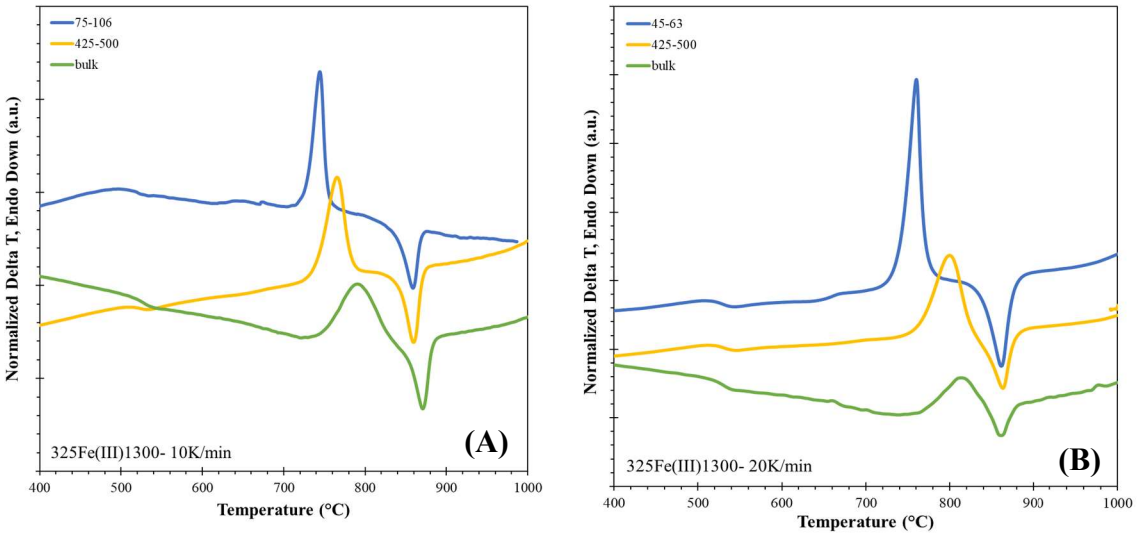

Figure 6.15. Effect of particle size on DTA spectra for 325Fe(III)1300 glass at (A) 10 K/min and (B) 20 K/min.

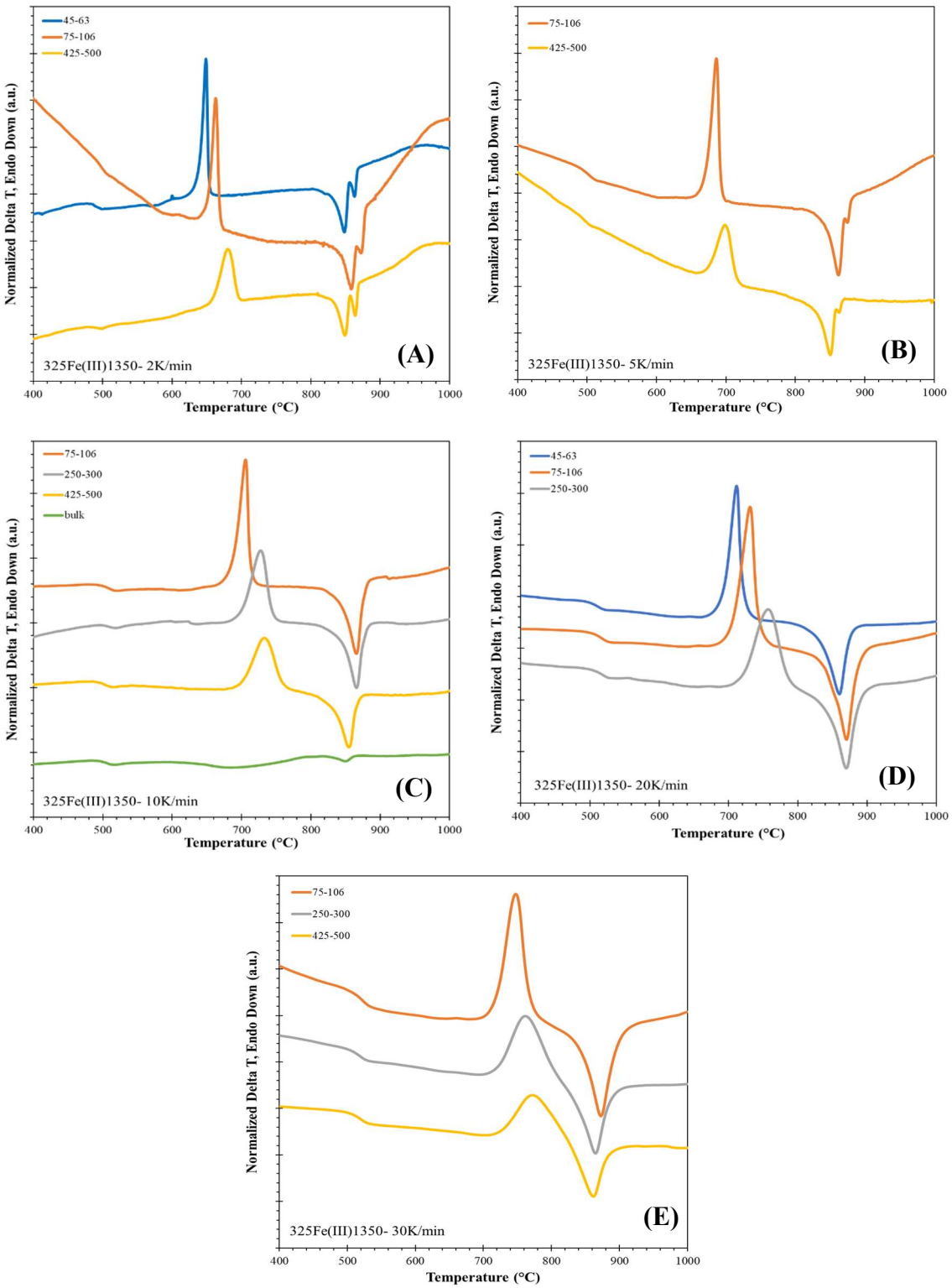

Figure 6.16. Effect of particle size on DTA spectra for 325Fe(III)1350 glass at (A) 2 K/min, (B) 5 K/min, (C) 10 K/min, (D) 20 K/min, and (E) 30 K/min.

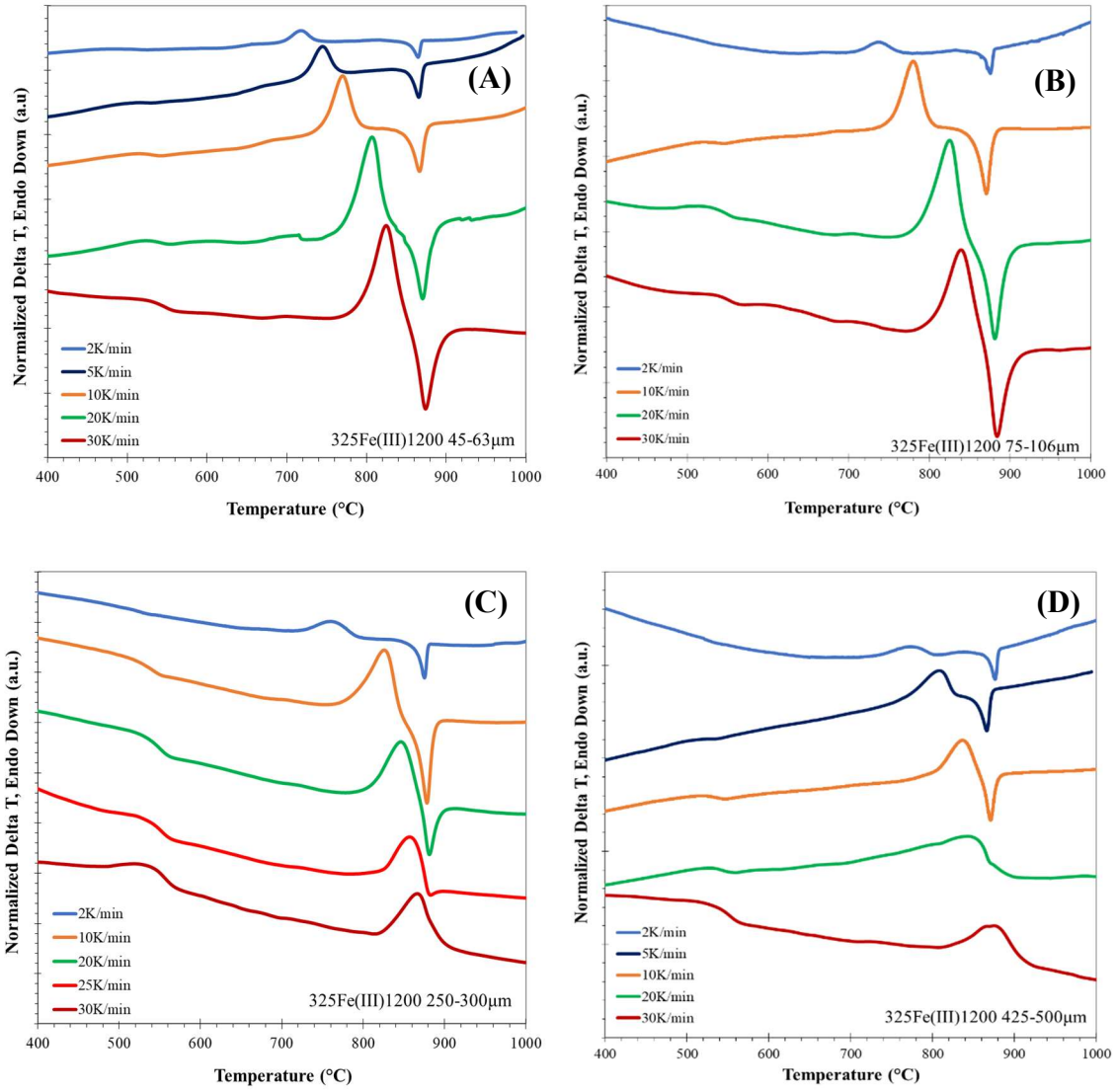

Figure 6.17. Effect of heating rate on DTA spectra of 325Fe(III)1200 glass for (A) 45 – 63 µm, (B) 75 – 106 µm, (C) 250 – 300 µm and (D) 425 – 500 µm particle sizes.

For samples with smaller particle sizes, the crystallization temperature and enthalpy, which is related to the area under the exothermic crystallization peak, increase with increasing heating rate, while the temperature corresponding to the endothermic melting peak remains relatively constant. The crystallization peak and the melting peak

are two distinct features. This trend is not observed for all samples with larger particle sizes and faster heating rates.

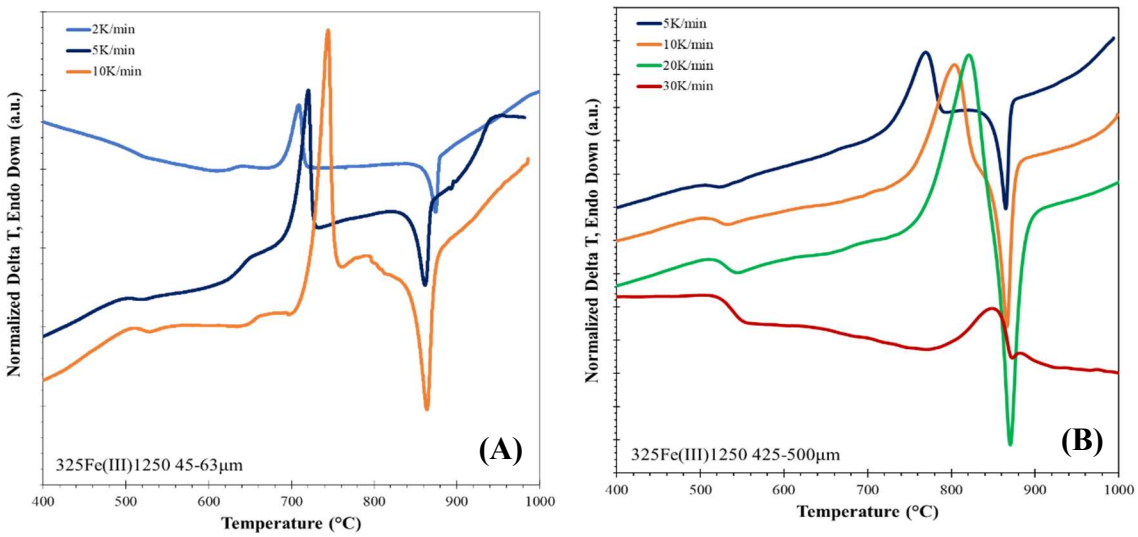

Figure 6.18. Effect of heating rate on DTA spectra of 325Fe(III)1250 glass for (A) 45 – 63 µm and (B) 425 – 500 µm particle sizes.

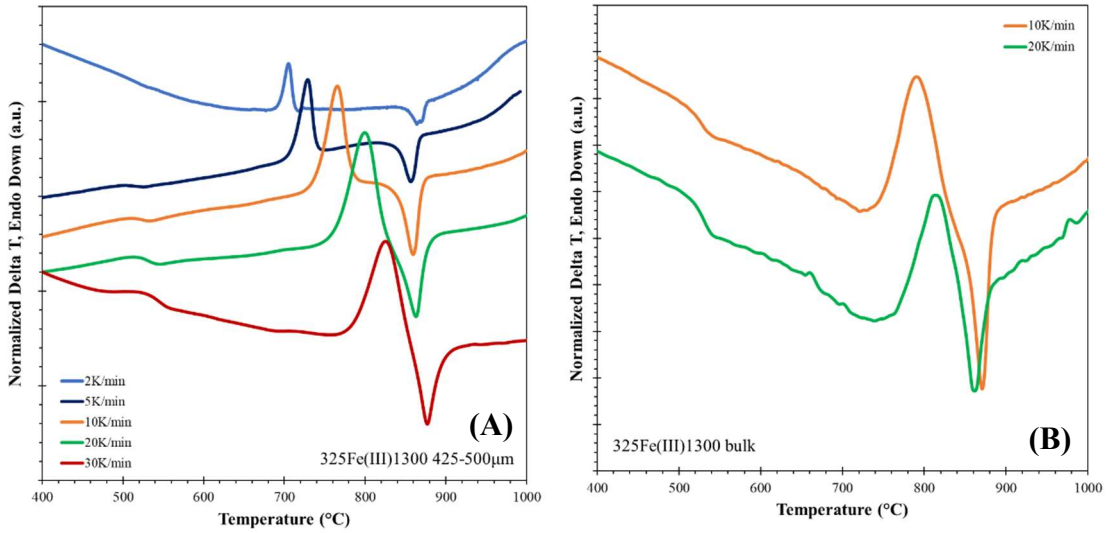

Figure 6.19. Effect of heating rate on DTA spectra of 325Fe(III)1300 glass for (A) 425 – 500 µm and (B) bulk particle sizes.

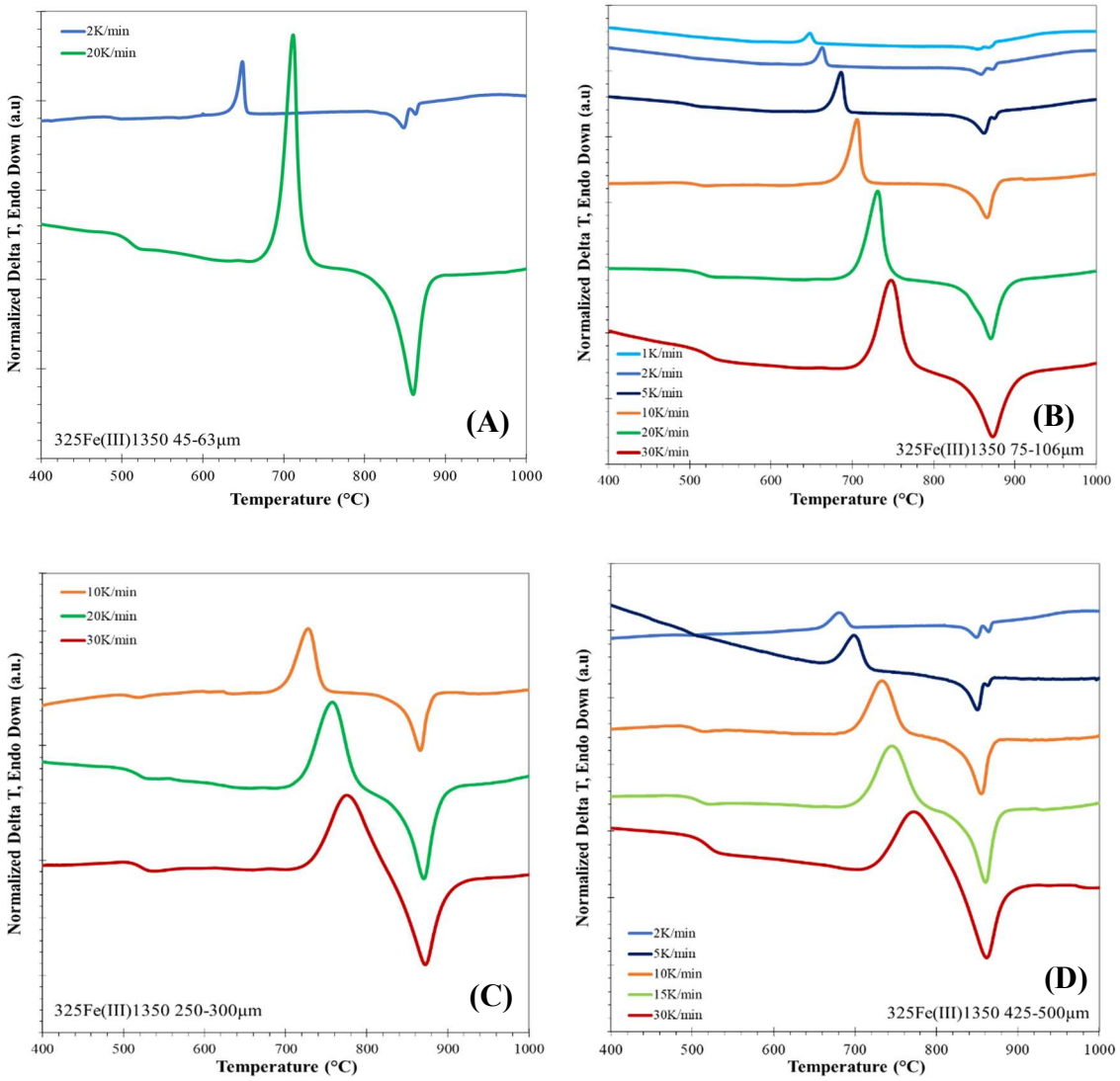

Figure 6.20. Effect of heating rate on DTA spectra of 325Fe(III)1350 glass for (A) 45 – 63 µm, (B) 75 – 106 µm, (C) 250 – 300 µm and (D) 425 –500 µm particle sizes.

While the onset crystallization temperature does increase with increasing heating rate, the enthalpy of crystallization for some samples appears to decrease at the highest heating rates as the melting peak decreases in area and shifts to higher temperatures, then eventually disappears. These observations are most likely due to the amalgamation of energies associated with the exothermic crystallization and endothermic melt, as the

crystallization peak approaches the melting peak with increasing heating rate. It should also be noted that at slower heating rates, it is easier to distinguish melt features. For example, two distinct melt peaks are apparent for 325Fe(III)1350 at heating rates of or less than 5 K/min, but are not distinguishable at heating rates of or more than 10 K/min.

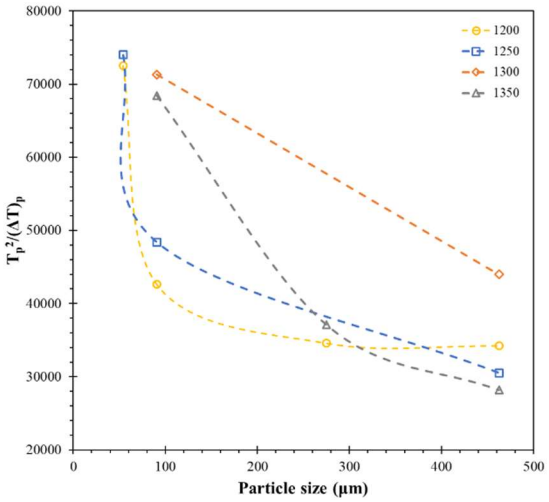

Figure 6.21. Decrease in $T_p^2/(\Delta T)_p$ with increasing particle size, indicating surface crystallization of all 325Fe(III) series.

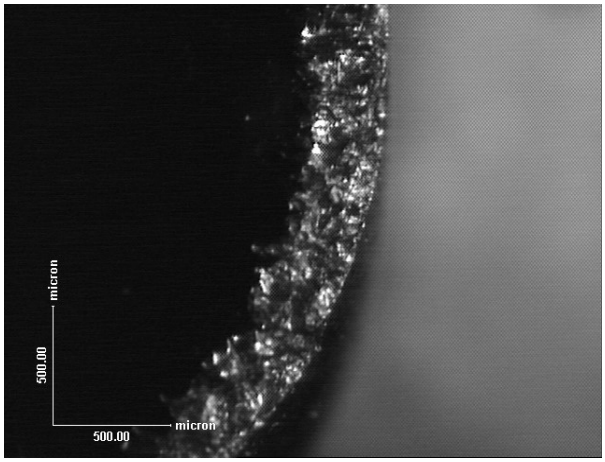

Figure 6.22. 325Fe(III)1200 glass heat treated at 800°C for 30 minutes, showing predominant surface crystallization.

Calculating the Weinberg stability parameter using Equation 6.1 is complicated for samples for which the onset melting temperature is obscured by the crystallization exotherm or for which the endothermic glass transition feature at slower heating rates was too insignificant to accurately determine a glass transition temperature. Weinberg stability parameters that could be calculated are given in Table 6.5, and Figure 6.23 shows the effect of particle size on glass stability. Results indicate an increase in stability with increasing particle size for all samples, as well as support previous results in Section 6.3.2 suggesting an increase in stability with increasing heating rate and a decrease in stability with increasing ferrous iron content.

Heating rate data was used to determine the effect of particle size on crystallization activation energies. Kissinger plots are shown in Figure 6.24 and calculated crystallization activation energies are given in Table 6.6.

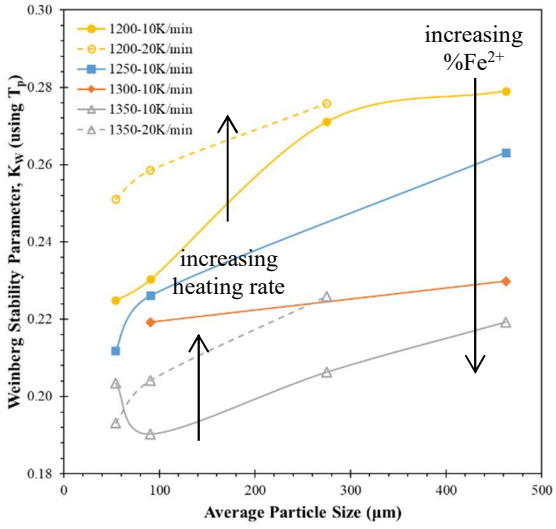

Figure 6.23. Weinberg stability parameter as a function of particle size for the 325Fe(III) glass series.

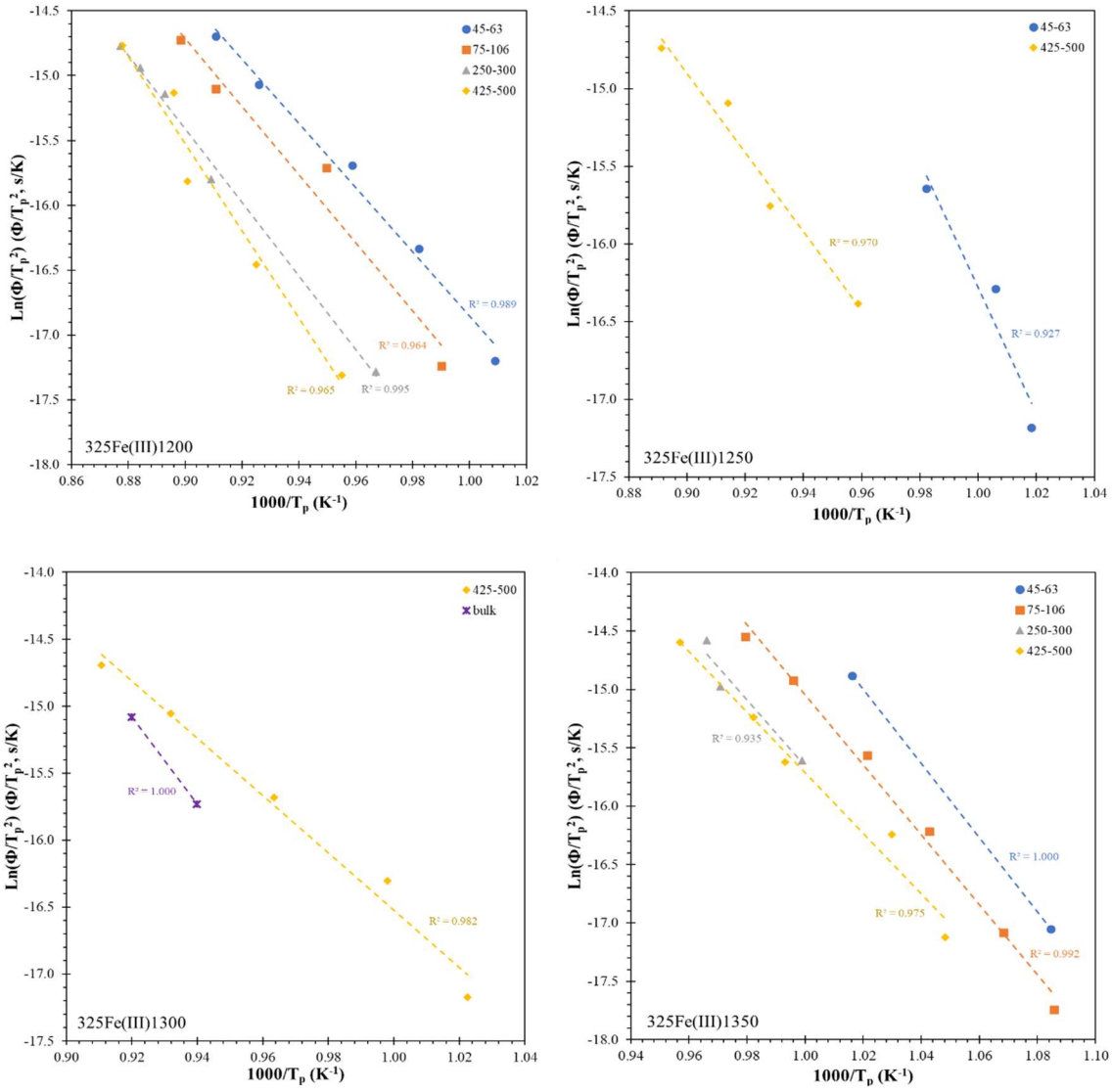

Figure 6.24. Kissinger plots for 325Fe(III) glass series at varying particle sizes.

Trends in crystallization activation energy with particle size differ between the glasses within the 325Fe(III) series. Figure 6.25 shows the change in crystallization activation energy with average particle size for the glasses with the smallest and largest ferrous iron contents, 325Fe(III)1200 and 325Fe(III)1350 respectively. The activation energy for crystallization increases with increasing particle size for 325Fe(III)1200 yet

decreases with increasing particle size for 325Fe(III)1350. This contrasting behavior may be due to the formation of different crystalline phases for glasses with different ferrous iron contents.

Table 6.6. Crystallization activation energies for 325Fe(III) glass series at various melting temperatures and particle sizes.

Glass Series	Melting Temp (°C)	Particle Size Range (μm)	Average Particle Size (μm)	Slope	E (kJ/mole)
325Fe(III)	1200	45-63	54.0	-24.772	206
		75-106	90.5	-26.217	218
		250-300	275.0	-28.313	235
		425-500	462.5	-33.599	279
	1250	45-63	54.0	-40.606	338
		425-500	462.5	-25.384	211
	1300	425-500	462.5	-21.382	178
		bulk	-	-32.704	272
	1350	45-63	54.0	-31.789	264
		75-106	90.5	-30.024	250
		250-300	275.0	-28.362	236
		425-500	462.5	-25.937	216

Figure 6.26 shows how the crystallization activation energy changes with ferrous iron content for glasses of a given particle size, with the smallest particle size showing a maximum and the largest particle size showing a minimum between 20 – 25% Fe^{2+}. The effect of particle size on crystalline phase formation will be discussed further in Section 6.3.6.

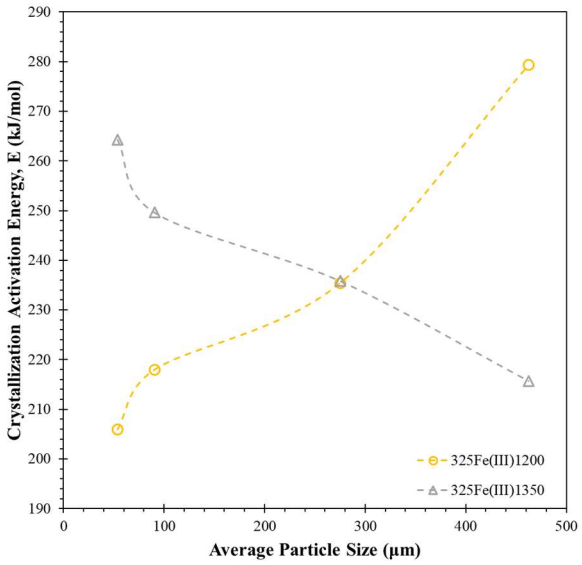

Figure 6.25. Change in crystallization activation energy with increasing particle size for 325Fe(III)1200 and 325Fe(III)1350 glasses.

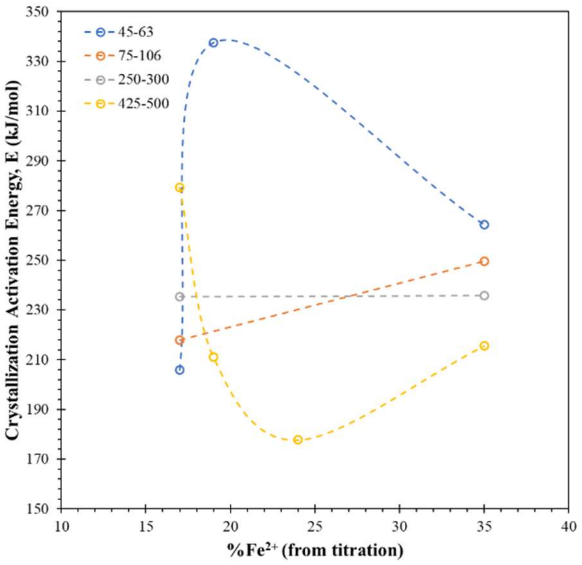

Figure 6.26. Change in crystallization activation energy with increasing ferrous iron content for the 325Fe(III) glass series with various particle sizes.

6.3.5. Atmospheric Effects. Although performing DTA and DSC experiments in an inert environment such as nitrogen is important to understanding how the chemistry of

the glass will influence crystallization, it is also necessary to determine how the crystallization behavior will be affected by changes in atmosphere. All practical applications for these glass compositions will involve exposure to air, and the crystallization behavior may be different in an oxidizing environment than in an inert environment due to changes in the iron redox ratio upon heating.

The sensitivity of crystallization behavior to environment was investigated qualitatively by changing the amount of oxygen available to the glass upon heating. The 325Fe(III) glass series was again chosen for further investigation, and the samples melted at 1200 and 1350ºC were chosen to compare results from samples with the largest variation in initial ferrous iron content.

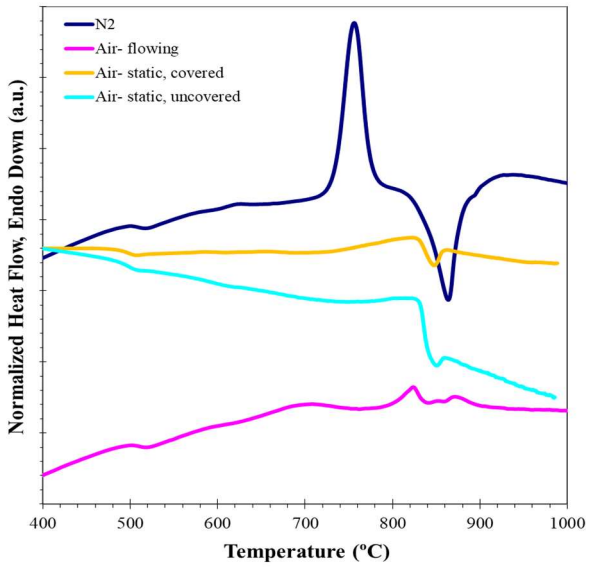

Figure 6.27. DSC/DTA patterns for 325Fe(III)1350 of 75-106 µm particle size and using a heating rate of 10 K/min in environments with different oxygen availability.

Figure 6.27 shows DSC/DTA patterns for 325Fe(III)1350 run under the same experimental conditions (10 K/min heating rate, particle size range of 75 – 106 µm),

except using different atmospheric conditions: flowing nitrogen (inert), static air with a covered crucible, static air with an open crucible, and flowing air with an open crucible. The T_g remains constant but the crystallization and melt features change dramatically, showing a strong dependence of crystallization behavior on the amount of oxygen in the environment surrounding the glass powder.

The influence of heating rate and particle size on crystallization were also studied under air. DSC patterns for the 325Fe(III)1200 and 325Fe(III)1350 samples at various heating rates are shown in Figure 6.28 and Table 6.7 gives characteristic temperatures, as well as stability parameters and crystallization activation energies

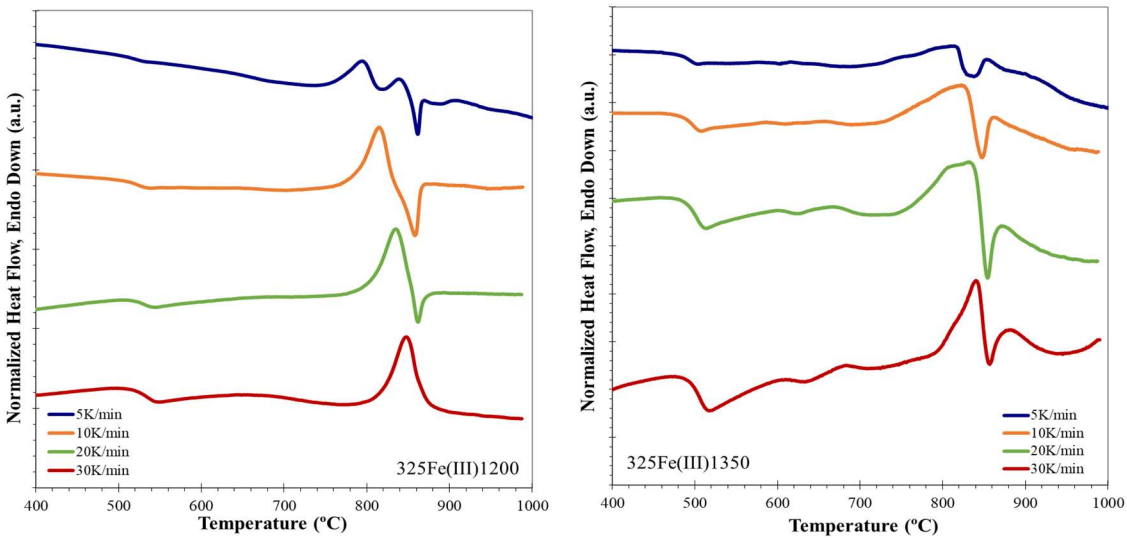

Figure 6.28. DSC patterns at various heating rates in air for 75-106 µm glass powder of (A) 325Fe(III)1200 and (B) 325Fe(III)1350 glasses.

. Due to the uncertainty of onset crystal melt temperature, the glass stability could not be calculated using the Weinberg or Hrüby parameters used previously. The stability was instead calculated using the parameter determined by Jiusti et al [253] to have the

best ability to predict glass formability without needing a melting temperature, which is a normalized form of the Angell stability parameter [255] given in Equation 6.4:

$$H' = \frac{T_p - T_g}{T_g} \quad \text{(Equation 6.4)}$$

Table 6.7. Characteristic temperatures, glass stability parameters and crystallization activation energy for 325Fe(III)1200 and 325Fe(III)1350 in air.

Glass	Heating Rate (K/min)	T_g (°C)	T_x (°C)	T_p(°C)	H' (T_p)	E (kJ/mol)
325Fe(III)1200	5	504	754	795	0.375	320
	10	508	780	815	0.393	
	20	514	802	835	0.408	
	30	516	812	848	0.421	
325Fe(III)1350	5	480	707	815	0.445	712
	10	484	730	824	0.449	
	20	486	752	833	0.457	
	30	490	793	840	0.459	

Figure 6.29 shows the change in glass transition and crystallization temperatures with heating rate. The glass transition temperature is higher for the 325Fe(III)1200 composition due to the larger proportion of trivalent Fe^{3+}, and glass transition temperature for both series increase slightly with increasing heating rate. Similar to the effect of increasing heating rates on crystallization in nitrogen, increasing heating rates in air yield higher crystallization temperatures, and in the extreme cases results in a "disappearance" of the melting peak due to a merging of the crystallization exotherm and the melting endotherm. While the onset crystallization temperature is notably higher for the 325Fe(III)1200 composition, the crystallization peak temperatures of the two compositions are quite similar. Although 325Fe(III)1350 contains a higher initial ferrous iron content (and lower viscosity) and begins to crystallize at lower temperatures, the

oxidation of ferrous to ferric iron upon heating may cause the compositions of 325Fe(III)1200 and 325Fe(III)1350 to approach each other at higher temperatures and potentially reach peak crystallization rates at approximately the same temperature.

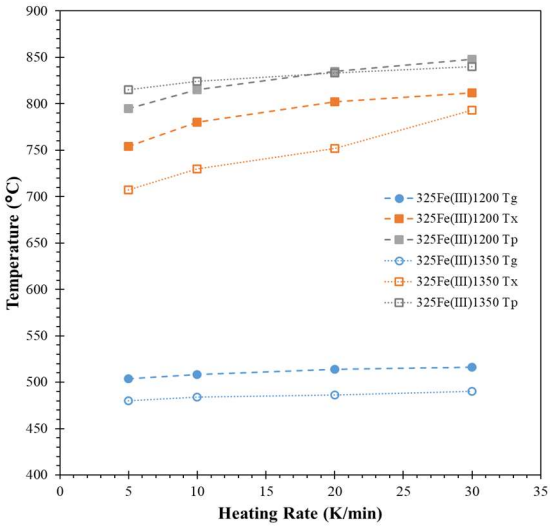

Figure 6.29. Characteristic temperatures for 325Fe(III)1200 and 325Fe(III)1350 in an air environment.

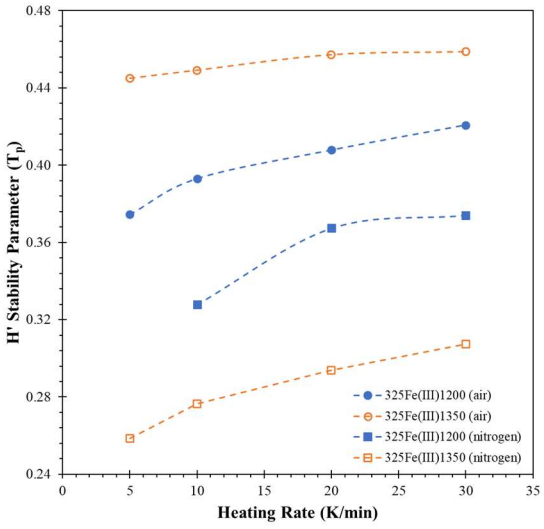

Figure 6.30. H' glass stability parameter as a function of heating rate for 325Fe(III)1200 and 325Fe(III)1350 in both air and nitrogen.

The change in glass stability with increasing heating rate is shown in Figure 6.30. Both glasses exhibit greater stability under faster heating rates, but in contrast to the results observed in nitrogen, greater ferrous oxide contents result in higher stability in air. Under equivalent experimental conditions, the glass crystallizes at higher temperatures in air than in nitrogen, which corresponds to greater glass stability in air. The glass stability parameter given by Equation 6.4 was calculated for the same glass compositions using the corresponding characteristic temperatures in nitrogen, and results are shown in Figure 6.30 for comparison purposes. The 325Fe(III)1350 composition exhibits a much larger increase in stability in air relative to nitrogen than the 325Fe(III)1200 composition. The greater initial ferrous iron content of the 325Fe(III)1350 sample and greater degree of iron oxidation upon heating may be the cause of the larger difference in crystallization behavior upon heat treatment in an oxidizing environment. The lower viscosity of the 325Fe(III)1350 composition may allow for faster oxygen diffusion, resulting in a greater degree of iron oxidation as the thermal analysis scan proceeds.

Kissinger plots used to calculate activation energies are shown in Figure 6.31, revealing a larger crystallization activation energy for the glass with greater ferrous iron content (325Fe(III)1350), which corresponds to the glass with the highest stability parameter.

Figure 6.32 shows DSC patterns for 325Fe(III)1350 with varying particle sizes. Similar changes to the crystallization behavior with particle size in nitrogen are again seen in air. The glass transition temperature is constant for varying particle sizes and the crystallization temperature appears to shift to higher temperatures with coarser particle sizes. However, in a nitrogen environment, the main crystallization peak is a sharp

feature occurring near 700°C. In air environment, a broad feature, possibly due to a slower crystallization process, is seen near 700°C and the intensity of the feature lessens with larger particle sizes. Sharper crystallization peaks occur at temperatures around 800°C and above, and crystal melt temperatures are not distinguishable for any particle size, suggesting crystallization of different phases upon heat treatments in different environments. Characteristic temperatures and stability parameters are given in Table 6.8 and shown in Figure 6.33 and Figure 6.34. Stability again increases with larger particle sizes, indicating a dependence of crystallization on surface area.

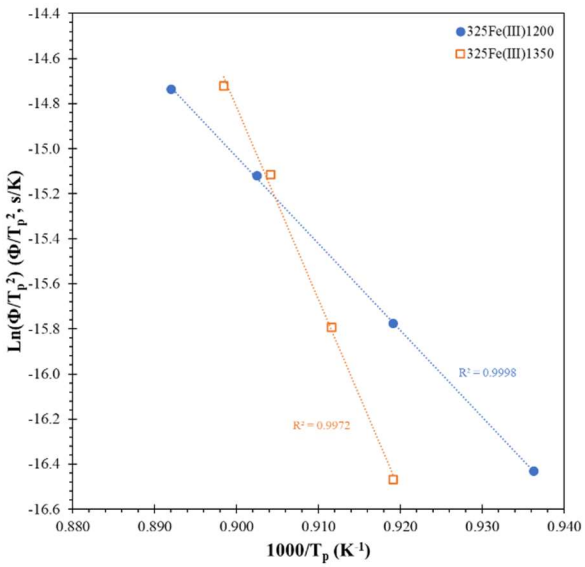

Figure 6.31. Kissinger plots for 325Fe(III)1200 and 325Fe(III)1350 in air.

Table 6.8. Characteristic temperatures and glass stability parameters for 325Fe(III)1350 glass of various particle sizes in air.

Glass	Particle Size (μm)	T_g (°C)	T_x (°C)	T_p(°C)	H' (T_p)
325Fe(III)1350	45-63	500	794	813	0.405
	75-106	498	796	824	0.423
	425-500	496	818	853	0.464

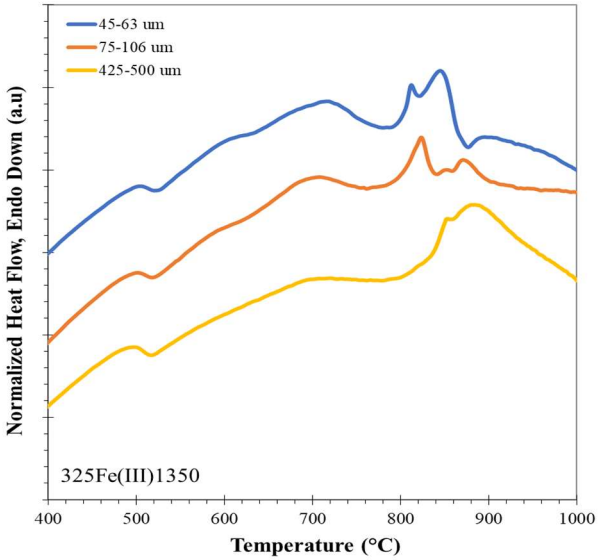

Figure 6.32. DSC pattern for 325Fe(III)1350 in flowing air at 10 K/min using different particle size ranges.

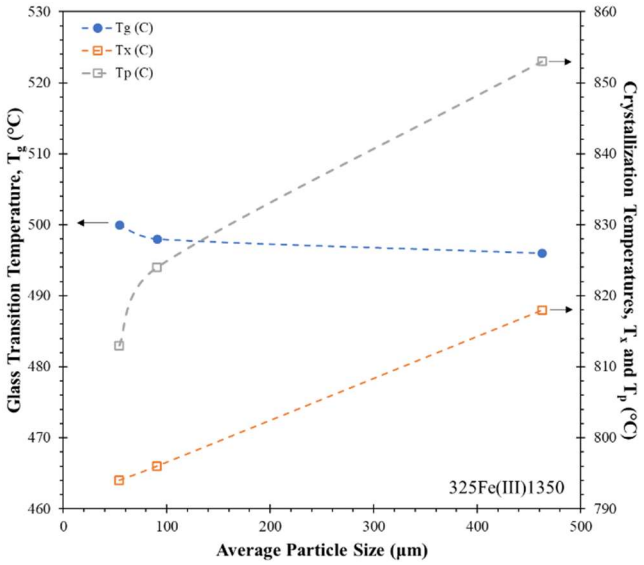

Figure 6.33. Change in characteristic temperatures with average particle size for 325Fe(III)1350 in air.

To better understand why the crystallization behavior changes in different environments, the glasses were run in the DTA-TGA to observe weight changes upon

heating. Figure 6.35 shows the results for 325Fe(III)1350 with a range of particle sizes run in both air and nitrogen. Results support the assumption that the increase in mass is attributed to the sample picking up oxygen from the environment as the iron oxidizes.

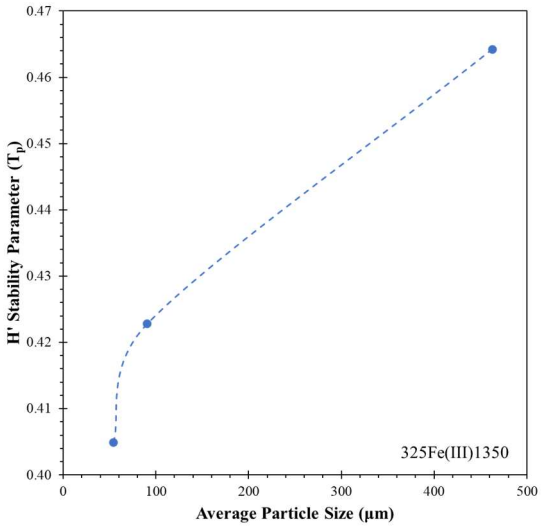

Figure 6.34. Change in glass stability with average particle size for 325Fe(III)1350 in air.

Samples heated in air exhibit more mass gain than those in nitrogen, and samples with smaller particle sizes (and thus greater surface areas exposed to the atmosphere) exhibit mass gain at lower temperatures and ultimately gain more mass after reaching 1000°C than samples with larger particle sizes. When heated in air, the 45 – 63 µm and 75 – 106 µm samples gain mass at temperatures near T_g (~500ºC), while the 425 – 500 µm and bulk samples do not increase in mass until crystallization temperatures (~700 – 800ºC). This oxidation of iron in smaller particles at temperatures near T_g will be further explored in Section 7. In nitrogen, the 75 – 106 µm sample exhibits a small mass gain just above T_g, while no such event is apparent in the bulk sample, and both samples ultimately experience similar mass gains.

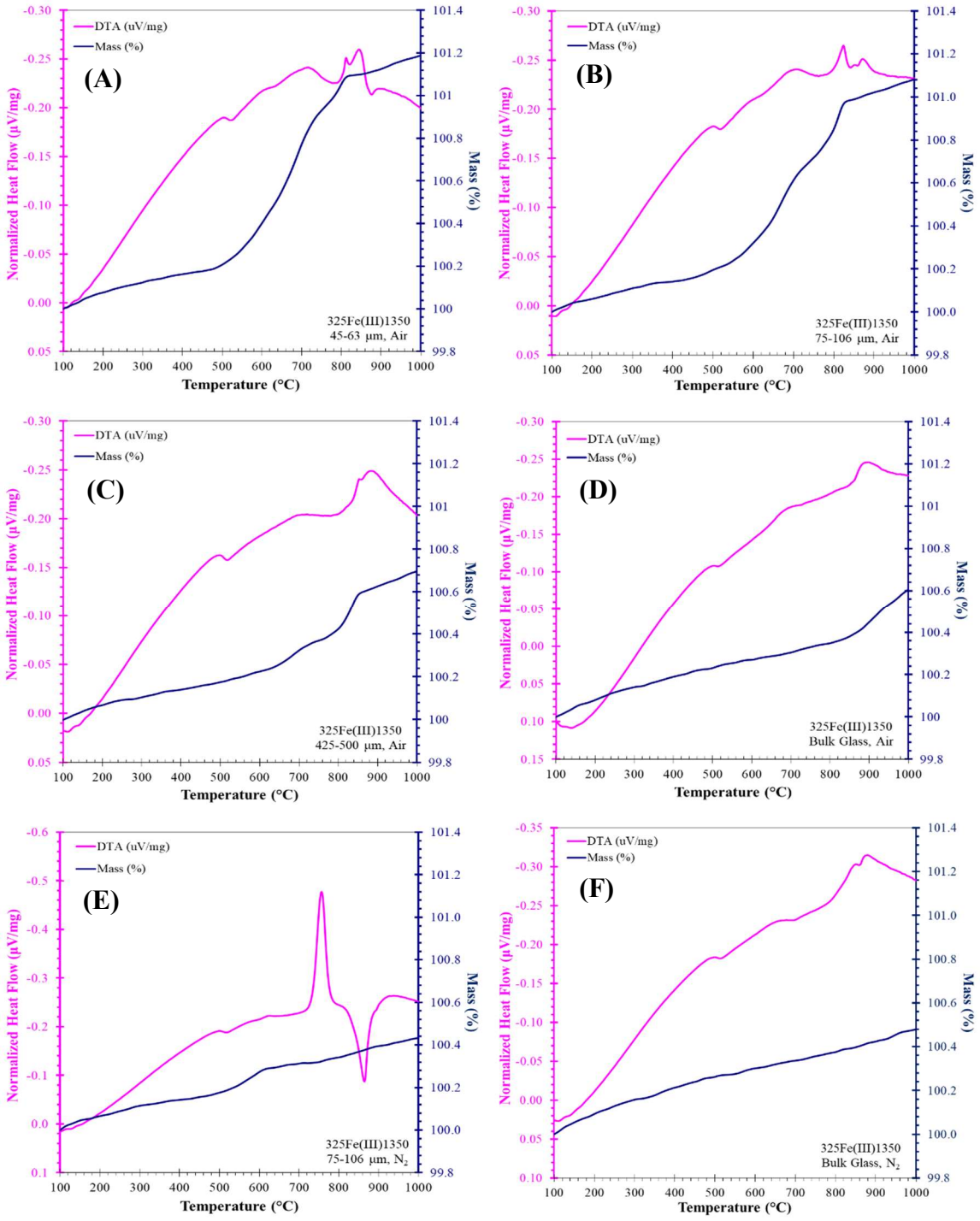

Figure 6.35. DSC-TGA patterns for 325Fe(III)1350 using 10 K/min in air with particle size ranges of (A) 45-63 µm, (B) 75-106 µm, (C) 425-500 µm and (D) a bulk, monolithic sample, and in nitrogen with particle sizes of (E) 75-106 µm and (F) a monolithic sample.

Using a starting composition of $19.8Fe_2O_3$-$21.4FeO$-$55.7P_2O_5$-$3.1Al_2O_3$ (mol%) as given in Table 3.3 and the assumption that the change in mass is solely attributed to oxidation of the ferrous iron, the percentage of mass gain can be used to calculate the extent of iron oxidation and the resulting glass composition after heat treatment, as seen in Table 6.9 and Figure 6.36.

Table 6.9. Extent of ferrous iron oxidation when 325Fe(III)1350 glass with different particle size ranges is heated to 1000°C at a heating rate of 10 K/min in air and nitrogen.

Atmosphere	Particle Size Range (µm)	Increase in Mass % (at 1000°C)	Final %Fe^{2+} in glass	% of initial Fe^{2+} oxidized
Air	45-63	1.19	1.0	97.0
	75-106	1.08	3.7	88.3
	425-500	0.70	13.6	56.9
	Bulk	0.61	16.0	49.4
N_2	75-106	0.43	20.4	35.4
	Bulk	0.48	19.3	39.1

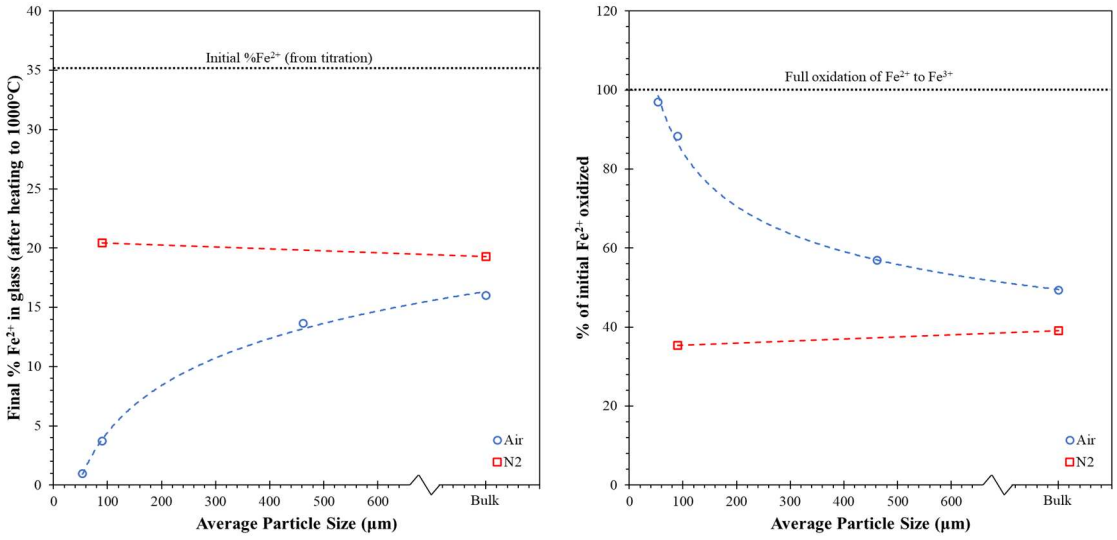

Figure 6.36. Extent of ferrous iron oxidation in 325Fe(III)1350 glass of different particle sizes upon heat treatment to 1000ºC in air and nitrogen.

Results indicate little change in the extent of oxidation of ferrous iron with particle size when the glass is heated in nitrogen. The final glass composition after heat treatment to 1000°C contains 19 – 20% ferrous iron, representing 35 – 40% oxidation of the initial ferrous iron present in the glass. When heated in air, the extent of oxidation is greatly dependent on surface area exposed to the atmosphere, and full oxidation is almost reached at 1000°C with particle sizes of 45 – 63 μm. As particle sizes approach larger monolithic pieces, similar degrees of ferrous iron oxidation are reached regardless of atmosphere, with 40 – 50% of the initial ferrous iron oxidizing to ferric iron. Mössbauer was used to measure ferrous iron content of 75 – 106 μm glass heated in air to 1000°C at 10 K/min and then quenched (Figure 6.37), and results show remarkable agreement with calculations based on mass gain.

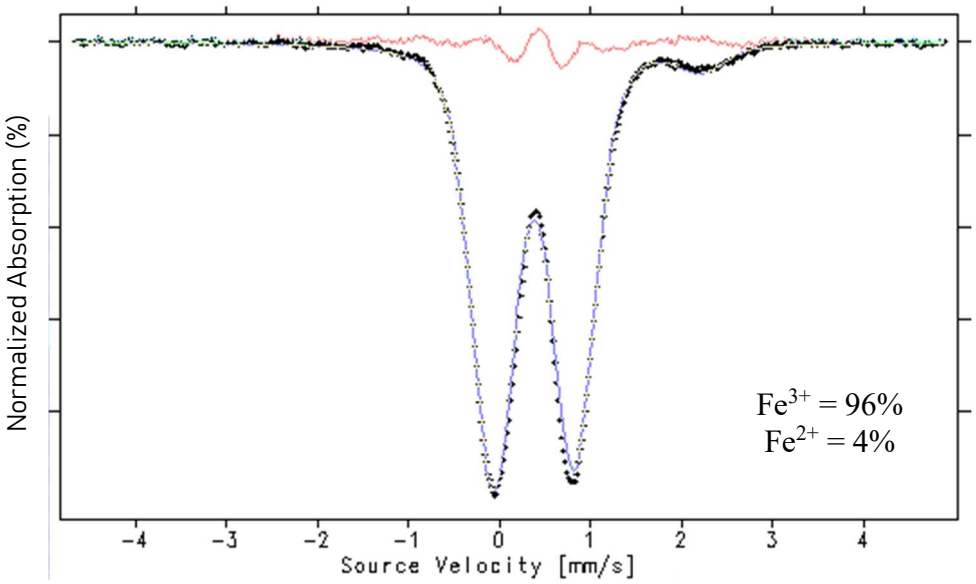

Figure 6.37. Mössbauer of 325Fe(III)1350 (75 – 106 μm) ramped to 1000°C in air at 10 K/min then quenched indicating ~4% Fe^{2+}.

6.3.6. Identification of Crystalline Phases. Identification of the crystalline phases which form under different conditions may provide insight in how to avoid devitrification and tailor the glass compositions to improve glass stability. Samples of 325Fe(III)1200 and 325Fe(III)1350 glasses were again studied here, due to the stability within the glass series and the variance in ferrous iron content. Crystalline phase identification and associated crystallization temperature were studied using DTA and optical microscopy in conjunction with x-ray diffraction and Raman spectroscopy.

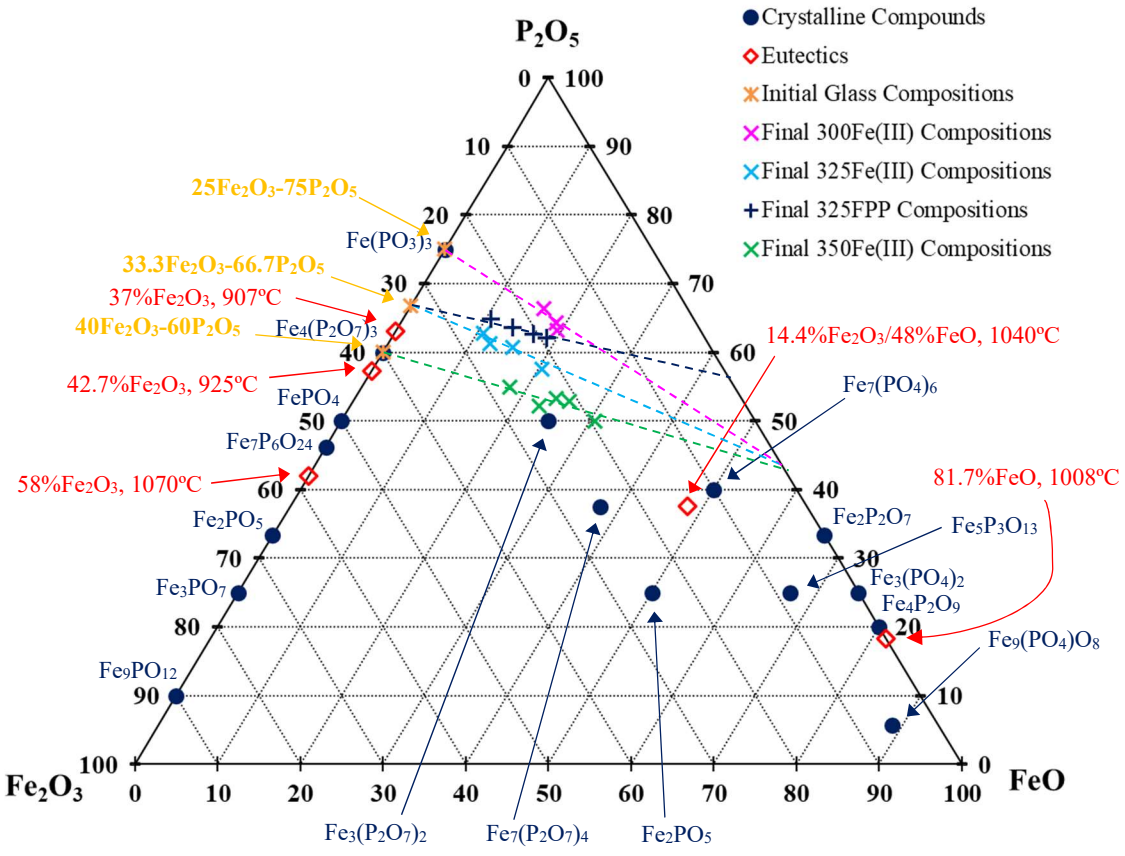

Figure 6.38. Ternary iron phosphate diagram showing crystalline compounds, eutectic compositions and temperatures, and glass compositions relevant to this study.

Many crystalline iron phosphate compounds have been identified and are summarized in Figure 6.38, along with eutectic compositions and temperatures [90]–[93]. Glass compositions relevant to this study are also included on the diagram, with starting ferric compositions shown in yellow and final, mixed valency compositions (as determined by compositional analysis) described in the legend. It is curious to note that all glasses within the three Fe(III) series, which were made with the same raw materials but different batched Fe/P ratios, approach the same ferrous iron phosphate composition (approximately 56FeO-44P_2O_5 with Fe/P = 0.64 and O/P = 3.14) with higher melting temperatures. Figure 6.39 shows the two glass compositions most thoroughly studied here, 325Fe(III)1200 and 325Fe(III)1350, and the crystalline compounds surrounding their compositional region.

6.3.6.1. Crystallization in inert environments. Crystalline phase formation in the 325Fe(III)1350 composition in inert environments was investigated. 325Fe(III)1350 was isothermally heated in argon for 2hr at 750°C, corresponding to a temperature within the main crystallization peak as revealed by the DTA, and the sample was analyzed using x-ray diffraction (Figure 6.40). Results indicate that the sample primarily consists of $Fe_3(P_2O_7)_2$ and $Fe(PO_3)_3$ crystals, with some evidence of very small amounts of $Fe_4(P_2O_7)_3$. However, the peaks associated with $Fe_4(P_2O_7)_3$ which are present in the diffraction pattern overlap with peaks for the other two crystalline phases, so it is not clear whether or not ferric pyrophosphate has truly formed. No $FePO_4$ is evident in the diffraction results. As seen in Figure 6.39, the 325Fe(III)1350 glass composition lies very close to the $Fe(PO_3)_3$-$Fe_3(P_2O_7)_2$ tie-line.

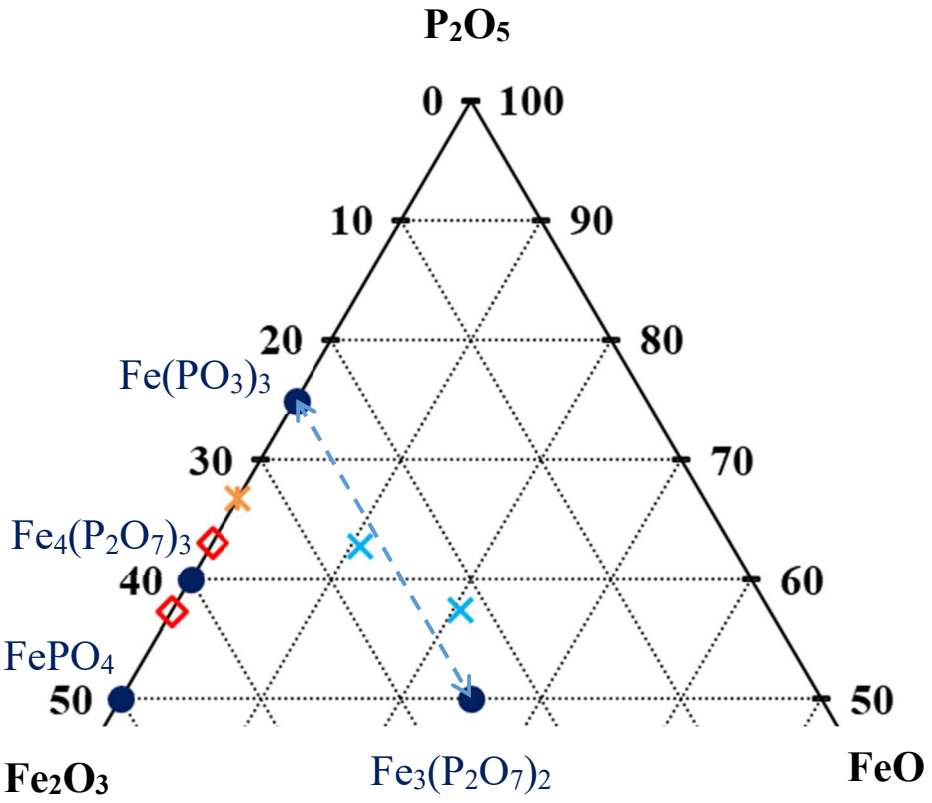

Figure 6.39. Ternary iron phosphate composition region containing the glass compositions of interest.

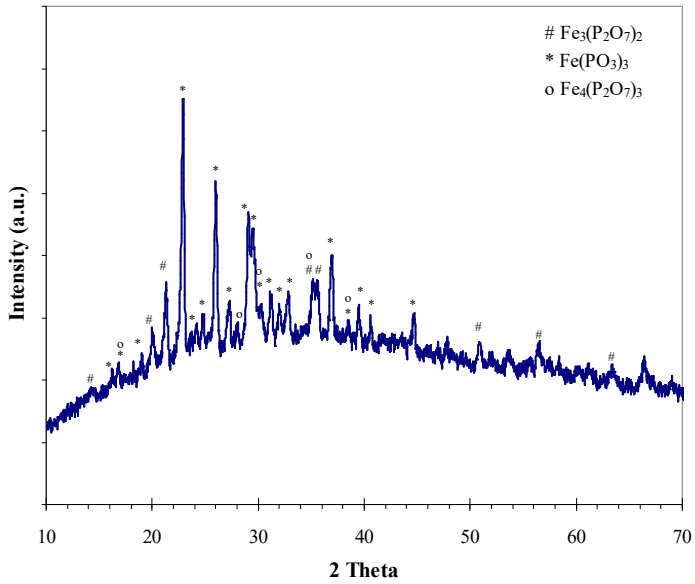

Figure 6.40. XRD pattern and peak identifications for 325FP1350 heat treated in argon at 750ºC for 2hr.

Bulk samples of 325Fe(III)1350 glass were then heat treated using a 10 K/min heating rate in an argon atmosphere to both 750°C and to a temperature above the main melt temperature (950ºC). The samples were quenched and observed using Raman, as were $Fe(PO_3)_3$ and $Fe_3(P_2O_7)_2$ crystals to serve as references (Figure 6.41).

Raman spectroscopy results suggest that the sample heat treated to 750ºC contains both $Fe(PO_3)_3$ and $Fe_3(P_2O_7)_2$ crystals. The sample heat treated to 950ºC, however, appears to contain mainly $Fe(PO_3)_3$ and loses the features associated with the $Fe_3(P_2O_7)_2$ crystal, which suggests that the main melting peak at ~840ºC is due to $Fe_3(P_2O_7)_2$. It should be noted that these results are in agreement with Zhang et al.'s work concerning the liquidus surface of the $Fe(PO_3)_3$-$Fe_4(P_2O_7)_3$ system [263], which suggests a melting temperature for $Fe(PO_3)_3$ of ~1200ºC. Results are also consistent with Marasinghe et al. [82], who reported crystallization of $Fe_3(P_2O_7)_2$ near 640°C, and partial transformation of $Fe_3(P_2O_7)_2$ to $Fe_4(P_2O_7)_3$ near 800°C.

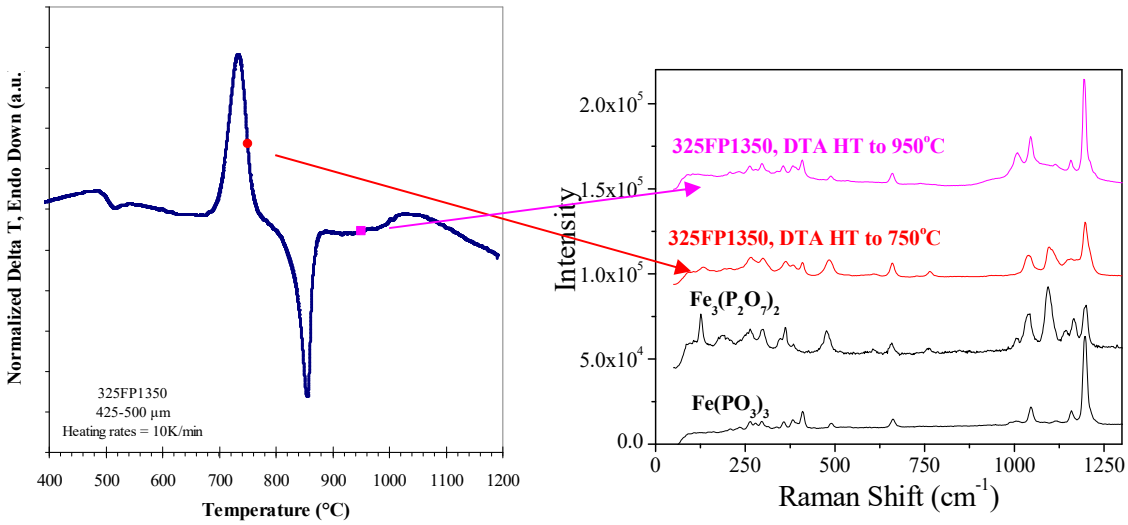

Figure 6.41. Raman results for 325Fe(III)1350 glass samples which were ramped to 750ºC (prior to main melt peak) and 950ºC (past the main melt peak).

Successive heating and cooling cycles were performed on 325Fe(III)1350 of large particle size (425 – 500 µm) in the DTA under nitrogen environment to study the glass forming ability upon cooling from different temperatures. For the first cycle, the glass is heated above the first melt to 1000ºC at 10 K/min, and then cooled at 10 K/min below the crystallization temperature to 525ºC. This cycle was immediately followed by a second cycle, where the glass is heated at 10 K/min to 1200ºC and then again cooled at 10 K/min to 525ºC (Figure 6.42(A)). The plots show a sharp crystallization peak and melting upon the first heating and re-crystallization upon cooling. Melting of these crystals is observed in the second heating, although no re-crystallization is observed upon the second cooling. This procedure was repeated with a set point temperature of 1200ºC for both heating cycles (Figure 6.42(B)), and similar results were obtained; no re-crystallization occurred upon cooling from 1200ºC and no melting was observed during the second heating cycle.

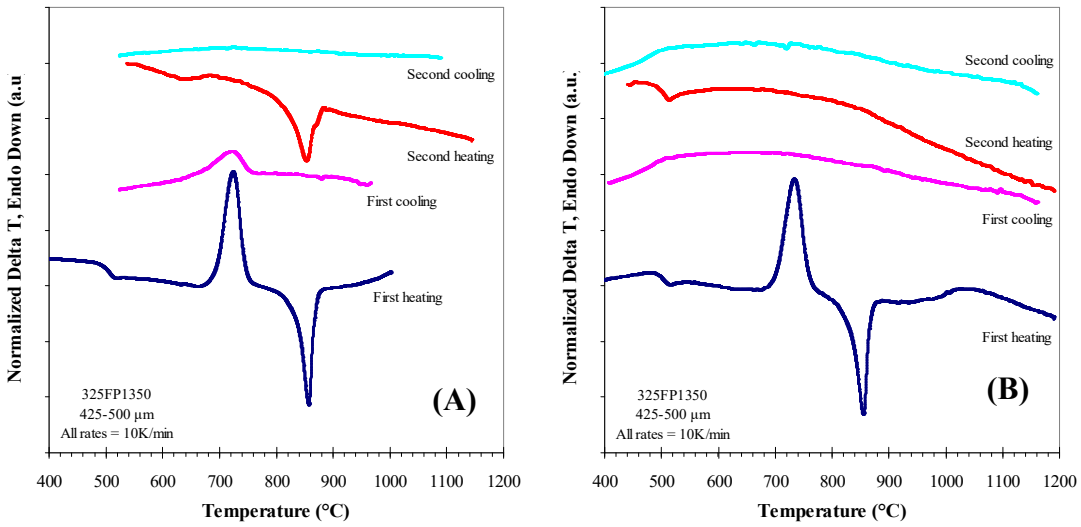

Figure 6.42. DTA curves showing successive heating and cooling cycles for 325Fe(III)1350. The glass recrystallizes upon cooling from 1000ºC but not upon cooling from 1200ºC.

The heating and cooling rates are kept constant and thus are not a factor in the observed behavior. The author suggests two possible causes for the difference in crystallization behavior upon cooling from 1000ºC and 1200ºC: (1) The iron redox ratio may have changed between 1000ºC and 1200ºC to such an extent as to alter the phases which crystallize upon cooling; (2) One of the phases formed upon heating may melt between 1000ºC and 1200ºC, and thus remains in the glass after the first heating cycle and acts as nucleation sites for the crystallization of a second phase, but is absent after the second heating cycle and therefore cannot facilitate re-crystallization. These results support those from Raman and XRD and suggest that $Fe(PO_3)_3$ remaining in the glass act as nucleation sites for $Fe_3(P_2O_7)_2$ upon cooling from 1000°C.

6.3.6.2. Crystallization in air atmosphere. Further crystallization experiments were completed in air atmosphere to better mirror conditions in potential applications of the iron phosphate glasses.

325Fe(III)1200 glass was isothermally heat treated at temperatures near T_g and throughout the crystallization range according to DTA results. All samples were held at temperatures for 2hr with the exception of the 500°C sample, which was held for 2 weeks. The samples were then characterized using a low grazing angle x-ray diffractometer to identify crystalline phases (Figure 6.44).

When held at temperatures near T_g (500°C) for extended times, $FePO_4$ is the predominant crystalline phase formed. Raman spectroscopy confirms the presence of $FePO_4$ on the sample surface (Figure 6.45). When held at temperatures above T_g but below the main crystallization feature (740°C), little to no crystallization is detected for 2 hour heat treatments. At temperatures within the main crystallization range, the

diffraction patterns are fairly complicated and suggest the presence of several crystals and at least two of $FePO_4$, $Fe(PO_3)_3$, $Fe_4(P_2O_7)_3$ and $Fe_3(P_2O_7)_2$ phases in most glasses. Higher heat treatment temperatures seem to favor the crystallization of $FePO_4$ and $Fe_4(P_2O_7)_3$, while $Fe_3(P_2O_7)_2$ is mostly present at lower temperatures within the crystallization range. It should be noted that the crystals that are detected with the greatest intensity are ferric iron phases. The phases are not easily distinguishable using x-ray diffraction and available JCPDS cards and thus further analysis is needed to deduce which crystals form under given conditions.

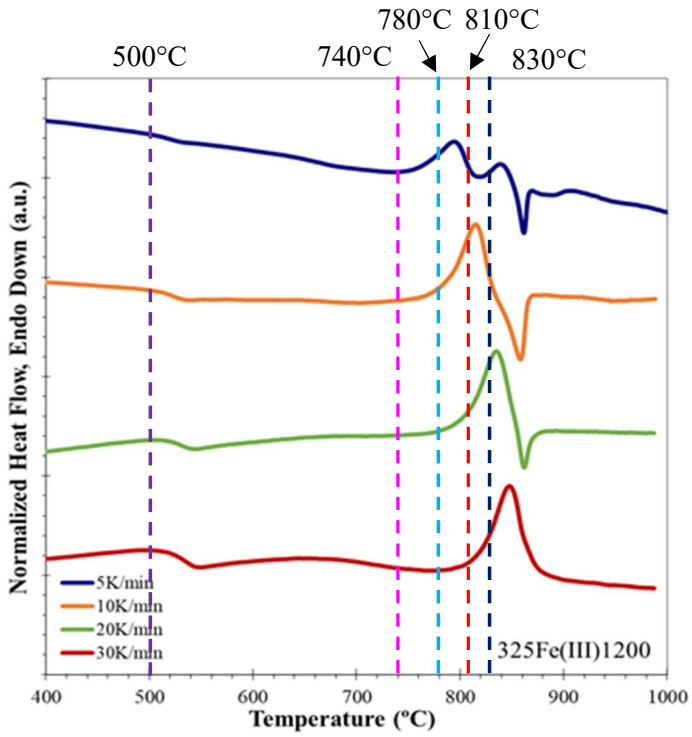

Figure 6.43. DTA patterns for 325Fe(III)1200 with lines indicating crystallization heat treatment temperatures.

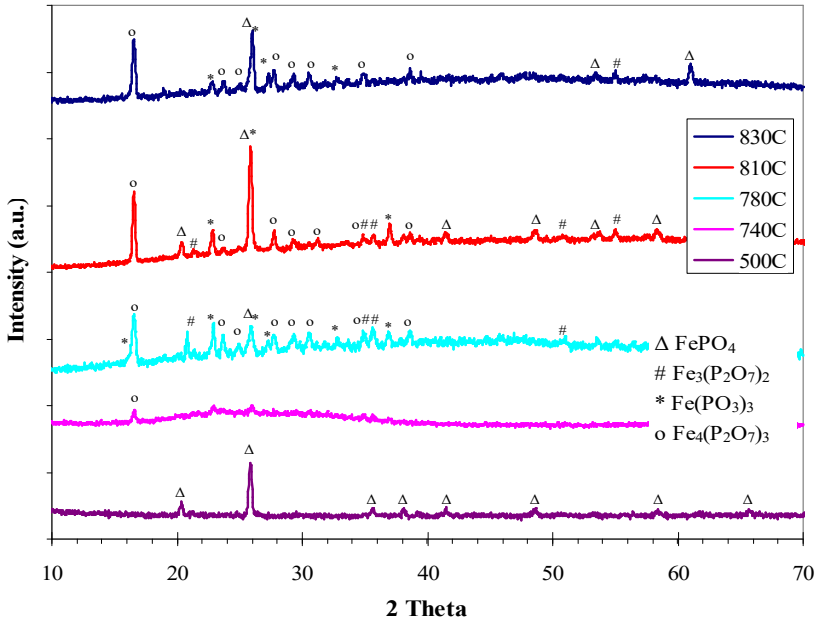

Figure 6.44. XRD patterns and peak identifications for 325Fe(III)1200 isothermally heat treated in air.

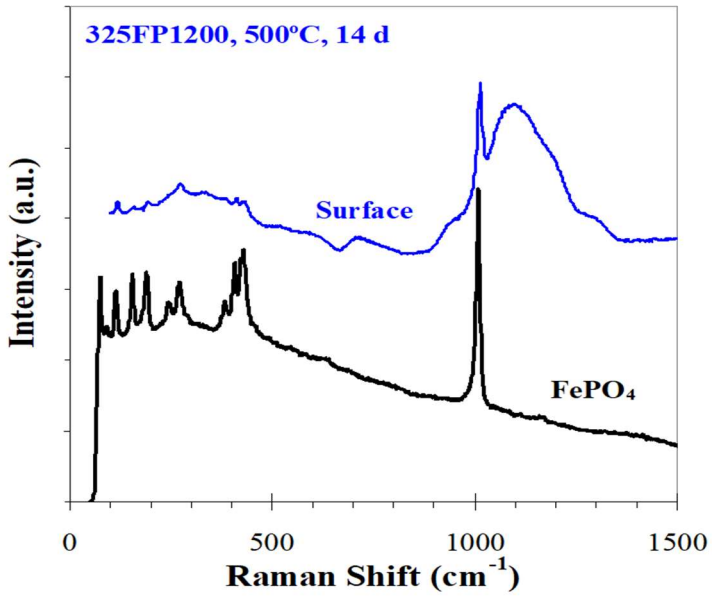

Figure 6.45. Raman spectra for 325Fe(III)1200 heat treated at 500°C in air for 14 days.

Figure 6.46 shows the Raman spectra of sections of a monolithic piece of 325Fe(III)1200 glass approximately 3mm thick which was isothermally heat treated in air at 810°C for 2 hours. Results indicate that different crystalline phases form throughout the bulk of the glass, with ferric compounds $Fe(PO_3)_3$ and $Fe_4(P_2O_7)_3$ being the predominant phases present on the surface and mixed valency $Fe_3(P_2O_7)_2$ being predominantly present in the bulk and center of the glass piece.

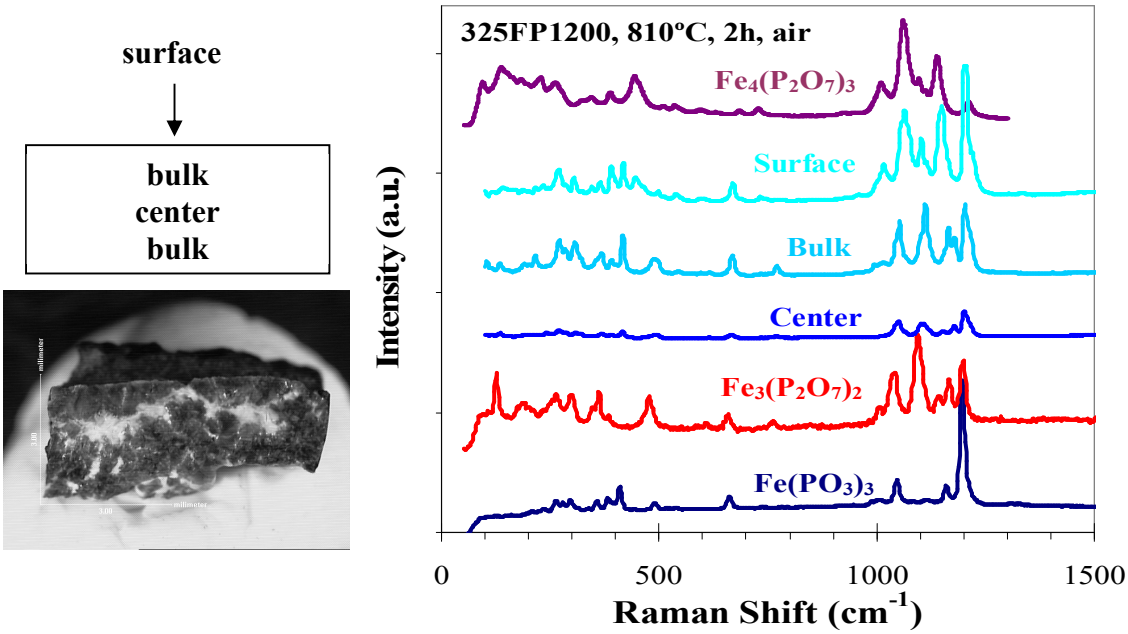

Figure 6.46. Raman spectra throughout bulk of monolithic 325Fe(III)1200 sample heated at 810°C in air for 2hr.

Visual observations of crystal morphologies were conducted following isothermal and dynamic heat treatments of monolithic glasses pieces. Isothermal heat treatments were carried out by placing the glass into a preheated furnace for a set amount of time and then removing the sample from the furnace and quenching in room temperature air.

Dynamic heat treatments were conducted by ramping the sample at 10 K/min to the set point, holding for 5 minutes and then quenching the sample in room temperature air.

Figure 6.47 shows a sample of 325Fe(III)1200 held in air near T_g at 511ºC for 260 hours. One crystalline morphology of uniform size is observed and is proposed to be $FePO_4$ based on the x-ray diffraction results from similar experiments shown in Figure 6.44.

Despite crystals being undetectable by x-ray diffraction for short heat treatment times between T_g (~500ºC) and T_x (~780ºC), crystals were visually detectable using optical microscopy. After heat treatment at 600ºC, several crystalline phases are observed with a range of crystal sizes (Figure 6.48). The three morphologies observed here are (1) a "flower-like" phase with six distinct "petals" (in blue), (2) a flat, round phase with striations extending from the center of the crystal (in red), and (3) a smaller, round phase with a raised center (in green). These three phases may include $FePO_4$, $Fe(PO_3)_3$, $Fe_4(P_2O_7)_3$ or $Fe_3(P_2O_7)_2$.

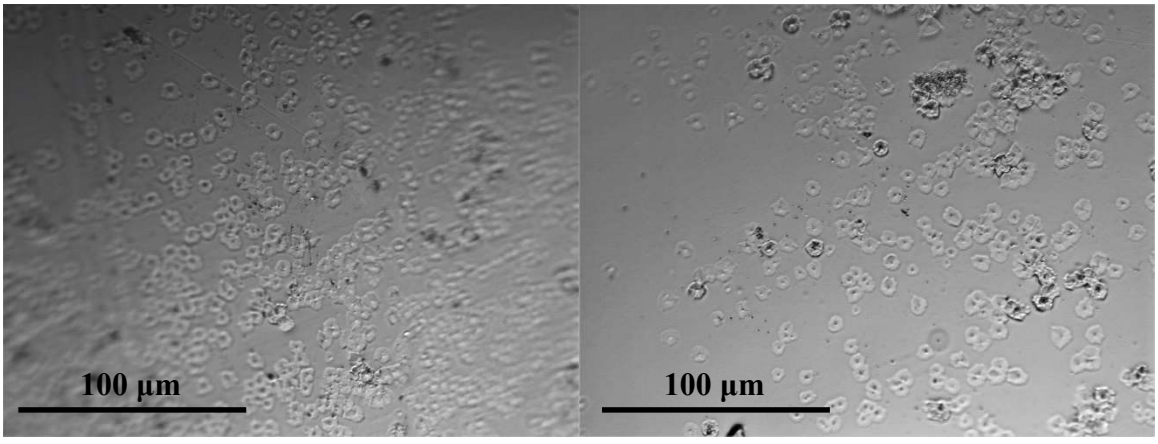

Figure 6.47. Images of 325Fe(III)1200 isothermally heat treated in air at 511ºC for 260 h.

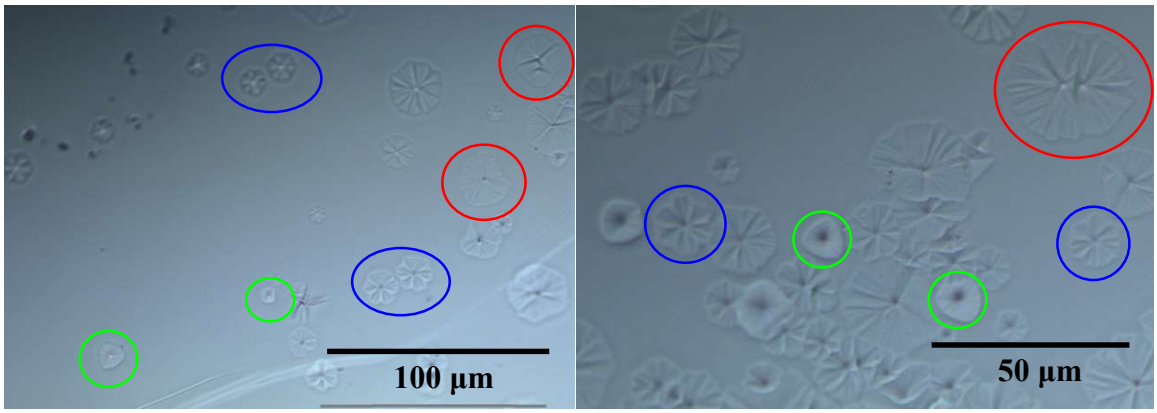

Figure 6.48. Images of 325Fe(III)1200 isothermally heat treated in air at 598ºC for 130 min (10+30+30+60 min).

Figure 6.49 shows a 325Fe(III)1200 sample ramped to ~700ºC at 10 K/min from room temperature, held for 5 minutes and then quenched in room temperature air. The three main morphologies observed differ from those at previous heat treatment temperatures and can be described as rectangular (yellow), round (green) and hexagonal (purple).

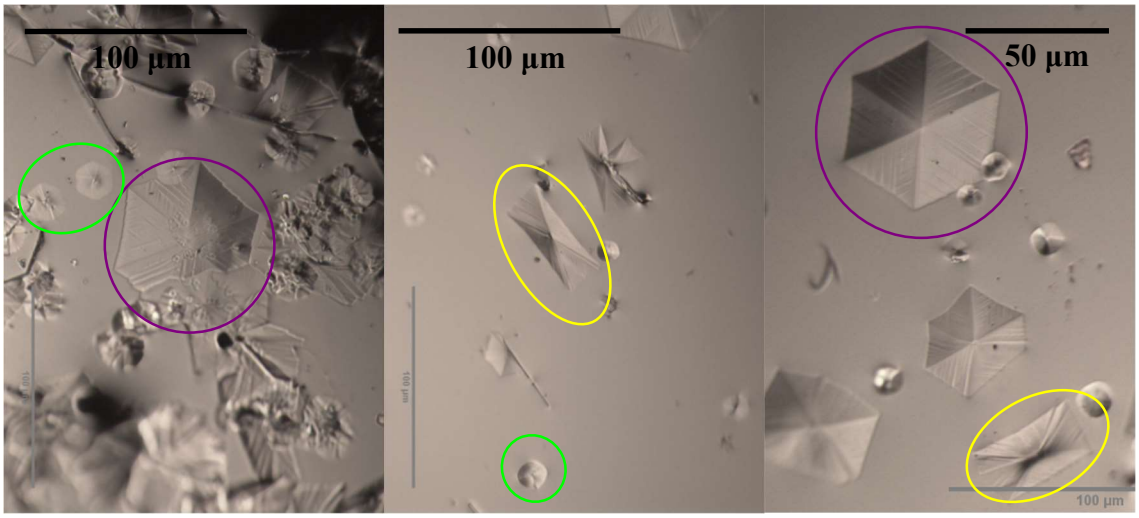

Figure 6.49. Images of 325Fe(III)1200 ramped to 694ºC in air at 10 K/min.

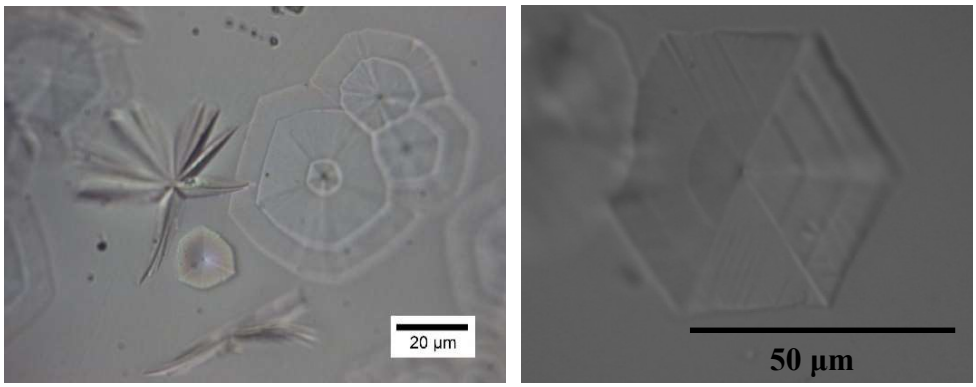

Figure 6.50. Image of 325Fe(III)1200 isothermally heat treated at 700ºC in air for 10+10+10 minutes.

Consecutive, 10-minute isothermal heat treatments at ~700°C result is identical morphologies and clear crystal growth lines (Figure 6.50). Further work into crystal growth rates using isothermal heat treatments and optical measurements of growth lines is suggested.

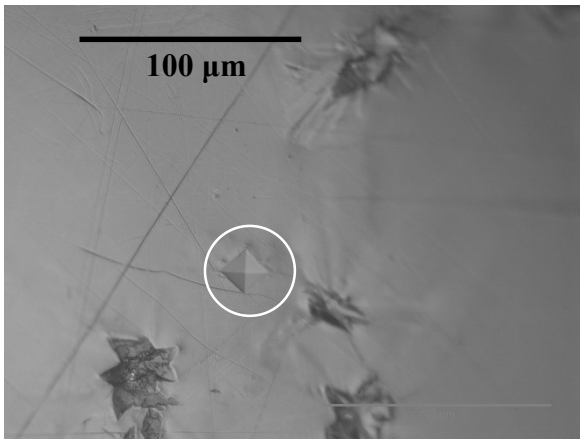

Figure 6.51. Image of 325Fe(III)1200 isothermally heat treated in air at 834ºC for 10 min.

Lastly, a 325Fe(III)1200 sample was isothermally heat treated at 834ºC, corresponding to a temperature just before the observed crystal melt temperature. The

images were again not very clear and many crystals were obscure and difficult to find. Yet, a new, square-pyramidal morphology was observed (Figure 6.51), although XRD patterns do not identify a new phase is formed at these temperatures. However, as mentioned previously, Marasinghe et al. [82] report a transformation of $Fe_3(P_2O_7)_2$ to $Fe_4(P_2O_7)_3$ near 800°C, and this new morphology may correspond to the formation of $Fe_4(P_2O_7)_3$.

Crystallization in air was also investigated for the 325Fe(III)1350 composition. 325Fe(III)1350 glass was isothermally heat treated at temperatures above T_g and was ramped to temperatures above the main crystallization and melt features indicated by the DTA (Figure 6.52). Isothermal heat treatments were held at temperatures for 2hr with the exception of the 511°C sample, which was held for 260hr.

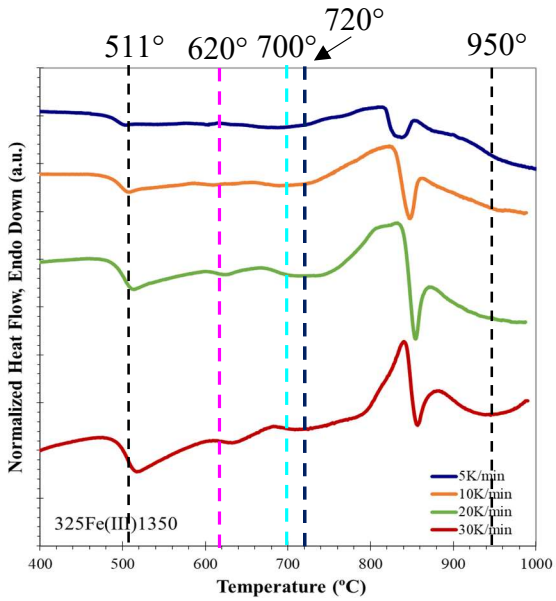

Figure 6.52. DTA patterns for 325Fe(III)1350 with lines indicating crystallization heat treatment temperatures.

XRD results indicate that $FePO_4$ is the predominant crystalline phase present at heat treatment temperatures below 700°C, while $Fe(PO_3)_3$ and $Fe_3(P_2O_7)_2$ are also present at heat treatment temperatures of 720°C. However, ferric pyrophosphate ($Fe_4(P_2O_7)_3$) is not detected by x-ray diffraction at any of the heat treatment temperatures used here, and rather the mixed valence pyrophosphate crystal ($Fe_3(P_2O_7)_2$) appears to be present in much higher proportion than in the 325Fe(III)1200 sample. The 325Fe(III)1350 glass composition is closer to that of the $Fe_3(P_2O_7)_2$ crystal than the 325Fe(III)1200 glass (see Figure 6.39).

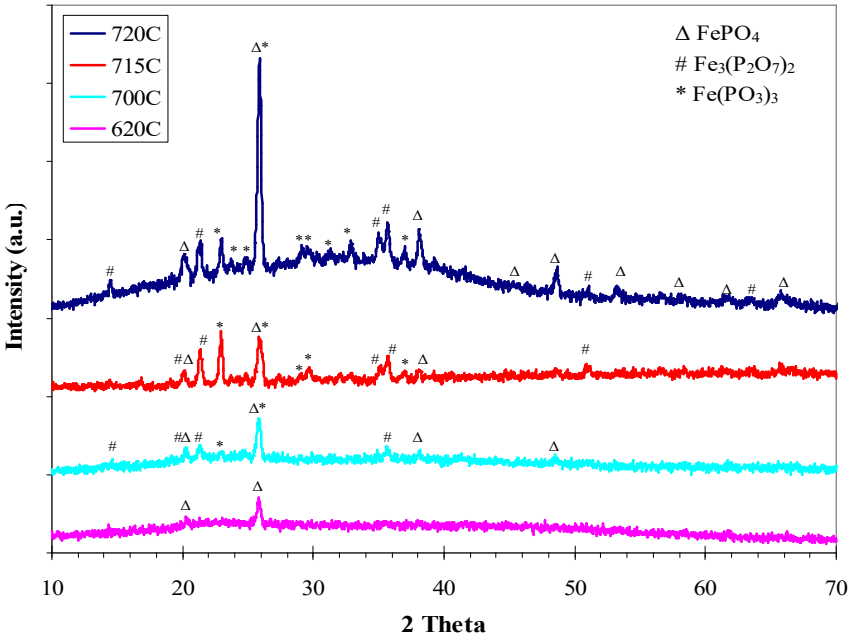

Figure 6.53. XRD patterns and peak identifications for 325Fe(III)1350 isothermally heat treated in air.

Raman spectra were taken through the cross-section of a monolithic 325Fe(III)1350 glass piece that was heat treated in air at 720°C for 3 hours (Figure 6.54). Results indicate that similar to the 325Fe(III)1200 sample, the predominant crystalline phases change

throughout the thickness of the glass piece. The mixed valency $Fe_3(P_2O_7)_2$ crystal is most prevalent on the surface of the sample, while ferric $Fe(PO_3)_3$ is most prevalent in the bulk of the piece.

Figure 6.55 shows optical microscopy images 325Fe(III)1350 heat treated just above T_g at 511ºC for extended periods of time (260 hours). Similar to the results for 325Fe(III)1200 at this temperature, only one phase is observed. The crystal appears to be uniformly sized and evenly dispersed throughout the glass surface. Similarities to results for 325Fe(III)1200 and formation at this low temperature again suggest that this phase is $FePO_4$.

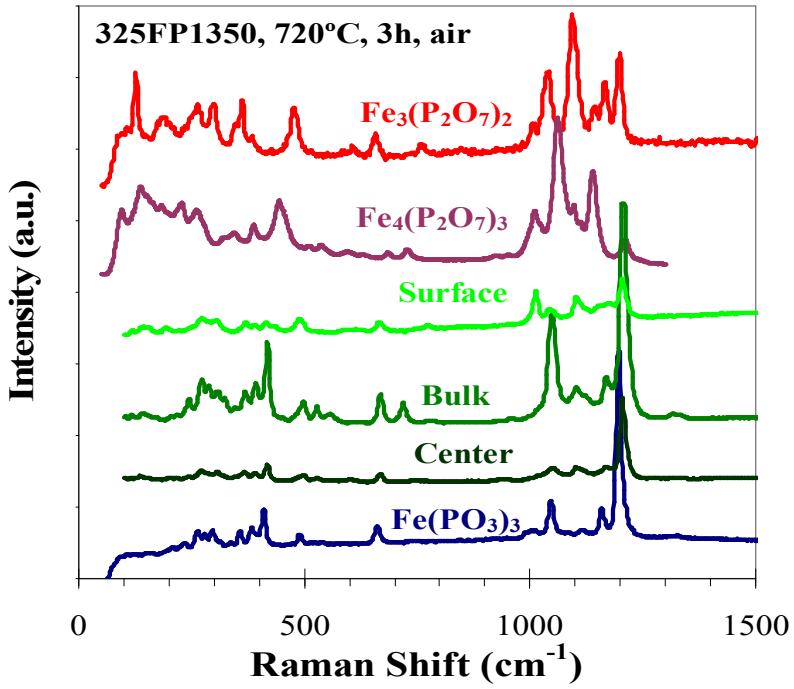

Figure 6.54. Raman spectra throughout bulk of monolithic 325Fe(III)1350 sample heated at 720°C in air for 3hr.

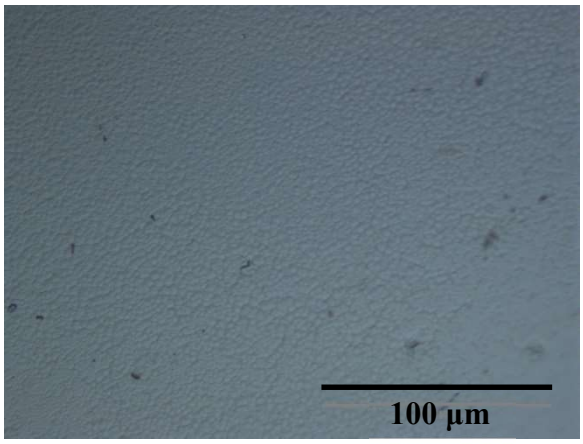

Figure 6.55. Image of 325Fe(III)1350 isothermally heat treated in air at 511ºC for 260h.

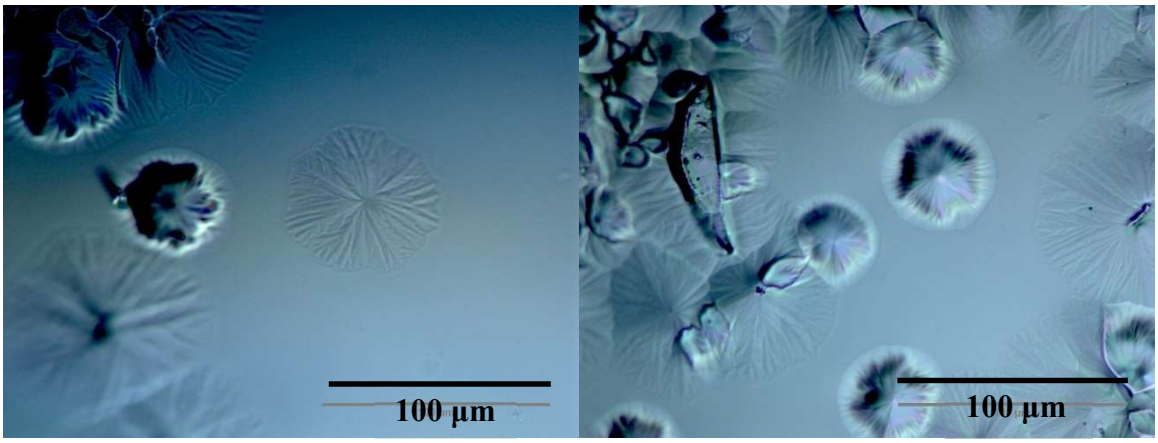

Figure 6.56. Images of 325Fe(III)1350 isothermally heat treated in air at 600ºC for 40 min (10+30 min).

Much different results are observed when 325Fe(III)1350 is heat treated at 600ºC (Figure 6.56). Two distinct crystal morphologies are seen, both rounded but one which appears flat and one which has a raised center. Morphologies, namely the flat crystal, appear similar to those seen in 325Fe(III)1200 at the same temperature (morphologies (2) and (3) as described for the 325Fe(III)1200 sample heat treated at 600ºC). Based on the

XRD patterns for samples which underwent similar heat treatments, it is most likely that these two phases are $FePO_4$ and $Fe_3(P_2O_7)_2$.

The final heat treatment conducted on 325Fe(III)1350 was a dynamic experiment ramped from room temperature to 950ºC at 10 K/min. The sample was held at temperature for 5 minutes and was quenched in room temperature air. It appears as though some crystals melted, leaving only one discernable morphology, as seen in Figure 6.57. Of the three crystalline phases identified by XRD for this glass (Figure 6.53), the phase observed is most likely a ferric phosphate phase. Zhang et al. [93] has determined $Fe_3(P_2O_7)_2$ to have a melting temperature of ~840ºC, while that of $FePO_4$ and $Fe(PO_3)_3$ are ~ 1200ºC.

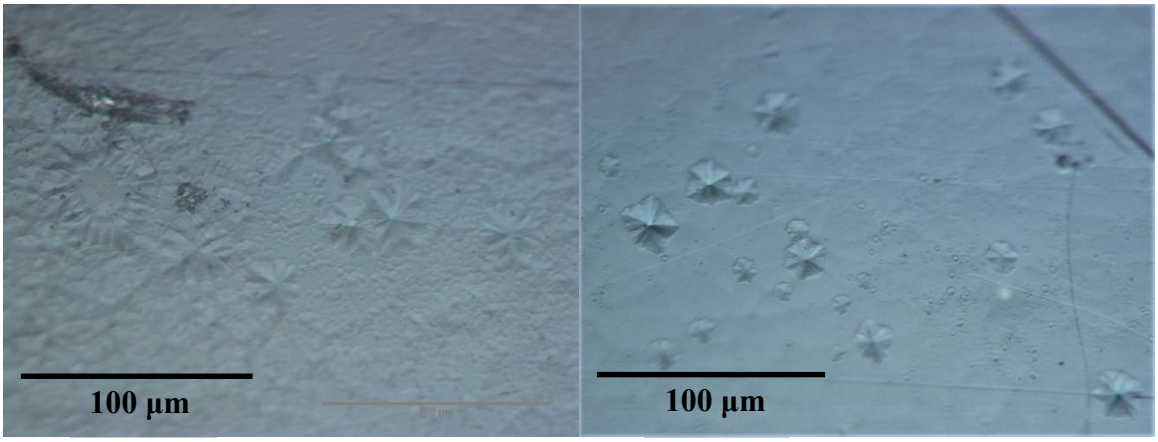

Figure 6.57. Images of 325Fe(III)1350 ramped to 950ºC in air at 10 K/min.

6.4. SUMMARY

Crystallization behavior and glass stability in iron phosphate glasses have been shown to be dependent on many variables, with variations occurring with sometimes

small changes in base glass composition, iron redox ratio, particle sizes, heating rate, and heat treatment atmospheres.

In general, the glass transition temperature of the iron phosphate glasses studied here increases with increasing proportion of trivalent Fe^{3+} relative to divalent Fe^{2+}. However, there is indication of competing influences on T_g for the pyrophosphate series, and is likely due to the increased structural connectivity caused by of polymerization from Q^0 and Q^1 units to longer phosphate anion chains occurring concurrently with decreased connectivity caused by the reduction of Fe^{3+} to Fe^{2+}. There is also evidence that batch materials may affect crystallization behavior of the glass. The batch material used may result in different short and intermediate range order, ie. different chain and ring distributions, causing some crystal structures to form more readily than others.

Unexpected glass stability has been shown for the iron phosphate glasses in the polyphosphate composition range. This observation suggests that average and distribution of chain lengths may play an important role in controlling parameters, such as melt viscosity and liquidus temperature, that affect crystallization kinetics. Changing the iron redox ratio (Fe^{2+}/Fe^{3+}) will change the O/P ratio and chain length within the glass, and thus understanding how to control the iron redox ratio is important to controlling crystallization behavior in iron phosphate glasses. Within the polyphosphate glass series, compositions with highest ferric iron content exhibit the greatest stability in nitrogen, while compositions with the lowest ferric iron content exhibit the greatest stability in air. This difference in behavior may be due to lower viscosity and increased oxygen diffusion (and extent of iron oxidation) in the polyphosphate glass with the lowest ferric iron

content. All compositions and environments yield greater stability with increases in heating rate and increases in particle size.

The iron polyphosphate series exhibits predominant surface crystallization in both inert environments and air, and the crystallization behavior is very dependent on the amount of oxygen available in the environment. The change in iron redox ratio and glass composition on surfaces with increasing temperatures is shown to play a large role in crystallization behavior and thus effects glass stability. TGA/DTA substantiated the oxidation of Fe^{2+} to Fe^{3+} upon heating, with almost complete oxidation occurring for particles of 45 – 63 μm heated in air to 1000°C. Because crystallization occurs primarily on the glass surface, particle size also greatly effects devitrification of iron phosphate glasses, and stability for all compositions increased with increasing particle size.

Crystalline phases formed during prolonged heat treatments vary from the surface into the glass bulk. This variation of phases crystallized throughout the depth of the sample may explain the differences seen in crystallization activation energy for varying particle sizes. Phases that form on sample surfaces will be predominant phases for smaller particle sizes, and phases that form within the bulk may be predominant phases for larger particle sizes. The crystallization activation energies are expected to change along with the predominant phases being formed.

When heated in air at temperatures near the main crystallization peak, compositions with greater amounts of ferric oxide are more likely to form ferric crystals ($Fe(PO_3)_3$ and $Fe_4(P_2O_7)_3$) on surfaces and mixed valent ($Fe_3(P_2O_7)_2$) crystals in the bulk, while compositions with greater ferrous oxide tend to form mixed valent ($Fe_3(P_2O_7)_2$)

crystals on the surface and ferric ($Fe(PO_3)_3$) crystals in the bulk. Both compositions predominantly form $FePO_4$ at temperatures near the glass transition.

6.5. COLLABORATOR CONTRIBUTIONS

The authors gratefully acknowledge Dr. Edgar Zanotto, Dr. Luciana Ghussn, and the entire research team at the Federal University of São Carlos, Brazil, for their assistance, discussion and use of equipment for crystallization studies and analysis. Thank you also to Dr. Eric Bohannon for assistance with the DTA and for being an overall amazing human being with an always smiling face.

7. PRELIMINARY INVESTIGATION OF IRON PHOSPHATE GLASSES USING UV-VIS SPECTROSCOPY: EFFECTS OF POST-MELT HEAT TREATMENT ON IRON REDOX RATIO

Optical analysis of iron phosphate glasses has been hindered by the opacity of the glasses in the visible spectrum. Iron phosphate glass "bubbles" with thicknesses ~50 μm were prepared, allowing enough transmission to study the absorption of the glasses in the UV-vis-NIR regions. Glass bubbles were heat treated at temperatures near T_g and the effects of heat treatment on optical band gap energy, Urbach energy, and absorption intensities were measured. Absorption edge background were fit and a methods analysis was performed to determine best deconvolution procedure for the resulting absorption peaks. Iron redox ratios of the glasses were measured using titration and results were correlated to multiple absorption parameters. It was determined that absorption coefficient of the iron peak spectra at 21008 cm^{-1} and the height of the deconvoluted absorption band associated with octahedral Fe^{3+} near 20500 cm^{-1} had the best correlation to iron redox ratio. Deconvolution results suggest mainly octahedrally coordinated Fe^{3+} but the presence of small amounts of tetrahedral Fe^{3+} in both glasses. Deconvolution results suggest Fe^{2+} exists in distorted octahedral coordination environments. Thermal analysis of the heat-treated glasses show changes in glass transition and onset crystallization temperatures upon heat treatment which suggest increased oxidation of iron with heat treatment time, supporting titration and optical results.

7.1. GENERAL PRINCIPLES

The use of UV-vis spectroscopy to qualitatively and quantitatively study the structure and iron valency of iron phosphate glasses is explored. UV-vis spectroscopy is a highly available experimental tool with relatively simple data collection procedures. However, the opacity of the black iron phosphate glass as prepared via traditional pour and quench methods makes it difficult to transmit enough light to obtain useful optical spectra. This problem was circumvented by producing extremely thin glass samples using the bubble-blowing technique described in Section 3.

As this is the first study to analyze UV-vis-NIR absorption of black iron phosphate glasses, absorption features and measurements are compared to measured redox ratios to determine which features provide the best correlation to ferrous iron content. Analysis of multiple deconvolution methods are compared to decide on the most appropriate fitting assumptions and procedures and to determine the feasibility of using this analysis technique for structural and coordination studies of these glasses.

UV-vis spectroscopy and titration were used to monitor the iron valence states and structural changes of two glasses with similar initial compositions throughout heat treatments near the glass transition temperature. Measurements of optical band gap energy and Urbach energy are used to support the observed changes in iron redox ratio and give insight into structural changes occurring with longer heat treatment times and iron oxidation.

7.2. EXPERIMENTAL PROCEDURES

See Section 3 for glass bubble preparation procedures and compositional analyses.

Fragments of 325Fe(III)1200bub and 325FPP1200bub glass bubbles were isothermally heat treated in air at 500°C for 48 hours, but were removed at 6, 12, and 24 hours to be analyzed with UV-vis spectroscopy. Samples were also analyzed before and after the 48 hour heat treatment. Thicknesses were measured using a digital micrometer. UV-visible optical absorption was measured on an Agilent Cary 500 using a scan rate of 600 nm/min with a baseline correction.

Titration could not be performed on the specific bubble fragments used for spectroscopy measurements because the same pieces were used for all spectroscopy measurements throughout the course of the heat treatment. However, additional bubble pieces that underwent identical heat treatments as those used in the UV-Vis study were ground with a silica mortar and pestle, sieved to <75 μm, and the iron redox ratio was measured using the titration technique described in Section 3.3.4.

Differential thermal analysis experiments were conducted using a Perkin Elmer DTA 7. Powdered samples (ground and sieved as described above) of mass ~50 mg were placed in alumina crucibles and powdered alumina was used as the reference sample. All experiments were performed under a nitrogen environment using a heating rate of 10 K/min to 1000ºC.

7.3. RESULTS AND DISCUSSION

Compositional analysis, thermal analysis and spectroscopy results are discussed below.

7.3.1. Titration Results. Fe^{2+} content as calculated from titration measurements are given in Table 7.1. The iron redox ratio, expressed as $Fe^{2+}/\Sigma Fe$, decreases for both glass series with increasing heat treatment time. Changes in redox ratios of transition metals during the annealing process at temperatures at or below T_g have been observed in other studies as well [123], [264].

Table 7.1. Ferrous iron content of glasses as measured by titration (with standard deviation of measurements in parentheses).

Sample	HT time (hr)	$\%Fe^{2+}$ (titration)
325Fe(III)1200bub	0	16.82 (0.60)
	6	16.00 (0.01)
	12	15.46 (1.00)
	24	15.14 (0.40)
	48	14.32 (0.62)
325FPP1200bub	0	18.88 (0.13)
	6	13.88 (0.73)
	12	12.20 (0.67)
	24	8.30 (0.28)
	48	4.85 (0.23)

The oxidation of iron exhibits a linear dependence on the square root of time in both cases, although the 325FPP1200bub sample experiences a much faster oxidation rate. Study of diffusion rates and kinetics is considered outside of the scope of this research, although this topic will be considered in the proposed future work.

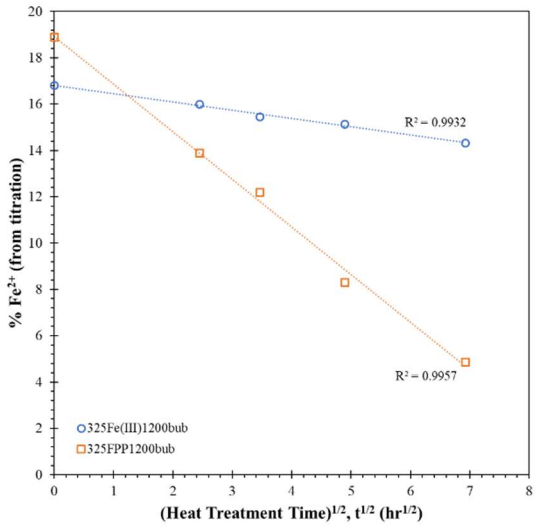

Figure 7.1. Fe^{2+} content of 325Fe(III)1200bub and 325FPP1200bub with increasing heat treatment time at 500ºC in air.

7.3.2. DTA Results. DTA results are shown in Figure 7.2 and values for characteristic temperatures are given in Table 7.2. DTA results indicate that the heat treatment temperature (500°C) is at or just above the T_g of 325FPP1200bub, yet is slightly below the T_g of 325Fe(III)1200bub. This proximity to the glass transition temperature may partly explain the difference seen in iron oxidation rate. 325Fe(III)1200bub is expected to have a higher viscosity at 500°C than 325FPP1200bub, which suggests a lower diffusion coefficient according to the Stokes-Einstein relation [19].

Both series exhibit an increase in T_g with heat treatment, suggesting a conversion of Fe^{2+} to Fe^{3+}. While the T_g of 325Fe(III)1200bub increases steadily with increasing heat treatment time and increasing proportion of Fe^{3+}, the T_g of 325FPP1200bub exhibits a more complicated trend. 325FPP1200bub experienced an overall smaller change in T_g despite a larger change in iron valence state, and the increase was not consistent with

increasing heat treatment time. These results suggest that multiple compositional or structural changes may be occurring in the 325FPP1200bub glass with conflicting effects on glass transition temperature. The annealing process may be resulting in relaxation of the structure and lowering of the fictive temperature while the oxidation of iron is resulting in increasing bond strengths and connectivity.

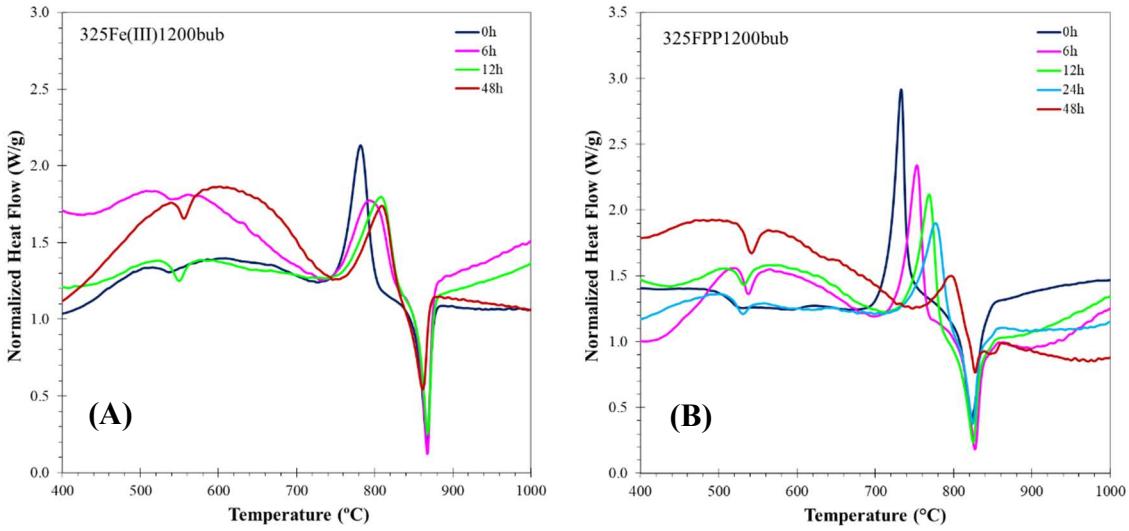

Figure 7.2. DTA patterns for (A) 325Fe(III)1200bub and (B) 325FPP1200bub with heat treatment in air at 500°C.

Both glass series exhibit an increase in T_x with increasing heat treatment time. The exaggerated asymmetry of the crystallization peak with increasing heat treatment time suggests that additional crystalline phases may be forming in samples with higher Fe^{3+} contents. Differences in onset crystallization temperatures and crystal melt features between the two glass series suggest that different crystalline phases may be forming or that viscosity disparities between the glasses are affecting the crystallization behavior, despite the similarity in base glass compositions.

Table 7.2. Glass transition and onset crystallization temperatures as measured by DTA.

Sample	HT time (hr)	T_g (°C)	T_x (°C)
325Fe(III)1200bub	0	507	750
	6	517	754
	12	531	762
	24	-	-
	48	544	767
325FPP1200bub	0	497	707
	6	522	724
	12	517	738
	24	516	746
	48	528	759

7.3.3. UV-vis Spectra. Samples of thicknesses 58 μm and 41 μm for 325Fe(III)1200bub and 325FPP1200bub, respectively, were chosen for UV-vis analyses throughout the heat treatment study. Sample choices were based on fragment size and lack of curvature so as to best be able to mount the pieces for optical analyses. Figure 7.3 shows the absorption spectra for 325Fe(III)1200bub and 325FPP1200bub samples after chosen heat treatment times.

The UV edge is attributed to oxygen-metal charge transfer bands caused by both iron valence states which occurs in the 370 – 390 nm region for phosphate glasses [265]–[269]. Absorptions between ~400 nm and ~700 nm are generally attributed to Fe^{3+}, while the broad feature near ~1100 nm is a well-known absorption band attributed to octahedral Fe^{2+} [265]–[268], [270]–[273]. Tetrahedral Fe^{2+} exhibits a well characterized absorption near ~2000 nm, although notably less intense than that at ~1000 nm [265]–[268], [271]–[273]. No such band is observed in these spectra.

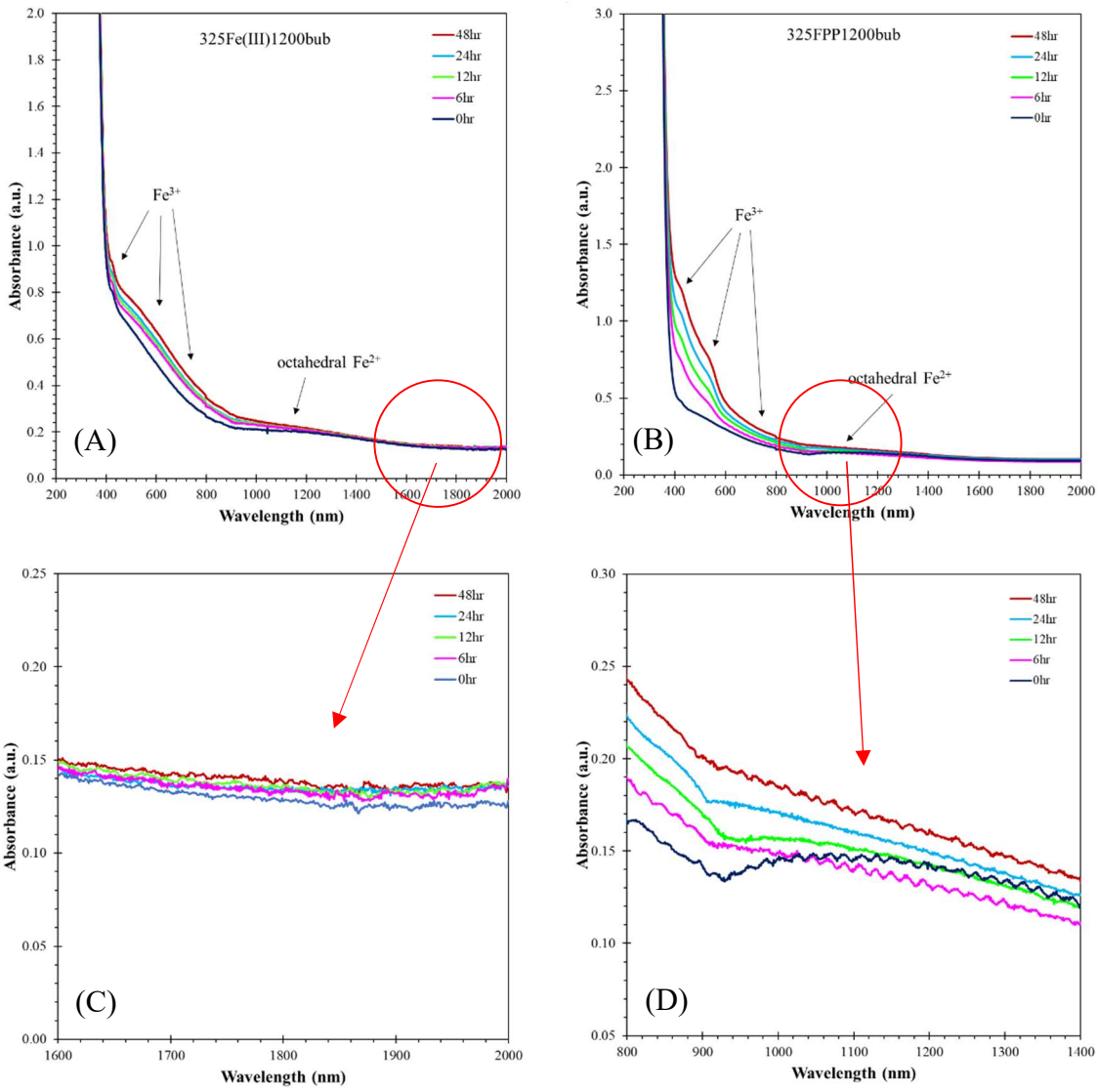

Figure 7.3. UV-Vis spectra showing increase in absorption due to Fe^{3+} with longer heat treatments times in air for (A) 325Fe(III)1200bub and (B) 325FPP1200bub, in addition to (C) the absence of an absorption peak for tetrahedral Fe^{2+} and (D) the obscuring of the absorption peak due to octahedral Fe^{2+} in the increasing tail of Fe^{3+} bands.

Absorption changes in the visible spectra are noticeable upon visual observation of the bubble samples. Heat treatment results in little or no change in the color of the 325Fe(III)1200bub pieces, yet causes a change in the 325FPP1200bub samples from black to sepia-toned (see Figure 7.4).

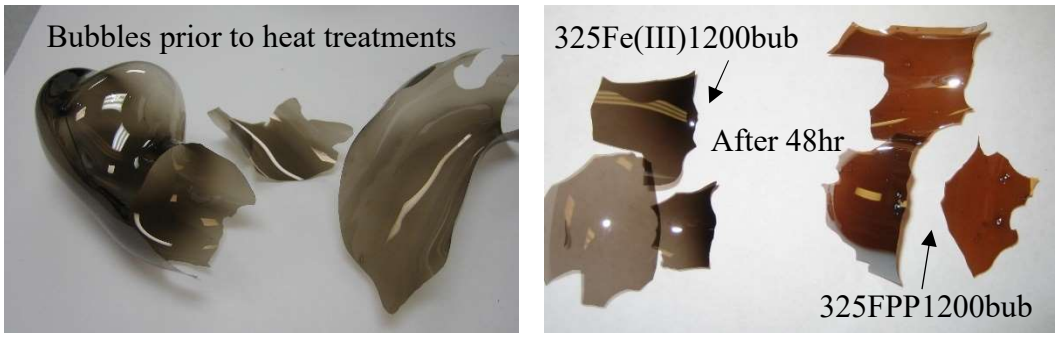

Figure 7.4. Image showing the difference in color change observed in the 325Fe(III)1200bub and 325FPP1200bub samples after heat treatment in air at 500°C.

To compare absorption spectra between the two glass series and account for the difference in thicknesses, the data can be expressed as absorption coefficient, α, as seen in Figure 7.5, using Equation 7.1 [269], [274], where *d* is the sample thickness (cm) and *A* is the optical absorbance.

$$\alpha(\omega) = \frac{2.303}{d} A \qquad \text{(Equation 7.1)}$$

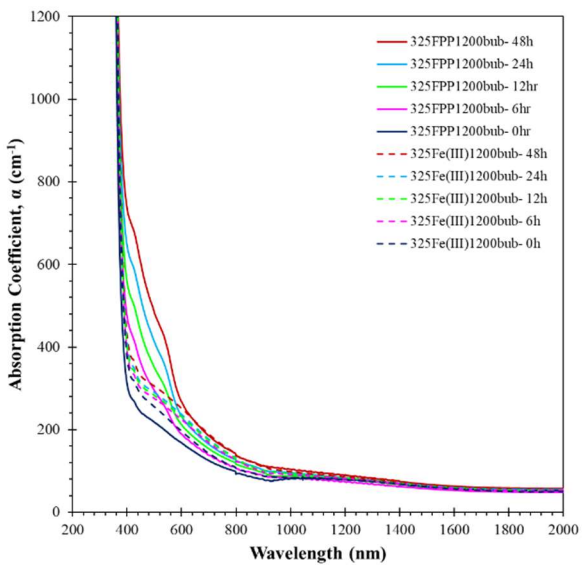

Figure 7.5. Absorption coefficient for 325Fe(III)1200bub and 325FPP1200bub as a function of wavelength.

Although both glasses show an increase in absorption associated with Fe^{3+} with longer heat treatment time in air, a much more dramatic increase is observed for 325FPP1200bub than 325Fe(III)1200bub. No similar increase in absorption associated with Fe^{2+} is evident in Figure 7.3(C), as the Fe^{2+} peak is obscured in the growing tail of the Fe^{3+} absorption region. Assignment and deconvolution of the absorption peaks is necessary to quantitatively investigate iron valence states and will be further explored in Section 7.3.6.

7.3.4. Optical Band Gap and Urbach Energies. UV-vis absorption spectra can be used to investigate optical band gap energies of glasses. The optical band gap energy, E_g, refers to the energy difference between the top of the valence band and the bottom of the conduction band. To the author's knowledge, this is the first study which allows for such absorption analyses of these dark iron phosphate glasses.

Davis and Mott [275] proposed a power law to describe the optical absorption of amorphous materials for photon energies greater than E_g, as given by

$$\omega\alpha(\omega) = B\left(\hbar\omega - E_g\right)^n \qquad \text{(Equation 7.2)}$$

where α is the absorption coefficient, B is a constant, E_g is the optical band gap energy, and n is an index related to the type of optical transition [19]. Indirect allowed transitions such as those occurring in amorphous materials will have n = 2. Rearranging this equation reveals a linear relationship between $(\hbar\omega\alpha(\omega))^{1/2}$ and photon energy ($\hbar\omega$), such that the x intercept is equal to E_g. This representation of the data and method for calculating E_g was proposed by Tauc [276] and is referred to as a Tauc plot [269], [277]. Tauc plots for all samples are seen in Figure 7.6, and calculated values of the optical band gap are given in Table 7.3.

Figure 7.7 shows the change in optical band gap energy with changes in iron redox ratio. A decrease in optical band gap energy with depolymerization of the structure (ie. oxidation of Fe^{2+} to Fe^{3+}) is observed and is consistent with results seen in other studies [269], [278]–[282]. The optical band gap energy is determined by the separation of the transition metal 3d states and the 2p oxygen states. Non-bridging oxygen have higher 2p oxygen energy levels than do bridging oxygen, and thus as the number of non-bridging oxygen increases, the optical band gap will decrease. An increase in bond strength, which is expected as divalent ferrous iron is replaced by trivalent ferric iron, will also decrease the optical band gap [201], [269].

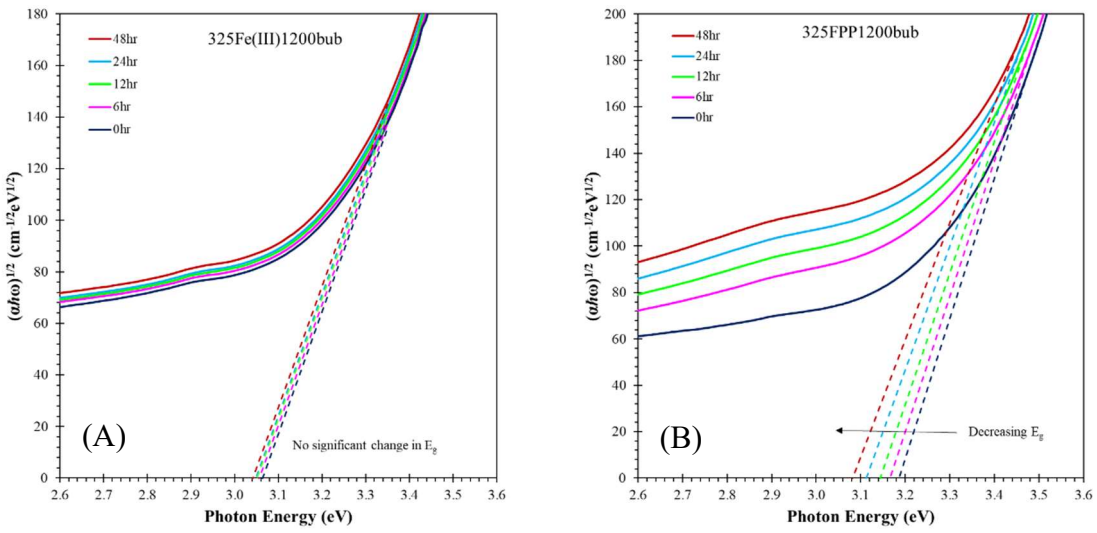

Figure 7.6. Tauc plots and extrapolations of linear regions for (A) 325Fe(III)1200bub and (B) 325FPP1200bub.

The optical band gap for the 325FPP1200bub series is higher than that for the 325Fe(III)1200bub series, even for similar iron redox ratios. This implies a potentially larger degree of polymerization of the structure or weaker bond strengths in the

325FPP1200bub series. As the base compositions of the two glasses are almost identical, this result is unexpected. Future structural studies could better resolve the cause of this difference.

Table 7.3. Calculated optical band gap and Urbach energies for heat treated glasses.

Sample	HT time (hr)	E_g (eV)	ΔE_{urb} (eV)
325Fe(III)1200bub	0	3.064	0.175
	6	3.056	0.179
	12	3.051	0.182
	24	3.048	0.183
	48	3.041	0.184
325FPP1200bub	0	3.186	0.167
	6	3.166	0.184
	12	3.144	0.191
	24	3.112	0.197
	48	3.082	0.209

The only reported optical band gap for similar glasses was calculated using diffuse reflectance spectra of powdered $40Fe_2O_3$-$60P_2O_5$ [280]. Although compositional analysis was not reported in the referenced study, batched $40Fe_2O_3$-$60P_2O_5$ pyrophosphate glass is expected to have a higher O/P ratio and higher fractions of non-bridging oxygens than the $33.3Fe_2O_3$-$66.7P_2O_5$ polyphosphate glasses in this study. The optical band gap of 2.90 eV reported for $40Fe_2O_3$-$60P_2O_5$ is slightly lower than the 3.0 – 3.2 eV observed for $33.3Fe_2O_3$-$66.7P_2O_5$ and thus the results are consistent with expectations.

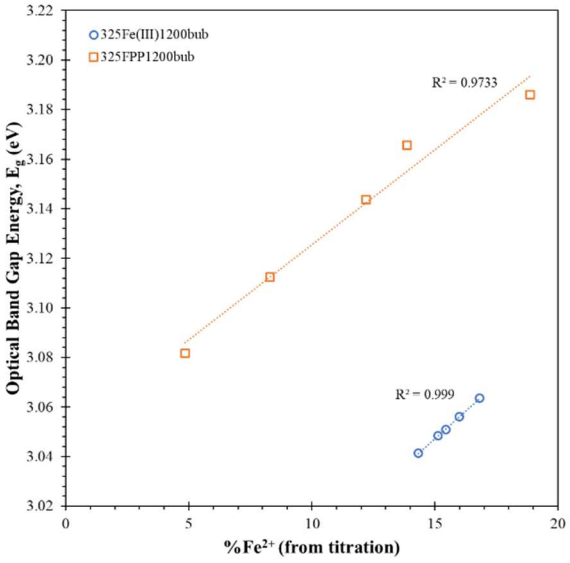

Figure 7.7. Changes in optical band gap energy with iron redox ratio.

At energies less than E_g, the absorption coefficient changes to an exponential dependency on photon energy as described by Urbach [283] and given by Equation 7.3,

$$\alpha(\omega) = B\exp\left(\frac{h\omega}{\Delta E_{urb}}\right) \qquad \text{(Equation 7.3)}$$

where B is a constant and ΔE_{urb} is the Urbach energy. The Urbach energy represents the width of the band tails of the localized states in the forbidden band gaps and is associated with defect levels and the structural disorder in amorphous solids [269], [277], [281]. Lower values of ΔE_{urb} correspond to greater degrees of disorder. By plotting $\ln(\alpha)$ versus photon energy, the slope of the linear region of the absorption spectra will be the reciprocal of the Urbach energy. Figure 7.8 and Table 7.3 show the absorption coefficient spectra and calculated Urbach energies for the iron phosphate glass bubbles studied here.

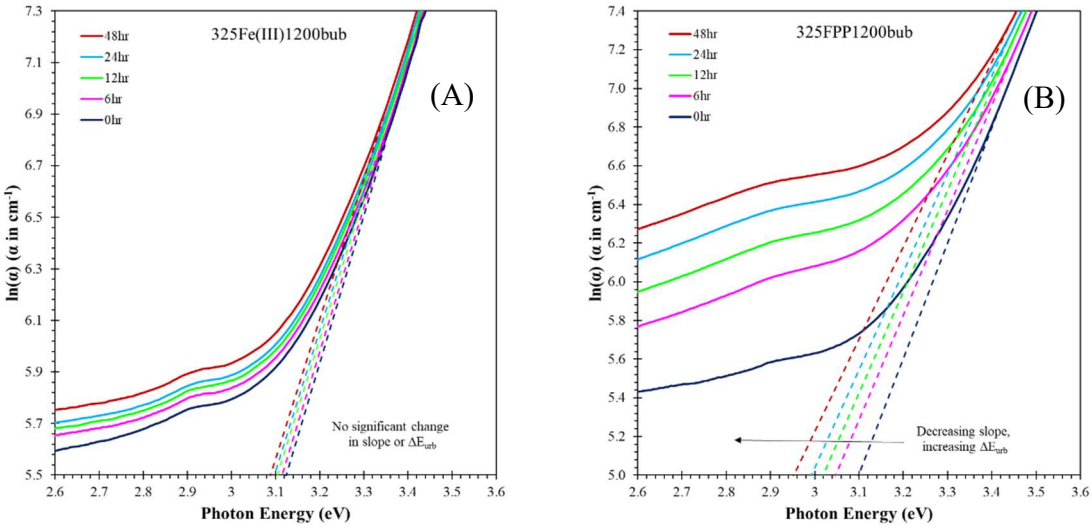

Figure 7.8. Urbach energy plots for (A) 325Fe(III)1200bub and (B) 325FPP1200bub.

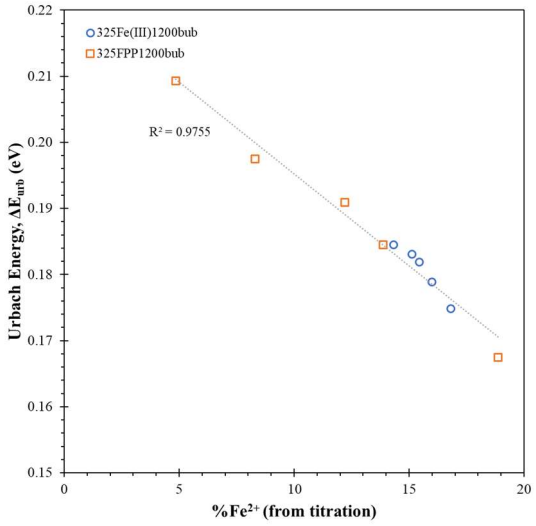

Figure 7.9. Urbach energy as a function of ferrous iron content.

Changes in Urbach energy with iron redox ratio are shown in Figure 7.9, indicating similar values and trends of Urbach energy as a function of iron redox ratio for both glass series. Urbach energies increase with decreasing Fe^{2+} content, which also

corresponds to increasing heat treatment time, suggesting a lessening of structural disorder within the glass upon heat treatment. Kaseman et al. [284] used NMR spectroscopy to show that "aging" a phosphate glass, or annealing at temperatures below T_g, caused structural relaxation, drove disproportionation reactions in the direction of binary distribution of Q^n species, and increased the symmetry of P sites. Results here are consistent with their findings.

7.3.5. Fitting the UV Edge and Background Absorption. In order to deconvolute the iron absorption peaks, the UV absorption edge background must be fit and subtracted from the optical absorbance spectra.

For photon energies less than E_g, the absorption coefficient has been shown to follow the exponential relationship [19], [275],

$$\alpha(\omega) = \alpha_o \exp\left[-\Gamma(E_c - \hbar\omega)\right] \qquad \text{(Equation 7.4)}$$

where α_o and Γ are constants, and E_c is an energy value approximately equal to E_g. This relationship was used with calculated values of E_g to fit the background of all optical spectra using a sum of least squares approach and the Solver function in Excel. Examples of the fit are seen in Figure 7.10 and values for the fitted constants α_o and Γ are given in Table 7.4. Data is represented as wavenumber instead of wavelength, as being expressed in this way results in more symmetric Guassian peaks [98] and assists deconvolution.

Figure 7.11 shows the optical absorption peaks of the glasses after the calculated absorption edges are subtracted out as described above. Lines are drawn at wavenumbers corresponding to peak maxima or features of interest, and absorption coefficient values at these wavenumbers are given in Table 7.4.

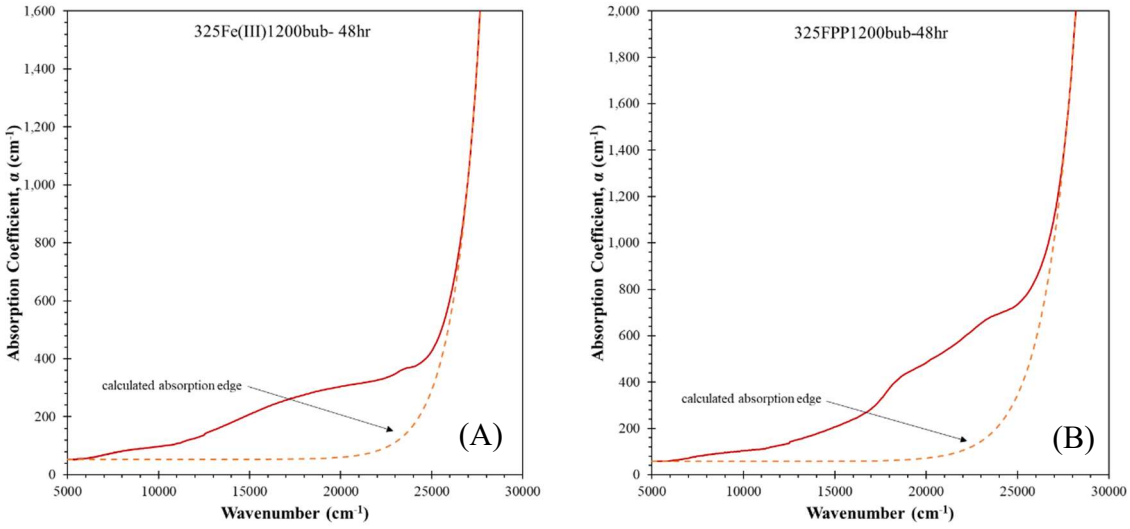

Figure 7.10. Examples of the calculated absorption edge using Equation 7.4 and the constants α_0 and Γ in Table 7.4.

Table 7.4. Absorption edge fitting parameters and absorption coefficient values at wavenumbers of interest.

Sample	HT time (hr)	Absorption Edge Parameters		Absorption Coefficient, α				
		α_0	Γ	9497 cm^{-1}	14993 cm^{-1}	18518 cm^{-1}	21008 cm^{-1}	23202 cm^{-1}
325Fe(III)1200bub	0	3.77E-05	0.941	32	109	180	209	208
	6	5.71E-05	0.919	37	134	202	221	214
	12	7.81E-05	0.903	37	138	208	227	217
	24	8.24E-05	0.902	37	142	215	234	223
	48	9.54E-05	0.895	40	155	229	247	235
325FPP1200bub	0	1.87E-05	0.970	30	85	144	170	173
	6	1.29E-04	0.870	32	105	203	260	300
	12	2.62E-04	0.835	34	117	225	317	366
	24	4.14E-04	0.812	38	127	293	381	440
	48	9.50E-04	0.769	43	149	352	449	510

The dependency of absorption coefficient on Fe^{2+} content is shown in Figure 7.12 for the selected wavenumbers. Previous studies of impurity and dopant levels of iron have determined that only the intensities of the absorption bands near 415 nm and 1050 nm follow Beer-Lambert's Law and can be used to accurately determine the distribution

of iron in valence states [265], [273], [285] or in Fe^{2+} coordination environments [286]. Beer-Lambert's Law generally applies only to cases of low concentration and non-linearity is often seen at concentrations greater than 10 mM. Although iron contents in the glasses studied here are far above the concentrations at which Beer-Lambert's Law applies, series independent linearity of the concentration-absorption relationship is observed at ~21000 cm^{-1} (476 nm), but not for the highest energy feature at ~23200 cm^{-1} (431 nm) or the feature at ~9500 cm^{-1} (1053 nm) associated with ferrous iron as may be expected.

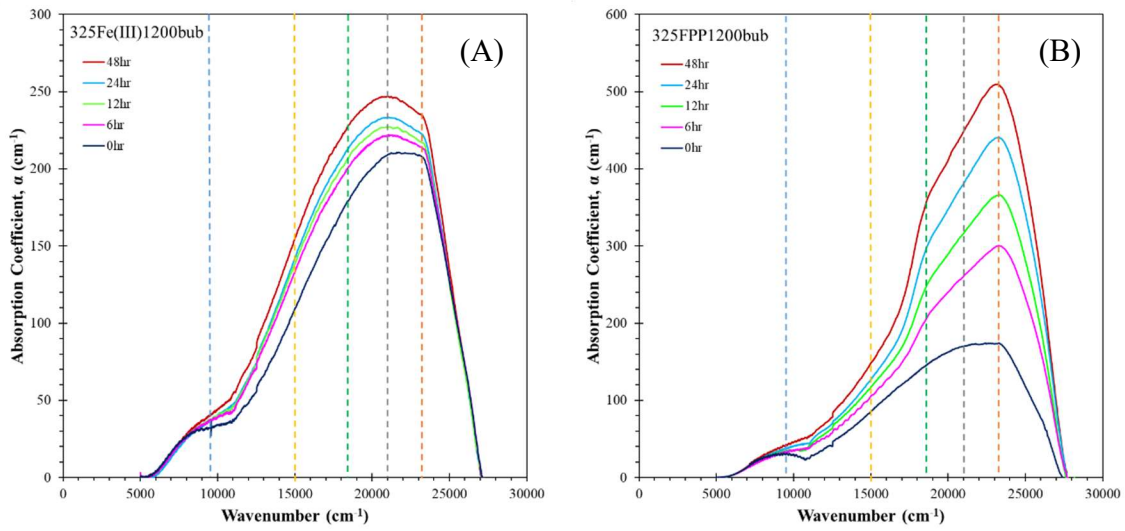

Figure 7.11. Iron absorption peaks for (A) 325Fe(III)1200bub and (B) 325FPP1200bub resulting from optical absorbance spectra in Figure 7.3 less the absorption edges calculated from Equation 7.4 and the fitting constants in Table 7.4.

From the linear fit of the concentration-absorption coefficient relationship at 21008 cm^{-1}, the following empirical relationship can be derived:

$$\%Fe^{2+} = 26.84 - \frac{\alpha_{21008cm^{-1}}}{20.47} \qquad \text{(Equation 7.5)}$$

where $\alpha_{21008cm}^{-1}$ is the absorption coefficient of the net absorption peaks at 21008 cm^{-1}.

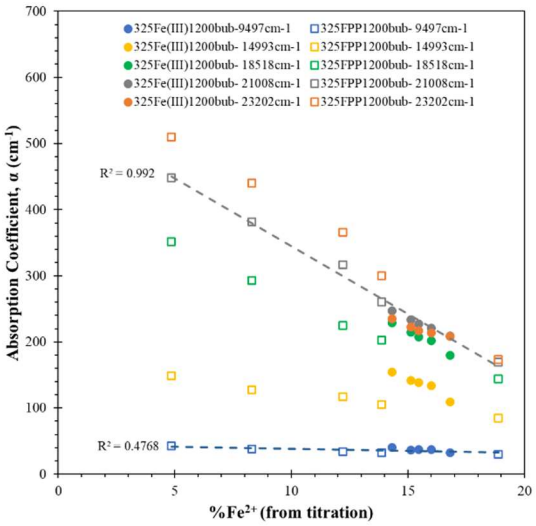

Figure 7.12. Absorption coefficient at selected wavenumbers as a function of Fe^{2+} content for both glass series.

7.3.6. Assigning Absorption Bands and Fitting the Absorption Peaks.

Absorption peak positions depend on the specific electronic transition occurring and the coordination number of the iron, as well as the symmetry of its complex [271]. Absorption features in the UV-vis-NIR region are more complex for Fe^{3+} than for Fe^{2+}.

Fe^{2+} has a $3d^6$ electronic configuration. The only spin allowed transition for octahedral Fe^{2+} is $^5T_{2g}(D) \rightarrow {}^5E_g(D)$, which results in a broad absorption band in the 1000 – 1200 nm region. The broadness of this absorption is indicative of distortions and is often a result of band splitting due to the Jahn-Teller Effect [266], [285], [287]. Tetrahedral Fe^{2+} exhibits an absorption band in the 2000 – 2200 nm region associated with the $^5E_g(D) \rightarrow {}^5T_{2g}(D)$ transition [267], [270], [288].

Fe^{3+} has a $3d^5$ electronic configuration which results in a half-filled *d* sub shell. Six unique *d-d* electronic transitions are possible [265], [289], all of which are spin forbidden [267], [287]. In order of increasing energy, they correspond to electrons in the $^6A_{1g}(S)$ ground state being excited to $^4T_{1g}(G)$, $^4T_{2g}(G)$, $^4A_{1g}(G)+^4E(G)$, $^4T_{2g}(D)$ and $^4E_g(D)$ levels [287].

Peak positions of the absorption bands depend not only on iron coordination numbers but will also shift for different structural sites and distortions around the iron ions [290]. Peak positions associated with Fe^{3+} have been reported at roughly 240 – 265, 330 – 385, 410 – 444, 500 – 560, and 650 – 800 nm [266], [270], [287], [291]. Absorption in the 650 – 750nm region has been attributed to both Fe^{3+} [268], [270], [272], [282], [287] and Fe^{2+} [123], [266], [290], and the research on this absorption region is much less clear than for the rest of the spectra.

Most studies specific to phosphate base glasses involve iron concentrations at impurity or dopant levels ranging from 12 ppm Fe to 5 mol% Fe_2O_3, and all involve additional glass components such as alumina, alkali, alkaline earth and rare earth oxides [98], [116], [268], [291]. Peak positions for iron in different base compositions and at larger concentration levels are expected to differ, however peak assignments in these reference studies served as a guideline to the fittings performed in this study. Ehrmann et al. [268] designated Fe^{3+} bands at 415, 520, and 735 nm, and Fe^{2+} at 1054 and 2100 nm, in close agreement with assignments made by Kumar et al. [116] of Fe^{3+} bands at 385, 415, and 525 nm, and Fe^{2+} bands at 1100 and 2170 nm. Bamford [291] determined slightly higher peak positions for octahedral Fe^{3+} bands at 410, 560 and 770 nm. Kurkjian et al. [98] determined positions and also attributed transitions to absorption bands,

assigning octahedral Fe^{3+} features at 365 nm to the $^4T_2(D)$ transition, 410 – 420 nm to $^4E^4A_1$, 520 –545 nm to $^4T_2$, and 720 – 760 nm to $^4T_1$. He also assigned a 450 nm band to the tetrahedral Fe^{3+} transition to $^4T_2$.

In deciding how many peaks to fit to the spectra, the number of expected transitions in the region of interest must be considered. Fe^{3+} absorption bands for the $^6A_{1g}(S) \rightarrow {}^4E_g(D)$ and $^4T_{2g}(D)$ transitions are expected at wavelengths below the observed absorption edge (<380nm) and therefore will not be discernible in the glasses analyzed here. The three remaining absorption bands expected for octahedral Fe^{3+} correspond to the $^6A_{1g}(S) \rightarrow {}^4E_g(G) + {}^4A_{1g}(G)$, $^6A_{1g}(S) \rightarrow 4T_{2g}(G)$, and $^6A_{1g}(S) \rightarrow {}^4T_{1g}(G)$ transitions and are all considered in current peak fittings.

Both ferric and ferrous iron are known to exist in octahedral and tetrahedral coordination environments in glasses [285], [292]. However, structural studies on iron phosphate glasses have determined that mostly octahedral Fe^{3+} is present in iron phosphates containing less than 40% Fe_2O_3 [101] and that both valence states exist in mainly octahedral and distorted octahedral coordination [82], [98], [270], [272]. Distortion of both valence states was found to increase with increasing total iron content [128]. UV-vis spectra for both glass series indicate undetectable absorption near 2000 nm as would be expected for tetrahedral Fe^{2+}, confirming mainly octahedral coordination for Fe^{2+}. As such, only octahedral Fe^{2+} is considered in peak fitting here. Peak fitting was completed both with and without consideration of Jahn-Teller splitting of the ferrous absorption band.

Absorption of tetrahedral Fe^{3+} is expected to overlap with octahedral Fe^{3+} absorption. It is not possible to easily discern from the spectra whether both coordination

environments of ferric iron are present and therefore peak deconvolutions were performed both with and without consideration of tetrahedral Fe^{3+} absorption bands.

Axes were chosen as absorption coefficient instead of absorbance to best compare results from different samples, and as wavenumber instead of wavelength to optimize the Guassian symmetry of the absorption peaks. The three approaches to fitting are:

1) Assumption of octahedral Fe^{3+} bands (3 peaks) and unsplit octahedral Fe^{2+} band (1 peak),

2) Assumption of octahedral and tetrahedral Fe^{3+} bands (5 peaks) and unsplit octahedral Fe^{2+} band (1 peak), and

3) Assumption of octahedral and tetrahedral Fe^{3+} bands (5 peaks) and Jahn-Teller split bands for octahedral Fe^{2+} (2 peaks).

Peaks were assumed to follow a Guassian profile [293] according to

$$y = A\exp\left(\frac{-(\lambda-\mu)^2}{2\sigma^2}\right) \qquad \text{(Equation 7.6)}$$

where A is the peak height, μ is the peak position, and σ is the standard deviation. Values for μ were constrained to being equal for all samples within a series, but values of A and σ were allowed to change for each sample. Peaks were fit to the absorption curves (for wavenumbers less than that corresponding to the optical gap) using the sum of least squares approach and Solver in Excel. Peak areas were calculated using the area equation for Guassian peaks,

$$Area = A\sigma\sqrt{(2\pi)} \qquad \text{(Equation 7.7)}$$

where A and σ are given by the fitting parameters. R-squared values for each fit were calculated over the entire spectrum as well as for regions of interest– the main absorption peak at 18500 – 24500 cm^{-1} and the shoulder at 7000 – 12000 cm^{-1}.

7.3.6.1. Assumption #1: Octahedral Fe^{3+} only. Figure 7.13 and Figure 7.14 show the spectra deconvolution assuming four total absorption peaks. Fitting parameters are given in Table 7.5. R^2 values for all assumptions and fits are compared in Table 7.6.

The base glasses are nearly identical in composition and are assumed to have similar electronic transitions, yet differences are seen in their absorption spectra. The 325Fe(III)1200bub spectra are dominated by the octahedral Fe^{3+} absorption band near 20000 cm^{-1}, which most likely corresponds to the $^6A_{1g}(S) \rightarrow {}^4E_g(G) + {}^4A_{1g}(G)$ transition, while the 325FPP1200bub spectra are dominated by the octahedral Fe^{3+} absorption band near 24000 cm^{-1} associated with the $^6A_{1g}(S) \rightarrow 4T_{2g}(G)$ transition.

Table 7.5. Peak fitting parameters for Assumption #1 and four absorption bands.

Sample	HT time (hr)	Peak: Fe^{3+} Octahedral#1					Peak: Fe^{3+} Octahedral#2					Peak: Fe^{3+} Octahedral#3				
		μ (cm^{-1})	λ (nm)	A (cm^{-1})	σ	Area	μ (cm^{-1})	λ (nm)	A (cm^{-1})	σ	Area	μ (cm^{-1})	λ (nm)	A (cm^{-1})	σ	Area
325Fe(III)1200bub	0	23516	425	61	1482	225712	20491	488	192	3696	1775284	14350	697	47	2775	327341
	6			50	1334	167973			209	3843	2013385			60	2818	423315
	12			49	1296	158362			216	3818	2063168			64	2801	446848
	24			49	1316	160668			220	3852	2128497			64	2902	462633
	48			51	1320	167921			233	3858	2254923			72	2913	525089
325FPP1200bub	0	23949	418	103	1947	502908	19756	506	147	2987	1104435	14300	699	47	2254	263536
	6			237	2027	1205457			198	2527	1255804			71	2575	457858
	12			295	1997	1475307			246	2421	1493207			83	2382	494932
	24			363	2008	1828766			293	2341	1721775			90	2484	558261
	48			416	1984	2068068			355	2332	2073628			103	2484	642539

Sample	HT time (hr)	Peak: Fe^{2+} Octahedral				
		μ (cm^{-1})	λ (nm)	A (cm^{-1})	σ	Area
325Fe(III)1200bub	0	8669	1154	25	1462	91079
	6			23	1346	78840
	12			24	1352	80476
	24			21	1273	67626
	48			23	1340	76078
325FPP1200bub	0	8853	1130	28	1426	99865
	6			23	1434	80945
	12			26	1429	93401
	24			26	1442	95410
	48			29	1434	104022

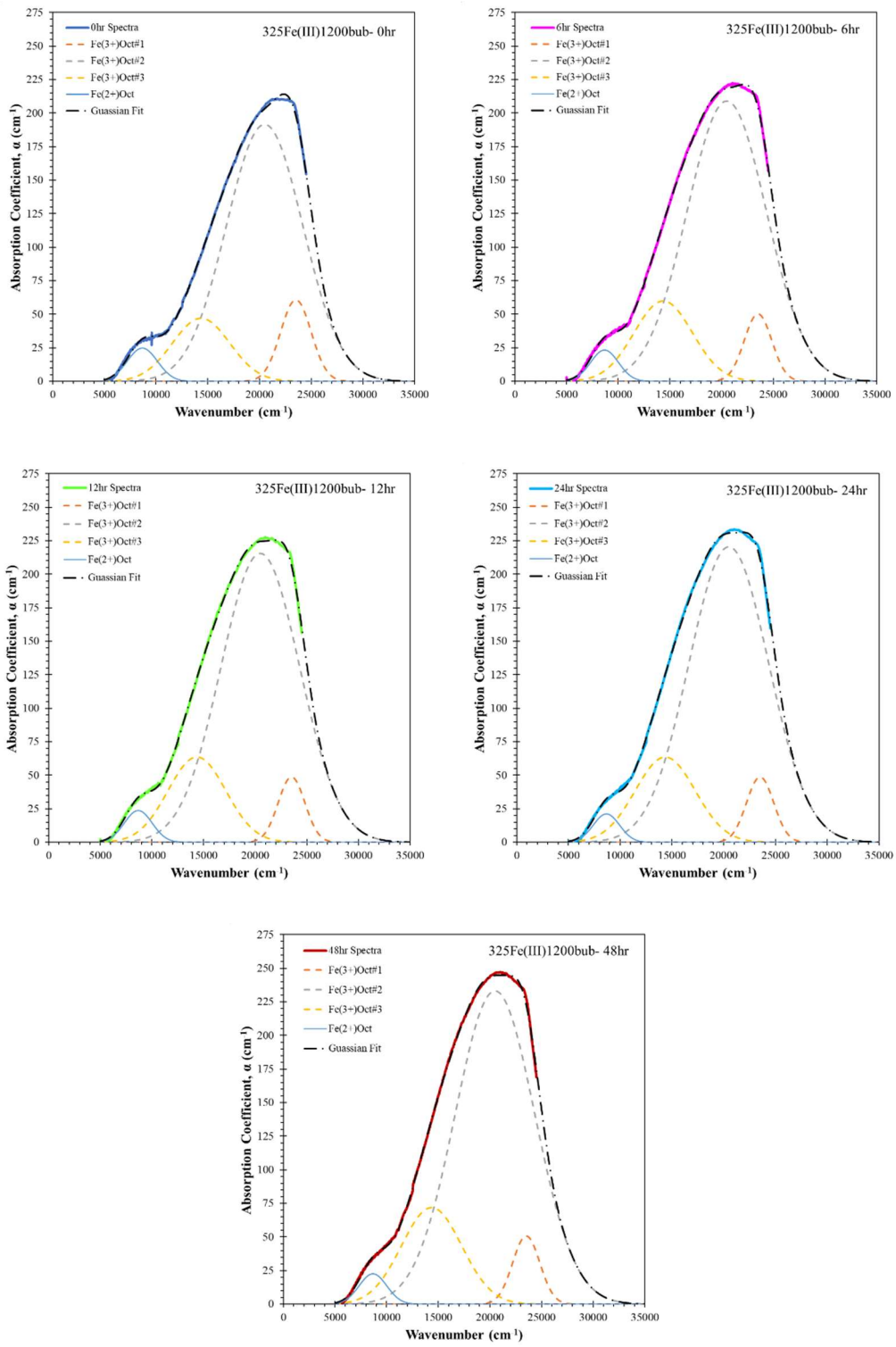

Figure 7.13. Peak deconvolutions for 325Fe(III)1200bub series assuming four total absorption bands.

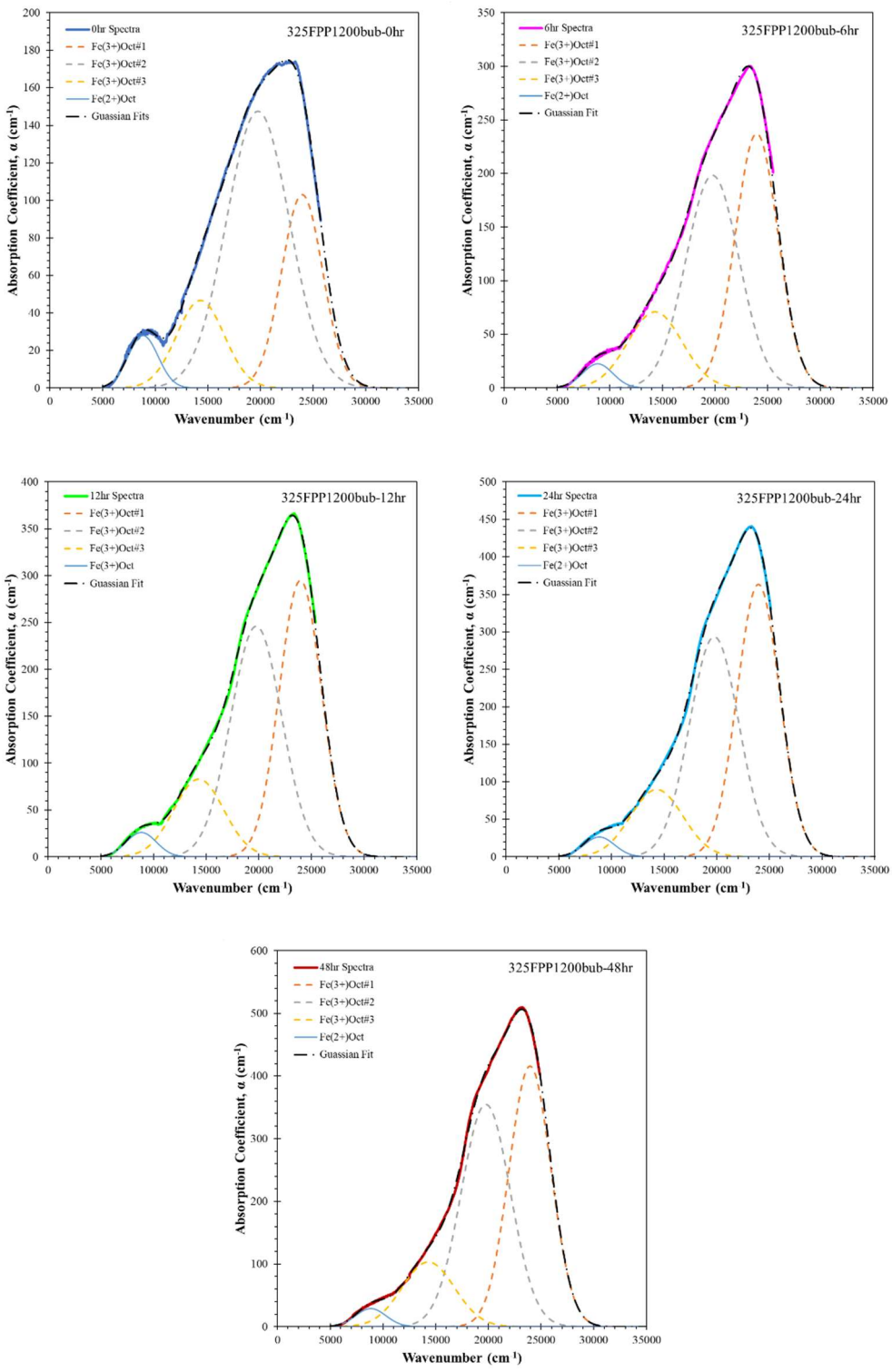

Figure 7.14. Peak deconvolutions for 325FPP1200bub series assuming four total absorption bands.

Table 7.6. R^2 values over entire spectra (5000-35000 cm^{-1}), absorption shoulder (7000-12000 cm^{-1}) and main absorption peak (18500-24500 cm^{-1}) for all fitting assumptions.

Assumption #1- Octahedral Fe^{3+} only				
Sample	HT time (hr)	R^2 of fit- Assumption #1 (only oct. Fe^{3+})		
		5000-35000 cm^{-1}	7000-12000cm^{-1}	18500-24500 cm^{-1}
325Fe(III)1200bub	0	0.99941	0.94806	0.94929
	6	0.99959	0.98292	0.93373
	12	0.99962	0.98637	0.94699
	24	0.99958	0.98693	0.94674
	48	0.99969	0.99229	0.95160
325FPP1200bub	0	0.99928	0.91002	0.97755
	6	0.99963	0.98933	0.99423
	12	0.99975	0.98654	0.99791
	24	0.99970	0.99079	0.99659
	48	0.99963	0.98896	0.99283

Assumption #2- Octahedral and tetrahedral Fe^{3+}				
Sample	HT time (hr)	R^2 of fit- Assumption #2 (oct+tetra Fe^{3+})		
		5000-35000 cm^{-1}	7000-12000cm^{-1}	18500-24500 cm^{-1}
325Fe(III)1200bub	0	0.99970	0.99749	0.99998
	6	0.99978	0.99866	0.99998
	12	0.99981	0.99889	0.99998
	24	0.99979	0.99866	0.99998
	48	0.99985	0.99910	0.99998
325FPP1200bub	0	0.99930	0.92019	0.97273
	6	0.99973	0.98817	0.99810
	12	0.99985	0.98589	0.99900
	24	0.99988	0.99112	0.99933
	48	0.99988	0.99037	0.99902

Assumption #3- Jahn-Teller Effect splitting of Fe^{2+} band				
Sample	HT time (hr)	R^2 of fit		
		5000-35000 cm^{-1}	7000-12000cm^{-1}	18500-24500 cm^{-1}
325Fe(III)1200bub	0	0.99987	0.99954	0.99998
	6	0.99989	0.99950	0.99999
	12	0.99991	0.99972	0.99999
	24	0.99992	0.99970	0.99999
	48	0.99993	0.99963	0.99999
325FPP1200bub	0	0.99966	0.96404	0.98488
	6	0.99992	0.99344	0.99976
	12	0.99991	0.98887	0.99970
	24	0.99994	0.99494	0.99928
	48	0.99992	0.99795	0.99800

The difference in absorption band positions between the series ranges from 50 cm^{-1} to 735 cm^{-1}, which corresponds to energy differences of 0.006 – 0.091 eV for equivalent transitions. The absorption band positions associated with Fe^{2+} (1130 – 1154 nm) and the highest energy octahedral Fe^{3+} transition (418 – 425 nm) are in close agreement to those reported in literature, although the deconvoluted positions for the second and third octahedral Fe^{3+} bands (488 – 506 nm, 697 – 699 nm) occur at higher energies than previously reported. (See the beginning of Section 7.3.6 for reported positions and references)

R^2 values over the full spectra for both glasses are all greater than 0.999, but R^2 values for the shoulder (7000 – 12000 cm^{-1}) and main absorption peak (18500 – 24500 cm^{-1}) show a less accurate fit. In particular, the main absorption peak for the 325Fe(III)1200bub glass series exhibits the lowest R^2 values, and the main features of the spectra for both pre-heat treated glasses are not fit as well as any of the heat treated samples.

Figure 7.15 shows the relationship between peak heights and peak areas with Fe^{2+} content of the glasses. Linearity is seen in the relationships for most peaks within each glass series, but peak heights for the ~20000 cm^{-1} and ~14300 cm^{-1} octahedral Fe^{3+} peaks have the best correlation between both series as predictors of the iron redox ratio within the glass.

Figure 7.16 shows the fractions of total peak height and peak area associated with the Fe^{2+} absorption feature. Both plots appear to show two regions of linearity with a change in slope near 14 – 15% Fe^{2+}.

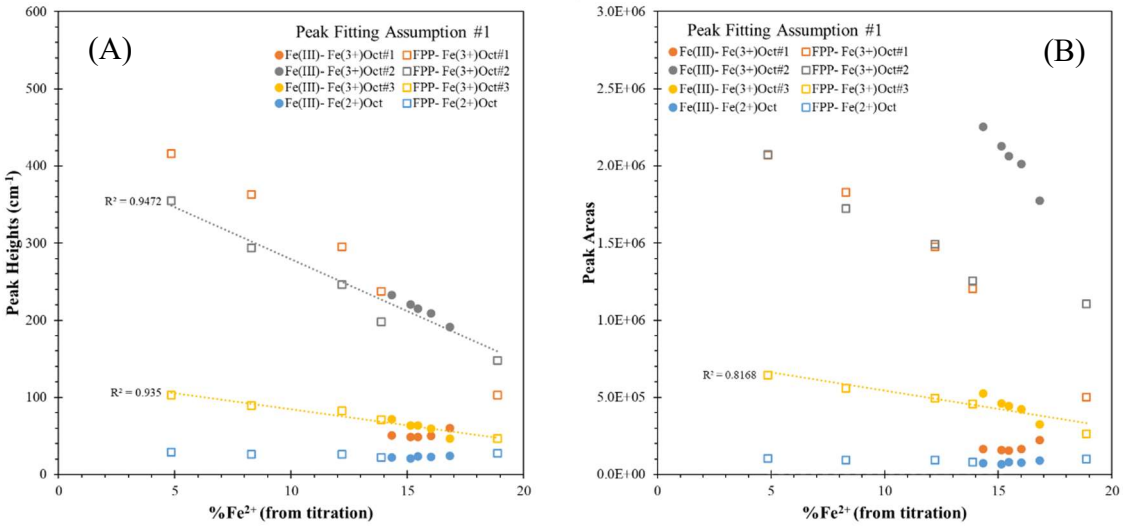

Figure 7.15. (A) Peak heights and (B) peak areas versus ferrous iron content for fitting Assumption #1.

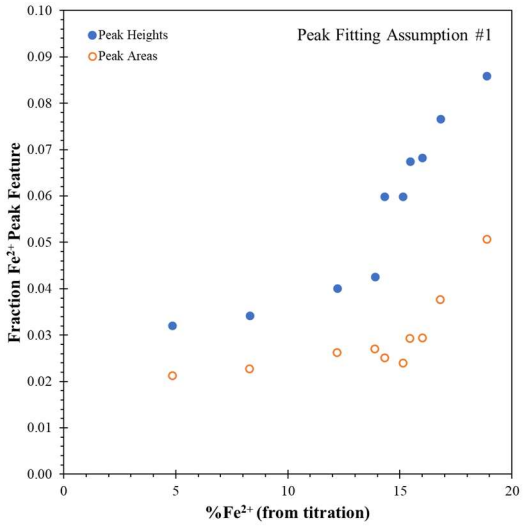

Figure 7.16. Proportion of total peak height and peak area associated with the Fe^{2+} absorption feature as a function of ferrous iron content.

7.3.6.2. Assumption #2: Octahedral and tetrahedral Fe^{3+}. Figure 7.17 and Figure 7.18 show spectra deconvolution assuming the presence of both octahedral and tetrahedral Fe^{3+} and six total absorption peaks. Fitting parameters are given in Table 7.7.

The addition of tetrahedral Fe^{3+} absorption bands does not significantly increase the R^2 value for the 325FPP1200bub peak fitting, but it does considerably improve the R^2 values of the shoulder and main absorption peak of the 325Fe(III)1200bub spectra. Results indicate a larger proportion of tetrahedral Fe^{3+} in 325Fe(III)1200bub than 325FPP1200bub. Including tetrahedral Fe^{3+} absorption bands to both spectra improve the agreement in absorption band position between the two series, with differences for equivalent transitions ranging from 95 – 379 cm^{-1}, corresponding to energy differences between 0.012 – 0.047 eV.

Table 7.7. Peak fitting parameters for Assumption #2 and six absorption bands.

Sample	HT time (hr)	Peak: Fe^{3+} Octahedral#1					Peak: Fe^{3+} Octahedral#2					Peak: Fe^{3+} Octahedral#3				
		μ (cm^{-1})	λ (nm)	A (cm^{-1})	σ	Area	μ (cm^{-1})	λ (nm)	A (cm^{-1})	σ	Area	μ (cm^{-1})	λ (nm)	A (cm^{-1})	σ	Area
325Fe(III)1200bub	0	23700	422	115	1451	419482	20542	487	136	2865	979908	15275	655	82	3004	614620
	6			112	1394	390011			146	2922	1069721			102	3089	791057
	12			109	1391	381493			151	2935	1110504			105	3100	816937
	24			107	1381	371342			154	3029	1167657			104	3198	830332
	48			116	1386	401776			164	2964	1216301			118	3187	939576
325FPP1200bub	0	24079	415	110	1889	520238	20373	491	128	2553	818502	15575	642	74	2844	525156
	6			230	1968	1136924			170	2377	1013179			91	3247	741882
	12			282	1896	1340406			221	2297	1271178			104	3113	815055
	24			339	1907	1619710			264	2307	1528380			110	3256	897129
	48			383	1921	1843770			316	2327	1840979			126	3259	######

Sample	HT time (hr)	Peak: Fe^{3+} Tetrahedral#1					Peak: Fe^{3+} Tetrahedral#2				
		μ (cm^{-1})	λ (nm)	A (cm^{-1})	σ	Area	μ (cm^{-1})	λ (nm)	A (cm^{-1})	σ	Area
325Fe(III)1200bub	0	21057	475	23	1067	62235	18801	532	28	2268	156500
	6			25	1085	66852			27	2403	160480
	12			24	1110	67156			27	2536	168567
	24			25	1133	70963			27	2680	183732
	48			25	1107	70744			27	2584	177088
325FPP1200bub	0	20861	479	4	919	10186	18543	539	3	883	6107
	6			5	938	11030			11	1186	34108
	12			6	1370	21305			14	578	19752
	24			7	1449	26956			22	611	34425
	48			7	1601	29087			32	641	50663

Sample	HT time (hr)	Peak: Fe^{2+} Octahedral#1				
		μ (cm^{-1})	λ (nm)	A (cm^{-1})	σ	Area
325Fe(III)1200bub	0	8651	1156	25	1447	88919
	6			23	1328	75388
	12			23	1332	75956
	24			20	1247	63074
	48			22	1315	71718
325FPP1200bub	0	8746	1143	26	1363	89671
	6			19	1355	65912
	12			22	1349	74607
	24			21	1353	72646
	48			23	1344	78046

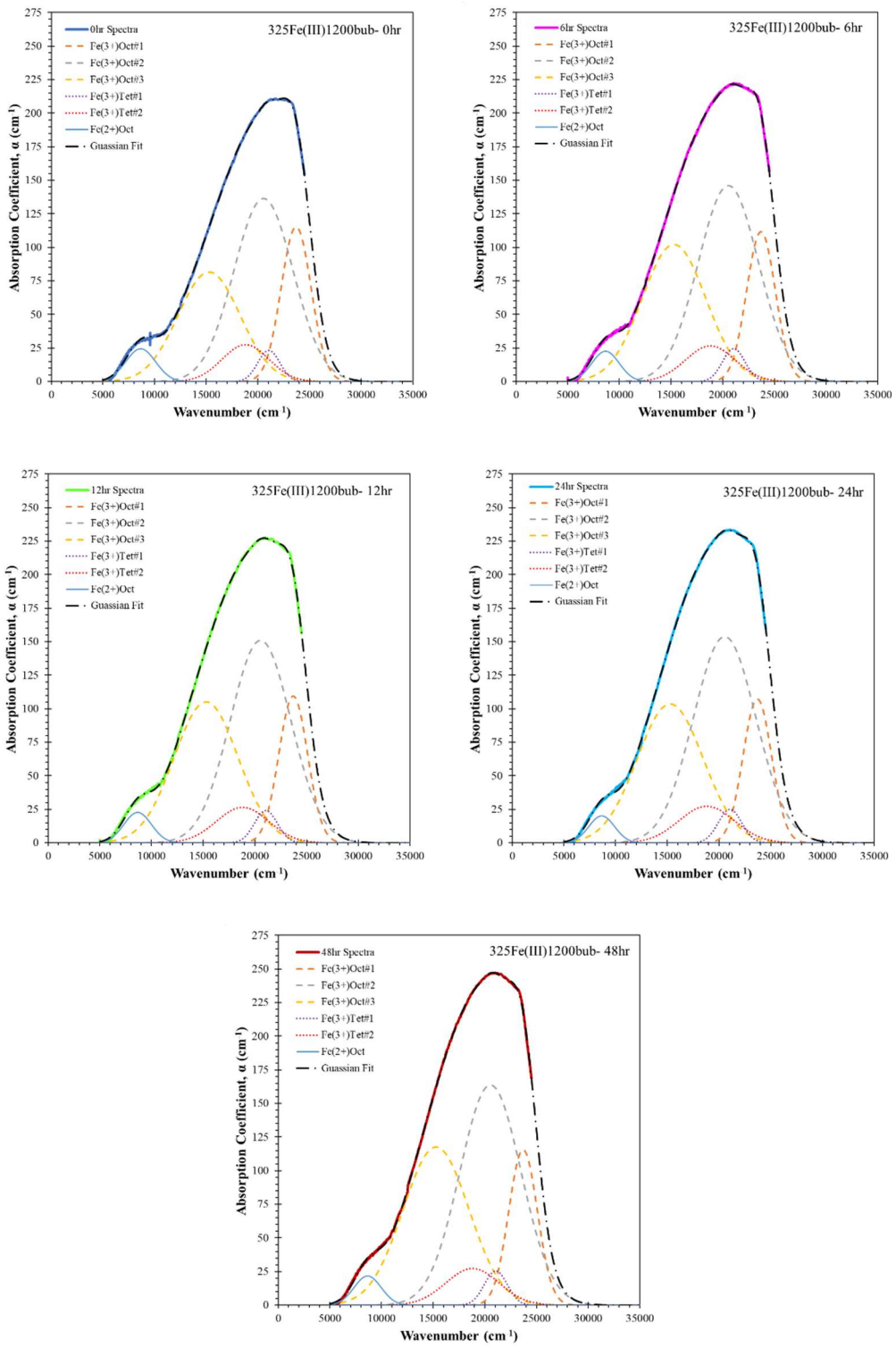

Figure 7.17. Peak deconvolutions for 325Fe(III)1200bub series assuming presence of tetrahedral Fe^{3+} and six total absorption bands.

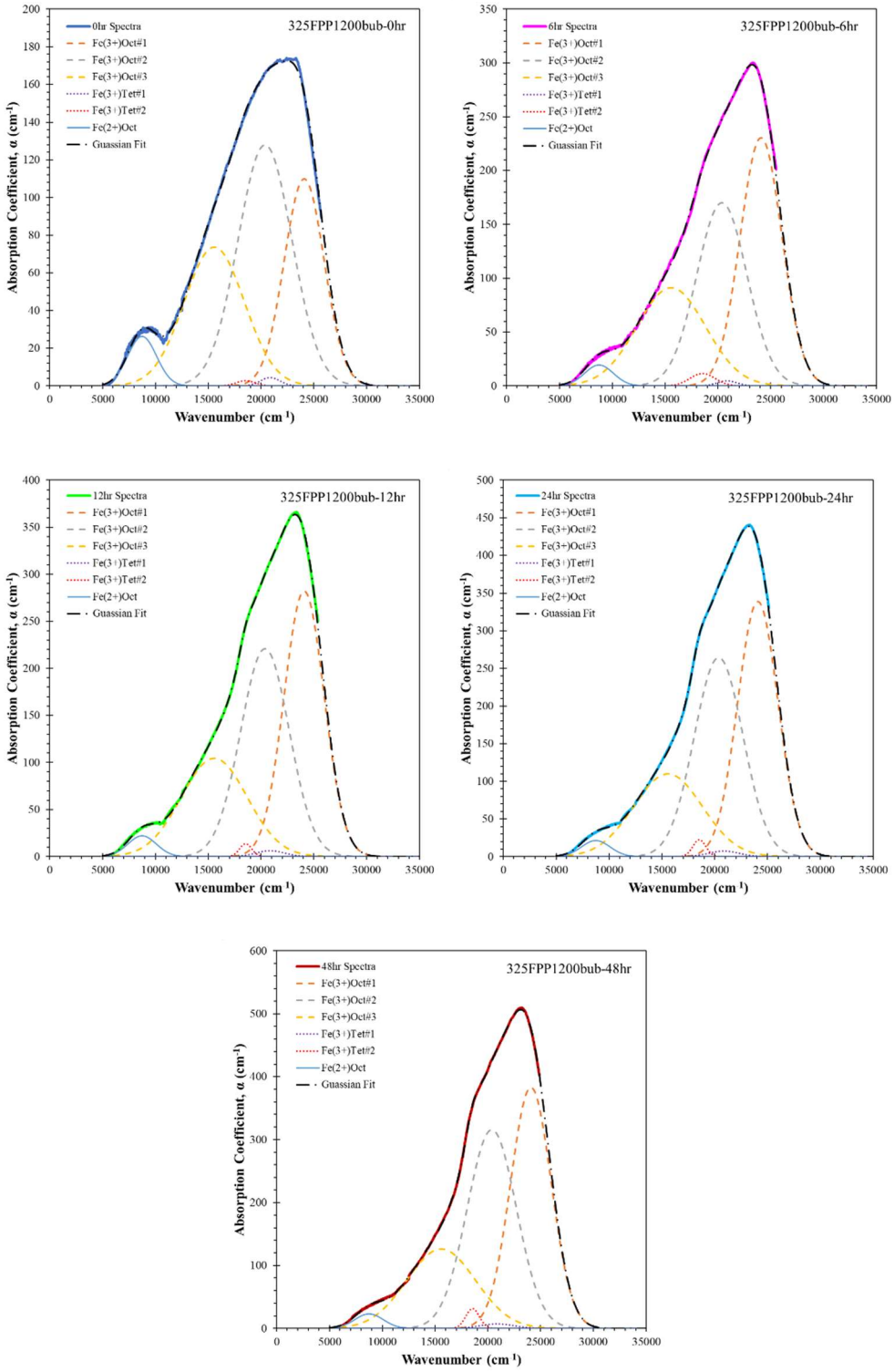

Figure 7.18. Peak deconvolutions for 325FPP1200bub series assuming presence of tetrahedral Fe^{3+} and six total absorption bands.

Similar to results of the first fitting assumption, the absorption band positions associated with Fe^{2+} (1143 – 1156 nm) and the highest energy octahedral Fe^{3+} transition (415 – 422 nm) are in close agreement to those reported in literature, although the band positions for the second and third octahedral Fe^{3+} bands (487 – 491 nm, 642 – 655 nm) occur at higher energies than previously reported (see beginning of this section). Conversely, the band positions for tetrahedral Fe^{3+} (475 – 479 nm, 532 – 539 nm) occur at slightly lower energies than those found in previous glass studies.

Figure 7.19 shows the change in peak heights and peak areas with Fe^{2+} content of the glasses. Only results from the ~20000 cm^{-1} octahedral Fe^{3+} peaks show a correlation between both series as predictors of the iron redox ratio within the glass.

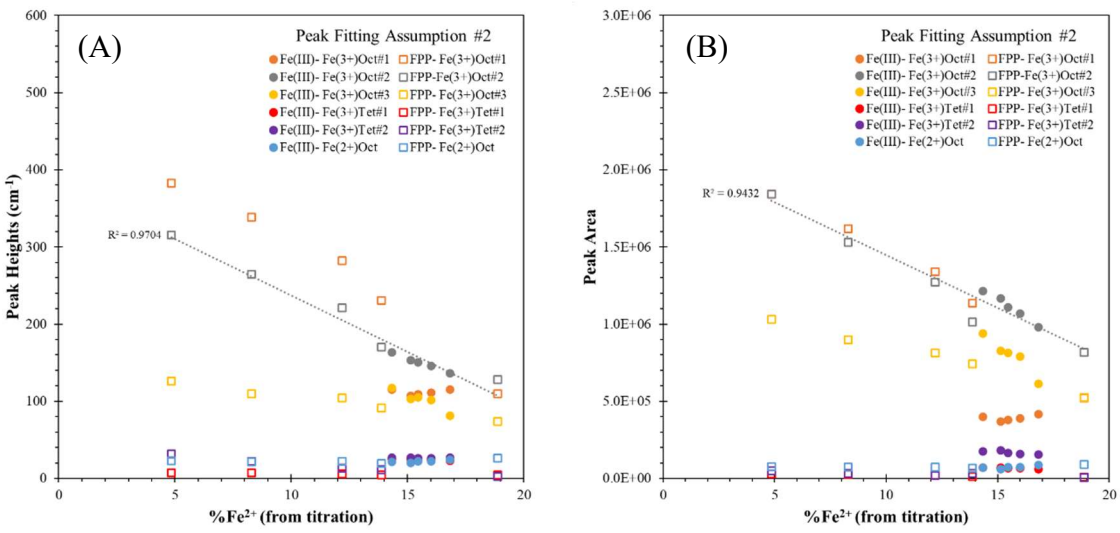

Figure 7.19. (A) Peak heights and (B) peak areas versus ferrous iron content for fitting Assumption #2.

Figure 7.20 shows the fraction of total peak height and peak area associated with the Fe^{2+} absorption feature. Both plots appear to show two regions of linearity with a change in slope near 14% Fe^{2+}, similar to the results from the first fitting assumption.

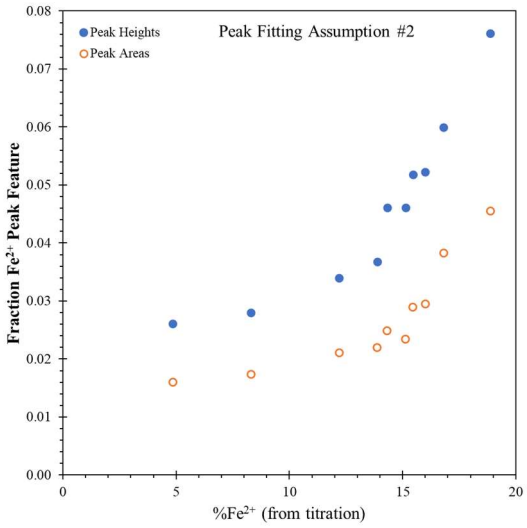

Figure 7.20. Proportion of total peak height and peak area associated with the Fe^{2+} absorption feature.

7.3.6.3. Assumption #3: Octahedral and tetrahedral Fe^{3+} and Jahn-Teller splitting of octahedral Fe^{2+} band. The final deconvolution assuming Jahn-Teller Effect splitting of the Fe^{2+} absorption band and seven total absorption peaks is shown in Figure 7.21 and Figure 7.22. Fitting parameters are given in Table 7.8.

The R^2 values of the fittings again improve, mainly in the shoulder associated with Fe^{2+} absorption. Similar discrepancies in band positions between the two series are seen as compared to the results of the second fitting assumption, with differences for equivalent transitions ranging from 85 – 350 cm^{-1}, corresponding to energies of 0.011 – 0.044 eV.

Both glass series exhibit a proportionally smaller amount of tetrahedral Fe^{3+} in this deconvolution than in the previous assumption. 325Fe(III)1200bub exhibits no detectable lower energy absorption band for tetrahedral Fe^{3+} and a small intensity higher energy band that does not change notably with heat treatment. The lower energy tetrahedral Fe^{3+} absorption band is barely detectable in the pre-heat treated sample of 325Fe(III)1200bub, and both tetrahedral bands increase slightly with heat treatment time.

Table 7.8. Peak fitting parameters for Assumption #3 and seven absorption bands.

Sample	HT time (hr)	Peak: Fe^{3+} Octahedral#1					Peak: Fe^{3+} Octahedral#2					Peak: Fe^{3+} Octahedral#3				
		μ (cm^{-1})	λ (nm)	A (cm^{-1})	σ	Area	μ (cm^{-1})	λ (nm)	A (cm^{-1})	σ	Area	μ (cm^{-1})	λ (nm)	A (cm^{-1})	σ	Area
325Fe(III)1200bub	0	23968	417	81	2384	486779	20791	481	149	3046	1137371	15747	635	88	3184	699531
	6			84	1999	419178			163	2951	1207302			113	3257	924966
	12			83	2017	417834			168	2918	1229408			119	3219	960454
	24			84	1987	416765			175	2910	1278941			122	3166	970295
	48			90	1999	450799			181	2925	1328523			134	3251	1089636
325FPP1200bub	0	24311	411	87	2326	510117	20475	488	127	2745	871579	15526	644	70	2975	518674
	6			205	2196	1127721			179	2509	1125505			89	3174	705217
	12			239	2377	1425771			206	2484	1283099			100	3224	807565
	24			291	2587	1889684			230	2521	1451971			106	3261	863672
	48			324	2597	2111936			276	2517	1743130			122	3208	984607

Sample	HT time (hr)	Peak: Fe^{3+} Tetrahedral#1					Peak: Fe^{3+} Tetrahedral#2				
		μ (cm^{-1})	λ (nm)	A (cm^{-1})	σ	Area	μ (cm^{-1})	λ (nm)	A (cm^{-1})	σ	Area
325Fe(III)1200bub	0	23396	427	16	653	26986	18367	544	0	571	0
	6			14	457	15487			0	647	0
	12			15	489	18449			0	820	0
	24			15	471	17943			0	820	0
	48			15	446	16624			0	820	0
325FPP1200bub	0	23563	424	17	783	33817	18717	534	2	437	2014
	6			17	770	32621			8	625	13155
	12			35	948	82973			17	667	27771
	24			43	970	104263			30	763	56987
	48			55	1083	149171			41	819	84968

Sample	HT time (hr)	Peak: Fe^{2+} Octahedral#1					Peak: Fe^{2+} Octahedral#2				
		μ (cm^{-1})	λ (nm)	A (cm^{-1})	σ	Area	μ (cm^{-1})	λ (nm)	A (cm^{-1})	σ	Area
325Fe(III)1200bub	0	9385	1066	18	1271	57038	7623	1312	14	914	32069
	6			18	989	45038			14	810	28916
	12			19	1057	49430			14	826	28460
	24			19	1187	57557			11	752	20358
	48			19	1202	56317			12	824	24447
325FPP1200bub	0	9243	1082	22	964	52647	7538	1327	14	790	28564
	6			18	1299	59478			7	783	13325
	12			18	939	41929			12	776	23157
	24			19	1199	56786			9	774	16960
	48			22	1266	68676			9	728	16112

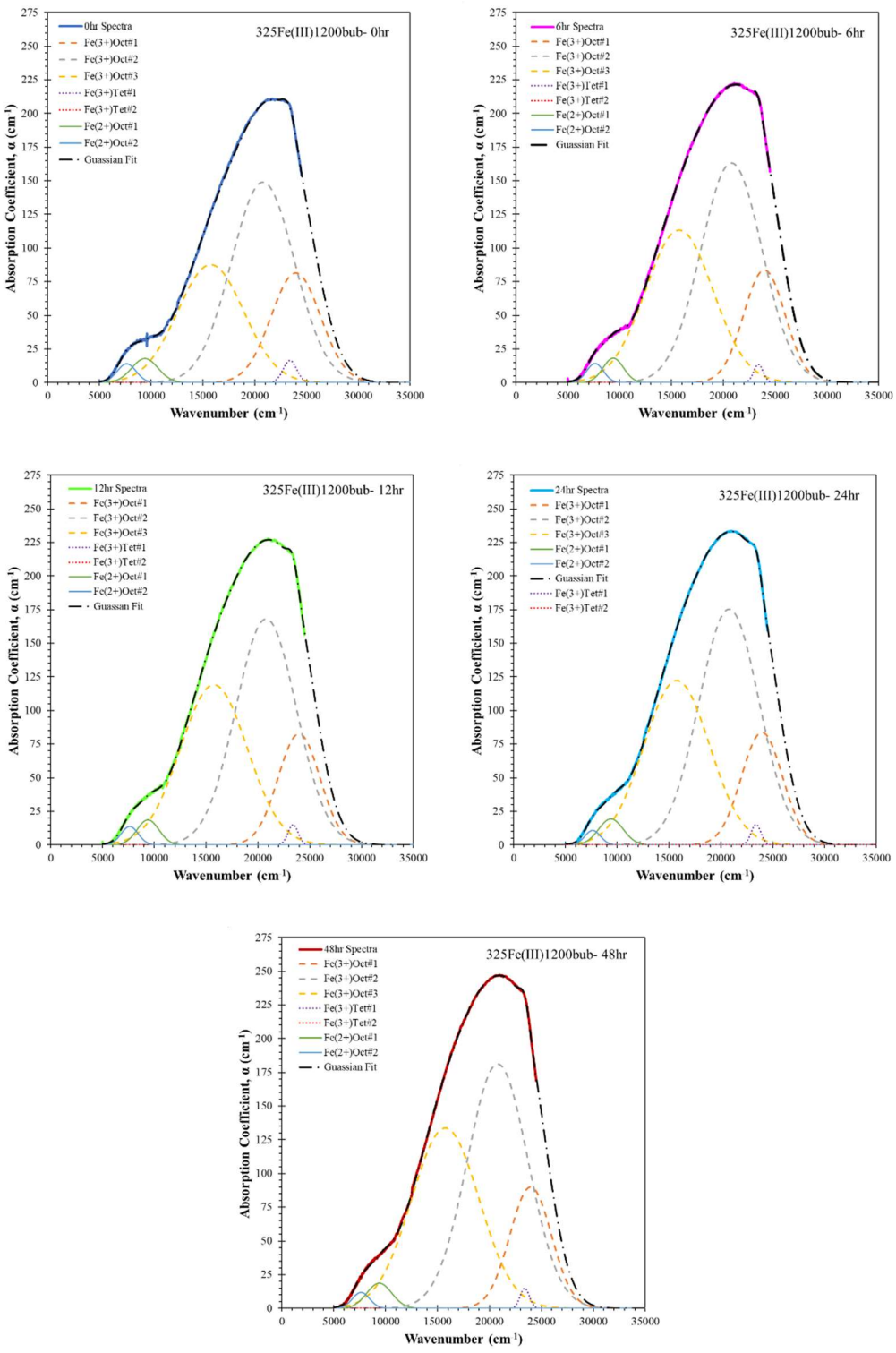

Figure 7.21. Peak deconvolutions for 325Fe(III)1200bub series assuming Jahn-Teller Effect band splitting for octahedral Fe^{2+} and seven total absorption bands.

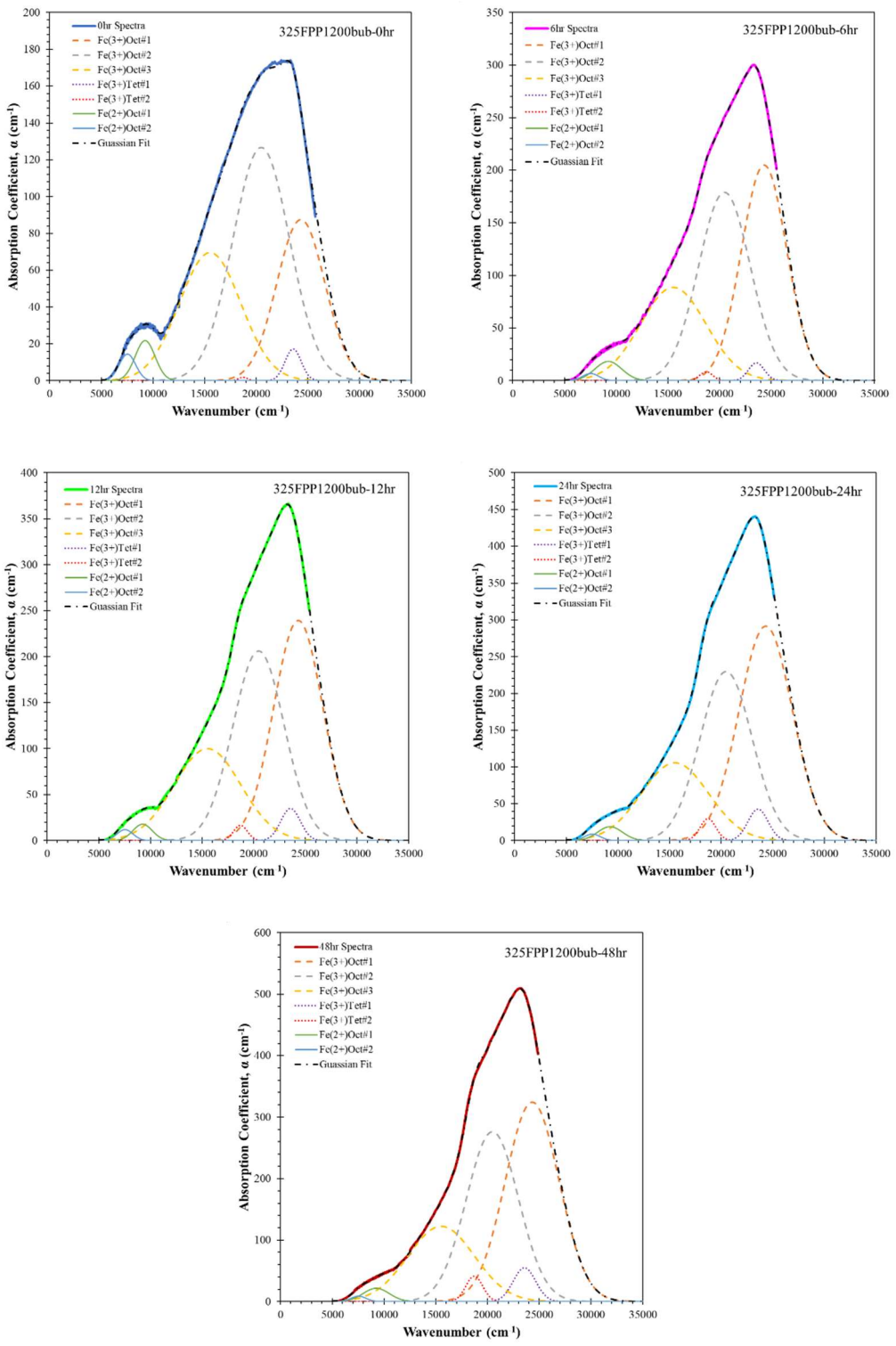

Figure 7.22. Peak deconvolutions for 325FPP1200bub series assuming Jahn-Teller Effect band splitting for octahedral Fe^{2+} and seven total absorption bands.

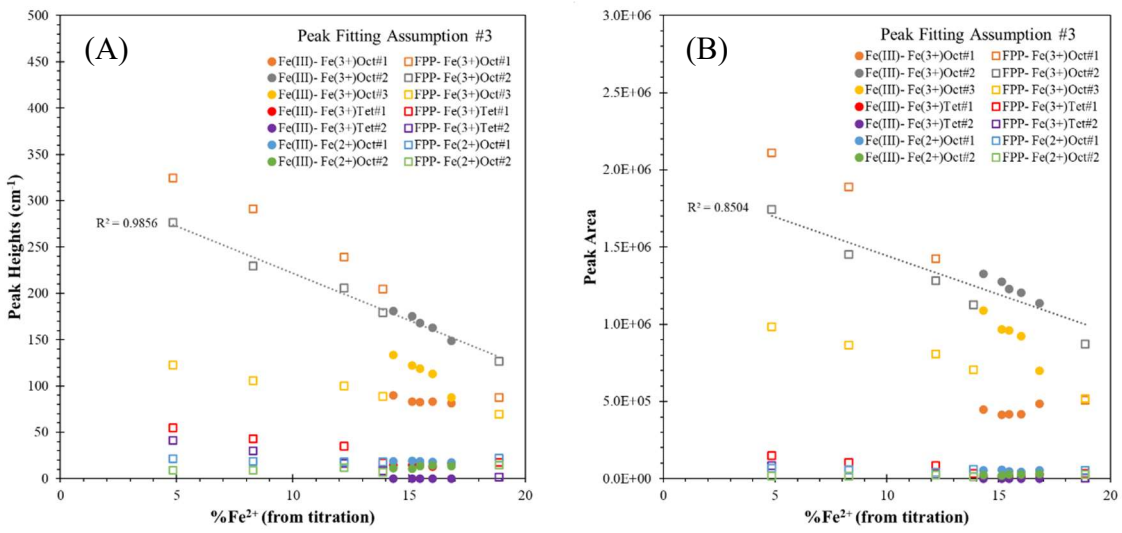

Figure 7.23. (A) Peak heights and (B) peak areas versus ferrous iron content for fitting Assumption #3.

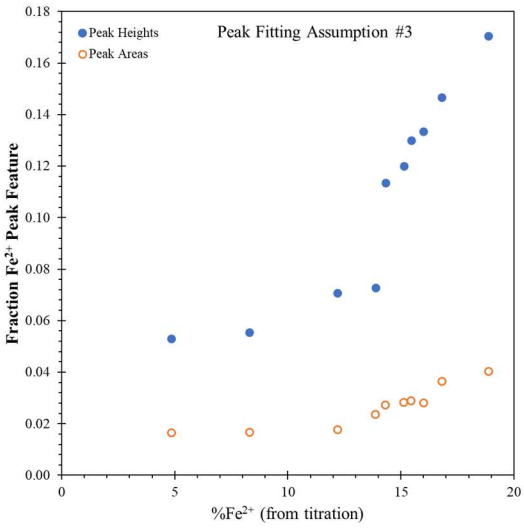

Figure 7.24. Proportion of total peak height and peak area associated with the Fe^{2+} absorption feature.

Figure 7.23 shows the change in peak heights and peak areas with Fe^{2+} content of the glasses. Only results from the ~20500 cm^{-1} octahedral Fe^{3+} peaks show a correlation between both series as predictors of the iron redox ratio within the glass. Figure 7.24

shows the fraction of total peak height and peak area associated with the Fe^{2+} absorption features. A change in slope is again seen in the same region as in the previous two fitting assumptions.

7.3.6.4. Proposed Peak Fitting Methods. Based on results of the three fittings assumptions presented above, it is proposed that all seven absorption bands must be considered to optimize deconvolution of the optical spectra of iron phosphate glasses- three bands associated with octahedral Fe^{3+} near ~24000, 20500, and 15500 cm^{-1}, two bands associated with tetrahedral Fe^{3+} near ~23500 and 18500 cm^{-1}, and two bands due to Jahn-Teller splitting associated with octahedral Fe^{2+} near ~9300 and 7500 cm^{-1}. Consideration of tetrahedral Fe^{3+} units resulted in improved fits of the main absorption peak, even for proportionally small absorption features compared to those associated with octahedral Fe^{3+}. Consideration of tetrahedral Fe^{3+} also resulted in closer band positions for equivalent transitions between the two series. Inclusion of band splitting for octahedral Fe^{2+} resulted in improved fits of the absorption shoulder associated with ferrous iron and decreased the presumed proportion of tetrahedral Fe^{3+}, supporting other research which suggests mainly octahedral coordination.

The absorption fitting parameter with the highest correlation to iron redox ratio is the peak height of the octahedral Fe^{3+} corresponding to the $^6A_{1g}(S) \rightarrow {}^4E_g(G) + {}^4A_{1g}(G)$ transition, which occurs near ~20500 cm^{-1}. An empirical relationship as seen in Equation 7.8 can be derived from the linear fit,

$$\%Fe^{2+} = 31.87 - \frac{A_{Fe(3+)Oct\#2}}{10.14} \qquad \text{(Equation 7.8)}$$

where $A_{Fe(3+)Oct\#2}$ is the deconvoluted peak height of the second octahedral Fe^{3+} absorption band (near ~20500 cm^{-1}) expressed as absorption coefficient in units of cm^{-1}.

7.4. SUMMARY

Titration, thermal and optical analysis results confirm that the iron redox ratio, and thus the properties and crystallization behavior of iron phosphate glasses, can be altered not just via composition and melt conditions but also via post-melt heat treatments at temperatures as low as the glass transition range. Temperatures even 7°C below T_g may result in slower oxidation of Fe^{2+} to Fe^{3+} than temperatures at or just above T_g.

Longer heat treatment times result in increased oxidation of Fe^{2+} to Fe^{3+}, which result in higher glass transition and crystallization temperatures. Depolymerization of the structure and increase in bond strength with increased oxidation result in decreases in optical band gap energy. Urbach energy increases with heat treatment time and increasing Fe^{3+}, which could be due to decreases in distortion upon structural relaxation with heat treatment or could be indicative of higher symmetry environments associated with Fe^{3+} as opposed to Fe^{2+}.

Deconvolution of absorption spectra proved very complex with many variables which could alter resulting peak positions and intensities. For this reason, using absorption coefficient of the non-deconvoluted spectra may provide the easiest method for assessing iron redox ratio from absorption spectra. Current results suggest absorption near ~21008 cm^{-1} has the highest correlation with ferrous iron proportion.

Deconvolution of spectra can, however, provide qualitative information concerning iron redox ratios, coordination environments, and structural distortions. Future work to further the experimental data and understanding in this area is needed.

7.5. FUTURE WORK

Preliminary studies suggest UV-vis spectroscopy may be a useful way to investigate structural and valence state changes in iron phosphate glasses and much can be learned from additional studies. Availability and ease of use of UV-vis spectroscopy make it a desirable tool for such research.

A wider compositional range with multiple Fe/P and O/P ratios can be prepared to further establish iron absorption band positions. Concurrent structural studies to verify coordination environments and investigate bond lengths and distortions could allow for determination of quantitative relationships between structure and deconvoluted peak heights and areas. Further studies in different melting atmospheres and at different melting temperatures could verify whether iron oxidation at temperatures near the glass transition are diffusion dependent or due to structural accommodations [268], [270] and would allow for calculations of diffusion coefficients. Focusing on glass bubbles of composition $40Fe_2O_3$-$60P_2O_5$ could be useful because the pyrophosphate composition is the most widely studied and reported on, so more data is currently available on structure and coordination environments for this glass composition.

8. CONCLUSIONS AND AFTERWORDS

8.1. AFTERTHOUGHTS

Investigation of phosphate glasses requires an understanding of many essential elements that make up the foundations of our knowledge of glass science. Phosphoric oxide is a primary glassformer, obeying Zachariasan's structural rules for glass formation and exhibiting electronegativity and bond strengths that safely fall within criteria established for glass formers. A wide range of phosphate structures readily form glasses. Phosphate glass structures range from invert glasses, with isolated phosphate tetrahedron linked via ionic bonds with non-phosphate cations, to interconnected networks, with covalent bonding between adjacent phosphate tetrahedra. The existence of phosphate anion chains results in polymeric structures with properties that balance both short-range bonding characteristics and the intermediate range order of phosphate chains and rings, which influence the kinetics of viscosity and crystallization. Understanding processing conditions are also of utmost importance due to the often hygroscopic and volatile nature of phosphate compositions. Phosphates, in a sense, require the "total package" of glass know-how.

An extensive variety of oxides are soluble in phosphates, the identity and concentration of which can dramatically change the properties of the resultant glass. Iron phosphate glasses are a particularly interesting family of glasses in that they retain desirable properties common to phosphates, such as low processing temperatures and high oxide solubilities, yet exhibit uncharacteristically high chemical durability, which is often the primary limitation of phosphate glasses in practical uses.

Much of the research presented in this dissertation includes novel approaches to understand the behavior and properties of iron phosphate glasses. Lack of crystal phase diagrams and thermochemical data for phosphate compounds have limited the use of property models that rely on free energy and enthalpy data for oxide or constitutional phases to predict behavior. The models proposed here use a statistical representation of the glass structure based on Q-units and cation bonds. Bonding characteristics are largely based on calculated phosphate group basicities and microscopic basicities of non-bridging oxygens. Optical basicity is directly related to electronegativity, which connects back to some of the original, fundamental theories of glass formation and bonding. While the concept of optical basicity has been considered in much research in the 50 years since it was first proposed, to the author's knowledge, it has not yet been applied in the ways that it has in this work. Conclusions from the research reported in this dissertation, as well as recommendations for future work, are summarized below.

8.2. CONCLUSIONS AND FUTURE WORK: PREPARATION AND CHARACTERIZATION OF IRON PHOSPHATE GLASSES

Characterization of the iron phosphate glasses herein suggests titration as a more reproducible method for determination of iron valence state than Mössbauer. Expected trends of increasing ferrous iron content with increasing melt temperature were observed, although variation in the melt environment yielded unexpectedly similar iron redox ratios despite differences in environmental oxygen concentrations. Use of different batch materials did not seem to affect the final iron redox ratio when the raw materials consisted of equivalent iron valence states. However, using mixed-valency raw materials did result in higher ferrous contents than using ferric-only raw materials.

Future work is recommended regarding the effect of melt environment and raw materials on iron redox ratios in phosphate glasses. A series of glasses can be melted under environments with different oxygen availability (ie. bubbling an inert gas, bubbling oxygen, melting in a closed system with flowing gas, sealed in an ampoule, etc) for extended lengths of time to see if the melts will eventually reach the partition equilibrium of oxygen. Oxygen diffusivity in the melt can also be studied to determine what factors may inhibit the melt from reaching equilibrium with the surrounding environment.

The effect of batch iron valency can be investigated by forming a series of melts with the same Fe/P ratio but different batched Fe^{2+}/Fe^{3+} ratios. Batches should be held at melt temperatures for increasing lengths of time to determine whether the same equilibrium redox ratio will eventually be reached. Viscosity measurements can be made to determine if disparities in melt viscosities caused by differences in raw materials may be affecting the final redox ratio. Measuring the water content in the glass could also provide insight into potential causes for the observed differences, as water in the atmosphere or raw materials may be affecting melt viscosity.

8.3. CONCLUSIONS AND FUTURE WORK: THERMODYNAMIC MODEL

The thermodynamic model developed here for the iron redox equilibrium in the melt shows great promise for being able to qualitatively and potentially quantitatively describe the melt equilibrium. A new method for calculating heats of formation of phosphate Q-groups based on group basicity is proposed and shows remarkable correlation with available data for equivalent crystalline compounds. When these enthalpy calculations are used in the proposed model for redox-structure equilibrium,

resulting calculations for entropy of reaction follow expected trends. Structural entropy changes are shown to be proportional to 1/T and ΔH_{str}, and follow expected trends with chain length and melt basicity. Large disparity between experimentally determined iron redox ratios for glasses with similar compositions and melting conditions complicates efforts to optimize the fitting parameters of the model, in addition to inconsistencies concerning the effect of melt atmosphere on iron redox ratio. One unexpected take away is the potential importance of melt viscosity on equilibrium redox ratio. Viscosity changes alone seem to affect the final redox ratio, and it is not immediately clear if the cause of this effect is attributed to changes in the entropy of the structural reaction or changes in the oxygen fugacity within the melt.

In order to apply this model and use it for its intended purpose to calculate the iron redox ratio based solely on glass composition and melt conditions, future work is required to determine the most accurate way to model the entropy of the structural reaction. Current research related to configurational entropy of glass-forming melts indicate that a computational approach may be necessary, although simpler calculations to describe changes within specific glass systems may be possible based on properties of glass subsystems, such as chain lengths and bulk basicity. Additional work to further our understanding of effects of melting atmosphere and batch materials is also recommended, as current research yields unexpected discrepancies in iron redox ratios for nearly equivalent experimental conditions.

8.4. CONCLUSIONS AND FUTURE WORK: DISSOLUTION MODEL

The aqueous dissolution model presented here also relies on compositional and basicity information to approximate free energies of reaction. In this case, the free energy of hydration was calculated based on a sum of bond hydration energies. Bond hydration energies were determined using a statistical representation of glass structure, similar to that proposed in the thermodynamic redox model. The overall hydration energy is taken as a sum of the energies associated with the dissociation of the cation – non-bridging oxygen bond and the bonding of hydrogen to the non-bridging oxygen. This model uses microscopic basicity, distribution of Q-units and cation bonds, as well as bond energy calculations based on oxide basicity values. Considering that this is the initial attempt at such a model, as well as the only dissolution model to the author's knowledge that does not rely on thermochemical data, the results were promising in their ability to predict trends in experimental dissolution data for glasses with O-to-P ratios ranging from 2.67 – 3.75 and a large selection of monovalent, divalent, and trivalent cations. However, many issues need to be addressed to improve model predictions.

The current model does not account for the effect of chelating structures, as the increase in valency of cations will reduce the dissolution in ways that cannot be described by basicity alone. The model also cannot account for the decrease in dissolution rate caused by increasing size of divalent cations that fill interstices and block the diffusion of water. Future work is needed to incorporate these potentially additive terms, and are likely to include factors regarding the concentration, size and valency of modifier additions. The optimized model should be applied to iron phosphate glass systems to

determine whether it can accurately predict changes in dissolution behavior with the addition of oxides commonly found in HLW.

8.5. CONCLUSIONS AND FUTURE WORK: CRYSTALLIZATION AND STABILITY STUDIES

Extensive thermal analysis of iron phosphate glasses was performed to assess the effects of composition, particle size, and atmosphere on crystallization behavior and glass stability. Stability against devitrification is greater in air than nitrogen, and increases with increasing particle size and heating rates. Results revealed unexpected thermal stability for glasses in the polyphosphate compositional range, as well as unexpected differences in crystallization behavior between the two polyphosphate glasses investigated. The two glasses have strikingly similar compositions but were prepared from different raw materials. Iron phosphate glasses are known to undergo disproportionation reactions. The polyphosphate composition studied here has an average chain length of ~4, but could potentially consist of a large distribution of chain lengths. The differences in crystallization behavior of the two polyphosphate glasses is potentially due to differences in the intermediate range order of the glasses. While the 325Fe(III) glass was investigated at length in this study, limited work was done on the 325FPP series. Future work can include identification of the predominant crystalline phases formed in the 325FPP series, as well as structural studies on both glass series to determine if chain or ring distributions could be the cause of disparity.

In addition, many other aspects of crystallization behavior could be studied which were not included here, such as critical cooling rates (which could be used to compare the glass forming ability to the measured glass stability) and crystal growth rates. Optical

microscopy suggests that growth rates may be easily measured using growth lines from isothermal experiments.

8.6. CONCLUSIONS AND FUTURE WORK: IRON REDOX MEASUREMENTS VIA UV-VIS SPECTROSCOPY

This was the first research to investigate the optical absorption spectra of iron in iron phosphate glasses using UV-vis spectroscopy, made possible by the formation of ultra-thin glass "bubbles". TGA/DTA results from the crystallization portion of this dissertation show that ferrous iron on the glass surface will begin to oxidize at temperatures as low as T_g on sufficiently small particles. These results were supported by titration results showing decreases in ferrous iron with heat treatment time near T_g, as well as the increase in UV-vis absorption due to ferric iron. A methods analysis determined high correlation between the absorption coefficient near ~21008 cm^{-1} and the ferrous iron concentration, and the value can be used to determine the iron redox ratio. Deconvolution of the absorption spectra provided additional information concerning coordination environments and structural distortions.

The availability and ease of use of UV-vis spectroscopy makes the analysis method presented here extremely valuable. Future work to substantiate the results of this study will allow for application of this analysis method to other research and potentially other dark, iron-containing glasses that are generally considered opaque in the UV-vis range. A wider compositional range of glasses can be prepared with concurrent structural studies to verify iron absorption band positions and establish quantitative relationships between spectra and structural features, such as coordination environments. It is not clear whether iron oxidation at temperatures near the glass transition are diffusion dependent or

due to structural accommodations, and additional studies of post-melt heat treatments in different melting atmospheres and at different melting temperatures could be used to calculate diffusion coefficients and determine the primary cause for oxidation.

APPENDIX A.

ENTHALPY AND ENTROPY CALCULATIONS FOR GIBBS FREE ENERGY OF REACTION

Table A.1 shows the data used in calculations to determine the standard Gibbs free energy change for Equation 4.3, as taken from Ottonello et al. [226]. Equations A.1 – A.6 show calculations for standard state enthalpies for each component and change in enthalpy for Equation 4.3, while Equations A.7 – A.12 show similar calculations for entropy.

Table A.1. Thermochemical data used to calculate the Gibbs free energy change for the redox reaction in Equation 4.3.

Component	T_r (K)	$H°(T_r)$ (kJ/mol)	$S°(T_r)$ (J/mol·K)	$C_p(T)$ (J/mol·K)	T_{range} (K)	Reference
$Fe^{3+}_{(melt)}$	1000	-45.735	46.226	58.655	1000-2000	Ottonello et al
$Fe^{2+}_{(melt)}$	1000	-17.000	85.902	42.371	1000-2000	Ottonello et al
$O^{2-}_{(melt)}$	1000	-177.468	63.636	41.197	1000-2000	Ottonello et al
$O_{2\ (gas)}$	298.15	0	205.040	$29.957+0.004184\cdot T-167360\cdot T^{-2}$	298-3000	Ottonello et al (from Barin and Knacke; Barin et al)

$$H^o_{Fe^{3+}_{(melt)}}(T) = -45735 + \int_{1000}^{T} 58.655dT$$

$$\therefore H^o_{Fe^{3+}_{(melt)}}(T) = -104390 + 58.655T \text{ (J/mol)} \qquad \text{(Equation A.1)}$$

$$H^o_{Fe^{2+}_{(melt)}}(T) = -17000 + \int_{1000}^{T} 42.371dT$$

$$\therefore H^o_{Fe^{2+}_{(melt)}}(T) = -59371 + 42.371T \text{ (J/mol)} \qquad \text{(Equation A.2)}$$

$$H^o_{O^{2-}_{(melt)}}(T) = -177468 + \int_{1000}^{T} 41.197dT$$

$$\therefore H^o_{O^{2-}_{(melt)}}(T) = -218665 + 41.197T \text{ (J/mol)} \qquad \text{(Equation A.3)}$$

$$H^o_{O_{2(gas)}}(T) = \int_{298.15}^{T} (29.957 + 0.004184T - 167360T^{-2})dT$$

$$\therefore H^o_{O_{2(gas)}}(T) = -9679 + 29.957T + 0.002092T^2 + 167360T^{-1} \text{ (J/mol)}$$

(Equation A.4)

$$\Delta H^o_{rdx} = 2H^o_{Fe^{2+}{}_{(melt)}} + \frac{1}{2}H^o_{O_{2(gas)}} - 2H^o_{Fe^{3+}{}_{(melt)}} - H^o_{O^{2-}{}_{(melt)}}$$

$$\therefore \Delta H^o_{rdx} = 303860 - 58.79T + 0.001046T^2 + 83680T^{-1} \text{ (J/mol)} \text{ (Equation A.5)}$$

$$\Delta H^o_{rdx(net)} = 2H^o_{Fe^{2+}{}_{(melt)}} + \frac{1}{2}H^o_{O_{2(gas)}} - 2H^o_{Fe^{3+}{}_{(melt)}}$$

$$\therefore \Delta H^o_{rdx(net)} = 85200 - 17.59T + 0.001046T^2 + 83680T^{-1} \text{ (J/mol)} \text{ (Equation A.6)}$$

$$S^o_{Fe^{3+}{}_{(melt)}}(T) = 46.226 + \int_{1000}^{T} \frac{58.665}{T}\,dT$$

$$\therefore S^o_{Fe^{3+}{}_{(melt)}}(T) = -359.02 + 58.665\,ln(T) \text{ (J/mol·K)} \quad \text{(Equation A.7)}$$

$$S^o_{Fe^{2+}{}_{(melt)}}(T) = 85.902 + \int_{1000}^{T} \frac{42.371}{T}\,dT$$

$$\therefore S^o_{Fe^{2+}{}_{(melt)}}(T) = -206.79 + 42.371\,ln(T) \text{ (J/mol·K)} \quad \text{(Equation A.8)}$$

$$S^o_{O^{2-}{}_{(melt)}}(T) = 63.636 + \int_{1000}^{T} \frac{41.197}{T}\,dT$$

$$\therefore S^o_{O^{2-}{}_{(melt)}}(T) = -220.943 + 41.197\,ln(T) \text{ (J/mol·K)} \quad \text{(Equation A.9)}$$

$$S^o_{O_{2(gas)}}(T) = 205.04 + \int_{298.15}^{T} \frac{29.957 + 0.004184T - 167360T^{-2}}{T}\,dT$$

$$\therefore S^o_{O_{2(gas)}}(T) = 32.168 + 29.957\,ln(T) + 0.004184T + 83680T^{-2} \text{ (J/mol·K)}$$

(Equation A.10)

$$\Delta S^o_{rdx} = 2S^o_{Fe^{2+}{}_{(melt)}} + \frac{1}{2}S^o_{O_{2(gas)}} - 2S^o_{Fe^{3+}{}_{(melt)}} - S^o_{O^{2-}{}_{(melt)}}$$

$$\therefore \Delta S^o_{rdx} = 541.0 - 58.81\,ln(T) + 0.002092T + 41840T^{-2} \text{ (J/mol·K)}$$

(Equation A.11)

$$\Delta S^o_{rdx(net)} = 2S^o_{Fe^{2+}{}_{(melt)}} + \frac{1}{2}S^o_{O_{2(gas)}} - 2S^o_{Fe^{3+}{}_{(melt)}}$$

$$\therefore \Delta S^o_{rdx(net)} = 320.0 - 17.61\,ln(T) + 0.002092T + 41840T^{-2} \text{ (Equation A.12)}$$

APPENDIX B.

IMPORTANT EQUATIONS CORRESPONDING TO DIFFERENT INITIAL BATCH CONDITIONS

Table B.1. Important equations corresponding to initial batch conditions for ferric iron phosphate and ferrous iron phosphate glasses.

Quantity	Starting batch → Final glass compositions (mol. fraction)	
	$(y)Fe_2O_3 \cdot (1-y)P_2O_5$ ↓ $\left(\frac{2x}{1+x}\right)FeO \cdot \left(\frac{y-x}{1+x}\right)Fe_2O_3 \cdot \left(\frac{1-y}{1+x}\right)P_2O_5$	$(x)FeO \cdot (1-x)P_2O_5$ ↓ $\left(\frac{x-2y}{1-y}\right)FeO \cdot \left(\frac{y}{1-y}\right)Fe_2O_3 \cdot \left(\frac{1-x}{1-y}\right)P_2O_5$
$\frac{X_{Fe^{2+}}}{X_{Fe^{3+}}}$	$\frac{x}{y-x}$	$\frac{x-2y}{2y}$
$\frac{X_{Fe^{2+}}}{\Sigma Fe}$	$\frac{x}{y}$	$\frac{x-2y}{x}$
$\frac{O}{P}$	$\frac{5-2y-x}{2(1-y)}$	$\frac{5+y-4x}{2(1-x)}$
X_{BO}	$\frac{3-6y+x}{5-2y-x}$	$\frac{3-y-4x}{5+y-4x}$
X_{NBO}	$\frac{2(1+2y-x)}{5-2y-x}$	$\frac{2(1+y)}{5+y-4x}$
$\frac{X_{BO}}{X_{NBO}^2}$	$\frac{(3-6y+x)(5-2y-x)}{4(1+2y-x)^2}$	$\frac{(3-y-4x)(5+y-4x)}{4(1+y)^2}$
Λ_{bulk}	$\frac{1.0(2x)+0.77*3(y-x)+0.4*5(1-y)}{5-2y-x}$	$\frac{1.0(x-2y)+0.77*3(y)+0.4*5(1-x)}{5+y-4x}$

Table B.2. Important equations corresponding to initial batch conditions for mixed valency iron phosphate glasses.

Quantity	Starting batch → Final glass compositions (mol. fraction)	
	$(x)FeO \cdot (y)Fe_2O_3 \cdot (1-x-y)P_2O_5$ $\downarrow$ $\left(\frac{x+2n}{1+n}\right)FeO \cdot \left(\frac{y-n}{1+n}\right)Fe_2O_3 \cdot \left(\frac{1-x-y}{1+n}\right)P_2O_5$	$(y)Fe_3O_4 \cdot (1-y)P_2O_5$ $\downarrow$ $\left(\frac{y+2x}{1+y+x}\right)FeO \cdot \left(\frac{y-x}{1+y+x}\right)Fe_2O_3 \cdot \left(\frac{1-y}{1+y+x}\right)P_2O_5$
$\frac{X_{Fe^{2+}}}{X_{Fe^{3+}}}$	$\frac{x+2n}{2(y-n)}$	$\frac{y+2x}{2(y-x)}$
$\frac{X_{Fe^{2+}}}{\Sigma Fe}$	$\frac{x+2n}{2y+x}$	$\frac{y+2x}{3y}$
$\frac{O}{P}$	$\frac{5-2y-4x-n}{2(1-y-x)}$	$\frac{5-y-x}{2(1-y)}$
X_{BO}	$\frac{3-6y-4x+n}{5-2y-4x-n}$	$\frac{3-7y+x}{5-y-x}$
X_{NBO}	$\frac{2+4y-2n}{5-2y-4x-n}$	$\frac{2+6y-2x}{5-y-x}$
$\frac{X_{BO}}{X_{NBO}^2}$	$\frac{(3-6y-4x+n)(5-2y-4x-n)}{(2+4y-2n)^2}$	$\frac{(3-7y+x)(5-y-x)}{(2+6y-2x)^2}$
Λ_{bulk}	$\frac{1.0(x+2n)+0.77*3(y-n)+0.4*5(1-y-x)}{5-2y-4x-n}$	$\frac{1.0(y+2x)+0.77*3(y-x)+0.4*5(1-y)}{5-y-x}$

APPENDIX C.

LITERATURE IRON REDOX RATIO DATA AND CONDITIONS

Table C.1. Summary of iron redox ratios in iron phosphate glass with melt conditions.

Batch Composition (mol%)	Raw Materials	Melt Temperature (°C)	Melt Time (hr)	Melt Atmosphere	pO_2 (atm)	$\%Fe^{2+}$	Analysis Technique	Reference
$0.25Fe_2O_3 \cdot 0.75P_2O_5$	Fe_2O_3, $NH_4H_2PO_4$	1250 1300 1350	2	Air	0.21	32 35 36	Titration	Schmitt (this work)
$0.33Fe_2O_3 \cdot 0.67P_2O_5$	Fe_2O_3, $NH_4H_2PO_4$	1200 1250 1300 1350	2	Air	0.21	17 19 24 35		
$0.40Fe_2O_3 \cdot 0.60P_2O_5$	Fe_2O_3, $NH_4H_2PO_4$	1200 1250 1300 1350 1400	2	Air	0.21	25 31 32 38 44		
$0.237Fe_3O_4 \cdot 0.763P_2O_5$	Fe_3O_4, $NH_4H_2PO_4$	1200 1250 1300 1350	2	Air	0.21	21 32 37 39		
$0.293Fe_3O_4 \cdot 0.707P_2O_5$	Fe_3O_4, $NH_4H_2PO_4$	1200 1350	2	Air	0.21	29 49		
$0.318Fe_3O_4 \cdot 0.682P_2O_5$	Fe_3O_4, $NH_4H_2PO_4$	1200 1350	2	Air	0.21	14 32		
$0.40Fe_2O_3 \cdot 0.60P_2O_5$	Fe_2O_3, P_2O_5	1150 1200 1250 1300 1350 1400 1450	1	Air	0.21	17 19 29 35 42 50 57	Mössbauer	Ray (1999)
$0.40Fe_2O_3 \cdot 0.60P_2O_5$	Fe_2O_3, $NH_4H_2PO_4$	1150	3	Air	0.21	13	Mössbauer	Bingham (2006)
$0.40Fe_2O_3 \cdot 0.60P_2O_5$	Fe_2O_3, $NH_4H_2PO_4$	1150 1200 1250	1	Air	0.21	15 18 25	Mössbauer	Ghussn
$0.40Fe_2O_3 \cdot 0.60P_2O_5$	Fe_2O_3, P_2O_5	1150 1200 1350 1450	1 – 2	Air	0.21	18 20 48 59	Mössbauer	Karabulut (2002)
$0.40Fe_2O_3 \cdot 0.60P_2O_5$	Fe_2O_3, $NH_4H_2PO_4$	1200	1 – 2	Flowing Ar	10^{-6*}	80		
$0.29Fe_2O_3 \cdot 0.71P_2O_5$	Fe_2O_3, P_2O_5	1250 1450	NA	Air	0.21	27 51	Mössbauer	Griscom (1998)
$0.40Fe_2O_3 \cdot 0.60P_2O_5$	Fe_2O_3, P_2O_5	1100 1450	NA	Air	0.21	19 57		
		1200	NA	Bubbled O_2	1	21		
$0.40Fe_2O_3 \cdot 0.60P_2O_5$	Fe_2O_3, P_2O_5	1200	2	Air	0.21	19	Mössbauer	Marasinghe (1997)
$0.31Fe_3O_4 \cdot 0.69P_2O_5$	Fe_3O_4, P_2O_5					24		
$0.24Fe_2O_3 \cdot 0.24FeO \cdot 0.60P_2O_5$	Fe_2O_3, FeO, P_2O_5					34		
$0.40Fe_2O_3 \cdot 0.60P_2O_5$	Fe_2O_3, P_2O_5			Nitrogen	10^{-3*}	22		
				Oxygen	1	21		

Table C.1. Summary of iron redox ratios in iron phosphate glass with melt conditions. (continued)

Batch Composition (mol%)	Raw Materials	Melt Temperature (°C)	Melt Time (hr)	Melt Atmosphere	pO_2 (atm)	$\%Fe^{2+}$	Analysis Technique	Reference
$0.05FeO{\cdot}0.95P_2O_5$	FeO, P_2O_5	1100	1	Sealed in ampoule (dry box + vacuum)	$1.6x10^{-7*}$	85	Mössbauer	Karabulut (2003)
$0.10FeO{\cdot}0.90P_2O_5$						85		
$0.15FeO{\cdot}0.85P_2O_5$						87		
$0.20FeO{\cdot}0.80P_2O_5$						82		
$0.25FeO{\cdot}0.75P_2O_5$						85		
$0.30FeO{\cdot}0.70P_2O_5$						88		
$0.35FeO{\cdot}0.65P_2O_5$						90		
$0.40FeO{\cdot}0.60P_2O_5$						95		
$0.45FeO{\cdot}0.55P_2O_5$						91		
$0.50FeO{\cdot}0.50P_2O_5$						94		
$0.333Fe_2O_3{\cdot}0.667P_2O_5$	Fe_2O_3, $NH_4H_2PO_4$	1100	2	Air	0.21	13	Titration	Zhang (2010)
		1200				21		
$0.354Fe_2O_3{\cdot}0.646P_2O_5$		1100				14		
		1200				25		
$0.372Fe_2O_3{\cdot}0.628P_2O_5$		1100				15		
		1200				27		
$0.40Fe_2O_3{\cdot}0.60P_2O_5$		1100				16		
		1200				31		
$0.50Fe_2O_3{\cdot}0.50P_2O_5$	Fe_2O_3, $FePO_4$	1250	2	Air	0.21	31	Titration	Zhang (2009)
		1300				51		
$0.565Fe_2O_3{\cdot}0.435P_2O_5$		1200				30		
$0.58Fe_2O_3{\cdot}0.42P_2O_5$		1150				32		
		1200				33		
$0.60Fe_2O_3{\cdot}0.40P_2O_5$		1200				36		
$0.615Fe_2O_3{\cdot}0.385P_2O_5$		1200				40		
$0.032Fe_2O_3{\cdot}0.387BaO{\cdot}0.581P_2O_5$	$BaCO_3$, Fe_2O_3, $NH_4H_2PO_4$	1000	2	Air	0.21	1.4	Mössbauer	Bergo (2004)
$0.064Fe_2O_3{\cdot}0.374BaO{\cdot}0.562P_2O_5$						4		
$0.090Fe_2O_3{\cdot}0.364BaO{\cdot}0.546P_2O_5$						5		
$0.110Fe_2O_3{\cdot}0.356BaO{\cdot}0.534P_2O_5$						6		
$0.135Fe_2O_3{\cdot}0.346BaO{\cdot}0.519P_2O_5$						9		
$0.155Fe_2O_3{\cdot}0.338BaO{\cdot}0.507P_2O_5$						10		
$0.36Fe_2O_3{\cdot}0.10Na_2O{\cdot}0.54P_2O_5$	Na_2CO_3, Fe_2O_3, P_2O_5	1200	2	Air	0.21	28	Mössbauer	Marasinghe (2000)
$0.32Fe_2O_3{\cdot}0.20Na_2O{\cdot}0.48P_2O_5$						32		
$0.36Fe_2O_3{\cdot}0.10Cs_2O{\cdot}0.54P_2O_5$	Cs_2CO_3, Fe_2O_3, P_2O_5					32		
$0.28Fe_2O_3{\cdot}0.30Cs_2O{\cdot}0.40P_2O_5$						29		
$0.40Fe_2O_3{\cdot}0.60P_2O_5$	NA	1150	2	Air	0.21	17	Mössbauer	Karabulut (1999)
		1200				19		
		1350				48		
$0.38Fe_2O_3{\cdot}0.05Cs_2O{\cdot}0.57P_2O_5$	NA	1250	2	Air	0.21	32		
$0.36Fe_2O_3{\cdot}0.10Cs_2O{\cdot}0.54P_2O_5$		1250				34		
$0.339Fe_2O_3{\cdot}0.156Cs_2O{\cdot}0.505P_2O_5$		1250				33		
$0.24Fe_2O_3{\cdot}0.16Na_2O{\cdot}0.60P_2O_5$	Na_2CO_3, Li_2CO_3, Fe_2O_3, P_2O_5	1200	1	Air	0.21	11	Mössbauer	Al Shahrani (2005)
$0.24Fe_2O_3{\cdot}0.12Na_2O{\cdot}0.04Li_2O{\cdot}0.60P_2O_5$						4.3		
$0.24Fe_2O_3{\cdot}0.08Na_2O{\cdot}0.08Li_2O{\cdot}0.60P_2O_5$						3.5		
$0.24Fe_2O_3{\cdot}0.04Na_2O{\cdot}0.12Li_2O{\cdot}0.60P_2O_5$						6.4		
$0.24Fe_2O_3{\cdot}0.16Li_2O{\cdot}0.60P_2O_5$						6.0		

Table C.1. Summary of iron redox ratios in iron phosphate glass with melt conditions. (continued)

Batch Composition (mol%)	Raw Materials	Melt Temperature (°C)	Melt Time (hr)	Melt Atmosphere	pO_2 (atm)	$\%Fe^{2+}$	Analysis Technique	Reference
$0.20Fe_2O_3 \cdot 0.20K_2O \cdot 0.60P_2O_5$	Na_2CO_3, K_2CO_3, Fe_2O_3, P_2O_5	1200	1	Air	0.21	26	Mössbauer	Fang (2000, 2003)
$0.20Fe_2O_3 \cdot 0.05Na_2O \cdot 0.15K_2O \cdot 0.60P_2O_5$						24		
$0.20Fe_2O_3 \cdot 0.10Na_2O \cdot 0.10K_2O \cdot 0.60P_2O_5$						25		
$0.20Fe_2O_3 \cdot 0.15Na_2O \cdot 0.05K_2O \cdot 0.60P_2O_5$						26		
$0.20Fe_2O_3 \cdot 0.20Na_2O \cdot 0.60P_2O_5$						24		
$0.32Fe_2O_3 \cdot 0.20K_2O \cdot 0.48P_2O_5$	Na_2CO_3, K_2CO_3, Fe_2O_3, P_2O_5	1200	1	Air	0.21	17		
$0.32Fe_2O_3 \cdot 0.05Na_2O \cdot 0.15K_2O \cdot 0.48P_2O_5$						13		
$0.32Fe_2O_3 \cdot 0.10Na_2O \cdot 0.10K_2O \cdot 0.48P_2O_5$						14		
$0.32Fe_2O_3 \cdot 0.15Na_2O \cdot 0.05K_2O \cdot 0.48P_2O_5$						14		
$0.32Fe_2O_3 \cdot 0.20Na_2O \cdot 0.48P_2O_5$						16		
$0.32Fe_2O_3 \cdot 0.20Cs_2O \cdot 0.48P_2O_5$	Na_2CO_3, Cs_2CO_3, Fe_2O_3, P_2O_5	1200	1	Air	0.21	20		
$0.32Fe_2O_3 \cdot 0.05Na_2O \cdot 0.15Cs_2O \cdot 0.48P_2O_5$						20		
$0.32Fe_2O_3 \cdot 0.10Na_2O \cdot 0.10Cs_2O \cdot 0.48P_2O_5$						20		
$0.32Fe_2O_3 \cdot 0.15Na_2O \cdot 0.05Cs_2O \cdot 0.48P_2O_5$						25		
$0.32Fe_2O_3 \cdot 0.20Na_2O \cdot 0.48P_2O_5$						16		

**partial pressures not noted in literature and are assumed based on common oxygen levels found in these research grade gases*

BIBLIOGRAPHY

[1] A. K. Varshneya, *Fundamentals of Inorganic Glasses*. San Diego: Academic Press, Inc., 1994.

[2] J. E. Shelby, *Introduction to Glass Science and Technology*, 2nd ed. Cambridge: The Royal Society of Chemistry, 2005.

[3] R. K. Brow, "Review: The Structure of Simple Phosphate Glasses," *Journal of Non-Crystalline Solids*, vol. 263–264, pp. 1–28, 2000.

[4] M. J. Weber, "Science and Technology of Laser Glass," *Journal of Non-Crystalline Solids*, vol. 123, pp. 208–222, 1990.

[5] X. Fang, C. S. Ray, and D. E. Day, "Glass Transition and Fragility of Iron Phosphate Glasses. II. Effect of Mixed-Alkali," *Journal of Non-Crystalline Solids*, vol. 319, no. 3, pp. 314–321, 2003.

[6] G. K. Marasinghe *et al.*, "Structural Features of Iron Phosphate Glasses," *Journal of Non-Crystalline Solids*, vol. 222, pp. 144–152, 1997.

[7] Y. M. Moustafa, K. El-Egili, H. Doweidar, and I. Abbas, "Structure and Electric Conduction of Fe2O3-P2O5 Glasses," *Physica B: Condensed Matter (Amsterdam)*, vol. 353, no. 1–2, pp. 82–91, 2004.

[8] B. Santic, A. Mogus-Milankovic, and D. E. Day, "The DC Electrical Conductivity of Iron Phosphate Glasses," *Journal of Non-Crystalline Solids*, vol. 296, no. 1–2, pp. 65–73, 2001.

[9] D. E. Day, Z. Wu, C. S. Ray, and P. Hrma, "Chemically Durable Iron Phosphate Glass Wasteforms," *Journal of Non-Crystalline Solids*, vol. 241, no. 1, pp. 1–12, 1998.

[10] X. Fang, C. S. Ray, A. Mogus-Milankovic, and D. E. Day, "Iron Redox Equilibrium, Structure and Properties of Iron Phosphate Glasses," *Journal of Non-Crystalline Solids*, vol. 283, no. 1–3, pp. 162–172, 2001.

[11] H. Haworth, D. J. Wronkiewicz, and D. E. Day, "Long-Term Durability Testing of Simulated Iron-Phosphate Nuclear Waste Glass," *Materials Research Society Symposia Proceedings*, vol. 757, pp. 207–209, 2003.

[12] W. Huang, D. E. Day, C. S. Ray, C.-W. Kim, and A. Mogus-Milankovic, "Vitrification of High Chrome Oxide Nuclear Waste in Iron Phosphate Glasses," *Journal of Nuclear Materials*, vol. 327, no. 1, pp. 46–57, 2004.

[13] G. K. Marasinghe, M. Karabulut, X. Fang, C. S. Ray, and D. E. Day, “Iron Phosphate Glasses: An Alternative to Borosilicate Glasses for Vitrifying Certain Nuclear Wastes,” in *Environmental Issues and Waste Management Technologies VI*, Westerville, OH: The American Ceramics Society, 2001, pp. 361–368.

[14] G. K. Marasinghe *et al.*, “Properties and Structure of Vitrified Iron Phosphate Nuclear Wasteforms,” *Journal of Non-Crystalline Solids*, vol. 263–264, no. 1, pp. 146–154, 2000.

[15] M. G. Mesko and D. E. Day, “Immobilization of Spent Nuclear Fuel in Iron Phosphate Glass,” *Journal of Nuclear Materials*, vol. 271, no. 1, pp. 27–36, 1999.

[16] H. Matzke and E. Vernaz, “Thermal and Physicochemical Properties Important for the Long Term Behavior of Nuclear Waste Glasses,” *Journal of Nuclear Materials*, vol. 201, pp. 295–309, 1993.

[17] M. O. Prado, N. B. Messi, T. S. Plivelic, I. L. Torriani, A. M. Bevilacqua, and M. A. Arribere, “The Effects of Radiation on the Density of an Aluminoborosilicate Glass,” *Journal of Non-Crystalline Solids*, vol. 289, no. 1–3, pp. 175–184, 2001.

[18] K. Sun, L. M. Wang, R. C. Ewing, and W. J. Weber, “Electron Irradiation Induced Phase Separation in a Sodium Borosilicate Glass,” *Nuclear Instruments & Methods in Physics Research, Section B: Beam Interactions with Materials and Atoms*, vol. 218, pp. 368–374, 2004.

[19] A. K. Varshneya, *Fundamentals of Inorganic Glasses*. San Diego: Academic Press, Inc., 1994.

[20] J. S. McCloy, “Frontiers in natural and un-natural glasses: An interdisciplinary dialogue and review,” *Journal of Non-Crystalline Solids: X*, vol. 4, 2019, doi: 10.1016/j.nocx.2019.100035.

[21] W. H. Zachariasen, “The Atomic Arrangement in Glass,” *Journal of the Chemical Society*, vol. 54, pp. 3841–3851, 1932.

[22] A. G. Smekal, “On the structure of glass,” *Journal of the Society of Glass Technology*, vol. 35, p. 411, 1951.

[23] J. E. Stanworth, *Physical Properties of Glass*. London: Oxford University Press, 1950.

[24] K. -H Sun, “FUNDAMENTAL CONDITION OF GLASS FORMATION,” *Journal of the American Ceramic Society*, vol. 30, no. 9, 1947, doi: 10.1111/j.1151-2916.1947.tb19654.x.

[25] A. Dietzel, “Die Kationenfeldstärken und ihre Beziehungen zu Entglasungsvorgängen, zur Verbindungsbildung und zu den Schmelzpunkten von Silicaten,” *Z. Electrochem.*, vol. 48, pp. 9–23, 1942.

[26] R. K. Brow, “Review: The Structure of Simple Phosphate Glasses,” *Journal of Non-Crystalline Solids*, vol. 263–264, pp. 1–28, 2000.

[27] C.-K. Loong, K. Suzuya, D. L. Price, B. C. Sales, and L. A. Boatner, “Structure and Dynamics of Phosphate Glasses: From Ultra- to Orthophosphate Composition,” *Physica B: Condensed Matter (Amsterdam)*, vol. 241–243, pp. 890–896, 1998.

[28] N. Sharmin and C. D. Rudd, “Structure, thermal properties, dissolution behaviour and biomedical applications of phosphate glasses and fibres: a review,” *Journal of Materials Science*, vol. 52, no. 15, 2017, doi: 10.1007/s10853-017-0784-4.

[29] R. K. Brow, D. R. Tallant, J. J. Hudgens, S. W. Martin, and A. D. Irwin, “The Short-Range Structure of Sodium Ultraphosphate Glasses,” *Journal of Non-Crystalline Solids*, vol. 177, pp. 221–228, 1994.

[30] R. K. Brow, R. J. Kirkpatrick, and G. L. Turner, “The Short Range Structure of Sodium Phosphate Glasses 1. MAS NMR Studies,” *Journal of Non-Crystalline Solids*, vol. 116, no. 1, pp. 39–45, 1990.

[31] R. K. Brow, T. M. Alam, D. R. Tallant, and R. J. Kirkpatrick, “Spectroscopic Studies on the Structures of Phosphate Sealing Glasses,” *Materials Research Society Bulletin*, vol. 23, no. 11, pp. 63–67, 1998.

[32] Y. M. Moustafa and K. El-Egili, “Infrared Spectra of Sodium Phosphate Glasses,” *Journal of Non-Crystalline Solids*, vol. 240, no. 1–3, pp. 144–153, 1998.

[33] R. K. Brow and D. R. Tallant, “Structural design of sealing glasses,” *Journal of Non-Crystalline Solids*, vol. 222, 1997, doi: 10.1016/s0022-3093(97)90142-3.

[34] Y. B. Peng and D. E. Day, “High Thermal Expansion Phosphate Glasses. Part 1,” *Glass Technology*, vol. 32, no. 5, pp. 166–173, 1991.

[35] R. Morena, “Phosphate glasses as alternatives to Pb-based sealing frits,” *Journal of Non-Crystalline Solids*, vol. 263, 2000, doi: 10.1016/S0022-3093(99)00678-X.

[36] N. Mascaraque, H. Takebe, G. Tricot, J. L. G. Fierro, A. Durán, and F. Muñoz, “Structure and electrical properties of a new thio-phosphorus oxynitride glass electrolyte,” *Journal of Non-Crystalline Solids*, vol. 405, 2014, doi: 10.1016/j.jnoncrysol.2014.09.011.

[37] Z. A. Grady, C. J. Wilkinson, C. A. Randall, and J. C. Mauro, “Emerging Role of Non-crystalline Electrolytes in Solid-State Battery Research,” *Frontiers in Energy Research*, vol. 8. 2020. doi: 10.3389/fenrg.2020.00218.

[38] K. J. Hamam and F. Salman, “Dielectric constant and electrical study of solid-state electrolyte lithium phosphate glasses,” *Applied Physics A: Materials Science and Processing*, vol. 125, no. 9, 2019, doi: 10.1007/s00339-019-2868-2.

[39] M. M. Mahmoud, Y. Cui, M. Rohde, C. Ziebert, G. Link, and H. J. Seifert, “Microwave crystallization of lithium aluminum germanium phosphate solid-state electrolyte,” *Materials*, vol. 9, no. 7, 2016, doi: 10.3390/ma9070506.

[40] N. J. Lakhkar *et al.*, “Titanium phosphate glass microspheres for bone tissue engineering,” *Acta Biomaterialia*, vol. 8, no. 11, 2012, doi: 10.1016/j.actbio.2012.07.023.

[41] F. Hajiali, S. Tajbakhsh, and A. Shojaei, “Fabrication and Properties of Polycaprolactone Composites Containing Calcium Phosphate-Based Ceramics and Bioactive Glasses in Bone Tissue Engineering: A Review,” *Polymer Reviews*, vol. 58, no. 1. 2018. doi: 10.1080/15583724.2017.1332640.

[42] F. Alshomer, C. Chaves, T. Serra, I. Ahmed, and D. M. Kalaskar, “Micropatterning of nanocomposite polymer scaffolds using sacrificial phosphate glass fibers for tendon tissue engineering applications,” *Nanomedicine: Nanotechnology, Biology, and Medicine*, vol. 13, no. 3, 2017, doi: 10.1016/j.nano.2017.01.006.

[43] A. Patel and J. C. Knowles, “Investigation of silica-iron-phosphate glasses for tissue engineering,” *Journal of Materials Science: Materials in Medicine*, vol. 17, no. 10, 2006, doi: 10.1007/s10856-006-0183-x.

[44] R. Lachheb *et al.*, “Judd–Ofelt analysis and experimental spectroscopic study of erbium doped phosphate glasses,” *Journal of Luminescence*, vol. 201, 2018, doi: 10.1016/j.jlumin.2018.03.087.

[45] S. Fu *et al.*, “High-Efficiency Nd3+-Doped Phosphate Fiber Laser at 880 nm,” *IEEE Photonics Technology Letters*, vol. 32, no. 18, 2020, doi: 10.1109/LPT.2020.3016604.

[46] M. J. Weber, “Science and Technology of Laser Glass,” *Journal of Non-Crystalline Solids*, vol. 123, pp. 208–222, 1990.

[47] T. Hashimoto, H. Nasu, and K. Kamiya, “Ti3+-Free Multicomponent Titanophosphate Glasses as Ecologically Sustainable Optical Glasses,” *Journal of the American Ceramic Society*, vol. 89, no. 8, pp. 2521–2527, 2006.

[48] J. G. Vaughan, C. H. Perry, and D. L. Kinser, “ELECTRICAL TRANSPORT IN REDUCED TITANIUM PHOSPHATE GLASSES.,” *Physics and Chemistry of Glasses*, vol. 18, no. 5, 1977.

[49] T. Hayashi and H. Saito, “Structure and electrical properties of TiO2-Ti2O3-P2O5 glasses,” *Phys. Chem. Glasses*, vol. 20, no. 5, pp. 108–114, 1979.

[50] R. K. Brow, D. R. Tallant, W. L. Warren, A. McIntyre, and D. E. Day, “Spectroscopic studies of the structure of titanophosphate and calcium titanophosphate glasses,” *Physics and Chemistry of Glasses*, vol. 38, no. 6, 1997.

[51] B. Tischendorf, J. U. Otaigbe, J. W. Wiench, M. Pruski, and B. C. Sales, “A study of short and intermediate range order in zinc phosphate glasses,” *Journal of Non-Crystalline Solids*, vol. 282, pp. 147–158, 2001.

[52] G. Walter, U. Hoppe, J. Vogel, G. Carl, and P. Hartmann, “The structure of zinc polyphosphate glass studied by diffraction methods and 31P NMR,” *Journal of Non-Crystalline Solids*, vol. 333, pp. 252–262, 2004.

[53] R. Pyare, “Leachability of zinc ions from ternary phosphate glasses,” *Journal of Materials Science*, vol. 38, no. 9. 2003. doi: 10.1023/A:1023514210997.

[54] C. R. Kurkjian, “Mechanical Properties of Phosphate Glasses,” *Journal of Non-Crystalline Solids*, vol. 263–264, no. 1, pp. 207–212, 2000.

[55] M. Karabulut, G. K. Marasinghe, C. S. Ray, D. E. Day, O. Ozturk, and G. D. Waddill, “X-Ray Photoelectron and Mössbauer Spectroscopic Studies of Iron Phosphate Glasses Containing U, Cs and Bi,” *Journal of Non-Crystalline Solids*, vol. 249, no. 2–3, pp. 106–116, 1999.

[56] P. A. Bingham, R. J. Hand, and S. D. Forder, “Doping of Iron Phosphate Glasses with Al2O3, SiO2 or B2O3 for Improved Thermal Stability,” *Materials Research Bulletin*, 2006.

[57] R. K. Brow, “Alkali-Resistant Calcium Iron Phosphate Glass Fibers for Concrete Reinforcement,” *Utc R129*, 2008.

[58] J. Shi, “Properties of alkaline-resistant calcium-iron-phosphate glasses,” 2007.

[59] S. Lin, S. Krebs, A. Nazre, and R. King, “Totally Bioabsorbable Composites,” in *39th International SAMPE Symposium*, no. Y. Wang and D. Zhao, “Mechanical and Interlaminar Fracture Properties of Woven Fabric Reinforced Composites”, in Proceedings of the 39th International SAMPE Symposium, April, 1994, Anaheim, CA, 2693-2705., pp. 1981–1985.

[60] I. Ahmed, C. A. Collins, M. P. Lewis, I. Olsen, and J. C. Knowles, “Processing, Characterisation and Biocompatibility of Iron-Phosphate Glass Fibres for Tissue Engineering,” *Biomaterials*, vol. 25, no. 16, pp. 3223–3232, 2004.

[61] A. Moguš-Milanković, A. Šantić, S. T. Reis, K. Furić, and D. E. Day, “Studies of Lead-Iron Phosphate Glasses by Raman, Mossbauer and Impedance Spectroscopy,” *Journal of Non-Crystalline Solids*, vol. 351, no. 40–42, pp. 3246–3258, 2005.

[62] A. Moguš-Milanković, B. Šantić, D. E. Day, and C. S. Ray, “Electrical conductivity in mixed-alkali iron phosphate glasses,” *Journal of Non-Crystalline Solids*, vol. 283, pp. 119–128, 2001.

[63] Y. M. Moustafa, K. El-Egili, H. Doweidar, and I. Abbas, “Structure and Electric Conduction of Fe2O3-P2O5 Glasses,” *Physica B: Condensed Matter (Amsterdam)*, vol. 353, no. 1–2, pp. 82–91, 2004.

[64] B. Santic, A. Mogus-Milankovic, and D. E. Day, “The DC Electrical Conductivity of Iron Phosphate Glasses,” *Journal of Non-Crystalline Solids*, vol. 296, no. 1–2, pp. 65–73, 2001.

[65] C.-W. Kim and D. E. Day, “Immobilization of Hanford LAW in iron phosphate glasses,” *Journal of Non-Crystalline Solids*, vol. 331, no. 1–3, pp. 20–31, 2003.

[66] H. Haworth, D. J. Wronkiewicz, and D. E. Day, “Long-Term Durability Testing of Simulated Iron-Phosphate Nuclear Waste Glass,” *Materials Research Society Symposia Proceedings*, vol. 757, pp. 207–209, 2003.

[67] M. G. Mesko, D. E. Day, and B. C. Bunker, “Immobilization of CsCl and SrF2 in Iron Phosphate Glass,” *Waste Management*, vol. 20, no. 4, pp. 271–278, 2000.

[68] D. Zhu, C.-W. Kim, and D. E. Day, “Corrosion behavior of Inconel 690 and 693 in an iron phosphate melt,” *Journal of Nuclear Materials*, vol. 336, pp. 47–53, 2005.

[69] D. E. Day, Z. Wu, C. S. Ray, and P. Hrma, “Chemically Durable Iron Phosphate Glass Wasteforms,” *Journal of Non-Crystalline Solids*, vol. 241, no. 1, pp. 1–12, 1998.

[70] W. Huang, D. E. Day, C. S. Ray, and C. W. Kim, “High temperature properties of an iron phosphate melt containing high chrome nuclear waste,” *Journal of Nuclear Materials*, vol. 346, pp. 298–305, 2005.

[71] C.-W. Kim, D. Zhu, D. E. Day, and D. Gombert, “Iron Phosphate Glasses for Vitrifying Sodium Bearing Waste,” in *Environmental Issues and Waste Management Technologies VIII*, vol. 143, Westerville, OH: The American Ceramics Society, 2002, pp. 329–336.

[72] G. K. Marasinghe, M. Karabulut, X. Fang, C. S. Ray, and D. E. Day, “Iron Phosphate Glasses: An Alternative to Borosilicate Glasses for Vitrifying Certain Nuclear Wastes,” in *Environmental Issues and Waste Management Technologies VI*, Westerville, OH: The American Ceramics Society, 2001, pp. 361–368.

[73] W. Huang, D. E. Day, C. S. Ray, C.-W. Kim, and A. Mogus-Milankovic, “Vitrification of High Chrome Oxide Nuclear Waste in Iron Phosphate Glasses,” *Journal of Nuclear Materials*, vol. 327, no. 1, pp. 46–57, 2004.

[74] C. W. Kim *et al.*, “Chemically Durable Iron Phosphate Glasses for Vitrifying Sodium Bearing Waste (SBW) Using Conventional and Cold Crucible Induction Melting (CCIM) Techniques,” *Journal of Nuclear Materials*, vol. 322, no. 2–3, pp. 152–164, 2003.

[75] G. K. Marasinghe *et al.*, “Properties and Structure of Vitrified Iron Phosphate Nuclear Wasteforms,” *Journal of Non-Crystalline Solids*, vol. 263–264, no. 1, pp. 146–154, 2000.

[76] G. K. Marasinghe *et al.*, “Vitrified Iron Phosphate Nuclear Wasteforms Containing Multiple Waste Components,” in *Environmental Issues and Waste Management Technologies V*, vol. 107, Westerville, OH: The American Ceramics Society, 2000, pp. 115–122.

[77] B. C. Sales and L. A. Boatner, “Physical and chemical characteristics of lead-iron phosphate nuclear waste glasses,” *Journal of Non-Crystalline Solids*, vol. 79, no. 1–2, 1986, doi: 10.1016/0022-3093(86)90040-2.

[78] M. G. Mesko and D. E. Day, “Immobilization of Spent Nuclear Fuel in Iron Phosphate Glass,” *Journal of Nuclear Materials*, vol. 271, no. 1, pp. 27–36, 1999.

[79] R. K. Brow, C. W. Kim, and S. T. Reis, “Iron polyphosphate glasses for waste immobilization,” *International Journal of Applied Glass Science*, vol. 11, no. 1, 2020, doi: 10.1111/ijag.13565.

[80] V. v. Kushnikov, Y. I. Matyunin, T. v. Smelova, and A. v. Demin, “Use of induction melter with a cold crucible (CCIM) for HLLW and plutonium immobilization,” in *Materials Research Society Symposium - Proceedings*, 1997, vol. 465. doi: 10.1557/proc-465-55.

[81] A. P. Mukhamet-Galeyev, L. O. Magazina, K. A. Levin, N. D. Samotoin, A. v. Zotov, and B. I. Omelianenko, “Interaction of Na-Al-P-glass (Cs, Sr-bearing) with water at elevated temperatures (70-250 °C),” in *Materials Research Society Symposium - Proceedings*, 1995, vol. 353, no. 1. doi: 10.1557/proc-353-79.

[82] G. K. Marasinghe *et al.*, “Structural Features of Iron Phosphate Glasses,” *Journal of Non-Crystalline Solids*, vol. 222, pp. 144–152, 1997, doi: 10.1016/s0022-3093(97)90107-1.

[83] C. S. Ray, X. Fang, M. Karabulut, G. K. Marasinghe, and D. E. Day, “Effect of Melting Temperature and Time on Iron Valence and Crystallization of Iron Phosphate Glasses,” *Journal of Non-Crystalline Solids*, vol. 249, no. 1, pp. 1–16, 1999.

[84] X. Fang, C. S. Ray, A. Mogus-Milankovic, and D. E. Day, “Iron Redox Equilibrium, Structure and Properties of Iron Phosphate Glasses,” *Journal of Non-Crystalline Solids*, vol. 283, no. 1–3, pp. 162–172, 2001.

[85] C. L. Dube, M. C. Stennett, S. Akhmadaliev, and N. C. Hyatt, “Investigation of ion irradiation induced damages in iron phosphate glasses: Role of electronic and nuclear losses in glass network modification,” *Journal of Non-Crystalline Solids: X*, vol. 8, 2020, doi: 10.1016/j.nocx.2020.100055.

[86] K. Jolley and R. Smith, “Iron phosphate glasses: Structure determination and radiation tolerance,” *Nuclear Instruments and Methods in Physics Research, Section B: Beam Interactions with Materials and Atoms*, vol. 374, 2016, doi: 10.1016/j.nimb.2015.09.043.

[87] L. Petit, “Radiation effects on phosphate glasses: Review,” *International Journal of Applied Glass Science*, vol. 11, no. 3, 2020, doi: 10.1111/ijag.14075.

[88] K. Sun, L. M. Wang, and R. C. Ewing, “Analytical Electron Microscopy Study of Electron Radiation Damage in Iron Phosphate Glass Waste Forms,” *Materials Research Society Symposia Proceedings*, vol. 757, pp. 135–140, 2003.

[89] D. L. Griscom *et al.*, “On the Structure and Radiation Chemistry of Iron Phosphate Glasses: New Insights from Electron Spin Resonance, Mössbauer, and Evolved-Gas Mass Spectroscopy,” *Nuclear Instruments & Methods in Physics Research, Section B: Beam Interactions with Materials and Atoms*, vol. 141, no. 1–4, pp. 600–615, 1998.

[90] A. Modaressi, J. C. Kaell, B. Malaman, R. Gérardin, and C. Gleitzer, “Etude du system Fe-P-O (pour Fe P ≥1) et d’une famille: les oxyphosphates de fer,” *Materials Research Bulletin*, vol. 18, no. 1, 1983, doi: 10.1016/0025-5408(83)90177-0.

[91] H. Wentrup, “Contribution on the System Iron-Phosphorus-Oxygen,” *Archiv für das Eisenhüttenwesen*, vol. 9, no. 7, pp. 57–60, 1935.

[92] G. Tromel and K. Schwerdtfeger, “A study of the system iron-phosphorous oxygen,” *Archiv für das Eisenhüttenwesen*, vol. 34, pp. 55–59, 1963.

[93] L. Zhang, M. E. Schlesinger, and R. K. Brow, “Re-determination of the liquidus surface of the Fe3PO7-Fe(PO3)3 system,” *submitted to Journal of Non-Crystalline Solids*.

[94] A. Wright, R. N. Sinclair, J. L. Shaw, R. Haworth, G. K. Marasinghe, and D. E. Day, “A Neutron Diffraction Study of the Structure of Iron Phosphate Glasses,” 2006.

[95] I. Kashif *et al.*, “Mossbauer, infrared and magnetic susceptibility studies of iron sodium borate glasses doped by sulphur,” *Journal of Physics and Chemistry of Solids*, vol. 67, no. 11, 2006, doi: 10.1016/j.jpcs.2006.06.011.

[96] U. Hoppe, M. Karabulut, E. Metwalli, R. K. Brow, and P. Jóvári, “The Fe-O coordination in iron phosphate glasses by x-ray diffraction with high energy photons,” *Journal of Physics: Condensed Matter*, vol. 15, pp. 6143–6153, 2003.

[97] M. Karabulut *et al.*, “An Investigation of the Local Iron Environment in Iron Phosphate Glasses Having Different Fe(II) Concentrations,” *Journal of Non-Crystalline Solids*, vol. 306, no. 2, pp. 182–192, 2002.

[98] C. R. Kurkjian and E. A. Sigety, “Co-ordination of Fe3+ in glass,” *Physics and Chemistry of Glasses*, vol. 9, no. 3, pp. 73–83, Jun. 1968.

[99] H. Doweidar, Y. M. Moustafa, K. El-Egili, and I. Abbas, “Infrared Spectra of Fe2O3-PbO-P2O5 Glasses,” *Vibrational Spectroscopy*, vol. 37, no. 1, pp. 91–96, 2005.

[100] S. T. Reis, D. L. A. Faria, J. R. Martinelli, W. M. Ponteschka, D. E. Day, and C. S. M. Partiti, “Structural Features of Lead Iron Phosphate Glasses,” *Journal of Non-Crystalline Solids*, vol. 304, no. 1–3, pp. 188–194, 2002.

[101] B. Pivac, A. Mogus-Milankovic, and D. E. Day, “Iron Valence and Coordination in Phosphate Glasses as Studied by Optical Spectroscopy,” *Journal of Non-Crystalline Solids*, vol. 226, no. 1–2, pp. 41–46, 1998.

[102] G. Concas, F. Congiu, E. Manca, C. Muntoni, and G. Pinna, “Mössbauer spectroscopic investigation of some iron-containing sodium phosphate glasses,” *Journal of Non-Crystalline Solids*, vol. 192 & 193, pp. 175–178, 1995.

[103] U. Natura and D. Ehrt, “Formation of radiation defects in silicate and borosilicate glasses caused by UV lamp and excimer laser irradiation,” *Glass Science and Technology: Glastechnische Berichte*, vol. 72, no. 9, 1999.

[104] G. H. Sigel and R. J. Ginther, “The effect of iron on the ultraviolet absorption of high purity soda-silica glass,” *Glass Technology*, vol. 9, p. 66, 1968.

[105] F. H. ElBatal, M. S. Selim, S. Y. Marzouk, and M. A. Azooz, “UV-vis absorption of the transition metal-doped SiO2-B2O3-Na2O glasses,” *Physica B: Condensed Matter*, vol. 398, no. 1, 2007, doi: 10.1016/j.physb.2007.05.004.

[106] J. H. Liu, G. H. Zhang, and K. C. Chou, “Estimation for Iron Redox Equilibria in Multicomponent Slags,” *High Temperature Materials and Processes*, vol. 36, no. 6, 2017, doi: 10.1515/htmp-2015-0228.

[107] J. M. Park, “Iron redox equilibria in BOF slag equilibrated with ambient air,” *Steel Research*, vol. 73, no. 2, 2002, doi: 10.1002/srin.200200171.

[108] M. Suzuki, M. Nakamoto, T. Tanaka, Y. Tsukaguchi, K. Mishima, and M. Hanao, “Effect of Sulfur in Slag on Dynamic Change Behavior of Liquid Iron/Molten Slag Interfacial Tension,” *ISIJ International*, vol. 60, no. 11, 2020, doi: 10.2355/isijinternational.ISIJINT-2020-144.

[109] Y. Park and D. J. Min, “Effect of Iron Redox Equilibrium on the Foaming Behavior of MgO-Saturated Slags,” *Metallurgical and Materials Transactions B: Process Metallurgy and Materials Processing Science*, vol. 49, no. 4, 2018, doi: 10.1007/s11663-018-1251-6.

[110] G. N. Elansky, D. Ameling, D. G. Elansky, and G. I. Kotelnikov, “Oxidation state of iron in different materials and processes part 1. Iron in materials and slags of equilibrium processes,” *Chernye Metally*, vol. 2020, no. 9, 2020.

[111] G. E. Toop and C. S. Samis, “Activities of ions in silicate melts,” *Trans. A.I.M.E.*, vol. 224, p. 878, 1962.

[112] H. D. Schreiber, L. J. Peters, J. W. Beckman, and C. W. Schreiber, “Redox chemistry of iron-manganese and iron-chromium interactions in soda lime silicate glass melts,” *Glass Science and Technology: Glastechnische Berichte*, vol. 69, no. 9, 1996.

[113] E. Meechoowas, S. Poosrisoma, P. Jampeeruang, and T. Jitwatcharakomol, “The effect of heat treatment on Fe2+/Fe3+ ratio in soda-lime silicate glass,” in *Key Engineering Materials*, 2015, vol. 659. doi: 10.4028/www.scientific.net/KEM.659.194.

[114] E. Meechoowas, B. Petchareanmongkol, P. Jampeerung, and K. Tapasa, “The effect of decolorizing agent on the optical properties of high iron contents soda-lime silicate glass,” in *Key Engineering Materials*, 2018, vol. 766 KEM. doi: 10.4028/www.scientific.net/KEM.766.28.

[115] S. B. Donald, A. M. Swink, and H. D. Schreiber, “High-iron ferric glass,” *Journal of Non-Crystalline Solids*, vol. 352, pp. 539–543, 2006.

[116] B. Kumar, “Redox State of Iron and Its Related Effects in the Ca0-P205-Fe203 Glasses,” *Journal of American Ceramic Society*, vol. 74, no. 1, 1991.

[117] L. Ghussn *et al.*, “Progress Report on Structural and Dynamic Properties of Iron Phosphate Glasses,” 2007.

[118] C. S. Ray, X. Fang, M. Karabulut, G. K. Marasinghe, and D. E. Day, “Iron Redox and Crystallization of Iron Phosphate Glasses,” in *Environmental Issues and Waste Management Technologies IV*, vol. 43, Westerville, OH: The American Ceramics Society, 1999, pp. 187–194.

[119] A. Paul, “No Title,” *Journal of Non-Crystalline Solids*, vol. 123, p. 354, 1990.

[120] L. Zhang, R. K. Brow, M. E. Schlesinger, L. Ghussn, and E. D. Zanotto, “Glass formation from iron-rich phosphate melts,” *submitted to Journal of Non-Crystalline Solids*.

[121] M. Karabulut, E. Metwalli, D. E. Day, and R. K. Brow, “Mössbauer and IR investigations of iron ultraphosphate glasses,” *Journal of Non-Crystalline Solids*, vol. 328, pp. 199–206, 2003.

[122] S. T. Reis *et al.*, “Iron redox equilibrium, structure and properties of zinc iron phosphate glasses,” *Journal of Non-Crystalline Solids*, vol. 353, pp. 151–158, 2007.

[123] E. Meechoowas, P. Jampeerung, K. Tapasa, and T. Jitwatcharakomol, “The decolorizing of high iron containing soda-lime silicate glass by annealing process,” in *Key Engineering Materials*, 2016, vol. 702. doi: 10.4028/www.scientific.net/KEM.702.130.

[124] S. Sumita, Y. Matsumoto, K. Morinaga, and T. Yanagase, “The Optical Basicity and Fe2+-Fe3+ Redox in Oxyacid Salt Systems,” *Transactions of the Japan Institute of Metals*, vol. 23, no. 7, pp. 360–367, 1982.

[125] J. A. Duffy, “Stability of Metal Ions in Molten Glass: The Definition of Reduction and Oxidation,” *Physics and Chemistry of Glasses*, vol. 40, no. 2, pp. 54–56, 1999.

[126] J. A. Duffy and F. G. K. Bauke, “Basicity of Solid Glasses and Glass Forming Melts,” in *Physics of Non-Crystalline Solids*, L. D. Pye, W. C. la Course, and H. J. Stevens, Eds. London, UK: Taylor & Francis, 1992, pp. 366–370.

[127] J. A. Duffy, “Redox Equilibria in Glass,” *Journal of Non-Crystalline Solids*, vol. 196, pp. 45–50, 1996.

[128] G. Concas, F. Congiu, C. Muntoni, and G. Pinna, “Mössbauer spectroscopic investigation of iron in sodium phosphate glasses,” *Journal of Physics and Chemistry of Solids*, vol. 56, no. 6, pp. 877–881, 1995.

[129] J. A. Duffy and M. D. Ingram, “Establishment of an optical scale for Lewis Basicity in inorganic oxyacids, molten salts, and glasses,” *Journal of the American Chemical Society*, vol. 93, pp. 6448–6454, 1971.

[130] J. A. Duffy and M. D. Ingram, “An Interpretation of Glass Chemistry in Terms of the Optical Basicity Concept,” *Journal of Non-Crystalline Solids*, vol. 21, pp. 373–410, 1976.

[131] R. Moretti and G. Ottonello, “Polymerization and disproportionation of iron and sulfur in silicate melts: insights from an optical basicity-based approach,” *Journal of Non-Crystalline Solids*, vol. 323, pp. 111–119, 2003.

[132] J. A. Duffy and M. D. Ingram, “Optical Basicity,” in *Optical Properties of Glass*, D. R. Uhlmann and N. J. Kreidl, Eds. Westerville, OH: American Ceramic Society, 1991, pp. 159–184.

[133] J. A. Duffy and M. D. Ingram, “Optical Basicity IV: Influence of electronegativity on the Lewis basicity and solvent properties of molten oxyanion salts and glasses,” *Journal of Inorganic and Nuclear Chemistry*, vol. 37, pp. 1203–1206, 1975.

[134] J. A. Duffy, “Relationship between optical basicity and thermochemistry of silicates,” *Journal of Physical Chemistry B*, vol. 108, no. 23, 2004, doi: 10.1021/jp031209c.

[135] P. Choudhury, S. K. Pal, and H. S. Ray, “On the prediction of viscosity of glasses from optical basicity,” *Journal of Applied Physics*, vol. 100, no. 11, 2006, doi: 10.1063/1.2372226.

[136] F. G. K. Baucke and J. A. Duffy, “The Effect of Basicity on Redox Equilibria in Molten Glass,” *Physics and Chemistry of Glasses*, vol. 32, no. 5, pp. 211–218, 1991.

[137] J. H. Binks and J. A. Duffy, “A Molecular Orbital Treatment of the Basicity of Oxyanion Units,” *Journal of Non-Crystalline Solids*, vol. 37, pp. 387–400, 1980.

[138] A. Lebouteiller and P. Courtine, “Improvement of a Bulk Optical Basicity Table for Oxidic Systems,” *Journal of Solid State Chemistry*, vol. 137, pp. 94–103, 1998.

[139] A. Klonkowski, “Changes in Optical Basicity in the Glass System M(II)O-P2O5,” *Physics and Chemistry of Glasses*, vol. 22, no. 6, pp. 163–167, 1981.

[140] V. Dimitrov and T. Komatsu, “Relationship between optical basicity and average single bond strength of oxide glasses,” *Physics and Chemistry of Glasses*, vol. 46, no. 5, pp. 521–529, 2005.

[141] E. I. Kamitsos, G. D. Chryssikos, A. P. Patsis, and J. A. Duffy, “Metal Ion Sites in Oxide Glasses: Relation to Glass Basicity and IonTransport,” *Journal of Non-Crystalline Solids*, vol. 196, pp. 249–254, 1996.

[142] J. A. Duffy, “Use of refractivity data for obtaining optical basicity of transition metal oxides,” *Ironmaking & Steelmaking*, vol. 16, no. 6, pp. 426–428, 1989.

[143] M. A. Algradee, M. Sultan, O. M. Samir, and A. E. B. Alwany, "Electronic polarizability, optical basicity and interaction parameter for Nd2O3 doped lithium–zinc–phosphate glasses," *Applied Physics A: Materials Science and Processing*, vol. 123, no. 8, 2017, doi: 10.1007/s00339-017-1136-6.

[144] H. S. Ray and S. Pal, "Simple method for theoretical estimation of viscosity of oxide melts using optical basicity," *Ironmaking and Steelmaking*, vol. 31, no. 2, 2004, doi: 10.1179/030192304225012097.

[145] A. B. Atkarskaya and V. N. Bykov, "The Effect of Basicity of Glass on Interaction of Variable-Valence Elements," *Glass and Ceramics (English Translation)*, vol. 61, no. 1–2, pp. 44–47, 2004.

[146] V. Dimitrov and T. Komatsu, "Electronic polarizability, optical basicity and non-linear optical properties of oxide glasses," *Journal of Non-Crystalline Solids*, vol. 249, no. 2–3, 1999, doi: 10.1016/S0022-3093(99)00317-8.

[147] R. W. Young, J. A. Duffy, G. J. Hassall, and Z. Xu, "Use of optical basicity concept for determining phosphorus and sulphur slag-metal partitions," *Ironmaking & Steelmaking*, vol. 19, no. 3, pp. 201–219, 1992.

[148] J. A. Duffy and R. J. Grant, "Effect of Temperature on Optical Basicity in the Sodium Oxide- Boric Oxide Glass System," *Journal of Physical Chemistry*, vol. 79, no. 25, pp. 2780–2784, 1975.

[149] F. G. K. Baucke and J. A. Duffy, "Redox Reactions Between Cations of Different Polyvalent Elements in Glass Melts: An Optical Basicity Study," *Physics and Chemistry of Glasses*, vol. 34, no. 4, pp. 158–163, 1993.

[150] J. A. Duffy and F. G. K. Baucke, "Effect of glass composition and basicity on reduction of metal ions to the metallic state in melts," *Physics and Chemistry of Glasses*, vol. 38, no. 1, pp. 25–26, 1997.

[151] J. A. Duffy, M. D. Ingram, and S. Fong, "Effect of Basicity on Chemical Bonding of Metal Ions in Glass and Its Relevance to Their Stability," *Physical Chemistry Chemical Physics*, vol. 2, pp. 1829–1833, 2000.

[152] J. R. Beckett, "Role of basicity and tetrahedral speciation in controlling the thermodynamic properties of silicate liquids, part 1: The system CaO-MgO-Al2O3-SiO2," *Geochimica et Cosmochimica Acta*, vol. 66, no. 1, pp. 93–107, 2002.

[153] J. A. Duffy, "Interrelationship between polarisability and polarising power of cations: Application to glasses containing zinc oxide," *Physics and Chemistry of Glasses: European Journal of Glass Science and Technology Part B*, vol. 47, no. 1, 2006.

[154] J. A. Duffy, “Polarisability and polarising power of rare earth ions in glass: An optical basicity assessment,” *Physics and Chemistry of Glasses*, vol. 46, no. 1, 2005.

[155] J. A. Duffy, “Ultraviolet transparency of glass: A chemical approach in terms of band theory, polarisability and electronegativity,” *Physics and Chemistry of Glasses*, vol. 42, no. 3. 2001.

[156] J. A. Duffy, “Optical basicity of fluorides and mixed oxide-fluoride glasses and melts,” *Physics and Chemistry of Glasses: European Journal of Glass Science and Technology Part B*, vol. 52, no. 3, 2011.

[157] V. Dimitrov and T. Komatsu, “Correlation between optical basicity and single bond strength of alkali borosilicate glasses,” *Physics and Chemistry of Glasses: European Journal of Glass Science and Technology Part B*, vol. 53, no. 6, 2012.

[158] V. Dimitrov and T. Komatsu, “Correlation between optical basicity and single bond strength of simple oxides and sodium containing oxide glasses,” *Physics and Chemistry of Glasses: European Journal of Glass Science and Technology Part B*, vol. 49, no. 1, 2008.

[159] V. Dimitrov and T. Komatsu, “Average single bond strength and optical basicity of Na2O- GeO2 glasses,” *Journal of the Ceramic Society of Japan*, vol. 117, no. 1370, 2009, doi: 10.2109/jcersj2.117.1105.

[160] V. Dimitrov, T. Komatsu, and T. Tasheva, “Group optical basicity and single bond strength of oxide glasses,” *Journal of Chemical Technology and Metallurgy*, vol. 53, no. 6, 2018.

[161] V. Dimitrov and T. Komatsu, “Correlation among electronegativity, cation polarizability, optical basicity and single bond strength of simple oxides,” *Journal of Solid State Chemistry*, vol. 196, 2012, doi: 10.1016/j.jssc.2012.07.030.

[162] V. Dimitrov and T. Komatsu, “Electronic polarizability, optical basicity and single bond strength of oxide glasses,” *Journal of Chemical Technology and Metallurgy*, vol. 48, no. 6, 2013.

[163] V. Dimitrov, T. Tasheva, and T. Komatsu, “Group optical basicity and single bond strength of lead borate glasses,” *Journal of Chemical Technology and Metallurgy*, vol. 53, no. 6, 2018.

[164] D. Ghosh, V. A. Krishnamurthy, and S. R. Sankaranarayanan, “Application of optical basicity to viscosity of high alumina blast furnace slags,” *Journal of Mining and Metallurgy, Section B: Metallurgy*, vol. 46, no. 1, 2010, doi: 10.2298/JMMB1001041G.

[165] Y. feng Chen, X. ming Lv, Z. de Pang, and X. wei Lv, “Effect of basicity and Al2O3 on viscosity of ferronickel smelting slag,” *Journal of Iron and Steel Research International*, vol. 27, no. 12, 2020, doi: 10.1007/s42243-020-00504-y.

[166] S. Sadaf, T. Wu, L. Zhong, Z. Y. Liao, and H. C. Wang, “Effect of basicity on the structure, viscosity and crystallization of CaO-SiO2-b2o3 based mold fluxes,” *Metals*, vol. 10, no. 9, 2020, doi: 10.3390/met10091240.

[167] J. Ma, W. Li, G. Fu, and M. Zhu, “Influence of Basicity on the Viscosity and Crystallization Characteristics of Chromium-containing High-titanium Slag,” *ISIJ International*, vol. 60, no. 11, 2020, doi: 10.2355/isijinternational.ISIJINT-2020-244.

[168] J. A. Duffy, “Ionic-covalent character of metal and nonmetal oxides,” *Journal of Physical Chemistry A*, vol. 110, no. 49, 2006, doi: 10.1021/jp063846j.

[169] J. A. Duffy, “Redox Equilibria and Stereochemistry of Metal Ions in Glass: A Chemical Bonding Approach,” *Proceedings of the International Congress on Glass, Volume 1. Invited Papers*, pp. 74–83, 2001.

[170] J. A. Duffy, “Back to Basics,” *Chemistry in Britain*, vol. 30, pp. 562–565, 1994.

[171] H. A. Othman, G. M. Arzumanyan, and D. Möncke, “The influence of different alkaline earth oxides on the structural and optical properties of undoped, Ce-doped, Sm-doped, and Sm/Ce co-doped lithium alumino-phosphate glasses,” *Optical Materials*, vol. 62, 2016, doi: 10.1016/j.optmat.2016.10.051.

[172] I. Kashif, A. Ratep, and G. Adel, “Polarizability, optical basicity and optical properties of SiO2B2O3Bi2O3TeO2 glass system,” *Applied Physics A: Materials Science and Processing*, vol. 124, no. 7, 2018, doi: 10.1007/s00339-018-1904-y.

[173] J. A. Duffy and F. G. K. Baucke, “Redox equilibria and corrosion in molten silicates: Relationship with electrode potentials in aqueous solution,” *Journal of Physical Chemistry*, vol. 99, pp. 9189–9193, 1995.

[174] F. G. K. Baucke, J. A. Duffy, F.G.K.Baucke, and J. A. Duffy, “Oxidation States of Metal Ions in Glass Melts,” *Physics and Chemistry of Glasses*, vol. 35, no. 1, pp. 17–21, 1994.

[175] D. S. GOLDMAN and D. E. BEWLEY, “Ferrous/Ferric Mössbauer Analysis of Simulated Nuclear Waste Glass with and without Computer Fitting,” *Journal of the American Ceramic Society*, vol. 68, no. 12, 1985, doi: 10.1111/j.1151-2916.1985.tb10126.x.

[176] R. A. Lange and I. S. E. Carmichael, “Ferric-ferrous equilibria in Na2O-FeO-Fe2O3-SiO2 melts: Effects of analytical techniques on derived partial molar volumes,” *Geochimica et Cosmochimica Acta*, vol. 53, no. 9, 1989, doi: 10.1016/0016-7037(89)90343-8.

[177] B. O. Mysen, I. S. E. Carmichael, and D. Virgo, “A comparison of iron redox ratios in silicate glasses determined by wet-chemical and 57Fe Mössbauer resonant absorption methods,” *Contributions to Mineralogy and Petrology*, vol. 90, no. 2–3, 1985, doi: 10.1007/BF00378253.

[178] G. Ottonello, R. Moretti, L. Marini, and M. V. Zuccolini, “Oxidation State of Iron in Silicate Glasses and Melts: A Thermochemical Model,” *Chemical Geology*, vol. 174, pp. 157–179, 2001.

[179] R. T. Hunter *et al.*, “Determination of the Fe2+/Fe3+ Ratio in Nuclear Waste Glasses,” *Journal of the American Ceramic Society*, vol. 72, no. 6, 1989, doi: 10.1111/j.1151-2916.1989.tb06249.x.

[180] K. Joseph *et al.*, “Iron phosphate glasses: Bulk properties and atomic scale structure,” *Journal of Nuclear Materials*, vol. 494, 2017, doi: 10.1016/j.jnucmat.2017.07.015.

[181] U. Hoppe, M. Karabulut, E. Metwalli, R. K. Brow, and P. Jóvári, “The Fe-O coordination in iron phosphate glasses by x-ray diffraction with high energy photons,” *Journal of Physics: Condensed Matter*, vol. 15, pp. 6143–6153, 2003.

[182] M. D. Dyar, M. T. Naney, and S. E. Swanson, “Effects of quench methods on Fe3+/Fe2+ ratios: a Mossbauer and wet-chemical study.,” *American Mineralogist*, vol. 72, no. 7–8, 1987.

[183] C.-W. Kim and D. E. Day, “Immobilization of Hanford LAW in iron phosphate glasses,” *Journal of Non-Crystalline Solids*, vol. 331, no. 1–3, pp. 20–31, 2003.

[184] C. S. Ray, X. Fang, M. Karabulut, G. K. Marasinghe, and D. E. Day, “Effect of Melting Temperature and Time on Iron Valence and Crystallization of Iron Phosphate Glasses,” *Journal of Non-Crystalline Solids*, vol. 249, no. 1, pp. 1–16, 1999.

[185] M. Karabulut *et al.*, “An Investigation of the Local Iron Environment in Iron Phosphate Glasses Having Different Fe(II) Concentrations,” *Journal of Non-Crystalline Solids*, vol. 306, no. 2, pp. 182–192, 2002.

[186] B. Pivac, A. Mogus-Milankovic, and D. E. Day, “Iron Valence and Coordination in Phosphate Glasses as Studied by Optical Spectroscopy,” *Journal of Non-Crystalline Solids*, vol. 226, no. 1–2, pp. 41–46, 1998.

[187] C. S. Ray, X. Fang, M. Karabulut, G. K. Marasinghe, and D. E. Day, “Iron Redox and Crystallization of Iron Phosphate Glasses,” in *Environmental Issues and Waste Management Technologies IV*, vol. 43, Westerville, OH: The American Ceramics Society, 1999, pp. 187–194.

[188] R. W. Douglas, P. Nath, and A. Paul, “Oxygen Ion Activity and Its Influence on the Redox Equilibrium in Glasses,” *Physics and Chemistry of Glasses*, vol. 6, no. 6, pp. 216–223, 1965.

[189] J. A. Tangeman, R. Lange, and L. Forman, “Ferric-ferrous equilibria in K2O-FeO-Fe2O3-SiO2 melts,” *Geochimica et Cosmochimica Acta*, vol. 65, no. 11, pp. 1809–1819, 2001.

[190] S. B. Donald, A. M. Swink, and H. D. Schreiber, “High-iron ferric glass,” *Journal of Non-Crystalline Solids*, vol. 352, pp. 539–543, 2006.

[191] O. Pinet, J. Phalippou, and C. DiNardo, “Modeling the redox equilibrium of the Ce4+/Ce3+ couple in silicate glass by voltammetry,” *Journal of Non-Crystalline Solids*, vol. 352, pp. 5382–5390, 2006.

[192] O. Pinet and C. diNardo, “Characteristic Oxygen Fugacity of Redox Couples in Glass Applied to the Analysis of the Redox State of Glass Melts,” in *Processing and Characterization of Electrochemical Materials and Devices*, vol. 109, American Ceramic Society, 2000, pp. 367–376.

[193] J. A. Duffy and F. G. K. Bauke, “Basicity of Solid Glasses and Glass Forming Melts,” in *Physics of Non-Crystalline Solids*, L. D. Pye, W. C. la Course, and H. J. Stevens, Eds. London, UK: Taylor & Francis, 1992, pp. 366–370.

[194] S. Ohashi, M. Kashimura, Y. Uchida, A. McLean, and M. Iwase, “Oxidation-reduction equilibria of ferrous/ferric ions in oxide melts,” *Steel Research*, vol. 71, no. 10, pp. 375–380, 2000.

[195] B. A. Shakhmatkin, N. M. Vedishcheva, and A. C. Wright, “Can thermodynamics relate the properties of melts and glasses to their structure?,” *Journal of Non-Crystalline Solids*, vol. 293–295, pp. 220–226, 2001.

[196] H. v Alberto, J. M. Gil, N. A. DeCampos, and B. O. Mysen, “Redox equilibria of iron in Ti-bearing calcium silicate quenched glasses,” *Journal of Non-Crystalline Solids*, vol. 151, pp. 39–50, 1992.

[197] B. O. Mysen, “No Title,” *American Mineralogical Journal*, vol. 75, p. 120, 1990.

[198] J. F. Stebbins, “No Title,” *Journal of Non-Crystalline Solids*, vol. 106, p. 359, 1988.

[199] D. B. Dingwell and S. L. Webb, “No Title,” *European Journal of Mineralogy*, vol. 2, p. 427, 1990.

[200] P. Richet and Y. Bottinga, “No Title,” *Review of Geophysics*, vol. 24, p. 1, 1986.

[201] B.-S. Bae and M. C. Weinberg, “Oxidation- Reduction Equilibrium in Copper Phosphate Glass Melted in Air,” *Journal of the American Ceramic Society*, vol. 74, no. 12, pp. 3039–3045, 1991.

[202] R. O. Colson *et al.*, “Activities of NiO, FeO and O2- in silicate melts,” *Geochimica et Cosmochimica Acta*, vol. 69, no. 12, pp. 3061–3073, 2005.

[203] W.-G. Seo and F. Tsukihashi, “Thermodynamic and structural properties for the FeO-SiO2 system by using molecular dynamics calculation ,” *Materials Transactions, JIM*, vol. 46, no. 6, pp. 1240–1247, 2005.

[204] F. Gaillard, M. Pichavant, and B. Scaillet, “Experimental Determination of Activities of FeO and Fe2O3 Components in Hydrous Silicic Melts Under Oxidizing Conditions,” *Geochimica et Cosmochimica Acta*, vol. 67, no. 22, pp. 4389–4409, 2003.

[205] J. A. Duffy, “The electronic polarisability of oxygen in glass and the effect of composition,” *Journal of Non-Crystalline Solids*, vol. 297, pp. 275–284, 2002.

[206] J. A. Duffy and M. D. Ingram, “Nephelauxetic effect and Pauling electronegativity,” *Journal of the Chemical Society, Chemical Communications*, pp. 635–636, 1973.

[207] J. A. Duffy and M. D. Ingram, “Establishment of an optical scale for Lewis Basicity in inorganic oxyacids, molten salts, and glasses,” *Journal of the American Chemical Society*, vol. 93, pp. 6448–6454, 1971.

[208] J. A. Duffy and M. D. Ingram, “An Interpretation of Glass Chemistry in Terms of the Optical Basicity Concept,” *Journal of Non-Crystalline Solids*, vol. 21, pp. 373–410, 1976.

[209] J. A. Duffy and M. D. Ingram, “Optical Basicity,” in *Optical Properties of Glass*, D. R. Uhlmann and N. J. Kreidl, Eds. Westerville, OH: American Ceramic Society, 1991, pp. 159–184.

[210] J. A. Duffy, “Redox Equilibria in Glass,” *Journal of Non-Crystalline Solids*, vol. 196, pp. 45–50, 1996.

[211] S. Sumita, Y. Matsumoto, K. Morinaga, and T. Yanagase, “The Optical Basicity and Fe2+-Fe3+ Redox in Oxyacid Salt Systems,” *Transactions of the Japan Institute of Metals*, vol. 23, no. 7, pp. 360–367, 1982.

[212] J. A. Duffy and R. J. Grant, “Effect of Temperature on Optical Basicity in the Sodium Oxide- Boric Oxide Glass System,” *Journal of Physical Chemistry*, vol. 79, no. 25, pp. 2780–2784, 1975.

[213] L. Pauling, *The Nature of the Chemical Bond*. Ithaca, New York: Cornell University Press, 1948.

[214] J. H. Binks and J. A. Duffy, “Chemical bonding in rock salt structured transition metal oxides,” *Journal of Solid State Chemistry*, vol. 87, no. 1, 1990, doi: 10.1016/0022-4596(90)90082-9.

[215] G. Adam and J. H. Gibbs, “On the temperature dependence of cooperative relaxation properties in glass-forming liquids,” *The Journal of Chemical Physics*, vol. 43, no. 1, 1965, doi: 10.1063/1.1696442.

[216] L. Berthier, M. Ozawa, and C. Scalliet, “Configurational entropy of glass-forming liquids,” *Journal of Chemical Physics*, vol. 150, no. 16. 2019. doi: 10.1063/1.5091961.

[217] A. Al-Shahrani, A. Al-Hajry, and M. M. El-Desoky, “Electrical relaxation in mixed lithium and sodium iron phosphate glasses,” *Physica B*, vol. 364, pp. 248–254, 2005.

[218] X. Fang, C. S. Ray, and D. E. Day, “Glass Transition and Fragility of Iron Phosphate Glasses. II. Effect of Mixed-Alkali,” *Journal of Non-Crystalline Solids*, vol. 319, no. 3, pp. 314–321, 2003.

[219] X. Fang, “An investigation of iron phosphate glasses,” 2000.

[220] P. A. Bingham, R. J. Hand, S. D. Forder, A. Lavaysierre, S. H. Kilcoyne, and I. Yasin, “Preliminary Studies of Sulphate Solubility and Redox in 60P2O5-40Fe2O3 Glasses,” *Materials Letters*, vol. 60, pp. 844–847, 2006.

[221] M. Karabulut, E. Metwalli, D. E. Day, and R. K. Brow, “Mössbauer and IR investigations of iron ultraphosphate glasses,” *Journal of Non-Crystalline Solids*, vol. 328, pp. 199–206, 2003.

[222] A. Bézos and E. Humler, “The Fe3+/ΣFe Ratios of MORB Glasses and Their Implications for Mantle Melting,” *Geochimica et Cosmochimica Acta*, vol. 69, no. 3, pp. 711–725, 2005.

[223] D. M. Christie, I. S. E. Carmichael, and C. H. Langmuir, “Oxidation states of mid-ocean ridge basalt glasses,” *Earth and Planetary Science Letters*, vol. 79, pp. 379–411, 1986.

[224] P. Wallace and I. S. E. Carmichael, “Sulfur in basaltic magmas,” *Geochimica et Cosmochimica Acta*, vol. 56, pp. 1863–1874, 1992.

[225] L. Zhang, R. K. Brow, M. E. Schlesinger, L. Ghussn, and E. D. Zanotto, "Glass formation from iron-rich phosphate melts," *submitted to Journal of Non-Crystalline Solids*.

[226] G. Ottonello, R. Moretti, L. Marini, and M. V. Zuccolini, "Oxidation State of Iron in Silicate Glasses and Melts: A Thermochemical Model," *Chemical Geology*, vol. 174, pp. 157–179, 2001.

[227] P. J. Flory, "Random Reorganization of Molecular Weight Distribution in Linear Condensation Polymers," *Journal of the American Chemical Society*, vol. 64, no. 9, 1942, doi: 10.1021/ja01261a049.

[228] B. C. Sales, L. A. Boatner, and J. O. Ramey, "Chromatographic studies of the structure of amorphous phosphates: a review," *Journal of Non-Crystalline Solids*, vol. 263 & 264, pp. 155–166, 2000.

[229] P. A. Bingham, R. J. Hand, O. M. Hannant, S. D. Forder, and S. H. Kilcoyne, "Effects of modifier additions on the thermal properties, chemical durability, oxidation state and structure of iron phosphate glasses," *Journal of Non-Crystalline Solids*, vol. 355, no. 28–30, 2009, doi: 10.1016/j.jnoncrysol.2009.03.008.

[230] X. Yu, D. E. Day, G. J. Long, and R. K. Brow, "Properties and structure of sodium-iron phosphate glasses," *Journal of Non-Crystalline Solids*, vol. 215, no. 1, pp. 21–31, 1997.

[231] S. T. Reis, M. Karabulut, and D. E. Day, "Structural Features and Properties of Lead-Iron-Phosphate Nuclear Wasteforms," *Journal of Nuclear Materials*, vol. 304, no. 2–3, pp. 87–95, 2002.

[232] X. Fang, C. S. Ray, G. K. Marasinghe, and D. E. Day, "Properties of Mixed Na2O and K2O Iron Phosphate Glasses," *Journal of Non-Crystalline Solids*, vol. 263 & 264, pp. 293–298, 2000.

[233] S. T. Reis, M. Karabulut, and D. E. Day, "Chemical Durability and Structure of Zinc-Iron Phosphate Glasses," *Journal of Non-Crystalline Solids*, vol. 292, no. 1–3, pp. 150–157, 2001.

[234] B. C. Bunker, G. W. Arnold, and J. A. Wilder, "Phosphate glass dissolution in aqueous solutions," *Journal of Non-Crystalline Solids*, vol. 64, pp. 291–316, 1984.

[235] R. Conradt, "A proposition for an improved theoretical treatment of the corrosion of multi-component glasses," *Journal of Nuclear Materials*, vol. 298, pp. 9–26, 2001.

[236] H. Gao, T. Tan, and D. Wang, “Effect of composition on the release kinetics of phosphate controlled release glasses in aqueous medium,” *Journal of Controlled Release*, vol. 96, no. 1, 2004, doi: 10.1016/j.jconrel.2003.12.030.

[237] H. Gao, T. Tan, and D. Wang, “Dissolution mechanism and release kinetics of phosphate controlled release glasses in aqueous medium,” *Journal of Controlled Release*, vol. 96, pp. 21–28, 2004.

[238] A. Paul, “Chemical durability of glasses; A thermodynamic approach,” *Journal of Materials Science*, vol. 12, pp. 2246–2268, 1977.

[239] C. M. Jantzen and M. J. Plodinec, “Thermodynamic model of natural, medieval and nuclear waste glass durability,” *Journal of Non-Crystalline Solids*, vol. 67, pp. 207–223, 1984.

[240] C. M. Jantzen, “Nuclear waste glass durability:I, Predicting environmental response from thermodynamic (Pourbaix) diagrams,” *Journal of the American Ceramic Society*, vol. 75, no. 9, pp. 2433–2448, 1992.

[241] M. J. Plodinec, C. M. Jentzen, and G. G. Wicks, “STABILITY OF RADIOACTIVE WASTE GLASSES ASSESSED FROM HYDRATION THERMODYNAMICS.,” in *Materials Research Society Symposia Proceedings*, 1984, vol. 26. doi: 10.1557/proc-26-755.

[242] M. J. Plodinec, C. M. Jentzen, and G. G. Wicks, “STABILITY OF RADIOACTIVE WASTE GLASSES ASSESSED FROM HYDRATION THERMODYNAMICS.,” in *Materials Research Society Symposia Proceedings*, 1984, vol. 26. doi: 10.1557/proc-26-755.

[243] R. Conradt, “Chemical durability of oxide glasses in aqueous solutions: a review,” *Journal of the American Ceramic Society*, vol. 91, pp. 728–735, 2008.

[244] R. Conradt and P. Geasee, “An improved thermodynamic approach to the stability of multi-component silicate glasses in aqueous solutions,” *Berichte der Bunsen-Gesellschaft fuer Physikalische Chemie*, vol. 100, no. 9, pp. 1408–1410, 1996.

[245] R. K. Brow, “Nature of alumina in phosphate glass: I, Properties of sodium aluminophosphate glass,” *Journal of the American Ceramic Society*, vol. 76, no. 4, pp. 913–918, 1993.

[246] J. E. Dickinson, “No Title,” *Chim. Chron.*, vol. 23, pp. 355–360, 1994.

[247] T. MINAMF and J. D. MACKENZIE, “Thermal Expansion and Chemical Durability of Phosphate Glasses,” *Journal of the American Ceramic Society*, vol. 60, no. 5–6, 1977, doi: 10.1111/j.1151-2916.1977.tb14113.x.

[248] J. A. Duffy and M. D. Ingram, “Solvent properties of glass melts: Resemblance to aqueous solutions,” *Comptes Rendus Chimie*, vol. 5, no. 11, 2002, doi: 10.1016/S1631-0748(02)01448-0.

[249] B. C. Tischendorf, “Interactions between water and phosphate glasses,” 2005.

[250] B. M. J. Smets, M. G. W. Tholen, and T. P. A. Lommen, “The effect of divalent cations on the leaching kinetics of glass,” *Journal of Non-Crystalline Solids*, vol. 65, no. 2–3, 1984, doi: 10.1016/0022-3093(84)90056-5.

[251] H. Takebe, Y. Baba, and M. Kuwabara, “Compositional dependence of water durability in meta-phosphate glasses.”

[252] R. D. Ewing, W. J. Weber, and F. W. Clinard, “Radiation effects in nuclear waste forms for high-level radioactive waste,” *Progress in Nuclear Energy*, vol. 29, no. 2, pp. 63–127, 1995.

[253] J. Jiusti, D. R. Cassar, and E. D. Zanotto, “Which glass stability parameters can assess the glass-forming ability of oxide systems?,” *International Journal of Applied Glass Science*, vol. 11, no. 4, 2020, doi: 10.1111/ijag.15416.

[254] A. Zawada, H. Hessenkemper, D. Hohne, and P. Bieniarz, “No Title,” *Glass Science and Technology (Amsterdam)*, vol. 78, p. 106, 2005.

[255] M. L. F. Nascimento, L. A. Souza, E. B. Ferreira, and E. D. Zanotto, “Can Glass Stability Parameters Infer Glass Forming Ability?,” *Journal of Non-Crystalline Solids*, vol. 351, no. 40–42, pp. 3296–3308, 2005.

[256] I. Avramov, E. D. Zanotto, and M. O. Prado, “Glass forming ability (on cooling) and stability (on heating),” pp. 60–65.

[257] I. Avramov, E. D. Zanotto, and M. O. Prado, “Glass-forming Ability Versus Stability of Silicate Glasses. II. Theoretical Demonstration,” *Journal of Non-Crystalline Solids*, vol. 320, no. 1–3, pp. 9–20, 2003.

[258] M. C. Weinberg, “No Title,” *Physics and Chemistry of Glasses*, vol. 35, p. 119, 1994.

[259] A. Hruby, “No Title,” *Czechoslovak Journal of Physics*, vol. B 22, p. 1187, 1972.

[260] H. E. Kissinger, “Variation of peak temperature with heating rate in differential thermal analysis,” *Journal of Research of the National Bureau of Standards*, vol. 57, no. 4, 1956, doi: 10.6028/jres.057.026.

[261] H. E. Kissinger, “Reaction Kinetics in Differential Thermal Analysis,” *Analytical Chemistry*, vol. 29, no. 11, 1957, doi: 10.1021/ac60131a045.

[262] C. S. Ray, Q. Yang, W. Huang, and D. E. Day, “Surface and Internal Crystallization in Glasses as Determined by Differential Thermal Analysis,” *Journal of the American Ceramic Society*, vol. 79, no. 12, pp. 3155–3160, 1996.

[263] L. Zhang, L. Ghussn, M. L. Schmitt, E. D. Zanotto, R. K. Brow, and M. E. Schlesinger, “Thermal stability of glasses from the Fe4(P2O 7)3-Fe(PO3)3 system,” in *Journal of Non-Crystalline Solids*, 2010, vol. 356, no. 52–54. doi: 10.1016/j.jnoncrysol.2010.03.044.

[264] L. Ghussn, R. M. C. V. Reis, R. K. Brow, and D. B. Baker, “Color bleaching and oxygen diffusion in a niobium phosphate glass,” *Journal of Non-Crystalline Solids*, vol. 401, 2014, doi: 10.1016/j.jnoncrysol.2013.11.004.

[265] C. Ades, T. Toganidis, and J. P. Traverse, “High temperature optical spectra of soda-lime-silica glasses and modelization in view of energetic applications,” *Journal of Non-Crystalline Solids*, vol. 125, no. 3, 1990, doi: 10.1016/0022-3093(90)90858-J.

[266] R. Carl, S. Gerlach, and C. Rüssel, “The effect of composition on UV-vis-NIR spectra of iron doped glasses in the systems Na2O/MgO/SiO2 and Na2O/MgO/Al2O3/SiO2,” *Journal of Non-Crystalline Solids*, vol. 353, no. 3, 2007, doi: 10.1016/j.jnoncrysol.2006.11.010.

[267] A. K. Mandal, P. K. Sinha, D. Das, C. Guha, and R. Sen, “Higher Fe2+/total Fe ratio in iron doped phosphate glass melted by microwave heating,” *Materials Research Bulletin*, vol. 63, 2015, doi: 10.1016/j.materresbull.2014.11.052.

[268] P. R. Ehrmann, J. H. Campbell, T. I. Suratwala, J. S. Hayden, D. Krashkevich, and K. Takeuchi, “Optical Loss and Nd3+ Non-Radiative Relaxation by Cu, Fe and Several Rare Earth Impurities in Phosphate Laser Glasses,” *Journal of Non-Crystalline Solids*, vol. 263 & 264, pp. 251–262, 2000.

[269] H. Es-soufi, L. Bih, B. Manoun, and P. Lazor, “Structure, thermal analysis and optical properties of lithium tungsten-titanophosphate glasses,” *Journal of Non-Crystalline Solids*, vol. 463, 2017, doi: 10.1016/j.jnoncrysol.2017.02.013.

[270] S. Rada, A. Dehelean, and E. Culea, “FTIR, Raman, and UV-Vis spectroscopic and DFT investigations of the structure of iron-lead-tellurate glasses,” *Journal of Molecular Modeling*, vol. 17, no. 8, 2011, doi: 10.1007/s00894-010-0911-5.

[271] D. Ehrt, M. Leister, and A. Matthai, “Redox behaviour in glass forming melts,” *Molten Salt Forum*, vol. 5–6, pp. 547–554, 1998.

[272] A. M. BISHAY and L. MAKAR, “Role of Iron in Calcium Phosphate Glasses,” *Journal of the American Ceramic Society*, vol. 52, no. 11, 1969, doi: 10.1111/j.1151-2916.1969.tb15849.x.

[273] E. N. Boulos, L. B. Glebov, and T. v. Smirnova, “Absorption of iron and water in the Na2O-CaO-MgO-SiO2 glasses. I. Separation of ferrous and hydroxyl spectra in the near IR region,” *Journal of Non-Crystalline Solids*, vol. 221, no. 2–3, 1997, doi: 10.1016/S0022-3093(97)00334-7.

[274] D. A. Rayan, Y. H. Elbashar, M. M. Rashad, and A. El-Korashy, “Optical spectroscopic analysis of cupric oxide doped barium phosphate glass for bandpass absorption filter,” *Journal of Non-Crystalline Solids*, vol. 382, 2013, doi: 10.1016/j.jnoncrysol.2013.10.002.

[275] E. A. Davis and N. F. Mott, “Conduction in non-crystalline systems V. Conductivity, optical absorption and photoconductivity in amorphous semiconductors,” *Philosophical Magazine*, vol. 22, no. 179, 1970, doi: 10.1080/14786437008221061.

[276] J. Tauc, “Optical Properties of Amorphous Semiconductors,” in *Amorphous and Liquid Semiconductors*, 1974. doi: 10.1007/978-1-4615-8705-7_4.

[277] T. S. Soliman and S. A. Vshivkov, “Effect of Fe nanoparticles on the structure and optical properties of polyvinyl alcohol nanocomposite films,” *Journal of Non-Crystalline Solids*, vol. 519, 2019, doi: 10.1016/j.jnoncrysol.2019.05.028.

[278] S. Rada, M. Rada, and E. Culea, “Structural and optical properties of the gadolinium-lead-germanate glasses,” *Journal of Non-Crystalline Solids*, vol. 357, no. 1, 2011, doi: 10.1016/j.jnoncrysol.2010.10.013.

[279] M. Rada, E. Culea, S. Rada, A. Bot, N. Aldea, and V. Rednic, “Anomalies of some physical properties and electrochemical performance of lithium-lead-germanate glasses,” *Journal of Non-Crystalline Solids*, vol. 358, no. 23, 2012, doi: 10.1016/j.jnoncrysol.2012.08.026.

[280] H. J. Li, X. F. Liang, H. J. Yu, D. Q. Yang, and S. Y. Yang, “Studies of structure of calcium–iron phosphate glasses by infrared, Raman and UV–Vis spectroscopies,” *Indian Journal of Physics*, vol. 90, no. 6, 2016, doi: 10.1007/s12648-015-0794-5.

[281] I. Jlassi, H. Elhouichet, and M. Ferid, “Influence of MgO on structure and optical properties of alumino-lithium-phosphate glasses,” *Physica E: Low-Dimensional Systems and Nanostructures*, vol. 81, 2016, doi: 10.1016/j.physe.2016.03.017.

[282] L. Rus *et al.*, “Structural and optical properties of the lead based glasses containing iron (III) oxide,” *Journal of Non-Crystalline Solids*, vol. 402, 2014, doi: 10.1016/j.jnoncrysol.2014.05.026.

[283] F. Urbach, “The long-wavelength edge of photographic sensitivity and of the electronic Absorption of Solids [8],” *Physical Review*, vol. 92, no. 5. 1953. doi: 10.1103/PhysRev.92.1324.

[284] D. C. Kaseman, T. Endo, and S. Sen, “Structural disorder and the effects of aging in a phosphate glass: Results from two-dimensional 31P PASS NMR spectroscopy,” *Journal of Non-Crystalline Solids*, vol. 359, no. 1, 2013, doi: 10.1016/j.jnoncrysol.2012.09.030.

[285] A. Montenero, M. Friggeri, D. C. Giori, N. Belkhiria, and L. D. Pye, “Iron-soda-silica glasses: Preparation, properties, structure,” *Journal of Non-Crystalline Solids*, vol. 84, no. 1–3, 1986, doi: 10.1016/0022-3093(86)90761-1.

[286] K. Zirkelbach and R. Brückner, “Spectroscopic Investigations of Barium Aluminophosphate Glasses Containing Vanadium, Iron and Manganese Oxide,” *Glastechnische Berichte*, vol. 60, no. 9, pp. 312–323, 1987.

[287] S. L. Reddy, T. Endo, and G. S. Reddy, *Advanced Aspects of Spectroscopy, Chapter 1: Electronic (Absorption) Spectra of 3d Transition Metal Complexes*. 2012. doi: 10.5772/2757.

[288] P. A. Bingham, J. M. Parker, T. M. Searle, and I. Smith, “Local structure and medium range ordering of tetrahedrally coordinated Fe3+ ions in alkali-alkaline earth-silica glasses,” *Journal of Non-Crystalline Solids*, vol. 353, no. 24–25, 2007, doi: 10.1016/j.jnoncrysol.2007.03.017.

[289] Y. Tanabe and S. Sugano, “On the Absorption Spectra of Complex Ions II,” *Journal of the Physical Society of Japan*, vol. 9, no. 5, 1954, doi: 10.1143/JPSJ.9.766.

[290] L. C. Xue *et al.*, “Study of electron transition energies between anions and cations in spinel ferrites using differential UV-vis absorption spectra,” *Physica B: Condensed Matter*, vol. 492, 2016, doi: 10.1016/j.physb.2016.04.002.

[291] C. R. Bamford, “The application of the ligand field theory to coloured glasses,” *Phys. Chem. Glasses*, vol. 3, 1962.

[292] C. R. Kurkjian, “Mössbauer spectroscopy in inorganic glasses,” *Journal of Non-Crystalline Solids*, vol. 3, no. 2, 1970, doi: 10.1016/0022-3093(70)90174-2.

[293] Chr. K. Jørgensen, C.-H. de Verdier, J. Glomset, and N. A. Sörensen, “Studies of Absorption Spectra. IV. Some New Transition Group Bands of Low Intensity.,” *Acta Chemica Scandinavica*, vol. 8, 1954, doi: 10.3891/acta.chem.scand.08-1502.

VITA

Melodie Linda Schmitt grew up in beautiful upstate New York and graduated as Valedictorian from Greece Arcadia High School in 1999. She continued on to Alfred University, where she earned six departmental awards and spent a semester studying in England and backpacking Europe. She graduated summa cum laude with honors in 2004 with a Bachelor of Arts in both Mathematics and Physics and Bachelor of Science in Ceramic Engineering, completing her undergraduate thesis under Dr. Arun Varshneya. Captivated by both the magic of Alfred and her affection for Harlan, she stayed on to earn a Master of Science in Glass Engineering Science in 2005 under Dr. James Shelby.

Melodie then moved to Rolla, Missouri to start her PhD studies under Dr. Richard Brow. After completing her coursework and research, presenting at many conferences, attending a workshop in Japan, spending a research semester in Brazil, and earning an Outstanding Graduate Student departmental award, she moved to Albuquerque, NM with her husband before having finished her dissertation or defending her degree. In the years that followed, Melodie pursued her passions for animals and running, working for Animal Humane New Mexico as well as running an ultramarathon. Her family grew to include 5 rescue animals, who were then joined by her two children, Lillietta and Porter. She relished in every moment of being their stay-at-home mom in the succeeding years.

In a serendipitous happenstance, Melodie was given the opportunity to complete her dissertation and defend her degree roughly ten years after leaving Rolla. With the support of her family and committee, she earned her Doctor of Philosophy in Materials Science and Engineering in May 2022 from Missouri S&T. Although now officially a Doctor, her favorite title is still Mom.